Doctorate Dissertation

博士論文

Investigation of the optical breakdown characteristics of dielectric materials induced by ultrashort laser pulses

(超短パルスレーザーによる誘電体破壊特性の探索)

A Dissertation Submitted for the Degree of Doctor of Philosophy
December 2018

平成30年12月博士（理学）申請

Department of Physics, Graduate School of Science,
The University of Tokyo

東京大学理学系研究科物理学専攻

Haruyuki Sakurai

櫻井　治之

Abstract

It has been over 50 years since the invention of the first laser, which opened the doors to the exploration of physical phenomena under unprecedented high intensity electric fields. The optical breakdown of dielectric materials is one such phenomenon which became observable. The process has attracted much attention from industry in recent years as an alternative to traditional machining techniques. By utilizing breakdown and ablation processes, the laser has developed as a versatile tool to realize precise, free-form materials processing.

Despite the increased application, there is still much to be uncovered regarding the basic physics of the process. The fundamental process of material breakdown involves phenomena rooted in a wide range of academic fields, from optics and condensed matter physics, to thermodynamics and mechanics. The theories involved must describe interactions evolving over multiple timescales in a non-equilibrium, non-perturbative regime. Experimental exploration is markedly difficult as well, for it requires the accurate measurement of the properties of breaking materials at ultrafast timescales. As such, despite decades of research, there is much left unknown about the physics governing the breakdown process. However, such elucidation is important for the continued development of industrial technology, and will serve to improve our understanding of physics in this extreme parameter regime.

In this dissertation, we focus on experimentally characterizing the breakdown characteristics of dielectric materials by ultrashort laser pulses. We focus mainly on morphological methods. Whereas the morphology is one of the first features studied in conventional analysis, it is also one of the most important result of ablation. The full information gained from morphology measurements has hardly been utilized in the literature. We show in this thesis how careful analysis of morphological data can shed light upon the processes involved in ablation both in the single and multiple-pulse regime.

Single Pulse Crater Analysis of Dielectric Materials

Traditional analysis of ablation morphology have mainly extracted a single representative value from a three-dimensional profile, such as the diameter of an ablation region, or the depth of the crater developed. However, far more information is contained within a single crater, where a full two-dimensional space of parameters is available for analysis.

In order to fully utilize this data, we develop the fluence mapping technique. It involves spatially correlating the local beam fluence (pulse energy/unit area) profile with

the local ablated volume. To do this, we use a home-made small-pixel beam profiler, and correlate this data to the morphology gained from laser scanning microscopy. We can then create a histogram of the local crater depths as a function of the local fluence. This analysis presents several advantages to traditional measurements, such as being able to accurately analyze data gained from notably non-Gaussian pulses, as well as the efficient extraction of threshold fluences. Fundamentally, it allows for the evaluation of the locality of the ablation phenomena.

As an application where we can fully utilize the robustness of this method to systematic errors induced by non-ideal spatial profiles, we measure the ablation due to a high-power optical parametric amplifier, a light source where the beam spatial profile is known to systematically vary between wavelengths. As representative samples, we measure the wavelength dependent ablation thresholds of two materials: TiO_2 (rutile) and Al_2O_3 (sapphire). We focus on solving a fundamental open question on ablation: whether the multiphoton nature of the initial excitation is imprinted on the final ablation thresholds. For both materials, and for the first time in the literature for a single pulse, we succeed in observing a step-like behavior in the threshold due to changes in the lowest-order allowed multiphoton transition. We analyze this data and discuss the implication they have on the traditional rate-equation approach to modeling the electronic excitation process in ablation.

Exploration of Multiple-Pulse Ablation Characteristics

While uncovering the fundamental processes occurring during single-pulse ablation is important from a fundamental perspective, there is a large gap between this situation and the actual processing conditions seen in applications. In general, a multitude of pulses are irradiated onto an evolving material surface. In order to address this gap, in the latter half of the dissertation, we focus on two intrinsically multiple-pulse features in ablation which must be qualified in order to properly model more realistic situations.

In the first half of this part, we address the problem of damage incubation, where the formation of defects within the material alters the light-absorption characteristics for later pulses. This effect can cause macroscopic changes in the way that material is ablated from the surface. This can be seen prominently in the laser grooving of sapphire, where pulses are scanned along the material surface. We create an empirical model for the light absorption in this scenario, and derive simple scaling relationships to predict the material morphology for varying pulse energies and spacing.

In the second half, we address the effect of the changing surface angles relative to the incident pulse. The angling behavior seen in grooving results in an eventual saturation of depth, due to a decreasing projected fluence and optical transmissivity. We then show how this saturation trend can be utilized to create uniform needle-like protrusions on a sample surface. We use this to create moth-eye anti-reflection structures on the surface of silicon. We demonstrate its performance with standard terahertz time-domain spectroscopy measurements.

Acknowledgment

The research presented in this dissertation was conducted during my PhD studies within the Gonokami-Yumoto-Ideguchi Group in the Department of Physics at the University of Tokyo. Parts of the research was also conducted at the Fraunhofer Institute for Laser Technology ILT in Aachen, Germany. I am blessed to have had the opportunity to study and research in such rich environments. The thesis was examined by an examination committee consisting of Prof. Ryo Shimano, Prof. Norikatsu Mio, Prof. Osamu Sugino, Prof. Yuichi Takase, and Lecturer Takuro Ideguchi. Their comments were critical in creating this final form, and I would like to express my gratitude for their time and efforts.

I would like to thank Prof. Makoto Kuwata-Gonokami and Prof. Junji Yumoto, my advisors in this academic endeavor. Prof. Gonokami first introduced me to laser processing as a topic of study, and it was every-bit as difficult as he cautioned. His insights regarding the optical processes within solids were always deeply appreciated. Prof. Yumoto provided me with not only advice, but with many opportunities to meet with a vast variety of people. His knowledge about industry provided a fresh point of view from which to analyze and present my work.

I am especially indebted to Assistant Prof. Kuniaki Konishi. As the direct overseer of my research, he played a crucial role in all experiments, from design to analysis. Associate Prof. Hiroharu Tamaru from the Institute for Photon Science and Technology has always provided valuable feedback regarding my research. In particular, the use of the Raspberry Pi camera module, crucial to the thesis, would not have materialized without discussions with him. Assistant Prof. Yasushi Shinohara from the Ishikawa group at the University of Tokyo has always come to my aid when the theory became difficult. I express my utmost gratitude for his assistance here.

Modern science is a group effort, and my research has been no exception. I would like to thank all the people, both past and present, who have worked on studying ablation with me in the lab in my five years at the university. These include Mr. Yo Iida, Mr. Hiroki Matsui, Mr. Akira Mizutani, Mr. Ryosuke Nakamura, Mr. Satoshi Tanimoto, Mr. Ryota Takaku, and Mr. Masaki Ochi. Together, we overcame many a frustrating obstacle in our day-to-day ablation experiments; there is a certain camaraderie to that experience, and though the tasks may have been difficult, I cherish the memories. Regarding the work done at ILT, I would like to thank my friend Mr. Chao He, who not only helped with experiment, but in day-to-day task in a foreign country. I am grateful for Dr. Arnold Gillner and Prof. Reinhart Poprawe for providing this opportunity to study in their lab. The work on the moth-eye structures would not have been possible without the

input from Associate Prof. Tomotake Matsumura, Prof. Nobuhiko Katayama, and Dr. Yuki Sakurai from the Kavli Institute for the Physics and Mathematics of the Universe (IPMU), in the University of Tokyo. I would also like to thank Dr. Natsuki Nemoto and Ms. Mizuho Matoba for assistance with terahertz measurements, both whom I consider good friends as well as colleagues.

Good science is not possible without good discussion. I appreciate all the input and feedback from the academic staff of the group (some former), including Dr. Kosuke Yoshioka, Dr. Takuro Ideguchi, Dr. Munekazu Horikoshi, Mr. Yusuke Morita, Dr. Junko Omachi, Dr. Natsuki Kanda, Dr. Daisuke Hirano, Dr. Davide Bossini, Mr. Kentaro Soeda, Mr. Hiroyuki Yasukochi, Dr. Faris Sinjab, and Dr. Venkata Ramaiah Badarla. Interactions with the students (both past and present) of the group were always very enjoyable. These include Mr. Hiroaki Kitanaka, Mr. Yuki Nagakubo, Dr. Takuya Ikemachi, Mr. Hirosuke Suzuki, Mr. Shuntaro Ishii, Mr. Yukihito Aratake, Mr. Kazuki Hashimoto, Mr. Peiyu Xia, Mr. Yiping Chen, Mr. Wataru Komatsubara, Mr. Miu Tamamitsu, Mr. Keiichiro Toda, Mr. Takahiro Tsumori, Mr. Akira Kawai, and Mr. Takehiro Kageyama.

I would also like to take a paragraph to thank Dr. Yusuke Arashida. His scientific and technical advice over the years were critical to my work. More importantly, and as promised, I would like to acknowledge his significant contribution of beer over the years, which has increased my quality of life greatly. May the hop be with him, always.

A great part of my student life was supported by the secretaries of the lab. I would like to express my gratitude to Ms. Akane Oshima, Ms. Masako Shirahama, Ms. Kimiko Kowashi, and Ms. Kimiko Kitakoji.

I would also like to express my gratitude to the Advanced Leading Graduate Course for Photon Science (ALPS) program for their academic and financial support. The quarterly meetings with Professor Hasegawa Tetsuya and other ALPS students served as good benchmarks to my research.

Lastly, special thanks should be said to my friends and family, who were always supportive of my ventures. I hope to one day be able to repay this kindness in full.

Contents

Chapter 1.

Introduction

Progress in physics has always walked hand-in-hand with progress in technology. For example, the field of nonlinear optics, where the nonlinear material response under high intensity electric fields is studied, became possible due to the invention of the laser. Second harmonic generation, perhaps the most renown phenomenon in nonlinear optics, was experimentally observed just one year after the invention of the laser. Inversely, principles from nonlinear optics, such as Kerr lensing, are now used in a wide range of modern pulsed-laser light sources.

Laser material processing is another such field which has a close fundamental-application relationship. The field is also almost as old as the laser itself, and has attracted the attention of many in academia for over half a century [1]. Progress in the field and surrounding laser technology has seen the quick rise of laser processing within industry to improve and/or replace traditional processing techniques. From cutting and drilling, to welding and cleaning, as well as exotic surface treatment processing, the laser has become a versatile tool in a wide range of applications [2].

However, while the adoption of the laser has been accelerating, its effective use is still a challenge. Current processing techniques are developed mainly from trial-and-error studies, which are both time-consuming and costly. To remove this obstacle, theoretical methods to predict, control, and enhance the process have come into high demand. A vibrant community has developed in academia to meet this demand, and study the physics of laser material processing [3]. However, it remains that there is a long list of issues needing study within this rapidly expanding field.

In this dissertation, we deal with a major subset of the study of laser processing: the study of optical breakdown induced on the material surface, causing material ejection, or *laser ablation*. We put a particular focus on transparent materials, where the added nonlinearity of the initial excitation complicates the process. For the light source, we deal with ultrafast pulsed-lasers, which holds several distinct advantages in the context of ablation. As the laser pulse is short, the effects of transport and relaxation processes can be ignored. The lattice can also be considered static at these time scales. From an experimental perspective, the high reproducibility of femtosecond ablation also makes it a good starting point for any study.

Ablation is a challenging field of study. The process involves fundamental processes rooted in a wide range of academic fields, from electromagnetism and condensed matter physics, to plasma physics, mechanics, and thermodynamics. Even with proficiency in the above fields, the applicability of conventional theories must also be put into question. Typical physical theories deal with perturbative, closed systems at equilibrium. The process of ablation, at a whole, is none of these.

1.1. Laser ablation as an experimental science

As is the case with difficult problems in physics, we seek to gain more information on the fundamental processes and interactions in ablation through experiment. A characterizing feature of ablation is that, inherently, the process is irreversible. The material under study is destroyed, thus leaving a large set of traditional optical techniques hard or impossible to implement. Thus, any feasible experimental study must come up with a way to extract high-quality information from a notedly finite number of experimental data.

As an overarching methodology in the studies in this dissertation, we focus on the morphology of ablated craters. The morphology is one of the most basic features studied in ablation, and one of the first things observed in experimental studies. It is also the final morphology which is, first-and-foremost, critical to applications in industry. While studies in morphology have generally fallen out of favor in many fundamental studies in lieu of more dynamic pump-probe techniques, the morphology, combined with purpose-designed experimental procedures, still remains a powerful tool. Analyzed properly, the morphology can yield a plethora of new and relevant data in all forms of laser ablation, from single-pulse ablation to multiple-pulse grooving schemes.

1.2. Aims and overview

This dissertation consists of seven chapters. Thematically, the chapters can be broken into three sections: theory (chapter 2), single-pulse ablation experiments (chapter 3 and 4), and multiple-pulse ablation experiments (chapter 5 and 6).

Chapter 2 details the theoretical background of the laser ablation phenomena, with a particular focus on the single-pulse ablation of dielectric materials. In the first-half, we introduce the spatiotemporal scales of ablation to familiarize the reader with the general assumptions made during discussions. In the latter half, we cover the rate equation model often used in modern ablation studies. It is the de facto standard model of ablation; while the specifics have been modified, it has generally stood the test of time for over two decades since its first formulation for ultrashort laser ablation by Stuart *et al.* in 1995 [4].

In ablation studies, one of the most important experimental observable is the ablation threshold of materials: the pulse energy density required to ablate the material. In chapter 3, we introduce a new method to better utilize the full morphological information contained in one single-pulse ablated crater. Whereas traditional measurements have focused on extracting a single representative value, such as depth or crater diameter, we develop a new method to fully correlate all microscope points to the incident fluence of the pulse. This new technique allows for robust and accurate measurements of ablation features, including the threshold, and also allows us to make some fundamentally new insights regarding the locality of ablation itself, a feature often taken for granted.

In chapter 4, we use the technique developed in chapter 3 to measure the wavelength dependence of the ablation threshold of materials. The new technique shows promising robustness, allowing us to extract data with unprecedented accuracy when compared to values in the literature. From the measured thresholds, we analyze the physics suggested, some of which highlight fundamental deficiencies in current rate equation models.

While chapter 3 and 4 deal with fundamentally important problems regarding ablation, the situation covered is that of a *single* pulse. While this allows for a clearer study of the physics involved, it is notably different from the irradiation schemes seen in real applications; it is almost never the case that materials processing is done with a single pulse. To bridge fundamental physics to applications, this divide must be bridged. In chapter 5 and 6, we study specific multiple-pulse effects encountered in real-life applications.

Chapter 5 involves the study of laser-induced changes in the material properties following successive laser irradiation. While a laser may not have the power to remove a material, it can still induce changes to its optical properties. This process, often called *damage incubation*, is critical in the first stages of multiple-pulse ablation. We study ways to predict its effects in the case of a representative case of laser grooving on the surface of sapphire.

In chapter 6, we study the effects of changing global morphology on the laser grooving process. As aspect ratios of grooves increase with the progression of processing, processing rates eventually saturate to create stable v-shaped grooves. In the first half, we characterize this saturation behavior on silicon with simple physical considerations. In the second half, we utilize this saturation behavior to create terahertz anti-reflection structures on the surface of silicon.

Chapter 7 provides a conclusion and outlook, while two appendices are presented to present relevant, yet somewhat tangential topics related to the dissertation.

Chapter 2.

Theory

2.1. Introduction

A trivial prerequisite for ablation to occur in a material is for energy transfer to occur from the laser field to the material. Exactly *how* this energy transfer occurs is a non-trivial matter, however, dependent on both material and laser properties. Elucidating the fundamental mechanisms in play has been and still remains a major goal in the study of light-matter interaction in solid-state physics.

Two features of *ultrashort* pulsed laser processing make the phenomenon particularly interesting in these regards. The first is the timescale of the laser pulse. At pulse durations shorter than 1 ps, the energy deposition occurs in a highly localized manner, both spatially and temporally. This allows for the exploration and utilization of physics far from thermal equilibrium. The second is the high peak intensity of such laser pulses. Peak intensities can easily reach the TW/cm^2 range with only moderate pulse energy and focusing; the induced field values approach that of the binding energy of electrons to their parent atoms. Such high peak intensities are able to induce highly non-linear absorption processes not possible with longer pulses.

In this dissertation, we focus mainly on ablation of transparent dielectrics. Dielectric materials are characterized by a wide band gap (with energy E_g) between a completely filled valence and an empty conduction band. By transparent, we mean here that E_g is larger than the photon energy of typical visible light, or larger than around 3 eV. Thermally excited carriers in the conduction band are roughly excited at an order of $e^{-E_g/2k_bT}$ [5], where k_b is the Boltzmann constant, and T is the temperature. At room temperature, this value is less than 10^{-26} for $E_g > 3$ eV, and as such, this population is often negligible. Consequently, single-photon absorption is not allowed in dielectrics due to a lack of vacant transition states for an electron to be excited to, as required by basic quantum mechanics. Thus, while the material may still be polarizable, and hence exhibit a dielectric response, ideally no energy absorption occurs; hence, the material is "transparent" in the normal sense of the word. This should be compared to that of the reaction in metals, where the conduction band is partially filled and intraband transition is allowed, or in semiconductors, where E_g can easily be provided by a single photon, or a significant thermal electron population already exists in the conduction band to allow for intraband transition. In these materials, single-photon absorption is allowed, leading to high energy absorption near the surface upon laser irradiation.

Due to the aforementioned characteristics, material absorption in ideal dielectrics must depend on absorption paths other than simple linear absorption for typical lasers operating at visible and near-infrared wavelengths. While *single-photon* absorption may not be allowed, higher-order processes, such as *multiphoton ionization* or *tunneling ionization* are still allowed and enabled by the high peak intensities of ultrashort lasers. Furthermore, once “free” carriers are excited into the conduction band via the aforementioned processes, these electrons may undergo single-photon absorption to become more energetic. If enough energy is absorbed from the field, these electrons may initiate *impact ionization* to excite other valence band electron into the conduction band. Improving the theoretical understanding of these higher-order phenomena is a major fundamental motivation for studying the laser ablation phenomenon. It should also be noted that if a significant amount of electrons are excited to the conduction band, the optical response of the material should change dramatically. A comprehensive model of the laser excitation phenomenon will require knowledge of how these factors interact dynamically. Laser ablation occurs when a significant portion of the valence band electron population is excited into the conduction band, destabilizing the material either thermally or electrically. The above is pictorially represented in Figure 2.1.1.

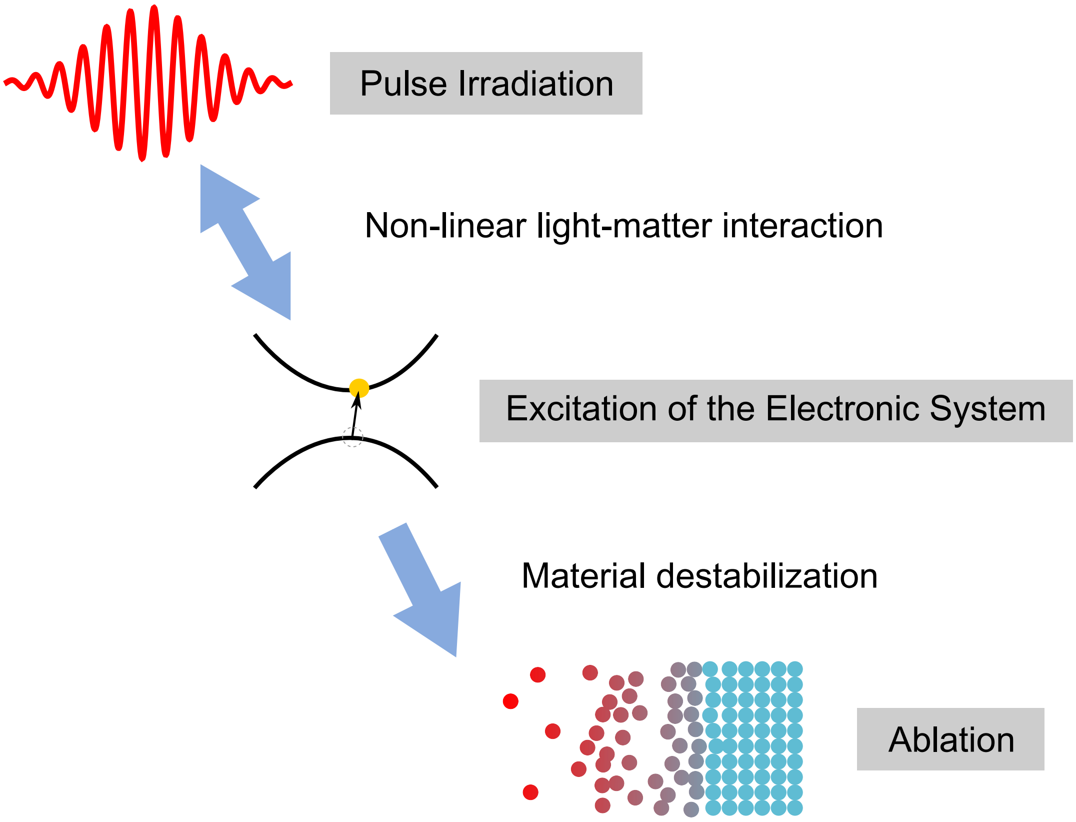

Figure 2.1.1.: Basic schematic of the ablation phenomenon

In this chapter, we review the current state of laser ablation theories. In section 2.2, we quickly estimate the scales, both temporal and spatial, involved in the laser ablation phenomenon. These scales often form the backbone of approximations utilized to simplify the problem. In section 2.3, we introduce the most widely used phenomenological model of the laser ablation phenomena: the rate equation approach. Here we go over the fundamental optical, electrical, and material properties governing single-pulse laser ablation and how they are incorporated into tractable forms, as well as the open questions present. The topics introduced here will provide the theoretical context used throughout the dissertation. In particular, the rate equation approach will be used to analyze and discuss results in chapter 4. While hardly exhaustive, we hope to provide a fair representation of the state of the art regarding the current understanding within the literature.

2.2. General overview of processes and their spatiotemporal scales

In order to arrive at tractable laser ablation models, a number of assumptions are often required. The justifications of such assumptions are often based on the spatial and temporal scales of the ablation phenomenon. While somewhat hand-wavy, even a brief overview of these relevant values will pay dividends later in helping the reader gain an intuitive understanding of why certain effects are omitted in subsequent discussions.

The lateral spatial scale at which the laser energy is deposited is of the order of the laser spot size. While this can theoretically reach diffraction limited values approaching the wavelength of the light in question, in practice, typical ablation setups see diameters in the lower tens of μm range, and we assume something around this value as well.

The depths involved in laser ablation is a less trivial matter. For metals and semiconductors, energy deposition can be intuitively estimated by the penetration depth, and is of the order of ten nanometers. However, the absorption process in transparent materials is more complex. Notwithstanding, we can arrive at an order estimate by considering the absorption lengths involved in multiphoton absorption [6]. If we assume a temporally square pulse with a local intensity of I, the change in the local intensity due to multiphoton absorption within the material at a depth z from the surface can be written as

$$\frac{dI(z)}{dz} = -\alpha_m I(z)^m, \tag{2.2.1}$$

where α_m is the m-photon absorption coefficient of the material in question. If we assume that ablation occurs at depths where the local intensity value is above a certain threshold value I_{th}, we can use equation (2.2.1) to determine the characteristic length of this depth.

Solving equation (2.2.1) for z, we gain a characteristic depth z_{abs} as follows:

$$z_{abs} = \frac{1}{\alpha_m(m-1)}(I_{th}^{-m+1} - I_0^{-m+1}). \tag{2.2.2}$$

Here, I_0 is the local intensity at the material surface. With this, we can estimate the relevant depth. We use sapphire as a typical dielectric material, and consider a 190 fs pulse with a central wavelength of 800 nm. Borrowing theoretical values derived in ref. [7], assuming a band gap of 8.5 eV, the lowest allowed multiphoton transition is the 6-photon absorption, and its value is calculated as 9.8×10^{-62} $\mathrm{cm^9W^{-5}}$. As we will see later, in typical laser ablation in dielectrics, incident fluence values are around 10 J/cm^2 and, threshold fluence values around 2-5 J/cm^2. We can divide these values by the pulse width to arrive at their respective incident and threshold intensity values. Altogether, through equation (2.2.2), we arrive at z_{abs} of around a couple tens to a couple hundred nm depending on the exact threshold fluence value used.

While a rough estimate, the above order estimation effectively highlights the typical aspect ratios involved in single-pulse ablation. Typical ablation craters around 10 μm wide and only a couple hundred nm deep results in very shallow aspect-ratios. As such, gradients in the initial excitation, as well as other physical parameters such as temperature and pressure, are expected to be predominantly perpendicular to the sample surface.

We will next attempt a general discussion on the timescales involved in ultrashort pulsed laser ablation. The electronic excitation of the sample naturally occurs at the same ultrafast timescale as the laser pulse, at approximately the spatial scales highlighted above. This triggers a series of events which culminates in the expulsion of matter from the material surface. The exact reactions involved at these ultrafast strong-field regimes is a matter of ongoing research and far from fully understood, but there is a general consensus as to the general picture, born from decades of experimental and theoretical work. Good reviews are given in ref. [8, 9, 10, 11, 12, 13]. The main processes and their timescales are gathered in Figure 2.2.1.

As mentioned in the previous section, as there are no easily excitable electrons, the laser ablation phenomenon must rely on non-linear interactions to transfer energy from the light field to the material electron system. Barring the effect of defects, this means that a large portion of the excitation occurs at the peak of the pulse when the instantaneous intensity is highest. These high fields are able to trigger direct photoexcitation processes between the valence band and conduction band; namely, electrons can undergo multiphoton and/or tunneling ionization. As these processes are highly nonlinear, they are isolated to the peak of the pulse, as stated above.

Once electrons are excited to the conduction band, and in combination with scattering processes, they undergo carrier heating in the electric field, mainly through inverse bremsstrahlung. Scattering is believed to be fast. For example, electron-phonon scattering was modeled to have time constants of 0.1 to 10 fs for momentum transfer, and 1-100 fs for energy transfer in fused silica [14]. This value is not static, but dependent on various

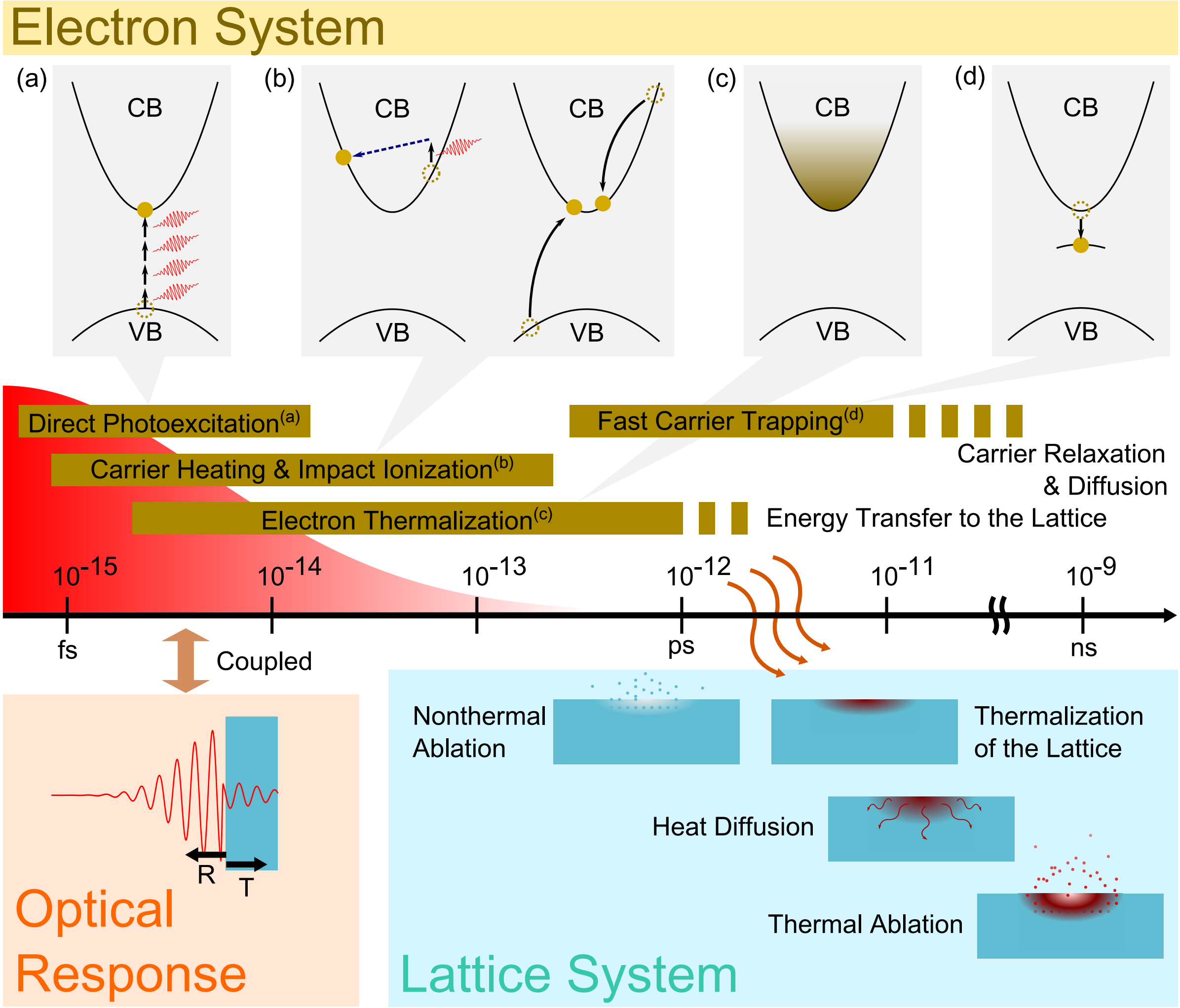

Figure 2.2.1.: Some of the main processes involved in the ablation of transparent dielectrics. Differing timescales allow us to highlight and isolate certain effects. Arranged from [8, 9].

factors such as electron temperature and carrier density. As the energy of individual electrons increase, a few gain enough energy to initiate impact ionization, where energetic conduction band electrons excite other valence band electrons into the conduction band in an inverse Auger process. Through this process, carriers are excited into the conduction band, each of which are heated and able to subsequently initiate impact ionization, resulting in even more carriers. This positive-feedback process results in an exponential increase in free-carriers, and is generally called the avalanche ionization process. Because avalanche ionization requires an initial population of “seed” electrons to set-off the process, it is believed to predominantly occur at the latter half of the laser pulse, after direct photoexcitation has occurred.

Through carrier scattering, the electron system relaxes into thermal equilibrium. Thermalization is believed to also be fast, in sub-picosecond timescales [15]. Also at subpicosecond timescales, trapping of free electrons into shallow self-trapped states is believed to occur, although the exact timescale is material dependent [16].

The optical response of the material at high intensity must also be considered. Various nonlinear phenomena, such as self-focusing and self-phase modulation, are able to occur well below the material damage threshold [17]. However, such effects are mitigated in surface ablation, as the incident light interacts in a thin layer on the material surface, in contrast to bulk processing within the material. Another factor to consider is the effect of laser excitation on the optical properties of the material. With a significant free-carrier population, the optical response of the material changes dynamically from transparent to nearly metallic [12]. These effects, when applicable, must be taken into account at the same timescales as the electronic excitation.

Finally, for material ablation to occur, the state of the lattice must change. Due to the three orders of magnitude difference between the mass of electrons and atomic cores, movement of the lattice is comparatively very slow. One can generally classify the reactions which occur into two groups: thermal and non-thermal processes.

Thermal processes are similar to that seen in long-pulse ablation. Through electron-phonon interaction, energy is transferred from the electronic system to the lattice, typically at picosecond timescales. The heated lattice undergoes a phase transition into liquid or gaseous states, which expand and are ejected from the material surface.

A consideration which dictates the locality of thermal processes is the heat diffusion of energy into the surrounding lattice. Following disucssions in [17], we can estimate general scales for this as well. Heat diffusion can be written as:

$$\rho C \frac{\partial T}{\partial t} - \kappa \nabla^2 T = S, \tag{2.2.3}$$

where ρ is the density of the material, C is the heat capacity, κ is the thermal conductivity, and S is the absorbed local incident energy (the source term). To estimate the heat diffusing out of the region at a given timescale, we set $S = 0$. We simplify the derivatives to simple fractions, and get

$$\rho C \frac{T}{\Delta t} \approx \kappa \frac{T}{(\Delta L)^2}. \tag{2.2.4}$$

ΔL is the characteristic length over which heat diffuses in time Δt. Solving in terms of ΔL, we get the following relationship:

$$\Delta L = \sqrt{D \times \Delta t}. \tag{2.2.5}$$

Here, $D = \kappa/(\rho C)$ is the thermal diffusivity of the material. For example, the thermal diffusivity of sapphire, using values from ref. [18], is calculated to be around $1.9 \times 10^{-5}\ \mathrm{m^2/s}$. Plugging this value into equation (2.2.5) gives us $\Delta L \approx 0.0039\sqrt{\Delta t}$, or lengths of around 10 nm for 10 ps pulses. Thus, in ultrashort pulsed laser processing, attainable temperatures are generally higher than that for their longer-pulsed counterparts, where heat dissipation out of the focal zone comes into play at similar time scales to the laser irradiation. Restated, a minimal amount of energy is required in thermal ultrashort pulsed-laser processing, and hence, less thermal damage is seen away from the irradiated region. This is often a reason why femtosecond laser ablation, even with thermal processes involved, is considered a non-thermal processing method. It should be emphasized that in this case, “non-thermal” regards the nature of the damage *surrounding* the ablated region, and not the method of material ablation itself.

As more “true” non-thermal ablation processes, mainly two categories are discussed in the literature. The first is lattice destruction due to electrostatic charging, a process referred to as *Coulomb explosion* [19]. A portion of excited electrons are expected to undergo photoemission from the material surface. As the electric conductivity of dielectrics is low, this charge imbalance is maintained at ultrashort time-scales; this leads to a build-up of positive charge at the sample surface. A giant electrostatic gradient between the predominantly positively-charged lattice and the ejected electron cloud forms, which can work to eject positive ions from the material surface.

A second class of non-thermal ablation is based on the high concentration of conduction-band electrons in relation to the valence band. This leads to a general destabilization of the solid. This has been explained for semiconductors in terms of bond-softening [20], and by similar bond-softening [21] and entropy-driven mechanisms [22] in metals. Taking into consideration the high excitation levels in dielectrics, non-thermal destabilization effects are believed to be even more pronounced here [12], although only the Coulomb explosion mechanism has been directly reported thus far in the literature.

These non-thermal processes have been experimentally shown to be very fast, with destructuring occuring generally directly after laser excitation [8]. They have no long-pulse analogue. However, it should be mentioned that while thermal and non-thermal processes exist, they are not mutually exclusive. Non-thermal processes may take place initially, but as heat is transferred from the electron system to the lattice, thermal processes may take place at later timescales concurrently. What process is favored is highly light and material specific, and may also change transiently during multiple-pulse laser processing.

Finally, a few notes on the mechanical scales involved in the actual material ejection should be done. The ablation mechanism is often violent, and induces a shockwave within the material. The velocity of sound traveling through a material is expressed by

$$v_{sound} = \frac{Y}{\rho}, \tag{2.2.6}$$

where Y is Young’s modulus, and ρ is the material density as before (ignoring shear forces for simplicity) [23]. For sapphire, Young’s modulus is around 400 GPa (the exact value depending on crystallographic direction), and the density is slightly below 4 g/cm^2 [24], giving a value $v_{sound} \approx 10^4$ m/s.

Another point is the speed at which particles leave the surface. In thermal ablation, the material reaches heats exceeding the vaporization temperature, which is over 2000 °C for sapphire. Assuming a temperature somewhat higher, for example 3000 Kelvins, we can derive the root mean square velocity $v_{particle}$ of an ideal gas from classical statistical mechanics by

$$v_{particle} = \sqrt{\frac{3k_bT}{m}}, \tag{2.2.7}$$

where k_b is the Boltzmann constant, T the temperature, and m the mass of the particle in question. Assuming an atomic mass of 27 atomic units (close to that of Aluminum), $v_{particle} \approx 1.7 \times 10^3\,\mathrm{m/s}$. More rigorous calculations, for example, molecular dynamics simulations, have yielded particle ejection speeds of around 200 m/s for silicon laser ablation [25], yielding similar ballpark values.

Again, while the above discussions are rough estimations, the derived values of v_{sound} and $v_{particle}$ shows us that the spatiotemporal scales of these mechanical effects are effectively ignorable at the femtosecond to picosecond timescale, and become appreciable only at the nanosecond timescale. Their effects generally dissipate away from the ablated zone to become negligible in the microsecond to millisecond timescale. Restated in terms of laser system timescales, the material response timescales are later than the typical ultrashort laser pulse, and faster than the timescales of the repetition rate of a typical high pulse-energy laser system, in the kHz range.

2.3. Modeling the electron population

As we have seen in the previous section, the timescales of the material response are far slower than the timescales of excitation of the electronic system. For this reason, in order to simplify the problem, most modern theories of ultrashort laser ablation initially decouple the material response when dealing with electronic excitation. The amount of electrons excited is calculated at ultrashort timescales, and a subsequent material response is either postulated or calculated based on this value.

The easiest and most popular way to follow the excited electron population is the formulation of a rate equation. The rate equation has a long history, being used in ablation studies as far back as the 1970s [1]. At its simplest, the rate equation is a differential equation for the conduction band population created and solved for in terms of time. In this section, we explain the mathematical features seen in many rate equations in the literature, mainly dealing with the various processes covered in the previous section.

2.3.1. The rate equation: overview

As introduced above, the electron rate equation has a long history. An early model proposed by Bloembergen [1] for the conduction band electrons during short pulse laser ablation is as follows:

$$\frac{\partial n_e}{\partial t} = \eta(E)n_e + \left(\frac{\partial n_e}{\partial t}\right)_{tunnel} - \left(\frac{\partial n_e}{\partial t}\right)_{loss}. \tag{2.3.1}$$

The first term is the impact ionization term (also called the cascade/avalanche term). As aforementioned in the previous section, impact ionization describes the process of heating of the free electrons in the conduction band by the electric field and a subsequent collision with neutral atoms causing the ionization of a new electron. When a moderately large conduction band electron density (provided by some source) is reached, this term becomes dominant, causing an exponential increase in free electron population, an "avalanche" so to say of excited electrons. The second term is the direct photoexcitation term, where valence band electrons are directly excited to the conduction band through strong-field effects: either tunneling at the low-frequency, high field limit, or by multiphoton excitation at the high-frequency, low-field limit. In nanosecond laser ablation, this term is small due to the smaller peak intensities of the pulses, insufficient to excite a significant electron population. Often, the presence of defects and impurities play a larger role as a source term for free carriers. The third term considers losses. Depending on the timescales considered, this can encompass relatively fast processes, such as recombination and exciton trapping, as well as slower processes, such as diffusion.

While the above model was proposed for nanosecond to picosecond pulses (which were the only pulses available at the time), femtosecond modeling of electron densities often takes a similar form. One of the first as proposed by Stuart [4] is given as such:

$$\frac{dn_e}{dt} = \alpha I(t)n_e(t) + \sigma_k I^k. \tag{2.3.2}$$

The first term is an analogous avalanche term, while the second term is a multiphoton ionization term, the value of k depending on the photon energy and band-gap value of the material under consideration. As simple as it is, the above equation proves to be an effective starting point to model the electron dynamics.

More modern variants of the electron excitation terms have a few notable differences. The key points may be listed as below:

1. With increasing peak intensities of pulses, the multiphoton excitation treatment becomes inappropriate. This is due to the effective widening of the band gap due to AC Stark shifts, causing simple power laws to overestimate ionization rates. The rates should instead smoothly connect to tunneling ionization rate values. Most modern theories employ an ionization rate introduced by Keldysh [26], which encompasses both multiphoton ionization and tunneling ionization mechanisms.

2. While most early theories fit the impact ionization rate from experimental data, most modern theories try to deduce its values from physical considerations. A plethora of customization is possible, such as energy and density dependent avalanche rates, and a joint consensus as to the best analytic form has yet to be reached.

3. Related to the above, the avalanche ionization term in the basic rate equation is *proportional* to the excited electron density. This assumes that a constant fraction of the excited conduction band electrons is always able to initiate impact ionization. This in turn implies a static electron energy distribution, which is not trivially guaranteed at the ultrafast timescales comparable to electron thermalization times at which femtosecond laser excitation occurs. How to deal with this issue has been a central issue in femtosecond laser ablation, and vastly affects the importance of the avalanche ionization term.

Other changes vary from experiment to experiment, such as the inclusion/exclusion of relaxation, diffusion, and trapping terms. There is yet to be a universal rate equation applicable for all materials. Many models still rely heavily on experimental data to determine parameter values.

We go over each of the terms individually in the following subsections.

2.3.2. Strong field ionization

Most early models of strong field ionization (SFI) rates for laser ablation use some form of multiphoton ionization, where the ionization rate W_{mpi} is described as

$$W_{mpi} = \sigma_k I^k, \tag{2.3.3}$$

where $k = \lceil \frac{\Delta}{\hbar\omega} \rceil$ (where $\lceil x \rceil$ denotes the smallest integer greater than or equal to x), or the lowest multiphoton order able to cross the band gap Δ. ω is the angular frequency of the laser.

While this model proves effective at lower intensities, it proves to overestimate the ionization rate at higher intensities. This is due to the fact that AC Stark shifts (or ponderomotive shifts) cause the effective band gap of materials to increase at high field amplitudes. The general change of the electron energies will be of the order of the ponderomotive energy for a free electron in an electromagnetic field:

$$\begin{aligned} U_p &= \frac{e^2 E^2}{4m\omega^2} \\ &= \frac{e^2}{2c\epsilon_0 m} \times \frac{I}{\omega^2} \\ &\approx 3.31 \times 10^{13} \frac{I}{\omega^2}\,[\mathrm{eV}]\,. \end{aligned} \tag{2.3.4}$$

For light at 800 nm, U_p becomes comparable to 1 eV at intensities around 10^{13} W/cm^2. Most threshold fluences for laser ablation of dielectrics are around 1 J/cm^2, which, for pulses of subpicosecond widths, corresponds to peak intensities in the TW range. Thus, it can be seen that these energy shifts play a non-negligible role. When shifts become great enough that $\Delta + U_p$ exceeds $k \times \hbar\omega$, an abrupt dip in the ionization rate is expected to occur[1]. As such, the multiphoton expression of (2.3.3) becomes increasing inappropriate for shorter pulses.

At the limit of strong intensities and small ω, the picture of tunnel ionization becomes more appropriate. In tunnel ionization, the bands are "bent" by the external electric field. With sufficiently strong electric fields, it then becomes possible for the electron to tunnel out of the valence band to the conduction band.

A simple measure of when tunnel ionization is expected to be dominant is provided in the form of the Keldysh parameter in solids[2][26],

$$\gamma = \omega \frac{\sqrt{m\Delta}}{eE}. \tag{2.3.5}$$

The Keldysh parameter is the ratio of the approximate semi-classical tunneling times compared with the laser frequency [27]. When $\gamma \ll 1$, tunneling times are fast enough for the oscillating field to appear almost static to the bound electrons; ionization in this regime is best described by a tunneling picture. When $\gamma \gg 1$, the fields are not strong enough to allow enough time for electrons to tunnel, and multiphoton ionization is expected to be a more proper representation. Of course, these "two" processes are simply two extremes of the strong-field ionization phenomena, not competing independent processes. Thus, in the ultrashort pulse regime, an ionization rate equation which continuously connects the multiphoton ionization to tunnel ionization rates is desired.

Such an equation was derived by Keldysh in 1965. He derived an equation describing the excitation rates of electrons by a monochromatic wave in a solid with a dispersion relation of the form

$$\epsilon_c(p) = \Delta \left(1 + \frac{p^2}{m\Delta}\right)^{1/2}. \tag{2.3.6}$$

The ionization rate is a first-order[3] perturbation calculation under several physical approximations, the most notable being:

- The Single Active-Electron Approximation (SAEA): the ionized electrons are assumed to be independent.
- The initial and final states are taken to be the valence and conduction band states under the influence of the laser field, and the effects of electron-hole interactions are ignored.
- The effects of carrier depletion in the valence band are ignored.

---

[1] This abrupt dip is sometimes referred to in the literature as a Keldysh-type singularity

[2] This parameter differs from the Keldysh parameter of gases by a factor of $\sqrt{2}$. As gases are beyond the scope of this thesis, all mention of the Keldysh parameter will refer to the form for solids.

[3] Higher order terms yield re-scattering terms

The calculations start from traditional perturbation calculations and use saddle-point methods to arrive at an analytical approximate solution. More information on the derivation is available in the literature, see [26, 28, 29, 30, 31].

Considering spin degeneracy, which increases the total rate by a factor of 2, the total Keldysh SFI rate (notation following [12]) often used in ablation modeling is:

$$W_{Keldysh} = 2\frac{2\omega}{9\pi}\left(\frac{m\omega}{\hbar\sqrt{\gamma_1}}\right)^{3/2} Q(\gamma, x)\exp\left(-\pi\left\lfloor x+1\right\rfloor\frac{\mathcal{K}(\gamma_1)-\mathcal{E}(\gamma_1)}{\mathcal{E}(\gamma_2)}\right). \tag{2.3.7}$$

$\mathcal{K}$ and $\mathcal{E}$ denote the elliptic integrals of the first and second kind, defined here as[4]:

$$\mathcal{K}(m) = \int_0^{\pi/2}\frac{d\theta}{\sqrt{1-m\sin^2\theta}}, \tag{2.3.8}$$

$$\mathcal{E}(m) = \int_0^{\pi/2}\sqrt{1-m\sin^2\theta}d\theta. \tag{2.3.9}$$

The bracket $\lfloor x\rfloor$ denotes the largest integer less than or equal to x. γ is the Keldysh parameter, while the other auxiliary γ are defined as such:

$$\gamma_1 = \frac{\gamma^2}{1+\gamma^2},\ \gamma_2 = \frac{1}{1+\gamma^2}. \tag{2.3.10}$$

The function Q is defined as

$$Q(\gamma, x) = \sqrt{\frac{\pi}{2\mathcal{K}(\gamma_2)}}\sum_{n=0}^{\infty}\exp\left(-n\pi\frac{\mathcal{K}(\gamma_1)-\mathcal{E}(\gamma_1)}{\mathcal{E}(\gamma_2)}\right)\Phi\left(\sqrt{\frac{\pi^2(\lfloor x+1\rfloor - x + n)}{2\mathcal{K}(\gamma_2)\mathcal{E}(\gamma_2)}}\right). \tag{2.3.11}$$

Here, $\Phi(x)$ is the Dawson integral defined as

$$\Phi(x) = e^{-x^2}\int_0^x e^{t^2}dt. \tag{2.3.12}$$

The function Q provides information on the spectrum structure connected with the discrete nature of the absorbed photons [26]. The parameter

$$x = \frac{2\Delta\mathcal{E}(\gamma_2)}{\pi\hbar\omega\sqrt{\gamma_1}}, \tag{2.3.13}$$

is the effective ionization potential in units of the photon energy.

---

[4] Some definitions define the integrals in terms of elliptic modulus k instead of the parameter $m = k^2$ used here. In most recent papers, m is used, a major practical advantage being that most numerical libraries use this definition.

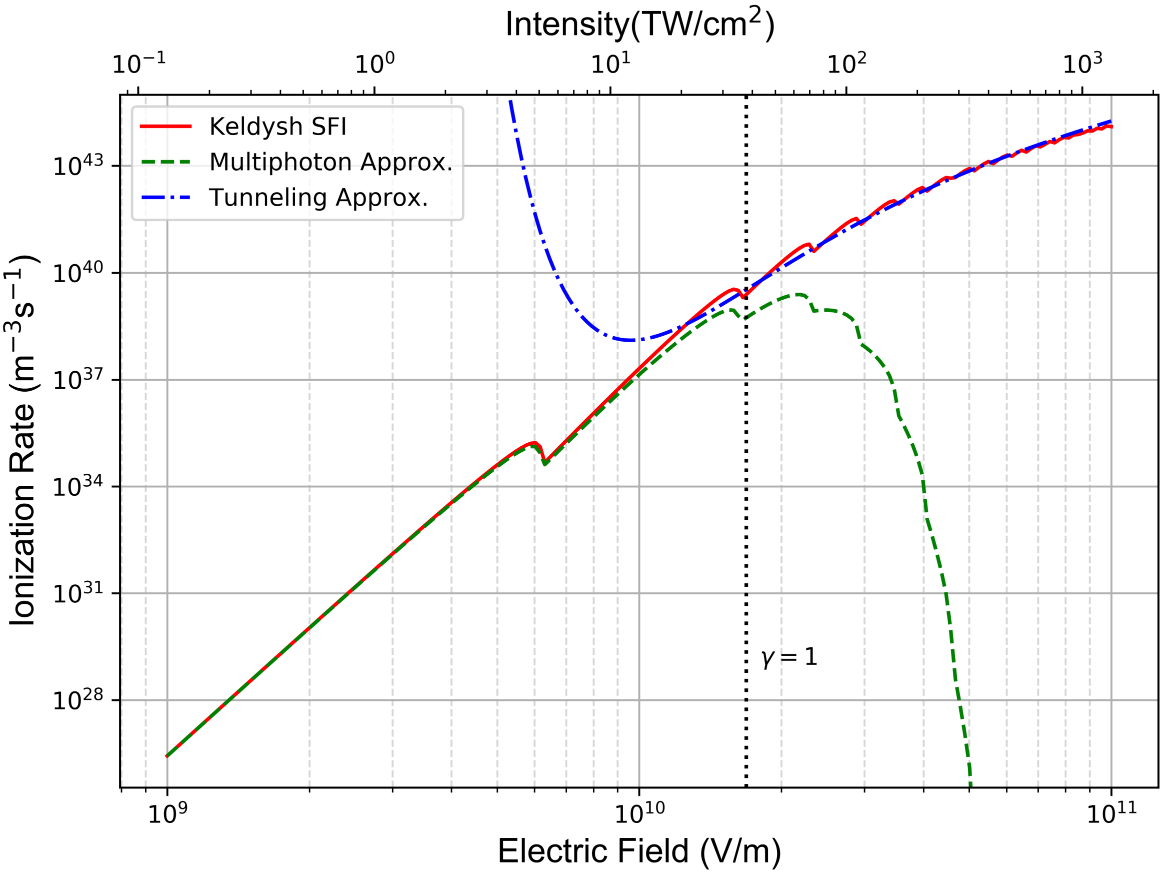

Figure 2.3.1.: The Keldysh SFI rate calculated according to equation (2.3.7) as a function of electric field strength (red, solid). For reference, an equivalent value of the electric field intensity in vacuum is provided in the top y-axis. A band gap of 9 eV, wavelength of 800 nm, and electron effective mass equivalent to the free electron mass were used as material and electric field parameters. The approximate forms for the multiphoton regime (green, dashed) and Tunneling regime (blue, dash-dotted) are given as well. Their forms are appropriate when the Keldysh parameter is below and above 1 (black, dotted), respectively.

An example of the Keldysh rate equation calculated at 800 nm is given in Figure 2.3.1. At lower intensities, a power-law dependence of the ionization rate can be seen, typical of multiphoton ionization. At higher electric field strengths, abrupt dips in the ionization rate can be observed. Mathematically, this originates from the discontinuities in the floor function within the function Q defined in equation (2.3.11). As intensities become higher, the dips become more frequent, and the ionization rate saturates.

In order to arrive at a more intuitive understanding of the Keldysh ionization rate, a couple remarks should be made regarding how the equation behaves at the following limits with regards to the Keldysh parameter:

1. $\gamma \gg 1$: the multiphoton limit. In this limit, $x \approx \frac{\Delta}{\hbar\omega}\left(1 + \frac{1}{4\gamma^2}\right) = \frac{1}{\hbar\omega}\left(\Delta + U_p\right)$, and the number of photons needed to ionize the material is equal to the band gap plus

the AC stark shift. The total ionization rate reduces to

$$W_{MPI} = 2\frac{2\omega}{9\pi}\left(\frac{m\omega}{\hbar}\right)^{3/2}\Phi\left(\sqrt{2\lfloor x+1\rfloor - 2x}\right) \times \exp\left[2\lfloor x+1\rfloor\left(1-\frac{1}{4\gamma^2}\right)\right]\left(\frac{1}{16\gamma^2}\right)^{\lfloor x+1\rfloor} \tag{2.3.14}$$

The last term (noting that $1/\gamma^2 \propto I$) displays the typical power-law dependence of the ionization rate characteristic of multiphoton ionization.

2. $\gamma \ll 1$: the tunneling limit. The total ionization limit becomes

$$W_{TI} = 2\frac{2}{9\pi^2}\frac{\Delta}{\hbar}\left(\frac{m\Delta}{\hbar^2}\right)^{3/2}\left(\frac{\hbar\omega}{\Delta\gamma}\right)^{5/2}\exp\left[-\frac{\pi}{2}\frac{\Delta\gamma}{\hbar\omega}\left(1-\frac{\gamma^2}{8}\right)\right] \tag{2.3.15}$$

The term linear in γ within the last exponent is characteristic of tunnel ionization, where $W_{TI} \propto \exp\left(-\frac{\Delta}{eE}\right)$. $\frac{\Delta}{eE}$ corresponds to the approximate tunneling length, or the length at which the potential drop due to the external field equals the band gap.

The use of the full Keldysh equation as introduced above to model femtosecond ablation electron dynamics was first implemented by Tien *et al.* in 1999 [32]. From its first adoption, it has remained the de facto standard in most calculations of the direct photoionization rate in wide band-gap solids. However, it is not without its shortcomings. Some points include:

- The formula was derived for a band dispersion of the form of equation (2.3.6). However, this structure is not always appropriate. The effect of the band structure in general on ionization-rates, following the same derivation as Keldysh, has been shown to have varying photoionization rates [33, 34, 35, 13].
- The formula was derived for a strong CW field. However, the amplitude of ultrashort lasers vary strongly over time, and their spectrum is non-negligible. Effects of the non-monochromatic nature of femtosecond laser pulses on the ionization rate, including the chirp of the laser, have been shown to cause notable quantitative differences [36, 37].
- The formalism ignores the effects of local electric field enhancement induced by holes on tunneling ionization rates, and corresponding "Forest Fire" processes, which were predicted to have important consequences for few cycle pulse excitation, where ionization values exceed those predicted by the Keldysh formalism [38, 39, 40].
- The effect of collision is not considered in the model. Du *et al.* have predicted that collision effects may reduce multiphoton ionization rates [41].

Despite its shortcomings, it has become fairly standard in the ablation community to use the Keldysh SFI rate of above to model the initial direct ionization rates for its simplicity and generality.

2.3.3. Impact ionization and the avalanche process

Electrons excited into the conduction band of the material are able to absorb energy efficiently through inverse Bremsstrahlung. Once they gain sufficient energy, they are able to initiate an impact ionization, or inverse Auger, process to excite more valence band electrons to the conduction band. In this section, we cover the theoretical framework of this modeling.

All forms of the impact ionization modeling in the rate equation approach aim to quantify the following values:

1. The rate at which electrons gain energy: S
2. The energy necessary for electrons to initiate impact ionization: ϵ_c
3. Some distribution factor which dictates the fraction of electrons which are energetic enough to undergo the above impact ionization process: P

The ionization rate then can be modeled as $SP/\epsilon_c \times n_e$ where n_e is the free electron density. The simplest example of this is the previously mentioned simple rate equation model of Stuart *et al.* [4]. In this model, the rate of electron energy gain was assumed to be proportional to the incident intensity I (as is the case for metallic absorption), βI. The electron distribution was assumed to be unchanging, as well as a constant threshold energy, i.e. ϵ_c and P were taken as constants. This allows us to gather these two values along with the proportionality constant β into one constant α. Hence the avalanche term takes the form $\alpha I n_e$, as was shown in equation (2.3.2). This α could be determined through fitting of data, or approximated from values taken from other theories.

Another form used in early ablation models for the heating term is the Thornber avalanche ionization model [42]. The semi-empirical model was constructed for modeling avalanche ionization in DC fields. In this model, electrons were believed to gain an energy of eEv_{drift} due to the application of an electric field, where e is the electron charge, E is the applied electric field, and v_{drift} is the electron drift velocity, often taken as a constant saturation drift velocity for high fields relevant to ablation. As electron velocities are saturated, this gained energy is balanced by impact ionization processes. However, field-dependent scattering rates results in only a portion of the electrons gaining this full energy, and a term $P(E)$ is required to be multiplied to the carrier population, taken as

$$P(E) = \exp\left(-\frac{E_i}{E(1 + E/E_p) + E_{kT}}\right). \tag{2.3.16}$$

Here E_kT, E_p, and E_i are the fields required for carriers to overcome the thermal, phonon, and ionization scattering deceleration effects. Through the $P(E)$ term, strong nonlinearities in the heating rate is introduced in contrast to the case of Stuart. The calculated DC avalanche rate is usually scaled to the AC rate through the following relationship proposed by Bloembergen [1]:

$$E_{thr}^{AC,rms}(\omega) = E_{thr}^{DC}(1+\omega^2\tau^2)^{1/2}. \tag{2.3.17}$$

Here, $E_{thr}^{AC,rms}$ is the AC root mean square (RMS) breakdown threshold field corresponding to the DC breakdown threshold E_{thr}^{DC}. Thornber's model, while seeing use in seminal papers such as ref. [43, 32], has seen less use in recent works in the literature. A total of four nontrivial parameters appear within the equation (the electron drift velocity and the three threshold field values), complicating comparison with experimental results.

Most recent ablation theory utilize models following classical electron heating in line with the Drude model of metals. Here, we take a classical approach as the results are intuitive. A more stringent derivation by Boltzmann transport equations yield equivalent results. In this case, the heating of an electron, on average, can be described from the classical equation of motion under an AC electric field:

$$\frac{dp}{dt} + \frac{1}{\tau}p = eE\exp(-i\omega t)\,. \tag{2.3.18}$$

Here, we assume all values are taken in the direction parallel to the electric field, where p is the electron momentum while τ is the scattering time of the electrons (assumed here to be constant). This differential equation can be solved to yield:

$$p = \frac{e\tau}{1-i\omega\tau}E\exp(-i\omega t)\,. \tag{2.3.19}$$

From this, the classical electron current can be calculated as $J = ep/m$. Hence the rate at which energy ϵ is transferred from the electric field to the electron is given by [44]:

$$\begin{aligned}\frac{d\epsilon}{dt} &= \frac{1}{2}\mathrm{Re}(\mathbf{J}\cdot\mathbf{E}^*) &(2.3.20)\\ &= \frac{1}{2}\frac{e^2\tau}{m(1+\omega^2\tau^2)}E^2 &(2.3.21)\\ &= \frac{1}{2}\sigma E^2. &(2.3.22)\end{aligned}$$

The above equation is equivalent to the standard AC electrical conductivity/resistivity discussions in most standard physics textbooks [5], σ being the electrical conductivity. Caution should be taken when comparing equation (2.3.22), as values in the literature are occasionally shown with a factor of $\frac{1}{3}$ (see for example, [45, 46, 47])[5].

Some earlier works include a loss term describing the energy transfer between the electron system and the lattice. An energy loss factor is multiplied by the average collision frequency. This energy loss is approximated either by the average phonon energy as

---

[5] This convention is justified by taking into account the random direction of momentum scattering. This should not be necessary in our current discussion. Furthermore, Sparks *et al.* in [45] derived this form for root mean square (RMS) field values, and thus, an additional factor of 1/2 must be applied for peak fields (i.e. the factor should be $\frac{1}{6}$ in this case).

$\hbar\omega_{phonon}$[45][6], or through classical elastic collision consideration[48]. In the latter, energy transfer between an electron with mass m_e and average energy ϵ_{av}, and a parent ion of mass M can be calculated to yield a value of $2m_e\epsilon_{av}/M$. For high electric fields, as is the case for femtosecond lasers at ablative intensities, loss rates calculated from either form are one or two orders of magnitude smaller than the energy gain rate, and thus are often omitted.

A large factor which complicates Drude models (and in part, the Thornber model as well through equation (2.3.17)) is the treatment of the collision time τ. The scattering rates are believed to depend both on the electron energy (or electron temperature) as well as the density of the excited carriers. As previously introduced, in SiO_2, it has been shown that the scattering times take values in the range of 0.1-10 fs range[14], and are expected to be similar for other dielectrics. However, there has yet to be a consensus on the exact functional form. This is complicated theoretically due to lack of information regarding both the interaction itself, as well as the transient electron temperature. Balling and Schou have classified electron scattering into mainly four components [12]. The first is the electron-phonon scattering rate, dominant for low excitation. When a sufficiently high population of electrons have been excited, the material should be considered a form of warm-dense matter. In such a state, three other scattering terms can be estimated from plasma physics considerations: electron-electron scattering, electron-neutral scattering, and electron-ion scattering. Of these components, the terms believed dominant are utilized, or else multiple values are combined by Mathiessen's law [5].

Due to its difficulties, many studies take the scattering time as a constant, either estimated from theory or fitted to experimental data. As this term mostly alters the avalanche ionization rate, which in turn only comes to play at high densities, this value most strongly reflects the scattering times within the highly excited electron plasma. A constant avalanche ionization rate proportional to the laser intensity can be considered a generalized example of this case.

In the simplest implementation of the Drude model, the transient electron distribution is ignored: P is taken as 1 and the total ionization rate is simply eq. (2.3.22) divided by ϵ_c. However, calculation in this method often overestimates the avalanche ionization rates, when compared to other calculation methods [15]. Most criticisms are rooted on the oversimplification of P.

One major criticism is that the rate equation fails to account for the finite time it takes for electrons excited to the conduction band to gain energy from the field. Noack and Vogel have proposed introducing an ionization delay time t_{ion} to account for this delay time [49]. In their work, they assume that each collision event involving a conduction band electron is accompanied by an absorption of a photon (valid only for very large

---

[6] Models with this correction is often referred to as the Sparks model of impact ionization in the literature

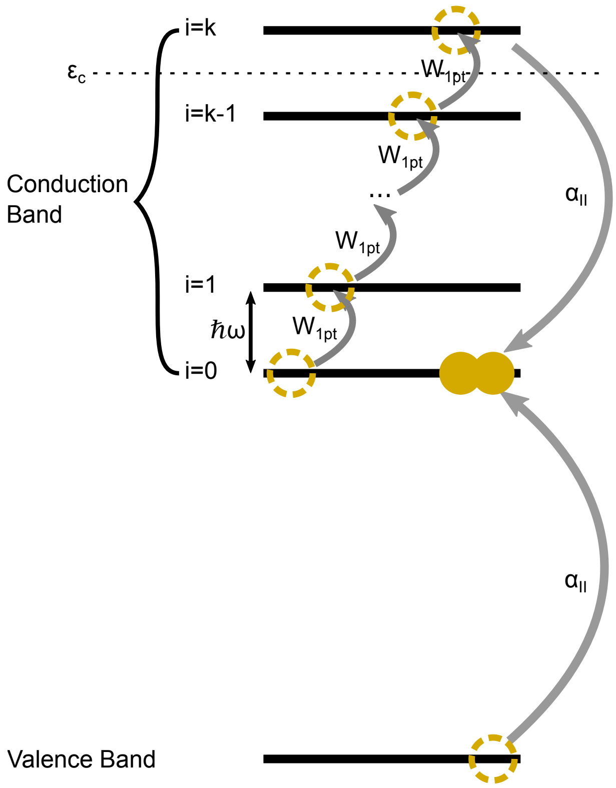

Figure 2.3.2: Energy level diagram of the multiple rate equation proposed by Rethfeld in [50]. By breaking the conduction band up into discrete levels, the transient energy distribution could be more accurately represented.

photon fluxes), and hence the ionization delay is expressed as:

$$t_{ion} = \tau \lceil \frac{\epsilon_c}{\hbar\omega} \rceil, \tag{2.3.23}$$

where $\lceil x \rceil$ denotes the smallest integer larger or equal to x. This factor can be incorporated by altering the impact ionization term in the main rate equation (2.3.2) to $\alpha I(t) n_e(t - t_{ion})$. Another method which simplifies implementation is to alter the impact ionization factor itself. Ignoring the direct photoionization term, the rate equation for the electron avalanche becomes

$$\frac{dn_e(t)}{dt} = \alpha n_e(t - t_{ion}). \tag{2.3.24}$$

Assuming a solution of the form $Ce^{\lambda t}$, the characteristic equation for this differential equation takes the form

$$\lambda - \alpha e^{-\lambda t_{ion}} = 0. \tag{2.3.25}$$

To first order, this equation can be solved to yield $\lambda = \alpha/(1 + \alpha t_{ion})$. Thus, a rescaling of the impact ionization rate to

$$\alpha_d = \frac{\alpha}{1 + \alpha t_{ion}}, \tag{2.3.26}$$

yields a delayed accumulation characteristic.

While this correction roughly accounts for the temporal characteristics of the electron thermalization process, it is expected to slightly underestimate the real rate, as the electron distribution is ignored. There exist high-energy electrons which should be able to initiate impact ionization faster [15]. To take this into account, Rethfeld proposed the multiple-rate equation (MRE) formalism to account for the transient electron distribution [50, 51, 52].

In the MRE implementation the conduction band is further discretized into sub-levels spaced one photon energy apart, as shown in Figure 2.3.2. Each electron must climb up k levels before being able to initiate impact ionization at a rate of α_{II}. The number of levels is taken such that when an electron climbs k levels, it has acquired enough energy to initiate impact ionization, i.e. $k = \lceil \frac{\epsilon_c}{\hbar\omega} \rceil$. The exact form for the rate at which the electrons climb up (W_{1pt} in figure 2.3.2) varies in the literature. Rethfeld uses a constant value fitted from experiment [50], while others employ the Drude rate from equation (2.3.22) rescaled in various ways, see, for examples, models in [53, 47, 54]. The impact ionization rate is assumed to occur at a rate much faster than one-photon absorption: $\alpha_{II} \gg W_{1pt}$. Such rates ensures that the population is always higher at the lower levels.

Written in equation form, the MRE is a set of $k+1$ coupled differential equations, expressed as below:

$$\frac{dn_{e,0}}{dt} = W_{SFI} + 2\alpha_{II} n_{e,k} - W_{1pt} n_{e,0} \tag{2.3.27a}$$

$$\frac{dn_{e,1}}{dt} = W_{1pt} n_{e,0} - W_{1pt} n_{e,1} \tag{2.3.27b}$$

$$\vdots$$

$$\frac{dn_{e,k-1}}{dt} = W_{1pt} n_{e,k-2} - W_{1pt} n_{e,k-1} \tag{2.3.27c}$$

$$\frac{dn_{e,k}}{dt} = W_{1pt} n_{e,k-1} - \alpha_{II} n_{e,k}. \tag{2.3.27d}$$

Here, W_{SFI} represents the direct photoionization term, usually taken as $W_{Keldysh}$. Occasionally, equation (2.3.27d) is omitted, and $2\alpha_{II} n_{e,k}$ in equation (2.3.27a) is replaced by $2W_{1pt} n_{e,k-1}$, taking advantage of the aforementioned condition $\alpha_{II} \gg W_{1pt}$ to reduce calculation cost. The total conduction band electron population is then expressed as

$$n_e = \Sigma_{i=0}^{k} n_{e,i}, \tag{2.3.28}$$

and can be seen to obey the equation

$$\frac{dn_e}{dt} = W_{SFI} + \alpha_{II} n_k. \tag{2.3.29}$$

The asymptotic solution for the multiple rate equations (2.3.27) at long times for constant intensities can be determined as [50] (i.e. after the electron distribution has stabilized)

$$n_e = \frac{W_{SFI}/W_{1pt}}{2k(\sqrt[k]{2} - 2 + \sqrt[k]{1/2})} \exp(t/t_{MRE}) \quad \text{for} \quad t \gg t_{MRE}, \tag{2.3.30}$$

where

$$t_{MRE} := [(|\sqrt[k]{2}| - 1)W_{1pt}t]^{-1}. \tag{2.3.31}$$

Comparing with the traditional avalanche parameter, the effective avalanche parameter for the stabilized multiple rate equation is simply

$$\alpha_{MRE} := 1/t_{MRE} = \ln(2)W_{1pt}/k + O(1/k^2). \tag{2.3.32}$$

For pulse durations longer than t_{MRE}, the asymptotic form for the multiple rate equation should be a good approximation. For example, we think of the case of an 800 nm (approx. 1.55 eV) laser pulse with peak electric field values around 10^{10} V/m, when the impact ionization rates are on the order of $10^{14}\,\mathrm{s}^{-1}$. We think of a material with a band gap of 9 eV, and take ϵ_c as this value. Then, $k = \lceil 9/1.55 \rceil = 6$, and t_{MRE} is calculated to be approximately 80 fs. Therefore, for pulses longer than 100 fs, the electron distribution should be somewhat stabilized, and a single rate equation with a corrected avalanche should still be a good approximation.

A final remark for the two scaled impact ionization coefficients derived, the delayed rate equation (2.3.26) and MRE (2.3.32), should be made here. To facilitate comparison, we first rework equation (2.3.26) into a consistent framework as equation (2.3.32). From the definition of k, a naive impact ionization coefficient would be taking $\alpha = W_{1pt}/k$; a consistent approximation of t_{ion} would be the inverse of this rate value. Replacing α and t_{ion} as such in equation (2.3.26) yields

$$\alpha_d = 1/2\frac{W_{1pt}}{k}. \tag{2.3.33}$$

It can be seen that the scale value $\frac{1}{2k}$ is smaller than that of equation (2.3.32). As aforementioned, this mainly has to do with overestimating the time required for an electron to gain enough energy to initiate impact ionization. However, this also suggests that it should also be possible to take an effective t_{ion} to compensate for this overestimation. Comparing the values of equation (2.3.32), we can retake t_{ion} as

$$t_{ion} = \frac{1 - \ln(2)}{\ln(2)} \frac{k}{W_{1pt}}, \tag{2.3.34}$$

to yield the same asymptotic form as the MRE for large k. The results of this rescaling can be seen in figure 2.3.3. As expected, the rescaled factor becomes a better approximation to the MRE results for larger k. Although derived as a mathematical relationship, the physical intuition provided from this result is nonetheless useful: assuming that the Drude rate is correct, discrepancies from the avalanche rate can be mapped into effective

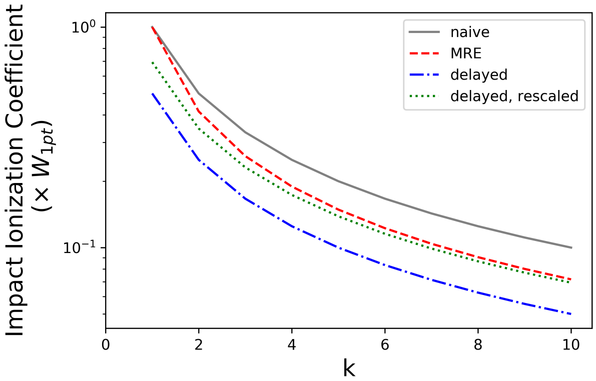

Figure 2.3.3.: Comparison of the various scaled impact ionization coefficients as a function of k, or the minimum number of photons required to overcome the critical energy for impact ionization

ionization delay times by use of equation (2.3.26), a parameter which is far less intuitive in a pure MRE approach. While we finish discussions here, a thorough comparison of the different Drude rate equation approaches introduced here in regards to pulse duration is given in, for example, ref. [54].

Lastly, we must determine the threshold energy for impact ionization: ϵ_c. Many early models use the band gap of the material as the threshold value. While intuitive from an energy conservation point of view, assuming a direct band gap material with the conduction band energy minimum at the gamma point, energy conservation would dictate that both electrons take final states around the gamma point minimum. However, this violates momentum conservation, as the initial energetic electron had a nonzero value.

Taking into account momentum conservation, many modern theories utilize the following relationship derived for parabolic bands [55]

$$\epsilon_c = \frac{1+2\mu}{1+\mu}\Delta. \tag{2.3.35}$$

Here, $\mu = m_{e,conduction}/m_{e,valence}$. In the case of similar valence and conduction band masses, the total energy necessary to initiate impact ionization becomes 1.5 times the energy of the band gap. In the case of sapphire, where hole masses are far greater than valence electron masses, the threshold is close to the band gap. This extra energy allows for the satisfaction of both fundamental conservation laws.

Another factor often taken into consideration is the pondermotive shift of the band gap [53], as was discussed in section 2.3.2. As the strong-field ionization rates are shifted due to this effect, it would be consistent to use this effective band-gap value as well. In this case, the band gap is shifted by U_p from equation (2.3.4), and the band gap is replaced by

$$\tilde{\Delta} = \Delta + \frac{e^2 E^2}{4m\omega^2}. \tag{2.3.36}$$

Before ending this section, it should be noted that the rate for impact ionization has been taken as one. This assumes that all electrons that can initiate impact ionization do so at a nearly instantaneous rate. This "flux doubling" condition originated from nanosecond to picosecond processing theories [45, 56], but is still often implicitly used in femtosecond laser ablation rate equation theories today. The validity of this assumption may be gauged by comparing impact ionization cross sections with the electron heating rate. For impact ionization cross sections, Keldysh derived the form [57]:

$$W_{imp} = C \left(\frac{\epsilon - \epsilon_c}{\epsilon_c} \right)^2 , \tag{2.3.37}$$

where ϵ is the energy of the electron and C is a prefactor. The prefactor for SiO_2 in the literature takes values in the range of a few to a few tens of fs^{-1} [14, 15]. While these values yield impact ionization rates which are generally higher than the heating rates achievable at the low peak intensities of longer-pulsed lasers, they become somewhat comparable in the case of femtosecond lasers, as noted by Stuart *et al.* [58]. While we mostly follow convention and omit this term in this thesis, there may be a correction necessary to take this effect into account in the future, especially for very short pulses.

2.3.4. Incorporating traps, recombination, and defects

Depending on the material, some groups include a decay term for the conduction band electron. Within the rate equation, only decay paths with timescales comparable to the laser pulse duration need to be taken into account. At ultrafast timescales, electron decay is mainly believed to occur into trap states (for example, self-trapped exciton states in fused silica and alkaline halides [59]). Electrons captured into these traps lose their free-electron-like characteristics and no longer participate in the avalanche process; thus, trapping generally is believed to raise the damage threshold. Decay into the valence band is usually believed to take a much longer time, in the nanosecond range.

In the simplest models, an exponential decay is postulated, and a term $-\frac{n_e}{\tau_{tr}}$ is added to the rate equation, where τ_{tr} is a decay time constant. See for example, [60, 61, 62, 63] among many others. The value of τ_d may be fit from data [60, 61], but often values determined from experiments on the time-resolved dynamics of the excited electron plasma are used [64, 16, 65]. In the latter case, fused silica was measured to have fast trapping times of approximately 150 fs, while sapphire and MgO had trapping times greater than 50 ps. From this, it is apparent that the trapping dynamics are highly material specific, and, for example, are often ignored for theories regarding sapphire.

Trapped electrons usually take energy states within the band gap of the material. In the case of dielectrics with wide band gaps, these electrons are far more easily excited back into the conduction band than electrons from the valence band. In order to take this effect into account, some more complex models follow the population of electrons within trapped state [66, 67]. In this case, the trapped electron density n_{tr} follows a function of the form:

$$\frac{dn_{tr}}{dt} = -W_{tr} n_e I^k + \frac{n_e}{\tau_{tr}} \left(1 - \frac{n_{tr}}{n_{tr,max}} \right), \tag{2.3.38}$$

where W_{tr} is the k-photon excitation cross section of the trapped state, and $n_{tr,max}$ is the maximum allowed trap density. A corresponding term to the second source term is provided as a loss term in the main conduction band electron rate equation.

Lastly, the effect of native defects should be mentioned. Most often, point defect states are considered, such as the F-center in sapphire, or E'-center in SiO_2. Electrons within these states are usually more easily excited into the conduction band, and thus can become seed electron sources for an electron avalanche, affecting the material damage characteristic. Often, a strict treatment of the state populations akin to equation (2.3.38) is replaced by a simple finite initial electron density to simulate this effect (see for example [32]). More regarding the treatment of defects will be given in subseuent chapters regarding multiple-pulse ablation.

2.3.5. Other considerations

A combination of the terms introduced in the previous sections encompasses the majority of ablation rate equation models. These are normally solved in a zero-dimensional manner to predict the electron excitation rates at the material surface. These values can then be compared to experimental observables both optical, such as reflectivity and transmissivity, or to morphological features, such as the damage threshold, and are often enough to extract a general understanding of the underlying physics. The rate equation approach provides a flexible approach to the problem of electronic excitation within the material, and has become the most popular approach to understanding experimental results. However, one must always be wary of the necessity to tailor the equation to the material and processes under question: it is hardly a one-size-fits-all solution.

In recent years, several groups have incorporated more features into the rate equation to try and raise its accuracy regarding input parameter values. One major direction in this direction is the incorporation of temperature effects in the electron system [68], or both the electron and lattice system [63]. This allows the utilization of electron temperature dependent forms for various parameters, such as the Drude collision time, with less postulation.

One thing that is usually not addressed in full is the valence band population, estimated at around $10^{23}\,\mathrm{cm}^{-3}$. In most threshold calculations, a large number of valence band electrons are excited, reaching a few percent [53, 63]. While still small, the depletion of these electrons may lead to non-negligible contributions at higher excitation levels. Similar to the saturation term in the defect term, some groups opt to preface the strong-field ionization and avalanche ionization rates by a factor $\frac{n_0-n_e}{n_0}$ where n_0 is the initial valence band population. This thus prevents excitation of an electron plasma with a population greater than the valence band density, a markedly unphysical situation. Furthermore, regarding carrier density effects, carrier blocking, as well as many-body effects such as band-gap renormalization, which has recently been postulated to play a role [69], are usually not taken into effect.

Another factor that the rate equations cannot describe are spatial charge imbalances. Because the equation is solved in zero dimensions, the charge is always neutral within the rate equation approach: electrons are excited but never lost. This is problematic when one seeks to study Coulomb explosion effects, which are believed to be driven by massive local electric field gradients near the sample surface. To address this problem, Bulgakova *et al.* have formulated a 1-dimensional (in space) rate equation model which incorporates photoemission and electron spatial diffusion [70, 71, 10]. Such modeling has succeeded in recreating the qualitative features of Coulomb explosions for dielectrics, something which is impossible to do with the zero-dimensional model and effects discussed in this section.

2.4. Modeling the optical properties

In order to determine the electronic excitation of the material, information on the electric field within the material is necessary. In the case of low excitation, the optical response is relatively unchanged. However, when the excited conduction band electron density becomes significantly high, their free-electron-like characteristics begin to play non-negligible roles in the optical response. Their high coupling to the electric field leads to not only an increased amount of absorbed energy, but reflected energy as well.

In most studies of ablation, the effects of nonlinear propagation within the material are ignored. Self-focusing and defocusing due to the excited electron plasma, among other effects, are known to lead to complex changes of beam spatio-temporal properties [17, 72]. However, as ablation occurs at the material surface, these effects are believed to cause only minor changes. In general, the linear response of the excited electron plasma is believed to be dominant to the optical response.

As known from classical electrodynamics [44], the complex refractive index $\tilde{n}$ satisfies

$$\tilde{n} = n + i\kappa = \sqrt{\varepsilon_r \mu_r}, \tag{2.4.1}$$

where n and κ are the real and imaginary parts of the refractive index, and ε_r and μ_r are the relative dielectric permittivity and relative magnetic permeability. Most often $\mu_r = 1$ is assumed. Modeling of the optical properties thus boils down to determining values of ε when coupled with the local electronic excitation, which varies by time and space.

2.4.1. The refractive index

In the case of modeling the refractive index of dielectric materials, the Lorentz model is often used, or more empirically, the Sellmeier equation. However, while not nonexistent (see for example [73]), these models are rarely used to model the optical response of dielectric materials in ablation studies. This is due to the fact that the optical response is dominated by the conduction band electrons in highly excited dielectrics, the effects of which are hard to incorporate into the aforementioned models.

As the conduction band electrons are believed to behave like free electrons in a metal, the Drude model is often used to model their contribution to the optical response. The dielectric function within the Drude model is given as [44]

$$\varepsilon(\omega) = \varepsilon_b - \frac{n_e e^2}{\varepsilon_0 m(\omega^2 + i\omega/\tau)}. \tag{2.4.2}$$

Here, ε_b is the relative dielectric constant background due to contributions from other bound electrons. This is usually taken to be equal to the square of the refractive index of the unperturbed material at the laser wavelength. As before, n_e is the conduction band electron density, e the elementary electric charge, m is the electron effective mass, τ the effective collision time, and ω the laser angular frequency. It is often convenient to define a plasma frequency as

$$\omega_p^2 = \frac{n_e e^2}{\varepsilon_0 m}. \tag{2.4.3}$$

In this case, equation (2.4.2) is simplified to

$$\varepsilon(\omega) = \varepsilon_b - \frac{\omega_p^2}{\omega^2 + i\omega/\tau}. \tag{2.4.4}$$

The real and imaginary parts of the complex dielectric function can then be calculated as

$$\varepsilon_{Re}(\omega) = \varepsilon_b - \frac{\omega_p^2 \tau^2}{(1 + \omega^2\tau^2)}, \tag{2.4.5}$$

$$\varepsilon_{Im}(\omega) = \frac{\omega_p^2 \tau}{\omega\,(1 + \omega^2\tau^2)}. \tag{2.4.6}$$

The relationship between the complex dielectric function and the complex index of refraction can be found by squaring both sides of (2.4.1):

$$\varepsilon_{Re} = n^2 - \kappa^2,\ \varepsilon_{Im} = 2n\kappa, \tag{2.4.7}$$

or

$$n = \sqrt{\frac{|\varepsilon| + \varepsilon_{Re}}{2}},\ \kappa = \sqrt{\frac{|\varepsilon| - \varepsilon_{Re}}{2}}\,. \tag{2.4.8}$$

From the complex refractive index, the reflection and absorption coefficients can be calculated. Assuming that the pulse is normally incident upon the sample, the Fresnel reflection coefficient at the air-material interface is given by

$$R = \left|\frac{1-\tilde{n}}{1+\tilde{n}}\right|^2\,, \tag{2.4.9}$$

where we have taken the refractive index of air as 1. The absorption coefficient is given by

$$\alpha = 2\omega\kappa/c\,. \tag{2.4.10}$$

From classical electrodynamics, we also know that the electric field amplitude and intensity satisfies

$$I(\omega) = \frac{cn\varepsilon_0}{2}|E|^2. \tag{2.4.11}$$

By converting electric field values to the intensity, it can be verified that the absorption coefficient derived from (2.4.10) is consistent with the Drude absorption calculated in (2.3.22), when the latter is multiplied by n_e to give the absorption per unit volume, not per electron. From this standpoint, it also makes sense to use a Drude optical model when the Drude absorption model is used for the rate equation. However, it should be noted that this deals with only the absorption due to the free electron plasma. When a full description of the energy propagation into the material is desired, any absorption due to strong field ionization must be accounted for separately, as done, for example, in [74, 53].

In Figure 2.4.1, the refractive index and the reflectivity calculated according to equatoins (2.4.8) and (2.4.9) are shown. A critical electron density can be defined as

$$n_c = \frac{\varepsilon_0 \varepsilon m \omega^2}{e^2}, \tag{2.4.12}$$

where ω is the laser angular frequency. Around this density, it is apparent that the optical properties of the material changes drastically, where the material has essentially turned "metallic" for the laser frequency. There is an increased amount of reflection as well as absorption of the incident field. For these reasons, material ablation is believed to occur at densities close to this value, as will be further elaborated on in the next section. In the literature, the critical density is often defined as the electron density where the plasma frequency equals the laser frequency, not the plasma frequency *screened by the background permittivity.* Physically, this choice is justified for the case where ε_b is ignored (taken as one); however, as evident from the optical properties, this value has no physical

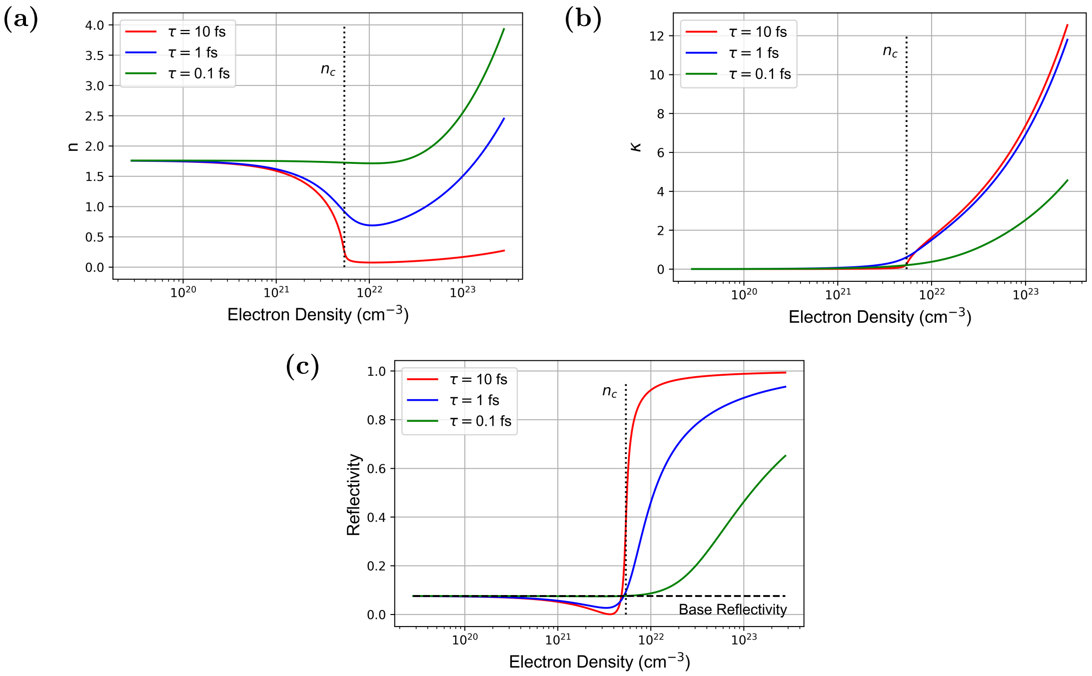

Figure 2.4.1.: The (a) real and (b) imaginary part of the refractive index, and (c) the reflection coefficient calculated as a function of the excited electron density and for different electron effective collision times is shown. An unexcited material reflectivity is marked for reference. The critical electron density where the screened electron plasma frequency equals the electron density is also shown as a dotted line. A wavelength of 800 nm and an effective mass equivalent to the free electron mass was used, while the background dielectric constant was calculated from Sellmeier's equation for sapphire at 800 nm.

significance in our current case, and we shall refer to the critical density in the form of equation (2.4.12) unless otherwise noted.

2.4.1.1. The background refractive index

Before moving on, we take a moment to address a trend in ablation theories where excitation density dependence is incorporated into the background dielectric function. The dielectric function of a material in the optical frequency can be attributed mostly to the coupling of the valence and conduction band [75]. With a greater degree of photoexcitation, the background refractive index ε_b can be expected to decrease to near unity as the valence band population becomes depleted.

There have been mainly two approaches to factor in this effect. The first is to consider the contribution of the valence band density to the electrical susceptiblity to be linear. Here, the total susceptibility at electronic excitation should scale with the fraction of the depleted valence band electron population relative to the initial valence band electron population [76, 77, 71, 78, 79]. In this case, the dielectric function reads

$$\varepsilon(\omega) = 1 + \frac{n_0 - n_e}{n_0}(\varepsilon_b - 1) - \frac{\omega_p^2}{\omega^2 + i\omega/\tau}, \tag{2.4.13}$$

where n_0 is the initial valence band population. When $n_e = 0$, it can be seen that this equation is equivalent to equation (2.4.4), and when $n_e \approx n_0$, the total of the first two terms approaches unity.

A second convention utilizes the Clausius-Mossotti equation (or Lorenz-Lorentz equation), where the microscopic polarizability χ_m of a constituent unit (formally for gasses and molecules) is related to the macroscopic polarizability in an isotropic medium [5, 17, 44]. Given a constituent density of N, the dielectric constant is related to χ_m as

$$\varepsilon = 1 + \frac{N\chi_m}{1 - (1/3)N\chi_m}. \tag{2.4.14}$$

In an analogue, the number of constituent units is taken as the valence band electron density, and hence, the total dielectric function becomes

$$\varepsilon(\omega) = 1 + \frac{3(n_0 - n_e)\chi_m}{3 - (n_0 - n_e)\chi_m} - \frac{\omega_p^2}{\omega^2 + i\omega/\tau}, \tag{2.4.15}$$

where χ_m is taken such that the first two terms of the background dielectric index at zero excitation [80, 12, 81].

In either case, changes to the background dielectric index do not become significant until a significant portion of the valence band electron has been excited. As apparent from Figure 2.4.1, for the case of optical frequencies in the near-infrared region, the evolution of the Drude term dominates the optical response, and any depletion effects are minor. However, at shorter laser wavelengths, the critical density moves to higher values, and the changes in the optical properties becomes potentially non-negligible. Calculated reflectivities for the various models is shown in Figure 2.4.2. The valence band electron density is taken as 2.8×10^{23} cm^{-3} [82]. As is expected, the Clausius-Mossotti formulation leads to the biggest difference with the static value.

Whether these effects are significant in ablation models depends on the ablation criterion used, addressed later. In most cases, the final excitation densities are believed to be of the order of a few percent of the valence band density, densities at which the background change is negligible. In any case, uncertainties in the electron collision times, and validity of the Drude model itself, would seem to be a more dominant factor, as can be seen from the vastly differing structures of the various optical responses calculated in Figure 2.4.1.

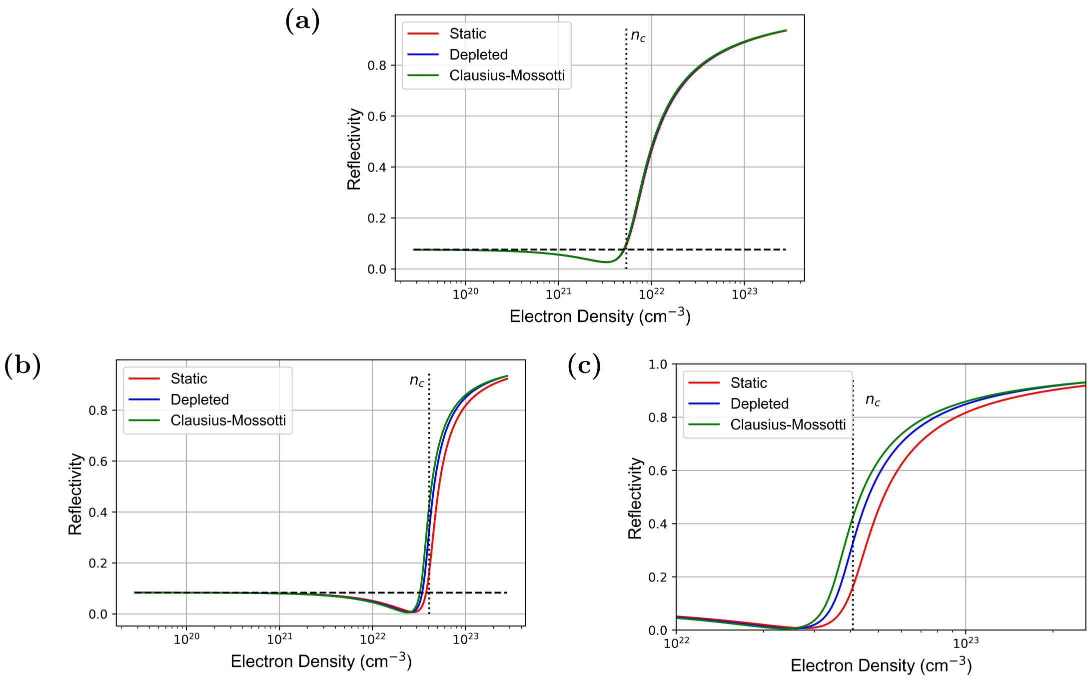

Figure 2.4.2.: The various reflectivities calculated according to a static background, depleted, or Clausius-Mossotti behavior. Material parameters are equivalent to Figure 2.4.1, with the collision time held at 1 fs. (a) is calculated for a laser wavelength of 800 nm, while (b) is calculated for 300 nm. (c) is a closeup of (b) near the plasma frequency.

2.4.2. Propagation

With the material optical properties calculated according to the electron-density dependent refractive index, it is possible to calculate the optical propagation into the material. The mismatch of the spatial scales and the temporal scales involved (a 1 fs time step spans an length of 300 nanometers) complicates the problem. At the strictest level, this involves solving the Maxwell equations, which is often a rather numerically intensive task, but have been done nonetheless [83, 84].

To simplify the problem, some groups use a matrix method, as often used to calculate transmission in a thin film stack [46, 47]. This involves splitting the bulk material into artificial layers (approx. 1 nm thick). The dielectric function for each time is calculated by the electron density calculated at each previous time step. The cw intensity distribution is calculated for the next time step for an incident wave with intensity $I(t)$. The local intensity within each slab is then used to calculate the evolution of the transient electron density, which is then used to calculate the dielectric function for the next time step. However, due to the linear nature of the transfer matrix approach, incorporation of nonlinear absorption is a non-trivial matter.

In a similar manner, some groups ease calculations by simply propagating the intensity [74, 53, 85]. Intensity differences at each spatial slab is calculated via local linear and nonlinear absorption. Density dependent absorption parameters are calculated with the electron density calculated at the previous time step.

With the local intensity determined for each time step, it becomes possible to calculate the cumulative electron density distribution. Coupled with a material breakdown criterion, it becomes possible to compare with more morphological features determined from experiment, such as crater depth dependence on the laser fluence [74, 85].

2.5. Breakdown criterion

At the ultrafast time scale, as outlined in the introduction, the electrical excitation model of section 2.3 and changes in the optical property modeled by the theories of section 2.4 are coupled and solved in a self-consistent manner to arrive at a final electron density (and in some cases, distribution). In order to predict material destruction, some sort of ansatz linking the final electronic states is required.

In this section, we introduce the electron density-based criterion as the most commonly used criterion in the literature, followed by several others as reference.

2.5.1. Electron density-based criterion

The electron rate equations mostly calculate the final electron excitation densities. Thus, the simplest candidate for the breakdown criterion is the assignment of some breakdown electron density. As the electrons in the valence band form the bonding orbitals of the solid, when a certain fraction has been excited, the material would be expected to become unstable [12].

The choice of this density is often somewhat phenomenological. Often, it is taken as the critical electron density defined in equation (2.4.12). Experimentally, this is consistent with the increased reflection coefficients seen near threshold intensities for near-infrared pulses, as would be expected from a Drude plasma [86, 62, 87, 85]. Physically, the Drude model predicts that at densities above the critical density, the material absorption increases drastically (see Figure 2.4.1). Any further increase in pulse energy is believed to be absorbed efficiently, making this density the threshold density required [12, 13].

However, equating the threshold density to the critical density gives this value a wavelength dependence. These differences result in an order of magnitude between ultraviolet and near-infrared pulses for the same material. Furthermore, the electron excitation rates already take into account the energy absorption difference at various electron densities, making the aforementioned logic somewhat circular, as argued by Christensen *et al.* [53]. For these reasons, some groups advocate for a static electron density. This density is often taken as a fitting parameter to match with experiments. Values are often around the critical density for 800 nm light (of the order of $10^{21\sim22}$ cm^{-3})

and retain consistency with past experiments. This equates to an excitation density of a few percent of the valence band electron density [53].

2.5.2. Other criteria

A major direction that has seen increased use is an energy density criterion. In this case, the total energy density is usually estimated from the total energy deposited into the electron system. Disregarding timescales, this energy will transfer to the lattice system, which will in turn lead to (thermal) material destruction. These values are often taken near the enthalpy of formation, of the order of a couple tens of kJ/cm^3 in typical dielectrics [80, 83, 81, 78, 46, 63]. Some have argued that this is essentially a similar criterion to a fixed density criterion [52], while others have argued otherwise, stressing that a more strict evaluation of the deposited energy is required [88].

In the case of electrostatic ablation by Coulomb explosion, the energy density held in the electric field created by the charged ions in the lattice is taken as the relevant ablation parameter [71]. This value is compared to the latent heat of sublimation calculated for a single atom (approx. 5 eV). Threshold fields are determined to be of the order of 5×10^{10} V/m.

2.6. Summary

In this chapter, we have covered the various theories and models presented within the literature, particularly with a focus on femtosecond laser ablation models presented in the last 20 years. We introduced the rate equation approach as the most accessible and widely used model of the ablation process. As the specific form of the rate equation depends heavily on the material in question, we defer actual construction of a rate equation to later sections, using concepts introduced in this chapter.

Lastly, we provide below a table of the various rate equation models for dielectrics (and water, as the theories used are similar) in the literature, used both for experimental analysis and theoretical studies. It is hardly an exhaustive list of all the work in the literature, but should give an idea as to the various trends in modeling throughout the last 20 years.

Table 2.6.1.: A list of experimental and theoretical studies utilizing the rate equation approach

Reference	Material	Laser Parameters		Electron Model				Optical		Criterion
		Wavelength (nm)	Pulse Width (fs)	Population	Strong Field Ion.	Avalanche	Collision Time (fs)	Model	Propagation	
Du 1994 [43]	SiO_2	780	>150	SRE	TI	Th	0.4	-	-	D-Crit
Stuart 1995 [4]	SiO_2	1053, 526	>270	SRE	MPI	Dru	E	Dru	-	D-Crit
Guizard 1995 [16]	MgO, SiO_2 Al_2O_3	620	70	SRE^{a}	MPI	-	-	-	-	-
Lenzner 1998 [89]	SiO_2, BBS	780	>5	SRE	MPI	Fit	-	-	-	D-Crit
Li 1999 [60]	SiO_2, BBS	800	25	SRE^{a}	MPI	Fit	-	-	-	D-Crit
Tien 1999 [32]	SiO_2	800	>20	SRE	KI	Th	0.4	-	-	D-Crit
Noack 1999 [49]	Water	532-1064	>100	SRE^{a,b}	MPI	Dru^{1,2}	1	-	-	D-Crit
Quéré 2001 [90]	MgO, SiO_2 Al_2O_3	800	60	SRE	MPI	Fit	0.77	Dru	Int	D
Guizrd 2002 [80]	Al_2O_3	800	>60	SRE	MPI	-	-	Dru	Int	E
Rethfeld 2004 [50]	SiO_2	500	300	MRE	KI	Const.	-	-	-	D-Crit
Bulgakova 2004 [71]	Al_2O_3	800	100	SRE^{a,e}	MPI	Dru	1.3	Dru	Int	ES
Starke 2004 [91]	SiO_2	800	100	SRE^{a}	KI	Dru	D	Dru^{i,i}	-	D-Crit
Jiang 2004 [74]	BBS	780	220	SRE^{c}	MPI	Const.	DT	Dru	Int	D-Crit
Mero 2005 [61]	Various	800	>25	SRE	MPI	Fit	-	-	-	D-Crit
Peñano 2005 [83]	SiO_2	800	>50	SRE^{c}	MPI	Dru^{2,4}	DT	Dru	Max	E, D
Aldana 2005 [92]	SiO_2	800	40	SRE	MPI	Lor	D	Lor	Max	D-Crit
Jia 2006 [46]	SiO_2, CaF_2	500-2200	150	SRE	KI	Dru^{3}	1-2	Dru	TM	E
Petrov 2008 [84]	SiO_2	800	>53.4	SRE^{a,c}	KI$^{\alpha}$	Dru^{4}	TD	Dru	Max	E, D
Jiang 2008 [93]	SiO_2	780	50	SRE^{d}	MPI	Const.	DT	Dru	Int	D-Crit
Christensen 2009 [53]	Al_2O_3	400-1060	>30	MRE	KI	Dru	D	Dru	Int	D
Jupé 2009 [94]	TiO_2	590-750	130	SRE^{a}	KI	Dru	D	Dru	-	D-Crit
Chimier 2011 [63]	SiO_2	800	>7	SRE^{a,d}	KI	Dru	DT	Dru	-	T
Takayama 2012 [95]	HfO_2, TiO_2 Al_2O_3	800	>25	SRE^{c}	MPI	Fit	-	Dru	Int	D-Crit
Jing 2012 [96]	SiO_2	400-1300	>5	SRE^{a}	KI	Var	Var	-	-	D-Crit
Sun 2013 [73]	K9 glass	532	10 ps	SRE^{b}	KI	Lor	D	Lor	Max	D-Crit
Geoffroy 2014 [97]	SiO_2, Al_2O_3	800	70	MRE^{a}	KI$^{\beta}$	Dru	5	Dru	-	ES
Wædegaard 2014 [81]	Al_2O_3	800	70	MRE	KI	Dru	D	Dru	Int	D-Crit
Gallais 2015 [47]	Various	310-1030	100	MRE	KI	Dru	D	Dru	TM	E
Linz 2016 [98]	Water	335-1085	120	SRE^{b}	KI	Dru^{1}	Fit	Dru	-	D
Sun 2016 [54]	Water	800	>140	SRE^{b}	KI	Dru	4	Dru	-	D-Crit
Garcia-Lechuga 2017 [82]	SiO_2, Al_2O_3	800	120	MRE^{a}	KI	Dru	D	Dru^{ii}	-	D

[a] With decay term ($\propto n_e$) [b] With recombination term ($\propto n_e^2$) [c] With electron temperature term
[d] With two-temperature model [e] With diffusion, photoemission
[α] Forest-fire correction [β] With multiplication factor
[1] Delayed [2] With inelastic correction [3] With sub-CB absorption [4] Distribution considered
[i] With Kerr non-linearity [ii] With exciton terms

SRE = Single and MRE = Multiple Rate Equation; TI = Tunneling, MPI = Multiphoton, and KI = Keldysh Ionization; Dru = Drude, Lor = Lorentz; E: energy, D: density, T: temperature (dependent); Int = Intensity Propagation, Max = Maxwell equation, TM = Transfer Matrix; Crit = Critical, ES = Electrostatic.

Chapter 3.

A Unified Study on Ablation Morphology: Fluence Mapping

In laser ablation studies, the most basic information comes from ex-situ morphological observation of the ablated regime. Through observation of the processed surface, and measurements of the relative physical features, comparison to theoretical predictions is made possible. However, in order to gain systematic data, characterization of the laser is just as important.

In this chapter, we detail the development of a new experimental procedure to directly measure the incident laser fluence distribution and map this onto ex-situ observed morphological characteristics. This "mapping" of the local fluence information onto the local morphology allows for the study of laser ablation beyond a typical Gaussian-approximation approach. Not only does this increase the robustness of measurements, but also allows us to assess the applicability of several major assumptions made in laser ablation studies.

3.1. Introduction

When studying ablated morphology, the two most common parameters characterized are the ablated area (also in the form of the diameter/radius in the case of a circular beam) and the ablated depth. These parameters are easy to determine from traditional microscopy techniques, and can be used to compare to theoretical studies in a relatively straightforward manner.

Apart from direct comparison to theoretical prediction, these morphological characteristics are also used to extrapolate the damage threshold of the material, arguably the most important physical parameter in this field. While the damage threshold is, in the purest sense of the word, the energy at which material surface modification becomes visible, its detection depends on the sensitivity of the technique used. In general, in-situ techniques, such as imaging of plasma luminescence or scattering of a probe laser, have been found to yield systematically higher thresholds (i.e. were worse at detecting smaller features) than ex-situ microscopy, while the scanning electron microscope was found to be the most sensitive of the various commonly used microscopy techniques available [99]. Even with microscopy, it is often hard to locate and identify small features which mark the onset of ablation.

In light of this complication, two main trends appeared to increase accuracy. The first was to increase the number of pulses to “magnify” the features created. Especially in early experimental studies, this was a common method [4, 89]. However, it was soon experimentally seen that multiple-pulse ablation thresholds varied from that of a single pulse, due to damage incubation effects [100]. The second and now standard method is morphology extrapolation. Three main schemes have been proposed: volume, depth, and area (diameter) extrapolation.

Volume extrapolation was propsed by Lenzner *et al.* from experimental observations that the ablated volume followed a linear trend when plotted as a function of the incident laser fluence (or pulse energy) [89]. By extrapolating a linear fit to experimental data, the threshold fluence could be determined as the value of the intercept. The physical reasoning was as such: above the threshold, a plasma is excited by the first half of the laser. The excess pulse energy in the latter half is beleived to be absorbed linearly by the induced plasma. This absorbed energy is proportional to the ablated volume (to first order), leading to the observed trend. While a mostly phenomenological method, the experimental ease in defining and measuring the ablated volume has helped in its longevity, and the method still sees use today, see for example [101, 102, 103, 104, 105].

Depth extrapolation is a method widely used for the study of metals and semiconductors, where the ablated depth is believed to follow the Lambert-Beer law for optical (low fluence) or thermal (high fluence) penetration depths [106]. In a similar analogue, Puerto *et al.* have proposed a scaling law based on the multiphoton absorption penetration depths [6]. In this case, the depth is expected to obey a polynomial relationship in regards to depth; this function can be fitted to determine the multiphoton absorption coefficient and the fluence threshold. However, the theory is relatively new, and has yet to be widely taken up in the literature [107]. Whether the effects of avalanche ionization can be ignored is also open to question, as acknowledged by Puerto *et al.* within their paper.

Diameter regression is perhaps the most widely used technique, proposed by Liu in 1982 for characterizing picosecond pulse beam diameters [108]. As a qualification of this technique will become a main motivation of this work, we will take a moment to go over the details of this method.

3.1.1. Diameter regression

As mentioned above, diameter regression[1] is a common technique utilized to characterize laser ablation. It works on two working assumptions:

---

[1] There are many names for this technique, such as Liu’s method/technique, area regression/extrapolation, D^2 method/extrapolation/regression/fitting, among others. Here we will stan-

1. That the beam has a Gaussian spatial profile, and
2. That there is no significant local radial dissemination of heat or carriers.

The local fluence at a radial position r of a Gaussian beam with a $1/e^2$ intensity radius of w_0 can be characterized by

$$F(r) = F_0 \exp\left(-\frac{2r^2}{w_0^2}\right). \tag{3.1.1}$$

Here, F_0 is the peak fluence of the pulse. If we define a local fluence threshold F_{th} at which material modification occurs, for a given pulse energy where $F_0 > F_{th}$, a circular area should be affected. Utilizing the second assumption, we see that the radius of the circle r_{th} should be the radius at which the local fluence equals the threshold fluence, or where

$$F_{th} = F_0 \exp\left(-\frac{2r_{th}^2}{w_0^2}\right), \tag{3.1.2}$$

is satisfied. Solving for r_{th}, the following logarithmic relationship is derived:

$$r_{th}^2 = (1/2)w_0^2 \ln\left(\frac{F_0}{F_{th}}\right). \tag{3.1.3}$$

More commonly, the relationship is written in terms of the diameter $D_{th} = 2r_{th}$ (which is the often measured value), and the logarithm is split:

$$D_{th}^2 = 2w_0^2(\ln F_0 - \ln F_{th}). \tag{3.1.4}$$

In principle, with information on the beam profile, a single ablation crater could be used to determine the ablation threshold through equation (3.1.4). In practice, in order to reduce statistical errors, several craters with several peak fluence values are used. The measured diameters (or its squared values) are then plotted against the corresponding peak fluence values, and fit with equation (3.1.4) to determine F_0, which graphically is manifested as the x-intercept of the plot. A general schematic of this process is presented in Figure 3.1.1.

While extrapolation techniques in general benefit from the reduction of statistical errors, the diameter regression technique possesses another unique characteristic which makes it particularly useful for ablation experiments. In equation (3.1.3), it can be seen that fluence values only appear as a ratio. As the peak fluence F_0 and the pulse energy E_p satisfy the following relationship,

$$F_0 = \frac{2E_p}{\pi w_0^2}, \tag{3.1.5}$$

---

dardize reference to it as “diameter regression” as one of the most common names within the literature.

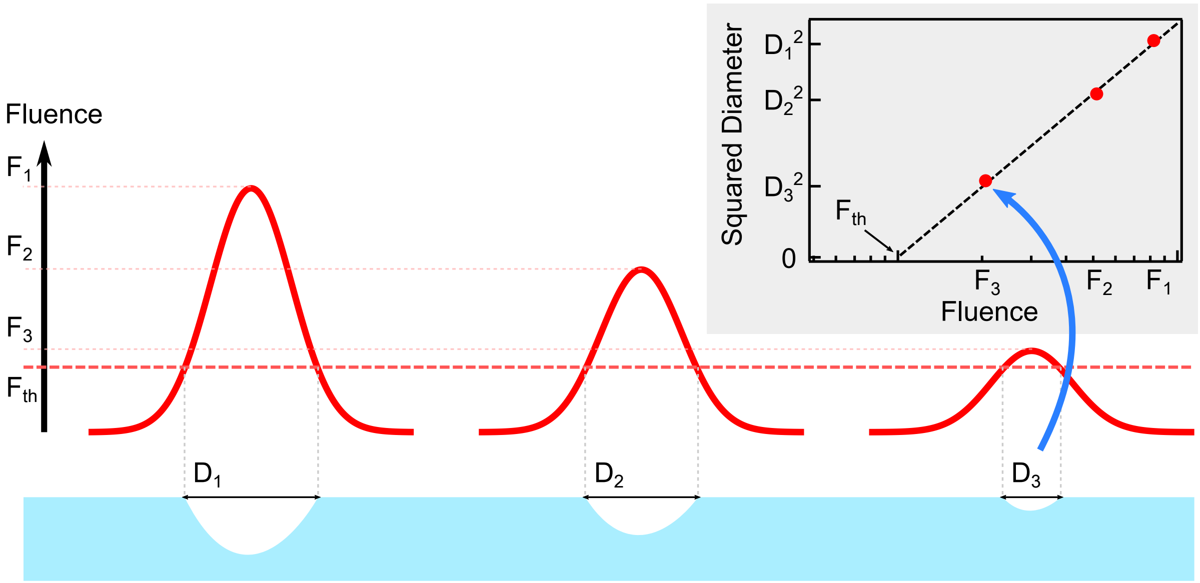

Figure 3.1.1.: A general overview of the diameter regression technique. Several craters are created by pulses of varying energies, and their diameters are measured. A linear regression of the squared diameter in terms of the logarithm of the fluence yields the threshold fluence, as shown in the inset graph.

it can be seen that the same relationship of equation (3.1.4) can be written in terms of the pulse energy. Setting the beam radius w_0 as a second fitting parameter allows us to derive a threshold pulse energy E_{th} and beam radius w_0, which can then be used to calculate the threshold fluence F_0 through equation (3.1.5). In the area vs log plot, the diameter corresponds to the slope of the line: the steeper the slope, the larger the radius.

This means that with the diameter regression technique, it is possible to derive threshold fluence values *without a priori information on the beam spatial diameters*. This in-situ beam profiling characteristic is especially beneficial for ablation setups, where the spot sizes are usually small and non-trivial to characterize. In fact, this ability was the key message of Liu's original paper, and such ablation "imprint" profiling has been used to characterize otherwise hard-to-characterize light sources, such as the beam profile at the focus of an X-ray free-electron laser [109].

While the diameter regression technique is the most popular method in determining damage thresholds of materials owing to its simplicity and ease of use, it does have its caveats stemming from the assumptions made in its formulation. When examined further, both statements are non-trivial constraints. The ultrafast transport dynamics occurring during femtosecond irradiation is far from well-known, and is an open question. The second condition poses a more technical difficulty, but important nonetheless for high-power ultrashort laser processing. High-power regenerative amplifiers are prone to distortions in the beam profile, and are hard to clean with traditional mode-cleaning methods owing to their high power. Furthermore, focusing conditions will also affect the profile at the focus.

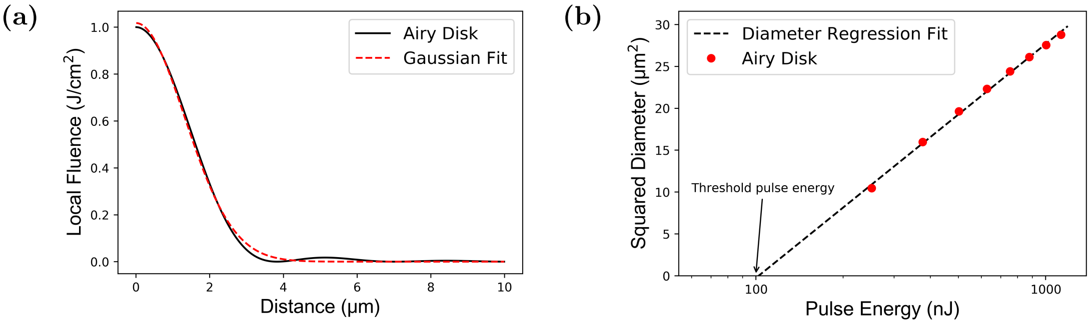

Figure 3.1.2.: (a) The Airy disk distribution, and a corresponding Gaussian fit. (b) Airy disk crater diameter "analyzed" by traditional diameter regression.

To illustrate the potentially misleading nature of the analysis, we think of an artificial case of a pulse with an Airy disk profile near the focus, where the local fluence at a radial position r is given by

$$F_{Airy}(r) = F_0 \left(\frac{2J_1(r)}{r} \right)^2 , \tag{3.1.6}$$

where $J_1(r)$ is the Bessel function of the first kind. The distribution and its Gaussian fit are shown in Figure 3.1.2a. If we assume a threshold intensity of 1 J/cm^2, the crater diameters made by this pulse for varying F_0 can be calculated by solving $F_{Airy}(r) = 1$.

Let us now analyze these diameter values as if they were extracted from experiment, believing the beam to be of a Gaussian profile and following the diameter regression technique. For "data," we assume 8 artificial craters made by pulses with peak fluences of 2, 3, 4, ... 9 J/cm^2, and calculate their diameters. We measure the energy in a single pulse of equation (3.1.6) by numerically integrating equation (3.1.6) over all space, yielding a pulse energy of $4\pi F_0$. We can "analyze" this data with the diameter regression technique, as shown in Figure 3.1.2b. The "data" points are provided as red circles plotted with regards to the corresponding pulse energy values, which would be the typical experimental observables. This is fit with the regression analysis (black dashed line). From the fit, we can retrieve the threshold pulse energy and beam diameter, which we use to derive the threshold fluence. This results in a value of 1.07 ± 0.04 J/cm^2, notably different from our initial assumption of a threshold of 1 J/cm^2.

The discrepancy in the above example mainly results from the energy stored in the satellite "disks" of the Airy disk profile, as well as the slightly sharper profile of the central distribution compared to a Gaussian. However, from an experimental point of view, due to the central peak being very well approximated by a Gaussian, simple chi-squared testing with typical errors seen in measured areas (a few percent) will not be able to detect this systematic error.

In general, it should be noted that diameter regression is only sensitive to the "midsection" of the pulse, and not to its peak or the fringes. As cautioned by Sanner *et al.*, when thresholds are near the peak of a pulse, the hole sizes are small and difficult to

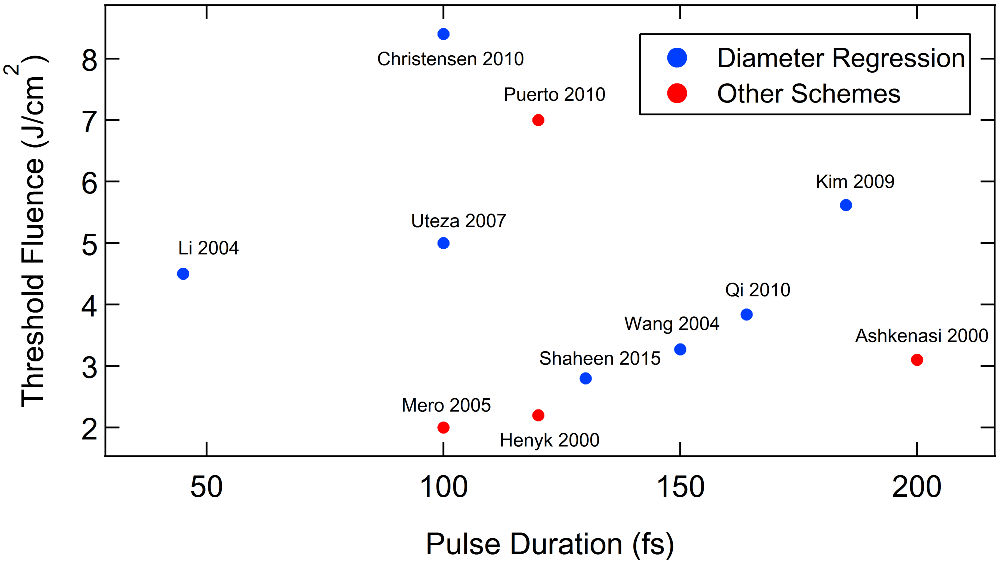

Figure 3.1.3.: Thresholds determined for sapphire in the literature for femtosecond lasers with a central wavelength close to 800 nm. Data from [101, 111, 112, 61, 6, 113, 114, 115, 116, 117, 118](left to right, top to bottom)

characterize. Conversely, when thresholds are near the fringes, the required pulse energies are usually too high and inaccessible, and even when accessible, the high pulse energies results in fracturing of the material, making a reliable measurement of the diameter/area difficult. This results in a misrepresentation of the pulse spatial profile skewed towards the "midsection" of the pulse [102]. As a result, total energy values and beam radii may be misconstrued, and consequently, the derived fluence values loses accuracy as well.

For dielectrics, it has been found that the diameter regression technique yield systemtically higher thresholds, and the derived beam radii, while in general agreement with other profiling techniques, are systematically smaller. Some groups have attributed this to the high degree of nonlinearity necessary for the excitation of dielectric materials [110]. However, it should be noted that the diameter regression technique is *not* concerned with the degree of non-linearity of the process concerned. It simply links the equal-contour fluence distribution in the beam to the morphology of craters, the morphology of which can be caused by an arbitrary-order process. Nonetheless the disentangling of these two factors, namely that of locality and that of beam systematics is key to overcome the current limits in accuracy in threshold fluence measurements.

3.1.2. Beyond Gaussian regression

In Figure 3.1.3, we gather experimentally measured threshold values in the literature for sapphire ($\alpha{-}\mathrm{Al_2O_3}$) for lasers with central wavelengths at or close to 800 nm. All experiments selected were done with single pulses, and thus incubation effects can be excluded. Even for similar pulse durations, a large discrepancy can be seen in the

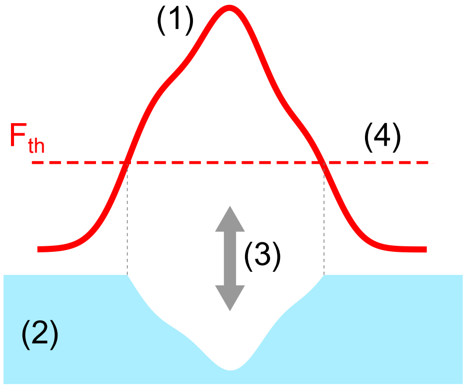

Figure 3.2.1.: In order to modify the diameter regression technique, information on the (1) beam profile, (2) ablated profile are required. In addition, (3) they must be spatially calibrated to each other, after which (4) relevant correlations can be made.

experimental values; the lowest values are around 2 J/cm^2 while the highest are around 8 J/cm^2. One could argue that this discrepancy is the result of the experimental procedures in determining the thresholds. However, even isolating experiments utilizing the diameter regression technique (shown in blue in Figure 3.1.3), discrepancies can still be seen.

In general, the statistical errors presented within ablation papers is in the sub-J/cm^2 order. However, it is apparent from the data that significant systematic errors exist. While this may be attributed in part to sample quality, it would still appear that there is room for improvement in the methodologies of the techniques utilized to define the ablation threshold. In order to elucidate the physics of the ablation process, determining the experimental fluence values, as well as the threshold fluence as a reference point, is of great importance.

In light of this current state of the field, we seek to develop a new methodology to extend the diameter regression technique beyond the simple Gaussian profile method proposed by Liu over three decades ago. In addition, we explore the extent of the locality of femtosecond laser ablation: does the local incident fluence determine the morphology (in this case, the depth) of the locally ablated material? Through this work, we propose a new threshold determination technique robust to beam profile induced systematic errors. This condition is required to extract meaningful data between different lasers, or even settings within the same laser system, such as wavelengths in an optical parametric amplifier.

3.2. Principles

In order to extend the diameter regression technique to an arbitrary beam profile, we need to determine a one-to-one correspondence between the incident fluence profile and the observed morphology. The required steps are broken down in Figure 3.2.1. The beam profile at the focus and the ablated profile must be obtained, after which their information can be aligned to the same spatial scale. Once this is done, the incident local fluence can be correlated to the local morphology, from which meaningful physical parameters can be extracted. Of these steps, the second step can be achieved with standard microscopy. The third and fourth step require some amount of image and data processing. It is the first step, imaging the beam at the focus, that proves to be the biggest technical bottleneck in the above scheme.

Traditionally, spatial information at the focal point of a Gaussian beam has been measured by the knife-edge method. In this method, a sharp planar object (i.e. a "knife") is translated across the beam, gradually blocking its path. The portion of the beam that passes is monitored, typically by a photodiode. As the differential of the photodiode signal is the integral of the beam intensity parallel the knife-edge, it is possible to numerically retrieve a 1-dimensional functional form of an arbitrary beam profile. In practice, a Gaussian spatial profile is postulated, and the knife-edge signal (the axis-integrated value of this signal) takes the form of the error function. Beam parameters are retrieved by fitting experimental values to the error function, and a corresponding Gaussian-profile is assumed to be formed at the focal point.

While the knife-edge method is generally accepted as a satisfactory characterization of the beam profile, there are several drawbacks. Measurements are often time consuming, and suffer from systematic errors caused by knife quality. Additionally, in its simplest implementation, the method postulates a Gaussian profile, a counter-intuitive condition for our current case, considering that deviations from a Gaussian profile are what we are concerned with. Without such postulation, scanning routines become even more time-intensive, and characterization of the noise and its differential signal becomes non-trivial.

In light of these disadvantages, a camera based method would possess certain key advantages. Measurements could be done relatively quickly, as signals are retrieved in two dimensions instead of zero. Additionally, noise and errors in the camera image could be more easily qualified than the random micron-order defects seen on the edge of a knife. Finally, and perhaps most important of all, the profiles would not require any prior postulation of beam profile distribution.

Unfortunately, traditional beam profilers are usually not meant for profiling beams at their focus. The biggest restriction is the pixel size. Pixel sizes of traditional beam profilers are usually at the order of a couple microns. As the laser spot diameters of typical ablation setups are somewhere around 20 microns, this results in only a dozen or so active pixels. Consequently, cameras-based beam profilers have typically been limited to beams in free-space or otherwise loosely-focused configurations. Of course, the focal plane may be imaged, but this also requires high-resolution magnifying lenses, which often have short working distances which pose difficulties in combination with ablation setups. Careful spatial calibration both in-plane and out of plane is also critical.

In order to overcome this difficulty, we focused our attention on cheap commercially available high-resolution cameras. With the spread of portable electronic technologies such as smartphones, these devices have become easily accessible with comparatively

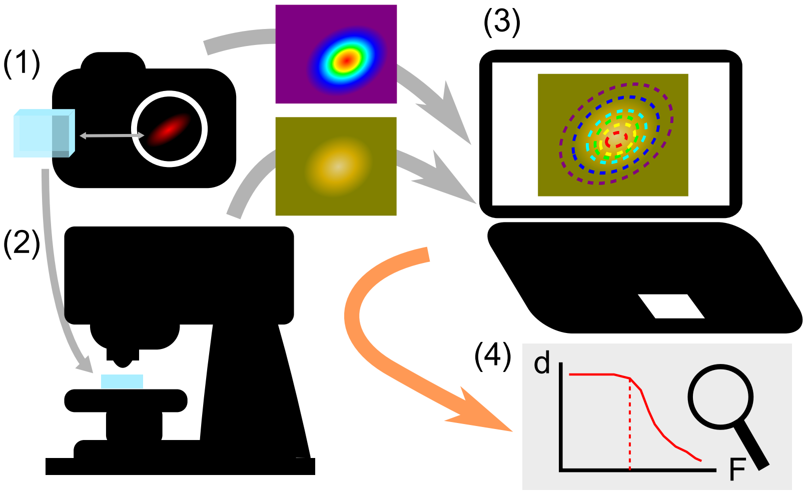

Figure 3.2.2.: The implementation of the steps outlined in Figure 3.2.1. The (1) camera beam profiler is used to image the beam at the focus after which the sample is processed. (2) The sample is subsequently observed by a microscope, and the morphology data is extracted. (3) The beam profile data and morphology data are superimposed with numerical methods, after which (4) the data may be sorted and analyzed.

high specifications for their value. In particular, we focus on the camera module to the popular single-board computer the Raspberry Pi. This camera module boasts a single-pixel size of a mere 1.12 microns square, small enough to resolve typical ablation spots at the focus. The module is also relatively compact, and can be easily integrated into traditional ablation systems.

Gathered altogether, the implemented methodology in order to achieve the outline of Figure 3.2.1 is shown in Figure 3.2.2. In the following sections, we cover the specifics of the experimental realization and procedures, and subsequently the numerical analysis process.

3.3. Experimental setup

3.3.1. Beam profiler

As mentioned in the previous section, a Raspberry Pi camera board was used to profile the sample. However, the camera bought off the shelf does not work as a beam profiler, and some hardware modifications are required.

The first modification is the removal of the imaging lens and protective glass slide and/or IR cut filter present. This can be done by mechanically removing the housing to the CMOS censor, to which the glass and lens are connected. This leaves the CMOS sensor of the camera exposed on the board.

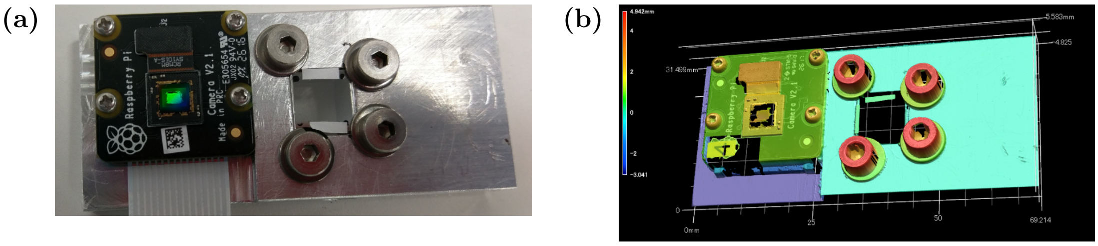

Figure 3.3.1.: (a) A picture of the sample holder (b) The scanned 3D information of the sample holder.

The second and biggest modification concerns the color filter array (or Bayer filter array) from the CMOS sensor. The surface of a typical color CMOS sensor is covered with a checkerboard pattern of red, green, and blue bandpass filters. In the Raspberry pi camera module, a group of four pixels (1 red, 2 green, and 1 blue) act as 1 color pixel in the retrieved color image in normal operation. Of course, when the beam sizes are not too small, the signal from a single channel sensitive to the current wavelength can be singled out, at the cost of spatial resolution (potentially only utilizing 1/4 of the pixels at a given time). However, for our current case, we seek to maximize the pixel density to compensate for the already large mismatch between the microscope spatial resolution (with pixels on the order of a couple tens of nanometers) and the camera pixel density.

One potential solution is using the camera with the spectral sensitivity of each channel calibrated at the laser wavelength. However, this leads to problems when: 1) a wide range of wavelengths are used, making calibration time-consuming, 2) the device is used outside of the visible wavelength range, where no filter may be transparent, and 3) when high dynamic range is required, as the gain/exposure times will be limited by the saturation of the most sensitive pixel.

In order to allow for a wide range of spectral sensitivity, here, we opt to remove the color pixel array. We achieve this by mechanically scraping the surface color filter layers off with a razor blade. To minimize the chance of damage, only the central region was modified this way. The sensor surface was cleaned in an ultrasonic acetone bath after the scraping process.

A program was made on the Raspberry Pi in python to extract the raw data before any color balancing between the channel. A graphical user interface was made to facilitate ease of use. The ability to receive simple TCP commands via ethernet cable was also implemented to allow for remote control. More regarding the camera are documented in Appendix B.

3.3.2. Sample mount

The ablation sample was mounted onto a custom-made aluminum frame, as shown in Figure 3.3.1a. Samples used in the experiment were all 1 cm square, and were typically 0.5 mm thick. To allow for easy placement, there is an incision 0.2 mm deep on the

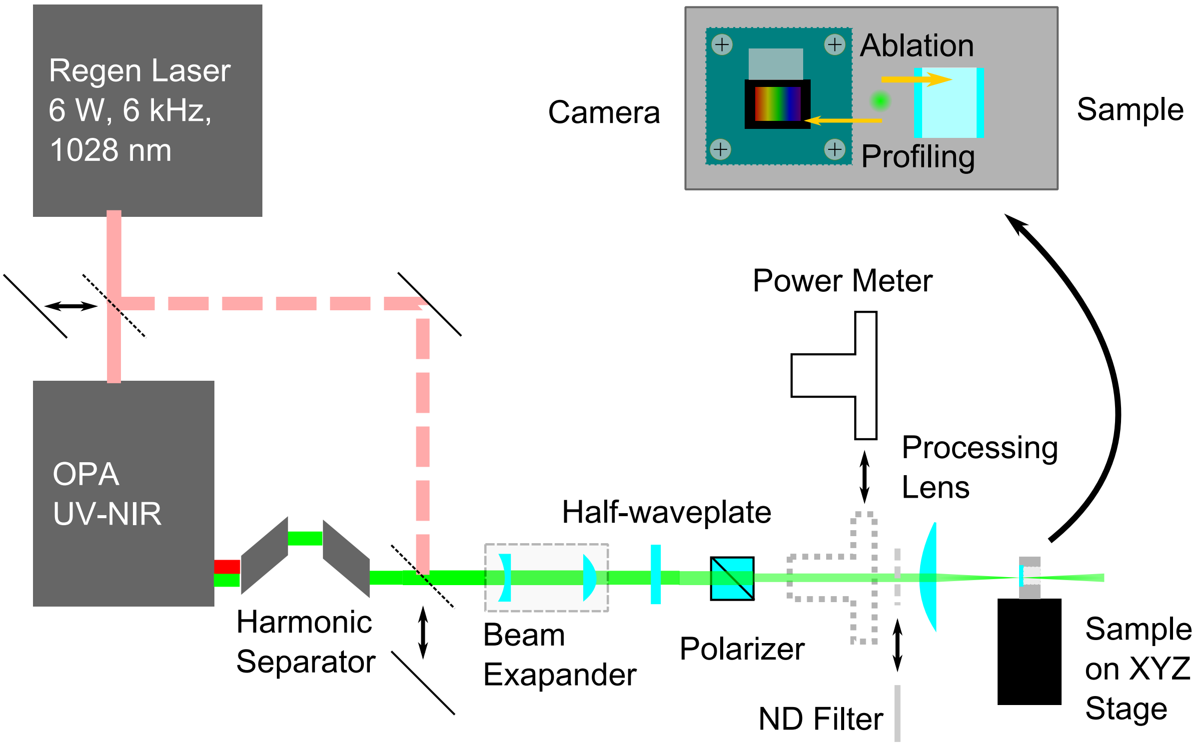

Figure 3.3.2.: The optical setup for the current experiment. Two optical paths allow for processing with either the fundamental beam or the output of an OPA.

sample holder to fit the sample; screws were used to hold the sample in place within the incision. The holder is hollowed out behind the sample, to allow for light to pass through.

The sample holder also has screws for mounting the beam profiler, roughly two centimeters laterally displaced from the sample. To calibrate the distance between the sample surface and the camera surface, the sample was mounted onto the holder, and the whole mount was scanned under a 3D scanner (Keyence VR-3200). In order to make the transparent sample visible under the 3D scanner which requires a reflected signal, a small strip of tape is placed on the edge of the sample surface for reference, the thickness of which was verified to be 70 microns by laser scanning microscope (Keyence VK-X260). The profiled sample holder with the camera and sample mounted are shown in Figure 3.3.1b. Heights are returned in micron resolution, and the difference between the camera and sample surface is typically around 1.5 mm.

3.3.3. Optical Setup

The optical setup for the experiment is shown in Figure 3.3.2. The Yb:KGW based regenerative amplified laser system PHAROS (Light Conversion Ltd.) was used as the fundamental laser in the system. The central wavelength is 1028 nm while the pulse length is approximately 190 fs at FWHM. Typical operation was done at 6 kHz. Pulse energies could be controlled by adjusting the pump power of the regenerative amplification cavity, reaching a maximum of 1 mJ at 6 kHz.

The laser has a built-in pulse-picker which allows for the control of the laser output repetition rate to integer fractions of the fundamental, as well as the number of pulses to emit. This feature was utilize to achieve single-pulse ablation.

In order to achieve wavelength tunability, the output of the regen laser could be used to alternatively pump an optical parametric amplifier (OPA), ORPHEUS (Light Conversion Ltd.). The system allows for automated tuning of the output wavelength from visible to near-infrared (NIR) through parametric conversion of the second harmonic of the PHAROS beam. Shorter wavelengths down to the UV regime are also available by taking the second harmonic of the signal or idler. Signal and idler beams are emitted collinearly. A harmonic separator consisting of specialized dichroic mirrors at the output allows the proper isolation of the desired wavelength from the collinear output. Typical output powers after filtering range in the 100 mW range for UV to visible, and 500 mW range for NIR wavelengths. For our experiments, a wavelength range of 400 nm to 960 nm was utilized. Pulse durations were characterized to be near 190 fs across all wavelengths by autocorrelation measurements. Corresponding properties are gathered in Figure 3.3.3.

The output from either the fundamental or OPA was guided into a half-waveplate and Glan-laser polarizer, allowing the tuning of the pulse energy. An exception is made for the second harmonic of the idler light, which had a notably small spot size. The high intensity was observed to be sufficient to cause self-phase modulation within the polarizer. Thus, before introduction into the waveplate/polarizer set, the light was first expanded by approximately four times by a concave-convex lens pair.

The power adjusted pulse is then focused onto the sample holder by a simple plano-convex lens. The in-plane beam position was adjusted by a mechanical XYZ stage. In order for single-pulse ablation to be possible, the beam must be focused so that its peak fluence is well above the ablation threshold. On the other hand, profiling is more accurate with a *larger* spot size. Larger spot sizes result in more active pixels, increasing the relative resolution, and the larger Rayleigh length also loosens the on-axis tolerance in placement. For the current pulse energies available, a good compromise was focusing to a spot radius of around 10-15 microns. The necessary lens depends on the wavelength of the light and the spot size at the focusing lens. The conditions used are listed in Table 3.3.1.

In order to determine the fluence, the beam profile and pulse energy are required. The profile is recorded at each wavelength once before processing. The pulse energy is measured directly before each processing step. Both are explained below.

For profiling, even with full attenuation of the laser with the waveplate/polarizer set, the laser intensity at the focus is still sufficiently high to cause the camera image to over-saturate. In order to attenuate the laser pulse further, reflective-type ND filters were placed directly in front of the processing lens, as shown in Figure 3.3.2. Furthermore,

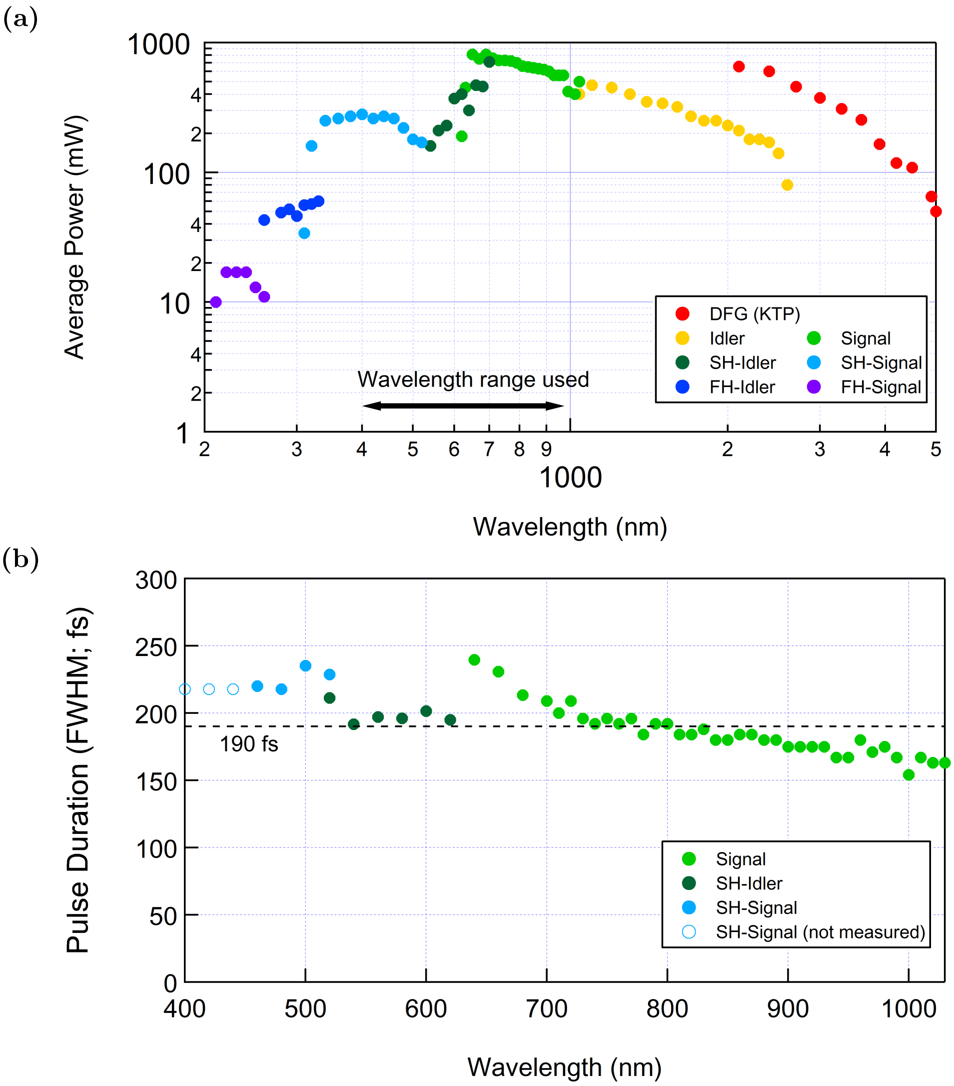

Figure 3.3.3.: (a) Mesured output of the OPA light source when pumped by 6 W of power at 6 kHz by the fundamental. (b) Measured Gaussian FWHM pulse duration by autocorrelator used in later calculations. 190 fs is highlighted for reference. Wavelengths shorter than 460 nm (open dots) were out of range for the autocorrelator, thus an approximate pulse width close to the value at 460-480 nm was asummed.

Table 3.3.1.: Processing lens used for each light source.

Source	Wavelength (nm)	Lens (mm)
Fundamental	1028	100
Signal	1040-620	75
Second Harmonic Idler	700-520	75
Second Harmonic Signal	520-310	100 or 50 (for 500-520 nm)

ablation is done with a single pulse (the limit at 0 Hz), and the profile should reflect this condition. It was found that the beam profile differed at 6 kHz than at lower repetition rates, most likely due to thermal effects within the laser system. In order to compensate for this effect, all beam profiling was done at 60 Hz, where all heat effects in the system should be mitigated to 1/100th of the situation at 6 kHz. Each profiling was done with an exposure time of 100 ms (or 6 pulses on average), and 10 frames were averaged for the final output. Frame-to-frame drifts were not observed, and we believe pulse-to-pulse spatial fluctuations to be negligible. While it is impossible to directly prove that the profiled beam and the profile of the pulse at ablation were identical, the above procedure was found to retrieve beam contour profiles which were consistent with the ablated spot, including the recreation of irregular aberrations, giving good reason for its confidence. In order to compensate for any misalignment along the beam propagation axis, backup profiles were taken at 25 to 50 μm intervals in a range of ± 200 μm around the target position.

In order to measure the absolute power of the laser pulse, a power meter (Gentec XLP12-3S-VP) measured the average laser output at 600 Hz before the processing lens, as shown in Figure 3.3.2. From this value, the single pulse energy could be calculated. To avoid the tedious (and potentially error-introducing) procedures required to accurately calibrate a photodetector to monitor pulse-to-pulse fluctuation during ablation, we opt to simply use this average value. Short-term pulse-to-pulse rms stability was found to be around 0.2% for the OPA, and we also verified by photodetector that single-pulse operation (on the short term) did not cause any significant deviation in pulse energy. While the OPA has non-negligible long-term output drifts, as the power measurements were done directly before ablation, these effects were believed to be negligible.

Ablated spots were all laterally displaced by 100 μm, typically in a lattice pattern depending on the experiment. Each crater was individually profiled by a laser scanning microscope (Keyence VK-X260). The microscope utilizes a pinhole confocal optical system to obtain both color and topographical data of samples. Images were observed with a 150× objective lens (working distance 0.2 mm, NA 0.95). The microscope laser operates at a wavelength of 408 nm; however with built-in image reconstruction algorithms, sub-wavelength resolutions are achieved. Reported accuracy values are given as $\sigma = 0.012$ μm in the vertical direction, and $3\sigma = 0.020$ μm in the lateral. In our settings, images were obtained at 2048×1536 pixels, with individual pixels correspond to a spatial scale of 47.518 nm square. The display resolution of the height data is 0.1 nm.

3.4. Analysis

To illustrate the fluence mapping procedure, we take for example a crater created by a single pulse on sapphire. The fundamental beam was utilized (1030 nm, 190 fs), with a pulse energy set to 50 μJ.

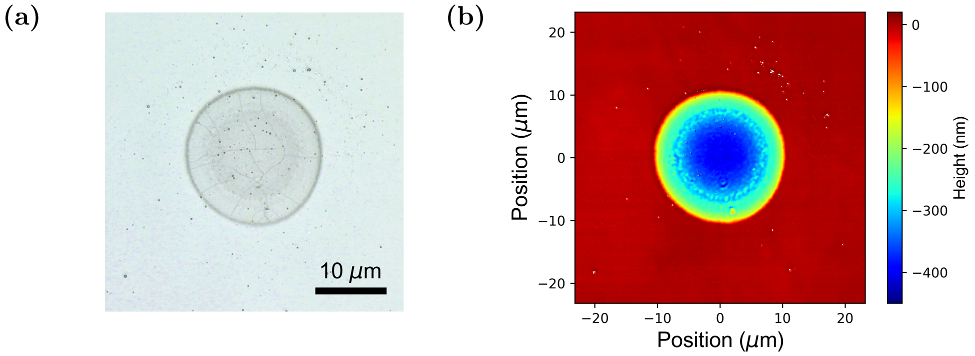

Figure 3.4.1.: A crater ablated by a 50 μJ pulse on sapphire with the fundamental beam. (a) Microscope image of the ablation crater and (b) the height profile of the image, both gained by laser scanning microscope. White speckles on the height profile correspond to values above 20 nm.

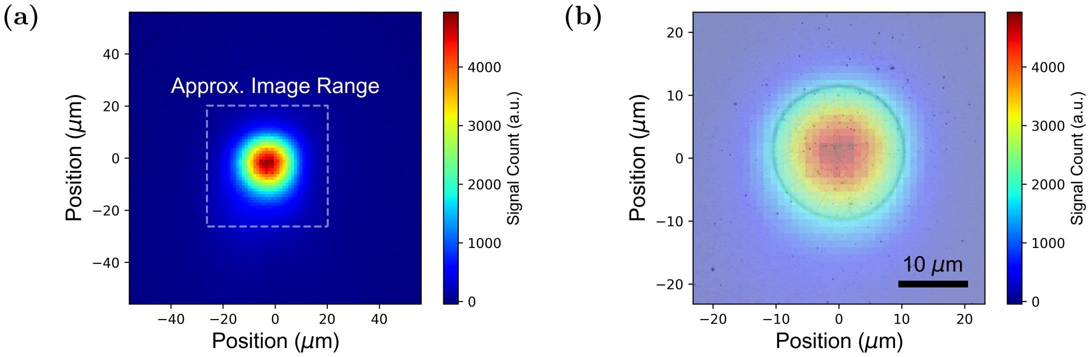

Figure 3.4.2.: (a) Obtained beam profile of the ablating beam at the focus. A dashed box is shown for reference corresponding to the size of the image in Figure 3.4.1. (b) The beam profile overlayed with the corresponding crater image of Figure 3.4.1.

The observed crater image is shown in Figure 3.4.1. The color image from the microscope is shown in Figure 3.4.1a, while the corresponding height data is shown in Figure 3.4.1b. Due to the relatively high fluence (the threshold pulse energy for the current focusing condition is around 1/3 of the current value), slight cracking can be seen in the crater bottom. Black speckles in and around the crater most likely correspond to debris which reattached to the sample surface. They appear as sudden spikes in the height profile, and correspond to the white dots seen in Figure 3.4.1b.

The corresponding beam profile taken directly prior to processing is shown in Figure 3.4.2. The raw profile is seen in figure Figure 3.4.2a. A square region, corresponding to the area in space taken by Figure 3.4.1 is shown as reference. A rough overlay of the crater and beam profile images is shown in Figure 3.4.2b. Even with the comparatively good spatial resolution of the beam profiler, the pixel-size mismatch between the two images is apparent.

In order to create a fluence map, several processing steps must be taken to prepare and align the images. In the next sub-sections, we detail the numerical procedures to these steps. All code was written in python, with utilization of the numpy[2] and scipy[3] libraries.

3.4.1. Preparing the crater

In order to detect crater morphology features, first, unwanted speckle-like features, such as dust and debris on the sample surface, should be eliminated. This increases the robustness of the other procedures to follow which usually depends on finding height gradients within the height data.

Usually, in order to achieve this, some sort of smoothing image filter such as a Gaussian, Fourier, or Wavelet filter would be employed. However, in general, the crater itself is a high-gradient feature, and these schemes often end up smoothing out the crater profile, which is an unwanted effect. A highly nonlinear filter is necessary to remove speckle points without distorting the macroscopic crater profile.

After trial and error, the best simple solution to this problem was found in the form of the median filter. In a median filter, the post-filtered value of a pixel is determined by the median value of the data contained in a square box surrounding that pixel. Although the filter requires extensive sorting operations, making the implementation numerically costly, the filter possesses a feature which makes it particularly attractive for our current application: the median filter is known to preserve edges. The crater “lip” being an edge, this property allows us to properly smooth the image without distorting the location of the crater edges.

This is illustrated in Figure 3.4.3. The median filter (left side) is shown to consistently remove the speckle features, as can be seen by the differential signal. Removal of points is effective relatively independent of location. A similar filtering using a common Gaussian filter is shown for reference on the right. The filtered image is apparently blurred compared to the median filter. Furthermore, the appearance of the crater features on the lower differential signal signifies macroscopic distortion. The negative to positive differential around the crater lip signifies that the implementation of the Gaussian filter would cause the crater to appear larger than expected. Typically, a median filter mask size of 7 pixels was used, but the value was adjusted depending on the extent of the extraneous features present.

After filtering, it is necessary to detect the location of the crater. Although in the current picture, the crater is in approximately the center of the image, this is not always the case.

In order to find the center of the crater, we use edge detection techniques to find the edge of the crater. While there are many edge detection algorithms available, we opt to use the Canny Edge Detection algorithm proposed by John Canny in 1986 for its general

---

[2] http://www.numpy.org/

[3] https://www.scipy.org/scipylib/index.html

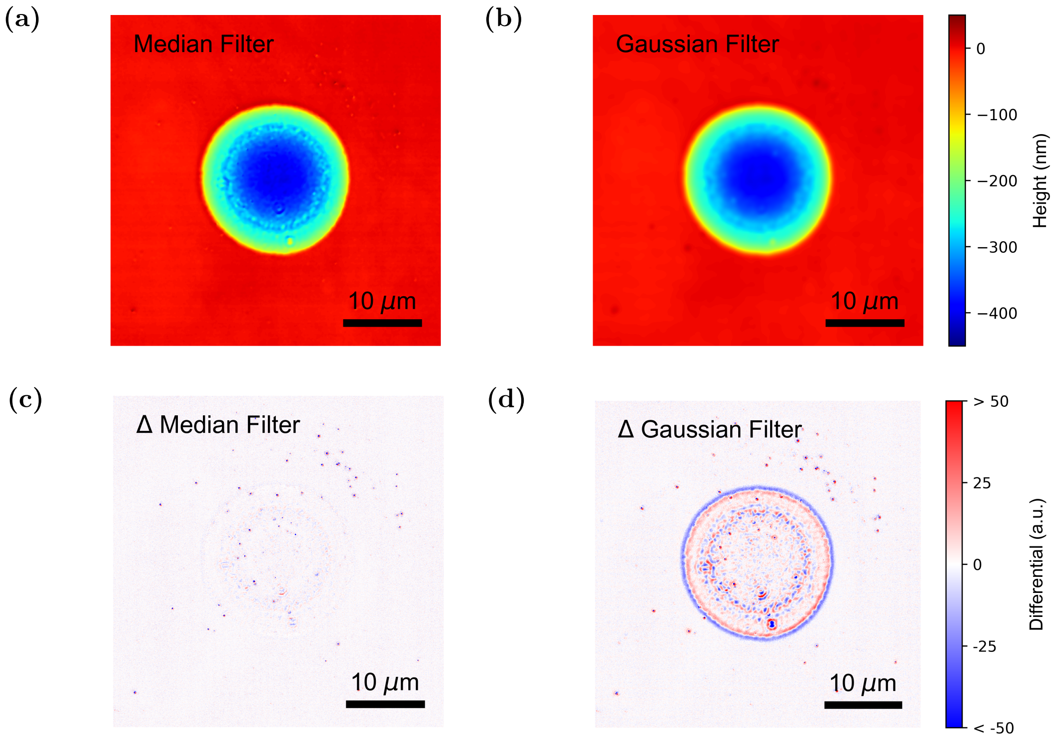

Figure 3.4.3.: (a) Median and (b) Gaussian filtered images of Figure3.4.1a, and their difference in height from the original for the (c) median and (d) Gaussian filter.

robustness to noise [119]. We apply a noise threshold based on the standard deviation of the image, and a somewhat large Gaussian width (10-50 pixels), reflecting the general extent of the crater slope.

Once the edges are detected, the image is divided into regions defined by the edge boundaries. The largest region is the region excepting the crater; the second is most likely the crater if the process has succeeded. The midpoint of the surrounded region in both x and y directions is taken as the center. We make two checks to check if the extracted area is a crater: 1) that the total area is bigger than 20 × 20 pixels, and 2) that the center pixel is below the surface. The result of such processing on the median smoothed image is shown in Figure 3.4.4.

With this central value, the image is cropped to a more manageable size, typically to a total width of a 500 pixels (the image shown is 1000 pixels in width), although the specifics depends on the crater size. The above process is all done by program, with error rates in the single-percentage range. The method generally is safe for large craters, but has a somewhat difficult time detecting/re-centering small craters. A log image file of the processed image is also outputted, to allow for easy manual detection of erroneous results.

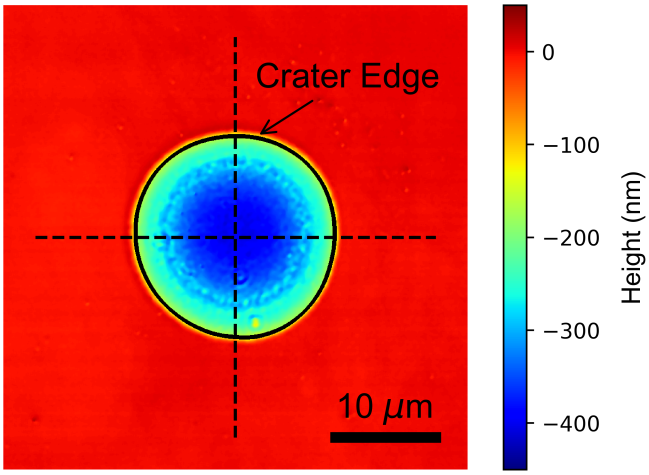

Figure 3.4.4.: The crater edge is detected by the Canny Edge Detection algorithm (the edge is thickened for visibility). The extracted center is shown by the intersection of the dashed lines.

3.4.2. Preparing the beam

The beam profile gained from the experiment has to undergo two main steps. The first is a general alignment and cropping of the profile to match the extent of the crater. The second is a smoothing and interpolation of the data. Smoothing is done to remove the pixel-to-pixel noise present in the camera image. Interpolation is required to overcome the large degree of pixel mismatch in the two images, where the camera pixel pitch is 1.12 μm as opposed to the crater profile's 0.046391 μm.

The former alignment is made simple by applying a Gaussian fit. To increase accuracy, we fit with a generalized elliptical Gaussian. The results can be seen in Figure 3.4.5. The center of the Gaussian fit is noted as the approximate center of the beam. For reference, the fit yields a major radii of 17.89±0.03 μm and minor radii of 16.86±0.03 μm. The laser profile is then cropped by a square of length 60 to 80 pixels (the exact value depending on the spot size and location of the beam center).

Within the cropped area, we next make a smoothing bivariate B-spline approximation of the beam profile [120], where the profile is approximated by a piecewise polynomial (in this case, set to order 5). The fidelity to the original data can be adjusted by a smoothing factor, where the case of highest fidelity reduces to an exact interpolation through all points. In general, we adjust this parameter manually so that fluctuations in the beam profile are smoothed out, but ripple artifacts do not appear in the surrounding regions. While a potential source of ambiguity, the overall results in analysis are generally insensitive to this smoothing factor.

In Figure 3.4.6 we show the result of such a spline as well as the differential from the original. Comparing the two differential figures of Figure 3.4.5b and 3.4.6b, it is apparent that the spoline causes less macroscopic distortion of the beam profile. Evidenced by the

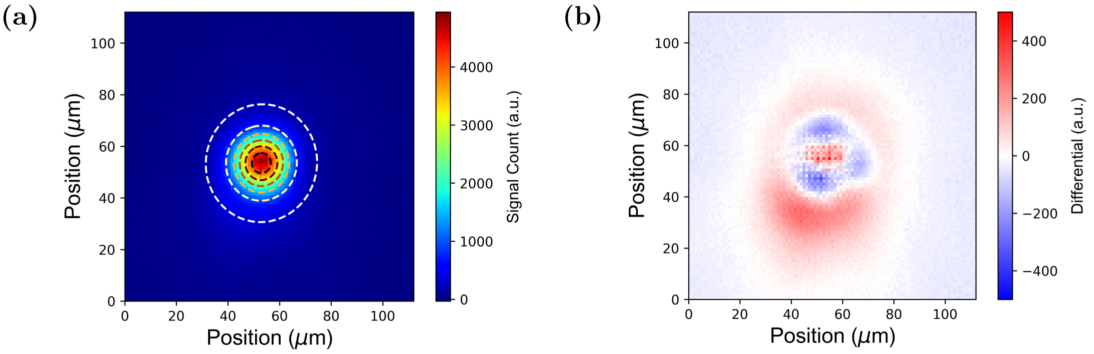

Figure 3.4.5.: (a) A 2D Gaussian fit of the beam, overlayed as a contour plot. (b) The differential between the fit and the original.

general lack of large positive (red) or negative (blue) regions. There are slight rippling artifacts in the spline fitting near the wings, but in general, their effects are small. They are well beyond the range of the crater itself, and mainly cancel out in an integral.

The spline form allows us to do two things with the beam. The first, as aforementioned, is the interpolation of points to up-sample data values at a spatial scale equal to that of the crater profile. The second is a numerical integration of the beam region. As the total volume of the beam signal should correspond to the value of the pulse energy, this allows us to calibrate the CMOS signal count of arbitrary unit into a local fluence value in terms of J/cm^2.

The result of such an up-sampling and calibration is shown in Figure 3.4.7. The peak fluence in the plot is 11.2 J/cm^2. A calculation from the fitted Gaussian yields 10.6 J/cm^2, and the two values are generally consistent, considering the differences in shape in the two fitted profiles.

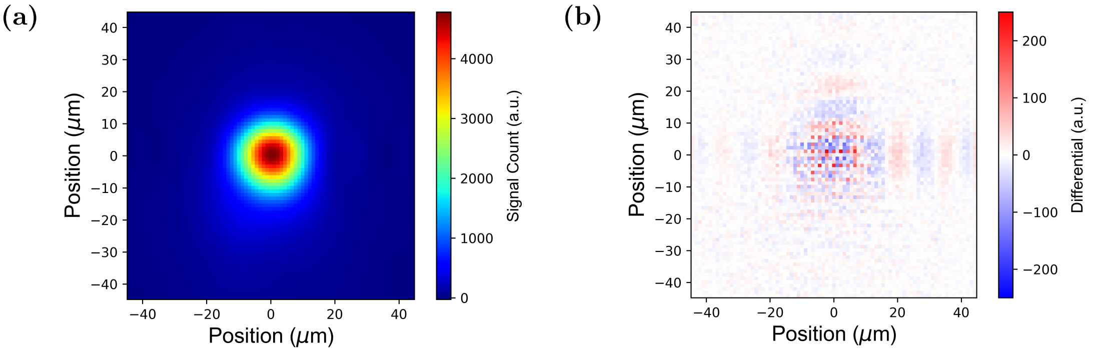

Figure 3.4.6.: (a) A 2D spline interpolation of the beam profile. (b) The differential between the fit and the original.

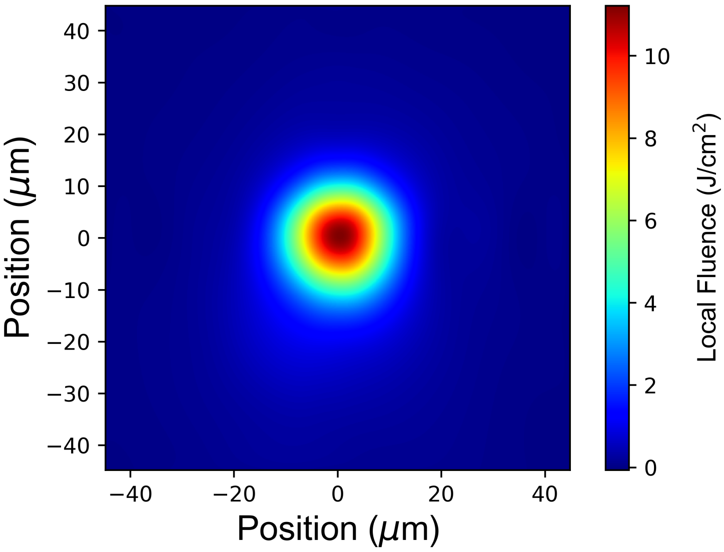

Figure 3.4.7.: The beam profile of Figure3.4.6a up-sampled to a smaller spatial step size, and calibrated to units of J/cm^2.

3.4.3. Aligning the images

With the preparation of the crater in Figure 3.4.4 and the beam in Figure 3.4.7, the final step remains to align the two images. The simplest method may be to match the deepest point in the crater to the highest point in the beam profile. However, this method is not very robust when the roughness of the crater bottom is high.

To increase robustness while maintaining relative simplicity, we opt to align the beam by reference to four points: the four edge points of the crater cross sections around the center in the x and y direction. We find the crater edge of a line profile by first calculating the median and mean values in a moving window of 7 pixels. We take the difference of these two values, which take peak values around the lip of edge points. This allows us to find edges which are relatively robust to roughness, and generally consistent in terms of height (near zero level). An example of this process for the x-direction cross section is shown in Figure 3.4.8.

By this procedure, four coordinates are extracted in terms of the crater coordinate system: (r_{+x}, 0), (-r_{-x}, 0), (0, r_{+y}), (0, -r_{-y}), where r are the extracted absolute radii in the positive or negative direction. We assume that the beam profile coordinate system is offset by a value of (Δx, Δy) from the optimum position[4]. We define the optimum position as the point which minimizes the fluence square difference between these points.

---

[4] In general, a rotational degree of freedom should also be considered, but the alignment between the camera pixel orientation and sample vertical orientation was found to be generally satisfactory, and thus, we opted to ignore this degree of freedom in this current work. In fact, we found that adding rotation occasionally caused *over*-optimization.

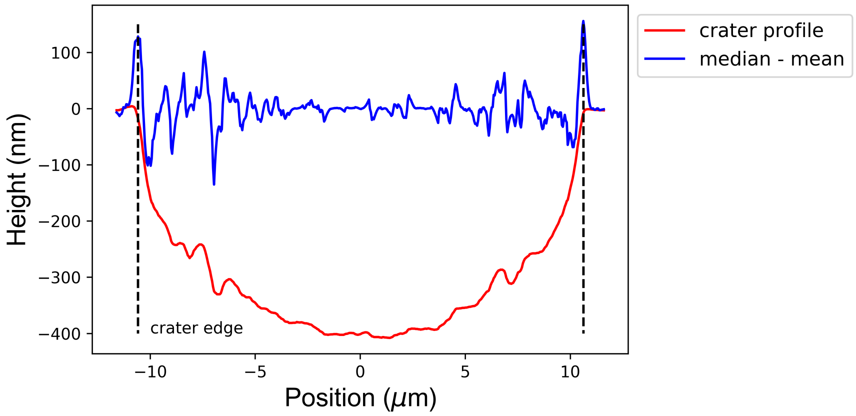

Figure 3.4.8.: Crater edge (red) and its windowed median-mean values (blue). The outermost peaks correspond to the approximate location of the crater edge (dashed black).

Restated, we want to find a Δx and Δy such that F_{sd} is minimized:

$$F_{sd} = \sum_{i \neq j} (F_i - F_j)^2 \quad (i, j = \{1, 2, 3, 4\}), \tag{3.4.1}$$

where $F_1 = F(\Delta x + r_{+x}, \Delta y)$, $F_2 = F(\Delta x - r_{-x}, \Delta y)$, $F_3 = F(\Delta x, \Delta y + r_{+y})$, $F_4 = F(\Delta x, \Delta y - r_{-y})$. Here, $F(x, y)$ is the beam local fluence value at (x, y).

The result of the alignment procedure is shown in Figure 3.4.9. We scan a range of ±3 μm in a grid pattern, and evaluate F_{sd} at each point, as shown in Figure 3.4.9a. A minimum point is found, which gives us the translation coordinates for the beam profile. The results before and after alignment are shown in Figure 3.4.9b and 3.4.9c, respectively.

3.4.4. Creating the fluence map

With the aligned crater and beam profile image, we now have a one-to-one correlation of the local fluence and the local height. This allows us to reorganize the height data not as a function of the spatial position, but as a function of the local fluence. This remapping of the data, or fluence map, is advantageous in that it allows us to compare morphology of beams with differing radii and pulse energies in a consistent scale.

The fluence map for the example crater is given in Figure 3.4.10. Each small red point corresponds to one pixel of the height profile data. A total of 250,000 points are gathered to make the plot. In general, the points all lie in good agreement to eachother. A perfect line would signify a true one-to-one correspondence to the local fluence. The "width" of the general distribution provides the rough estimate of the accuracy of a single fluence map. These include the experimental errors, such as errors in the beam profile measurement and accuracy of the microscope measurement, analysis errors, such as potential misalignment of the beam and crater profiles, and fundamental limits on locality. In our current case, the first two factors are believed to be dominant.

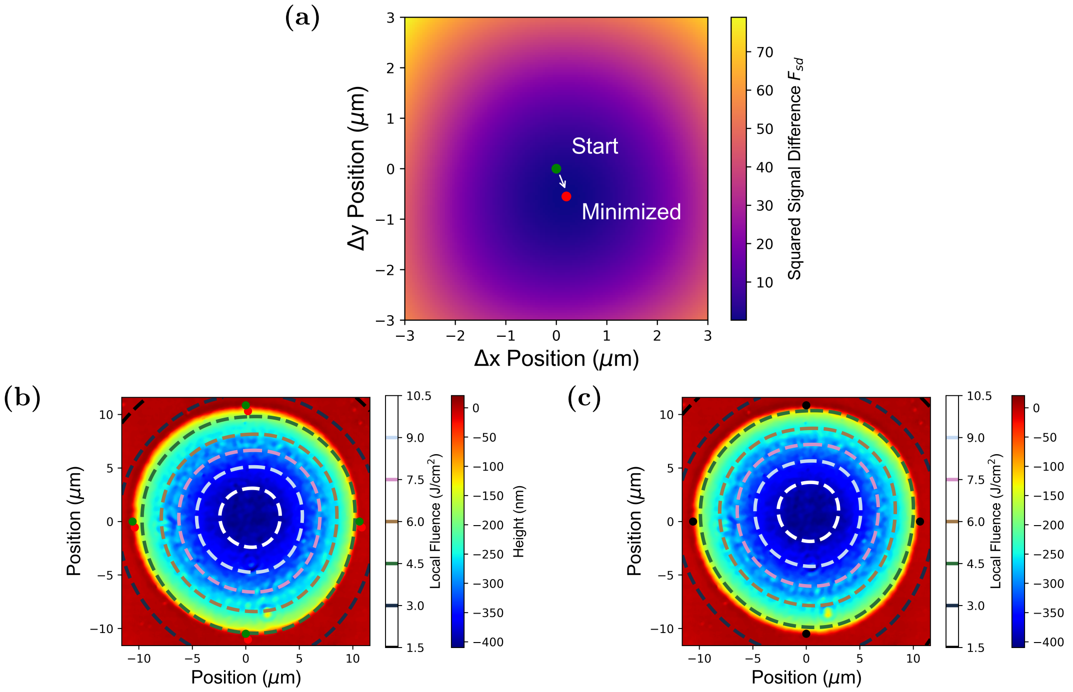

Figure 3.4.9.: (a) A search of Δx and Δy over a range of ± 3 μm, where the original origin and the minimized point is shown. (b) The beam and crater coordinate systems aligned at their origin. We want to translate the beam coordinate system so that the red dot (F_{sd} minimized position) is matched to the crater edge positions, shown by the green dot. (c) A result of the translation, where the black marker is the crater edge, now coinciding in space with the square minimized position.

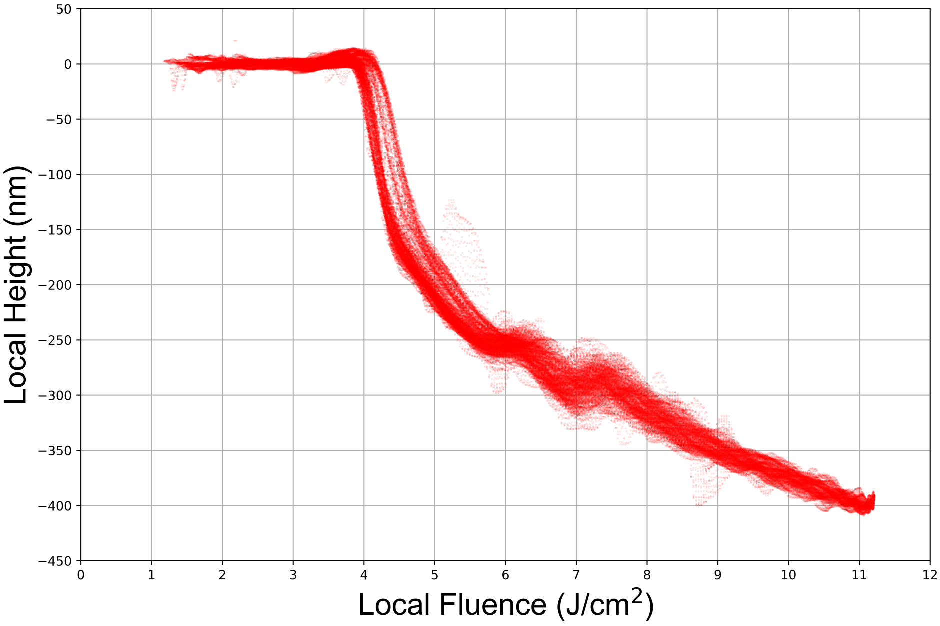

Figure 3.4.10.: A fluence map of the current crater. Each red dot corresponds to one pixel of the crater height data.

Several data can be read off the map directly with little analysis, something which is not possible with a conventional crater morphology picture. The rightmost point of the fluence map corresponds to the peak fluence incident in the crater, a value of around 11.2 J/cm^2 in our current example. It can be seen that below 4 J/cm^2, no large crater formation can be observed. This is believed to correspond to the "strong" ablation threshold in the literature [19]. We also can see features at around 6 J/cm^2 and 7.5 J/cm^2, corresponding to potentially new threshold values for other ablation mechanisms. The slight dip around 3 J/cm^2 may also correspond to a "gentle" ablation (or Coulomb explosion) threshold, although it is hard to know with certainty from the current map by itself. Testing with various pulse energies allows us to see if the morphology are truly local fluence-induced features, or a spatial correlation induced due to the near-circular symmetry of the system (such as a growth of a melt-front around the pulse center, the endpoints of which would have more correlation to the crater curvature than the local fluence).

In such manners, the fluence map provides a trove of information regarding the processes involved in ablation, from one single crater. This was achieved by the utilization of the full two-dimensional nature of the morphology and beam profile measurements, allowing for orders of magnitude increase in data acquisition efficiency.

3.5. Discussion

In the previous section, we introduced the methodology for the development of the fluence map. In this section, we comment on some of its properties.

3.5.1. Universality

The fluence map analysis may be done for arbitrary craters and beam profiles, each developing its own unique map. The generality of the results obtained is a concern. In particular, the pulse energy dependence is of particular interest.

In order to observe whether the fluence map holds pulse-energy dependence, we vary the pulse energy of the fundamental pulse of PHAROS from near the threshold to around 5 times that value. The craters created are shown in Figure 3.5.1. From these craters, we can create the individual fluence maps. The fluence maps, all gathered on one image for easy comparison, are shown in Figure 3.5.2.

From Figure 3.5.2, it can be seen that, in general, the locality of the ablation phenomenon is satisfied. However, there is a slight trend of the map shifting to the right (higher energy) with the increase of pulse energy. This signifies that the crater profiles are *smaller* than what would be expected from a scaling of the pulse profile. Three possibilities present itself as explanations. The first is a slight non-local effect, as the fluence gradients at the spatial positions at the higher pulse energies is greater (to be

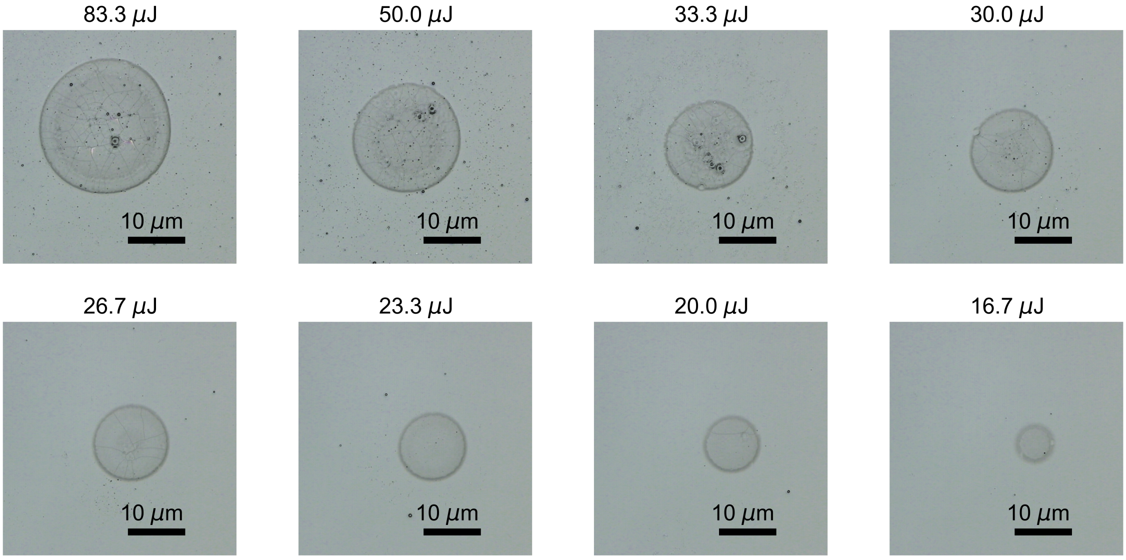

Figure 3.5.1.: 8 single-pulse ablation craters created with different pulse energies.

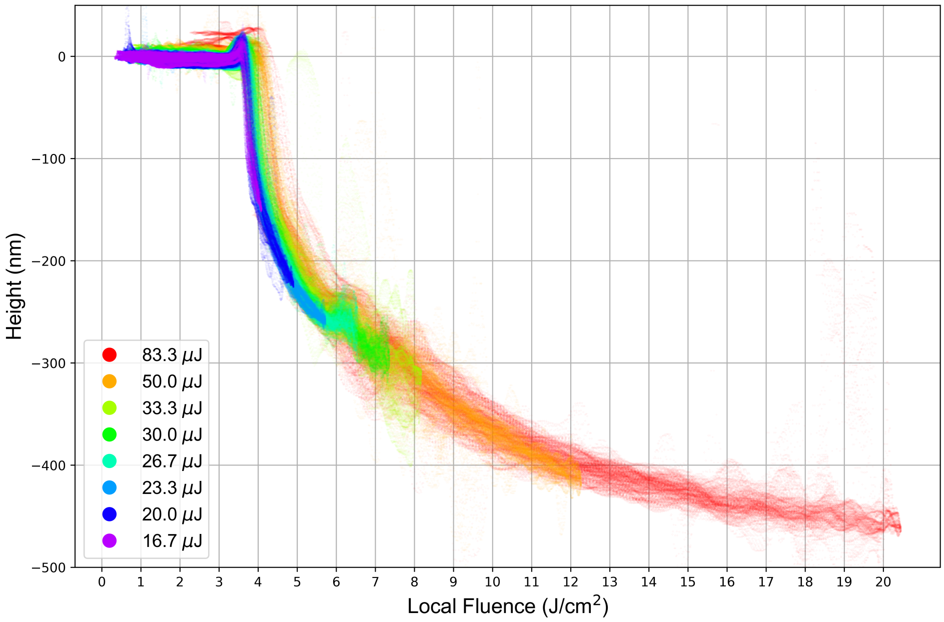

Figure 3.5.2.: Fluence maps of the eight craters gathered on one graph.

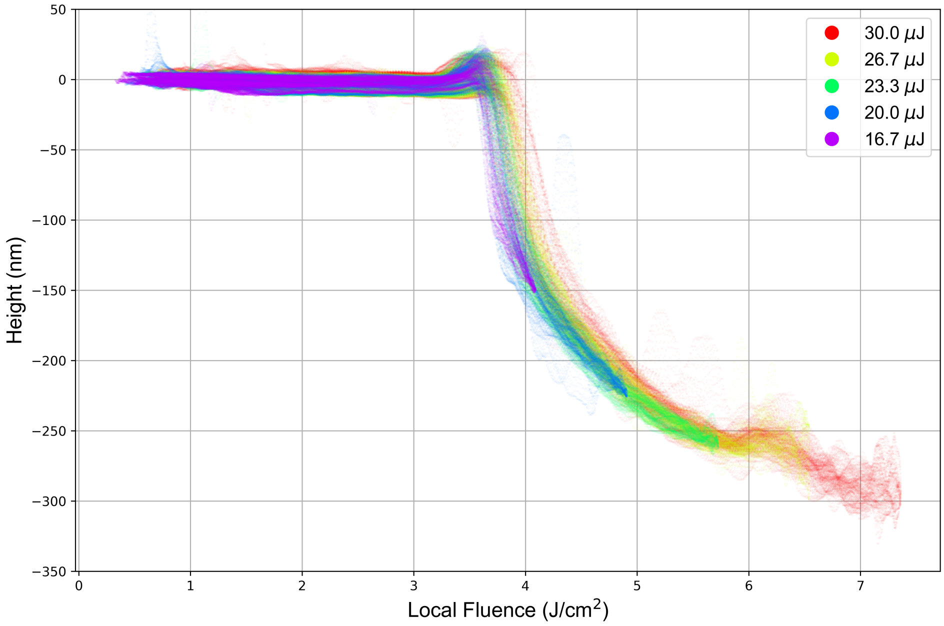

Figure 3.5.3.: Fluence maps of the five lower pulse energy craters from Figure 3.5.2.

elaborated on later). It may also be a result of nonlinear propagation effects within the air medium. At the highest fluence, the pulse energy approaches 20 J/cm^2, with peak intensities around 70 TW/cm^2, which is above some air-breakdown values reported in the literature [121]. The last possibility is that of a mismatch in crater and beam profile scales, which will be magnified at higher pulse energy ranges. It is difficult to discern between the three without further study, but practically, as long as the pulse energies are kept at moderate values near the threshold (a pulse energy regime usually analogous to that used in traditional diameter regression techniques), this slight drift is negligible compared to the current accuracy of the fluence map, and a unified analysis independent of the pulse energy of the local morphology based on local fluence is mainly justified.

Taking a look at the five lowest fluence maps, gathered in Figure 3.5.2, it can be seen that finer features are also well reproduced in the individual plots. Not only is the threshold fluence location for the strong ablation (at around 3.6 J/cm^2) well reproduced, but also the formation of a second lip-like feature with a threshold at 6 J/cm^2 is also consistent. Gentle ablation thresholds, however, cannot be discerned due to overlap with the strong ablation lip protrusion.

It should be noted that increased visibility of the various thresholds is a major advantage of the fluence mapping technique. For reference, we show the 23.3 μJ crater profile and the 30.0 μJ crater profile in Figure 3.5.4, which in the fluence map are clearly above and below the second threshold. While the strong ablation threshold (solid triangle) is apparent, whether a second threshold exists for the 30.0 μJ crater is not quite as obvious due to the high roughness of the crater bottom. By averaging the height over the equivalent-fluence positions, the fluence map “flattens out” this noise.

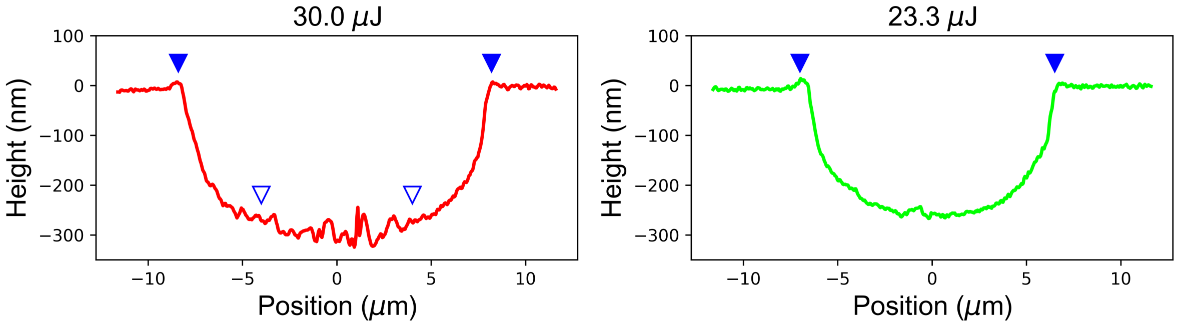

Figure 3.5.4.: Corresponding crater profiles of the 23.3 μJ and 30.0 μJ crater from Figure 3.5.3. The strong ablation threshold is shown as a solid triangle, while the second threshold-like feature is shown in open.

In regards to universality, dependence on spot size was also explored to an extent by ablating at two locations offset by 100 μm near the laser focus. This induced a moderate change of the beam radius (a maximum of around 10% change), but no discernible change in the fluence map could be observed. For very tight focusing conditions, where the lateral and vertical spatial extents of the excited region become comparable, the physics may differ. In any case, at beam profile-able spatial profiles, locality appears to be preserved for the current case.

Summarized, in general, the morphologies of various fluence maps at differing pulse energies are in agreement with each other. With universality assured, one fluence map at moderate intensity should be able to extract a pulse-energy independent ablated depth vs fluence relationships for the current laser conditions (such as wavelength and pulse duration). This property should be invaluable to many studies today which use morphology as a comparison point to theory.

3.5.2. Precision and accuracy

As mentioned in the previous section, the precision of the fluence map by itself manifests itself as the thickness of each “line”, at widths of around a couple hundred mJ/cm^2. A trend that is easily discernible in the fluence map is an increase in thickness of the “lines” with an increase in pulse energy. While a possibility is simple mismatch of the profiles, a main fundamental contribution to this broadening is believed to come from the increased fluence gradients present. The gradient of the spline interpolation beam profile is shown in Figure 3.5.5. The gradients are shown as a percentage of the peak fluence. Typical crater radii are in the range of 3 to 10 μm, for our current craters, or slightly below the 1/e^2 radius of the current beam. At those values, it can be seen that the fluence gradients become greater for larger pulse energies. Absolute errors are also magnified by a factor of the pulse energy. In terms of precision, any spatial mismatch is magnified by the gradient factor times the peak fluence. Assuming a spatial mismatch of Δx of 500 nm (or approximately 10 pixels in the microscope image) for the highest pulse energy,

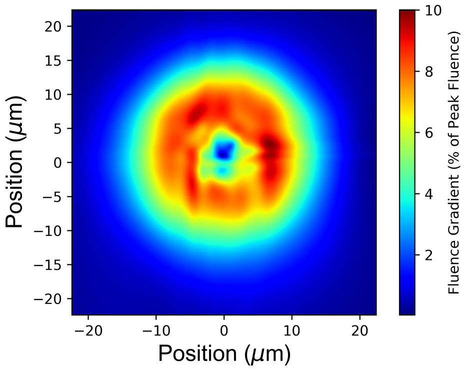

Figure 3.5.5.: The absolute value of the gradient vector at each point in the interpolated beam profile.

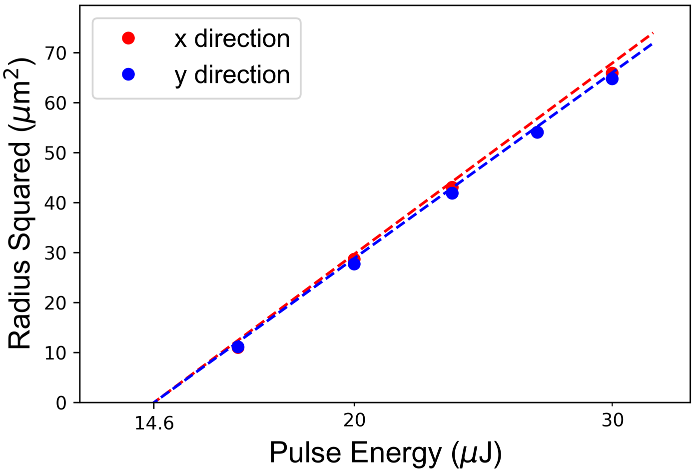

Figure 3.5.6.: Diameter regression analysis of the crater data.

we get a ΔF of $0.5 \times 10\% \times 20$ J/cm^2, or 1 J/cm^2 for the highest pulse energy fluence map, in general agreement with the approximate thickness of the red line of Figure 3.5.5. This decrease in precision above the threshold further justifies the use of the fluence map at relatively low pulse energies. However, it should also be noted that too low a fluence equates to a limited range of mapped fluences, one of the major advantages to this technique.

With craters of different pulse energies, it becomes possible to compare the results gained from the fluence mapping technique with that of the diameter regression. We measure the strong ablation threshold crater diameters in the x (horizontal) and y (vertical) direction for the first 5 craters of Figure 3.5.1. As in a traditional diameter regression analysis, we plot the measured radius (converted from the diameter) squared as a function of the pulse energy, and fit the data with equation (3.1.3). The results are shown in Figure 3.5.6. From the fit, we derive a threshold pulse energy of 14.61 ± 0.05 μJ, and radii of 13.73 ± 0.05 μm and 13.54 ± 0.05 μm. From these values, the threshold fluence is determined to be 5.00 ± 0.03 J/cm^2.

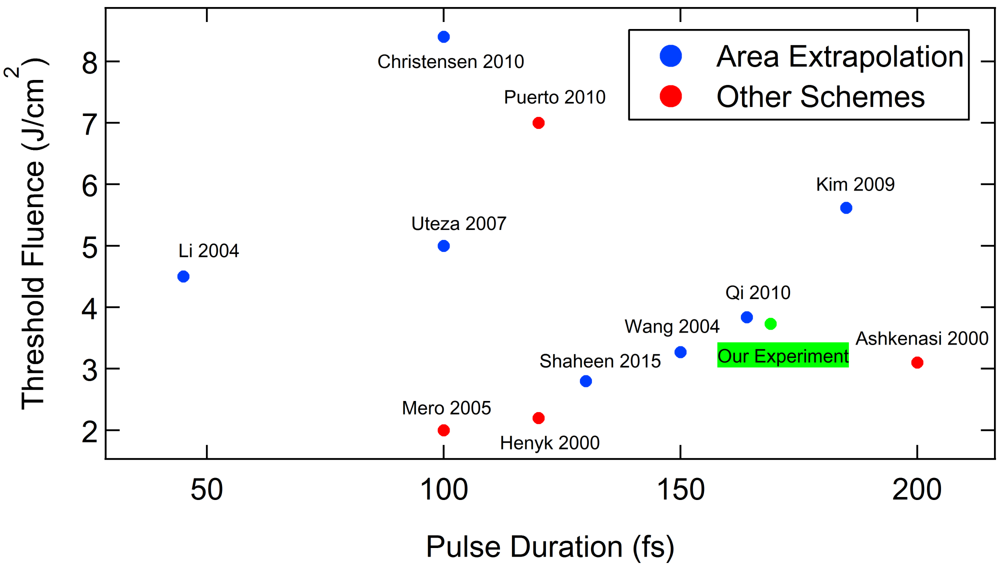

Figure 3.5.7.: Figure 3.1.3 with our current value added in green.

The results are notably higher than the results gained from the fluence map. The main contribution to this discrepancy is differences in the predicted beam radii. A 2 dimensional Gaussian fit of the beam profile used in this ablation experiment yields radii of 14.43 ± 0.02 μm and 15.81 ± 0.02 μm. Using these values reduces the fluence threshold values down to 4.07 J/cm^2, which, while still slightly higher, are closer to the threshold values in the fluence map. As the locality of the ablation was shown to be assured in this case, the errors in the diameter regression technique is shown to be related to the Gaussian profile approximation. As the fluence mapping technique uses less approximations compared to the diameter regression technique, its accuracy is believed to be higher.

Thus, while the diameter regression technique is *precise*, the *accuracy* of the measurement is shown to be low. In contrast, the precision of the fluence map itself is not as high, but the accuracy is shown to be more convincing. The fluence map technique can be refined and/or repeated to increase statistical accuracy to the required precision, which is not the case for diameter regression.

With that said, it should be noted that there are some new sources of systematic errors for the fluence map, such as errors in the determined beam profile and energy calibration of the pixel intensity. In either case, working with multiple differing profiles should help to reduce these effects, perhaps by vertical translation of the sample.

As a final conclusion regarding general accuracy, we give our results for the strong ablation threshold determined for 800 nm (generated by the OPA). The results are from averaging 6 fluence maps, and extracting the peak location near the crater edge. The results are, shown in Figure 3.5.7. Our thresholds are seen to be generally consistent with that given in the literature.

3.5.3. Limits

Although not a prerequisite to fluence mapping in particular, but to most extrapolation techniques, these techniques require a certain amount of determinism. When determinism is low, features will become irregular. In the case of diameter regression, several diameters are often measured and averaged. In the current case of fluence mapping, an added layer of increased uncertainty in beam-crater spatial alignment further complicates the situation.

Determinism in femtosecond laser pulses is known to increase for shorter pulse durations [122], as well as shorter wavelengths [46]. This is believed to be due to the higher contribution of the direct (either multiphoton or tunneling) excitation mechanism, offsetting the probabilistic nature of energy absorption through avalanche ionization of electrons in defect states.

As an example of the varying reproducibility of ablation according to the pulse duration, we create 10 craters with identical conditions at 50 μJ pulse energy on sapphire with the fundamental laser. Pulse durations are varied by adjusting the final compressor in the regen, to create three pulse durations: 190 fs, 1 ps, and 2 ps (FWHM). The resulting line profiles for the three pulse durations are shown in Figure 3.5.8. The degradation in reproducibility can clearly be observed with the increase of pulse duration. In such low reproducibility situations, an extension of the fluence map is required to take into consideration the probabilistic nature of the phenomenon. Additionally, care should be taken to avoid selection bias (only analyzing craters with macroscopic holes). In light of this, the fluence mapping technique should be considered a technique best suited for femtosecond laser studies.

In regards to the fluence mapping technique itself, a large factor affecting its application is the ability to align the craters. This requires that the crater morphologies be relatively easy to identify. This makes it particularly difficult for samples with shallow holes (metals and semiconductors), as well as samples with rough surfaces. In a similar sense, it may also be difficult to utilize this technique to multiple-pulse ablation, where complex propagation and material damage effects are believed to occur.

A final comment should be made regarding the universality. While the single fluence map is strictly correct in describing the *current* relationship regarding the local incident fluence and the ablated crater morphology, its *extension* to different pulse energies and beam profiles remains a nontrivial property. It was shown that locality generally holds for 190 fs pulses at 1028 nm for sapphire, however, there is no guarantee that this property upholds for different wavelengths, pulse durations, or materials. We believe this to be more of a feature than a limitation of the technique, as no other ablation analysis technique allows for analysis of morphology non-locality to this extent. In fact, we will see an example of this case in the next chapter. It goes without saying that systematic errors in the analysis should always be judiciously vetted, as these often manifest in the final fluence map as effects which resemble non-locality, such as a drift in the threshold fluence(s).

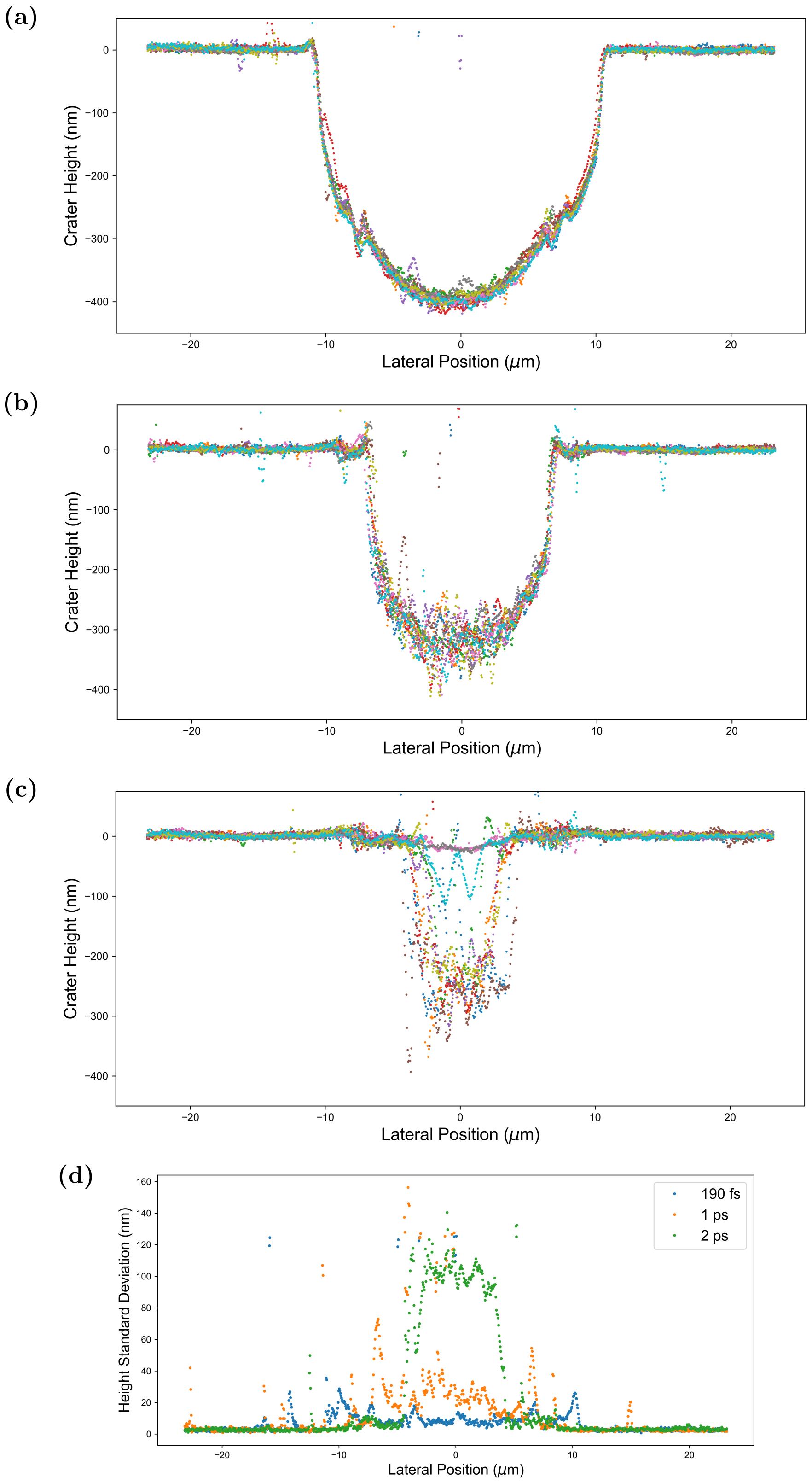

Figure 3.5.8.: Crater line profiles of 10 pulses at 50 μJ for pulses of pulse duration (a) 190 fs, (b) 1 ps, and (c) 2 ps, with different colors corresponding to different craters. (d) Their standard deviations as a function of location is also shown.

3.6. Summary

In this chapter, we introduced the fluence mapping technique, as a new way to analyze the dependence of morphology on the incident local fluence. Its advantages are discussed in contrast to conventional diameter regression analysis, currently the most popular method for determining ablation thresholds. These include the universality (for our current conditions) of the obtained depth-fluence relationship, the easy detection of thresholds, and a general robustness to beam profile deviations from the Gaussian.

In the following chapter, we employ this technique to explore the dependence of laser ablation to the wavelength of an ultrashort laser pulse.

Chapter 4.

Wavelength Dependence of Ablation in Dielectrics

In the previous chapter, we developed the fluence mapping technique as a robust way to determine thresholds even when spatial profiles deviate from the Gaussian profile. This is particularly important for high-powered light sources, required to study ablation, where the spatial profile often deviates from an ideal TEM_{00} mode.

In this chapter, we aim to reveal the wavelength dependence of ablation in dielectrics as a way to probe the fundamental excitation mechanisms involved in this phenomenon. This provides a fundamentally new way to vet current theories against experiment, where currently the main independent parameter controlled in the literature is the pulse duration.

4.1. Introduction

From the earliest studies in femtosecond abaltion of transparent materials, the functional form of many of the processes involved in the electronics excitation of materials has been under scrutiny. In order to compare experiment to theory, the most common experiment conducted was to compare the ablation threshold dependence on pulse duration. For example, the extensive pulse duration dependence studies by Stuart *et al.* revealed a deviation from the $\sqrt{\tau}$ (τ: pulse duration) relationship of the threshold which chracterized ablation at longer pulse durations, as well as cemented the rate equation model for femtosecond breakdown as the predominant theoretical model used to explain experimental results [4]. While insight from pulse duration dependence remains invaluable, still a great many material parameters and dependencies remain hard to probe.

A new parameter that has been under question is the wavelength dependence of the ablation phenomenon. A great many factors are predicted to depend on the wavelength. The most prominent factor would be the strong-field ionization rate. Values of the Keldysh strong-field ionization rates calculated for UV-NIR wavelengths are given in Figure 4.1.1. Where the peak electric field values are below the Keldysh parameter

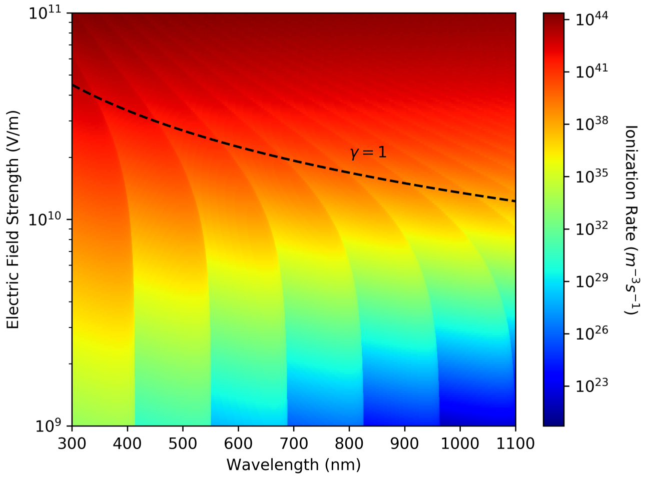

Figure 4.1.1.: The strong field ionization rate dependence on wavelength and electric field strength, with the strength where the Keldysh parameter $\gamma = 1$ is provided for reference. A band gap of 9 eV and an electron effective mass of the free electron mass were used.

$\gamma = 1$ line, discrete steps in the ionization rates, corresponding to differing multiphoton absorption orders, are predicted to dominate. In a similar manner, many other parameters are believed to depend on the wavelength, the most prominent gathered in Table 4.1.1

While various dependencies are predicted, it has been difficult to verify these trends systematically from data. Typical experimental accuracy of just a single-wavelength condition range somewhere in the 1 J/cm^2 range, which is more-or-less the same order as the wavelength dependence predicted by most theories. The already strained condition is further complicated by the fact that wavelength-variable high-power ultrafast light sources are practically limited to optical parametric amplifiers (OPAs). Especially with OPAs, the spatial profile and pulse duration vary over the various signal/idler settings, which each cause significant systematic changes in the measured threshold.

Despite this, several groups have attempted this challenging task. One of the earliest is the work by Jia *et al.* in 2006, where they utilized a Ti:Sapphire based OPA light source

Table 4.1.1.: Various parameters dependent on the wavelength.

Phenomenon	Dependence	Functional form (approximate)
Strong field ionization	Keldysh SFI rate	$\gamma \gg 1$: discrete steps $\gamma \ll 1$: nearly independent
Avalanche ionization	Drude absorption	$\propto \left(1 + (2\pi c\tau/\lambda)^2\right)^{-1}$
	Impact ionization delay	$\propto \lambda$
Effective band gap	Ponderomotive shift	$\propto \lambda^2$
Optical properties	Drude model	Critical density $\propto \lambda^{-2}$

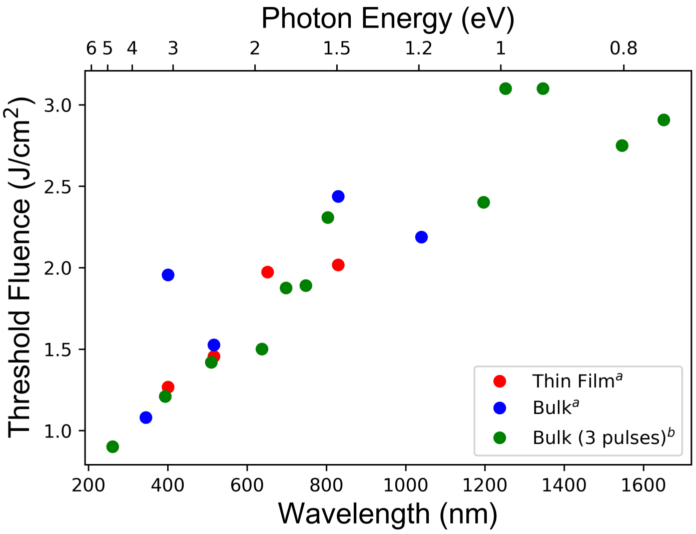

Figure 4.1.2.: Ablation thresholds determined for bulk and thin-film SiO_2 from the UV to NIR range, arranged from a: [47] and b: [46].

to determine the damage threshold dependence of SiO_2 and CaF_2 at 150 fs [46]. They determined the threshold by diameter regression of craters made by 3 pulses. Another more recent work dealing with SiO_2 and CaF_2 as well as other various thin-film materials was conducted by Gallais *et al.* in 2015, with a similar 100 fs Ti:Sapphire-based OPA system [47]. Their thresholds were determined by a single-pulse ablation test at various fluences, where the threshold was defined as the average of the highest fluence where no damage was observed and lowest fluence at which damage was always observed under Nomarski microscope. The results for the two experiments on SiO_2 are arranged and gathered in Figure 4.1.2.

In general, there is an observed trend of the threshold decreasing for shorter wavelengths (higher photon energy). However, the explanation for this differs in the two papers, where Jia *et al.* attribute this to increased intra-band absorption of photons from electrons in the conduction band, while Gallais *et al.* attribute this to the increased strong-field ionization rate from the Keldysh formula. The theoretical models utilized to explain the results were different, with Jia *et al.* using a single rate equation approach with a relatively long electron scattering time ($\tau = 1$ fs) while Gallais *et al.* used a multiple rate equation approach with a much shorter collision time (approx. 0.4 fs). These factors would alter the avalanche ionization rates considerably, which may have contributed to the altering interpretations.

The above experiments were mainly looking at the global trends, and thus, small structures such as steps in the threshold due to changing multiphoton absorption order could not be observed. The observation of these steps is believed to be particularly hard for wide band gap materials (around 9 eV for SiO_2) due to the fact that the changes in absorption are relatively small at longer wavelengths for varying multiphoton order. Furthermore, at the parameter range of SiO_2 ablation, the Keldysh parameter

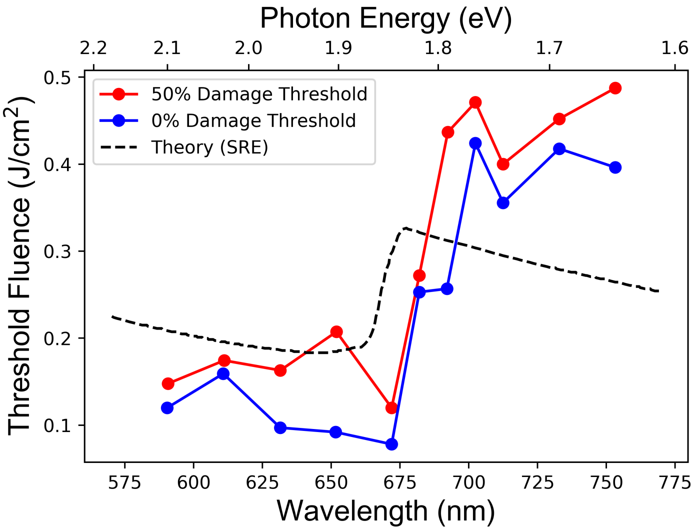

Figure 4.1.3.: Ablation thresholds determined TiO_2 for 1000 pulses compared with theory. Adapted from [94].

approaches 1, and the ionization behavior is expected to be a hybrid of multiphoton and tunneling process. The latter does not show a quantized behavior. Furthermore, avalanche ionization is believed to strongly mask any structures visible in the initial strong-field ionization process.

While no step-structures have been observed for a wide band gap dielectric, in a wide band gap *semiconductor*, however, the multiphoton step structure has been observed. Jupé *et al.* measured the damage threshold of thin film TiO_2 with a 130 fs Ti:Sapphire OPA system. A 440 nm thin film was ion beam sputtered onto a B270 substrate. The band gap of the material was determined by transmission measurements to be 3.61 eV. In this case, a step structure in the threshold resulting from changes in multiphoton absorption from 2 to 3-photon absorption is predicted to occur at around 1.8 eV. The relevant experimental and theoretical results are shown in Figure 4.1.3. While the results are in good agreement, it should be cautioned that the thresholds were determined by illuminating a region with 1000 pulses. It is known that damage incubation effects (elaborated again later) come into play in cases with repeated laser illumination, causing factor decreases in the ablation threshold. In the case of TiO_2 thin films, it has been shown experimentally that the threshold becomes half the value of the single-pulse ablation threshold [123]. This would suggest that varying physics (for example, that of laser-induced defects) should come into effect compared to the case of a pristine material surface, factors which are not considered within the rate equation model of Jupé *et al.*.

There are a few studies on wavelength dependence of breakdown in dielectrics for nanosecond lasers. An early work by Carr *et al.* have found discrete step structures in the internal (focused within the material) breakdown threshold of deuterated Potassium dihydrogen phosphate (DKDP), a material with a band gap somewhere between 7.5 to 9 eV [124]. In a very recent work by Cao *et al.*, the UV to NIR surface ablation

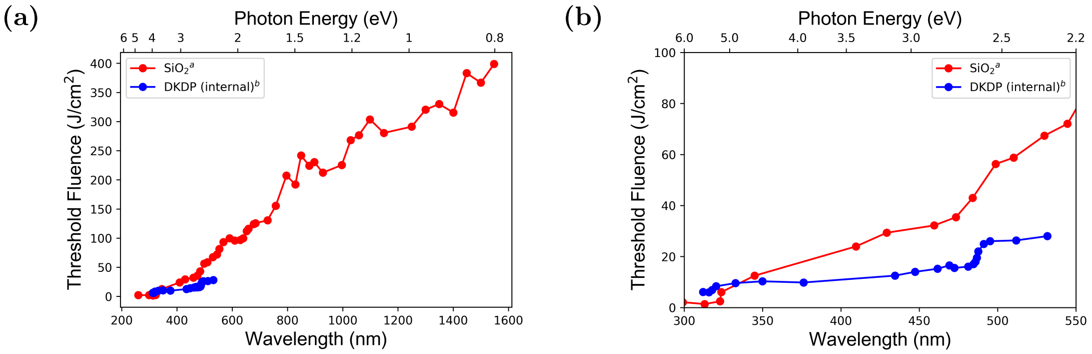

Figure 4.1.4.: (a) Ablation thresholds for SiO_2 and DKDP. (b) Expanded for the shorter wavelengths. Adapted from a: [124] and b:[125].

thresholds for SiO_2 are determined [125]. Both were done with single pulses. The results are gathered in Figure 4.1.4.

A key feature of the work by Carr *et al.* is the visibility of discrete steps in the threshold, seen at 2.55 (approx. 7.5/3) and 3.9 (approx. 7.5/2) eV. However, a pure multiphoton absorption model is inconsistent with theory, as the necessary multiphoton absorption coefficients would be too high for the low peak intensity of nanosecond lasers. Carr *et al.* thus instead postulate a defect-assisted multiphoton ionization model, where electronics defect states help electrons bridge the band gap in a series of lower-order absorption processes.

Cao *et al.* also see step-like structures in the UV near the same values as for DKDP, as evident in Figure 4.1.4b. While the band gap of SiO_2 is believed to be around 9 eV and significantly higher than the 7.5 eV of DKDP, Cao *et al.* attribute the similar step positions to excitionic effects: the effective band gap pertaining to ablation would be lowered by the exciton binding energy. They also note the possibility of surface defect states altering absorption as well. For longer wavelengths in the visible to NIR, step-like structures were seen to disappear. They propose an empirical power-law dependence to explain their experimental results.

In either case, photon-energy dependent threshold quantization is far more pronounced than that in the femtosecond regime, a counter-intuitive result considering the far lower peak energies. Both models rely on defect-based phenomenological explanations. These experiments still remain the only works where multiple multiphoton step structures were observed in the literature for laser-induced damage of dielectric solids with a *single* pulse.

While not a solid-state material, the results of laser-induced breakdown of water for fs and ns lasers studied by a German group should also be noted. Water is known to behave like a dielectric material with a band gap of approximately 9.5 eV, with a pronounced intermediate electronic state at 6.5 eV which was found to be key to nanosecond water breakdown [126]. In their work, Linz *et al.* focus laser pulses into water, and detect cavitation bubbles caused by laser-induced breakdown. By analyzing the probability of formation of these bubbles, they were able to define a cavitation threshold, or the liquid

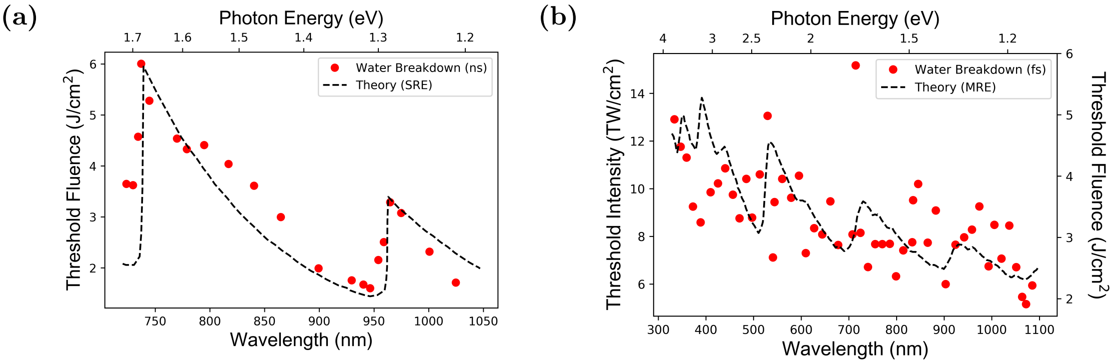

Figure 4.1.5.: (a) Ablation thresholds for water with a 2 ns pulse, adapted from [126]. (b) Ablation thresholds for water with a 250 fs pulse, adapted from [98].

analogue for the breakdown threshold, and measure these threshold in the nanosecond and femtosecond regime [126, 98]. The data is reproduced in Figure 4.1.5.

The ablation thresholds determined for the 2 ns pulses in Figure 4.1.5a are in striking agreement with dependencies predicted by a single rate equation theory. In particular, the threshold increase between the multiphoton steps is well reproduced, a feature which could not be observed in the other experiments. The steps they observed are believed to correspond to integer fractions of a 6.5 eV excited state, believed to be key to nanosecond breakdown.

In contrast, the 250 femtosecond thresholds of Figure 4.1.5b are far less straightforward; they see with fluctuations of around ± 20% even for similar wavelengths, despite utilizing the same methodology as the 2 ns experiment. In particular, step structures could not be resolved within experimental precision. The authors attributed the strong fluctuation in the data to mainly variations in the M^2 factor for different wavelengths within the OPA system. However, as a general trend, they do find a systematic *increase* of the threshold at lower wavelengths both for their theoretical calculations and experiment. This is in stark contrast to the previously introduced results for SiO_2.

4.2. Open questions

It is clear from the state of the literature that several fundamental questions remain unanswered regarding the wavelength dependence of the ablation threshold of materials. The two main questions we seek to address in this chapter are:

1. *Are multiphoton steps visible for single femtosecond pulses?* The work of Jupé *et al.* has been the only observation of multiphoton-steps in TiO_2, but it was determined with 1000 pulses. Is the single-pulse ablation threshold analogous to this situation?
2. *Are multiphoton steps visible for wide band-gap materials?* In all previous studies on materials with large band gaps (for example, the 9 eV of SiO_2), the quantized

step behavior of the multiphoton transitions could not be observed, despite there being clear steps predicted in theoretical calculations based on the rate equation.

Elucidating these questions will allow us to validate the range of applicability of the rate equation approach common to most modern studies. Any limitations will provide clear milestones for future theoretical studies.

To this end, we measure the ablation threshold of two materials with the fluence mapping technique developed in the previous chapter. We choose TiO_2 (rutile) and $\alpha-Al_2O_3$ (sapphire) for our test materials. TiO_2 is important first and foremost as a direct continuation of the work done by Jupé *et al.*. While studies on the fundamental ablation properties of rutile are relatively few, the properties of the material has been well-studied within the context of its photocatalytic properties [127]. On the other hand, $\alpha-Al_2O_3$[1] is one of the most-studied wide-band gap material in fundamental ablation studies, perhaps second to only fused silica. The crystalline nature of the material make it attractive for fundamental studies comparatively. It is also a material of high industrial value, valued for its general hardness and favorable heat conduction properties [24]. Both materials are common and relatively easy to buy commercially as well.

4.3. Experiment

For the experimental setup, we utilize the same fluence mapping setup covered in the previous chapter. In order to increase robustness and locality, samples were irradiated with single pulses of varying pulse energies. These were taken at two positions along the laser propagation axis, separated by 100 μm. This allowed us to check for potential errors in beam spot analysis.

For the TiO_2 experiments, we utilized the signal light from the OPA. We take data from 640 nm to 960 nm in 40 nm increments. Pulse energies were varied in the range of 1.7 to 13.3 μJ, the exact powers depending on the focusing conditions at the wavelength. Samples were purchased from Furuuchi Chemical Corporation, and ablated as-bought (without any pre-processing). Of the crystalline phases of TiO_2, the samples were in the rutile phase, which is also the most stable phase for the material. Samples were cut in the (100) plane; polarization of the ablation pulse was oriented perpendicular to the <010> direction. Samples were 10 mm square and 0.5 mm thick, with >99.99% purity.

For the Al_2O_3 experiments, a wider range of wavelengths was utilized, spanning from 400 nm to 900 nm at 20 nm increments. Pulse energies were varied from 8.3 to 33.3 μJ; the exact powers depended this time more on the limitations of the OPA output than the focusing conditions. To compensate for changing focusing conditions among the different wavelengths, the focusing lens were adjusted (see Table 3.3.1 of the previous chapter). A balance was required between sufficient focusing to ablate, and a relatively large spot

---

[1] We will henceforth refer to the material as Al_2O_3 (dropping the α), or simply as sapphire interchangeably unless otherwise noted.

Table 4.3.1.: Material properties of TiO_2 (from [127]) and Al_2O_3 (from [24]).

	TiO_2	Al_2O_3
Crystal System	Tetragonal	Trigonal - Heagonal Scalenohedral
Crystal Structure	Rutile	Corundum
Melting Point	1870°C	2050°C
Boiling Point	2927 °C	2980°C
Band Gap	3 eV -Indirect[a]	9.5 eV[b]-Direct[c]

[a] A forbidden direct transition is believed to exist at a slightly higher energy [128].

[b] Values given in the literature are inconsistent, varying from 8.8 [129] to 9.9 eV [130].

[c] From [129] and references therein.

to reduce errors in the beam profiling. (100)-cut Al_2O_3 samples were purchased from Shinkosha Co. Ltd. Polarization of the ablation pulse was oriented perpendicular to the $[11\bar{2}0]$ direction. Samples were likewise 10 mm square and 0.5 mm thick, with >99.99% purity.

Some relevant material properties for TiO_2 and Al_2O_3 are gathered in Table 4.3.1.

In the following sections, we first detail results for TiO_2, then subsequently move on to discussions for those results. Afterwards, we detail the results for Al_2O_3, and the discussions for the corresponding results.

4.4. Results: TiO_2

Pictures of a typical ablated crater are shown in Figure 4.4.1. Several features depending on the local fluence can be seen in the morphology. Three regions can be distinguished in the 8.3 μJ data through varying "striation" densities visible: a smooth region (near the crater lip), a sparsely striated area (the center), and a densely striated region between the two regions. With changes in the fluence, the respective regions are seen to shrink. At 5 μJ, the central sparsely striated area can no longer be discerned, while for the 3.3 μJ pulse, the area of the smooth region is clearly visible.

The three regions can also be discerned in the height profiles as well. They appear as discontinuities in the height profile. The onset of each region is shown by downward triangles, where the onset of the densely striated region is shown in solid, while the boundaries of the sparsely striated region is shown in open triangles. Such plateau like structures are unreported in the literature. The same qualitative features were observed at all the wavelengths tried. We expand more on these structures in the discussion.

Combined with the beam profiles taken of the ablating beams, the corresponding fluence maps for each crater can be created. An example of the fluence map for the 8.3

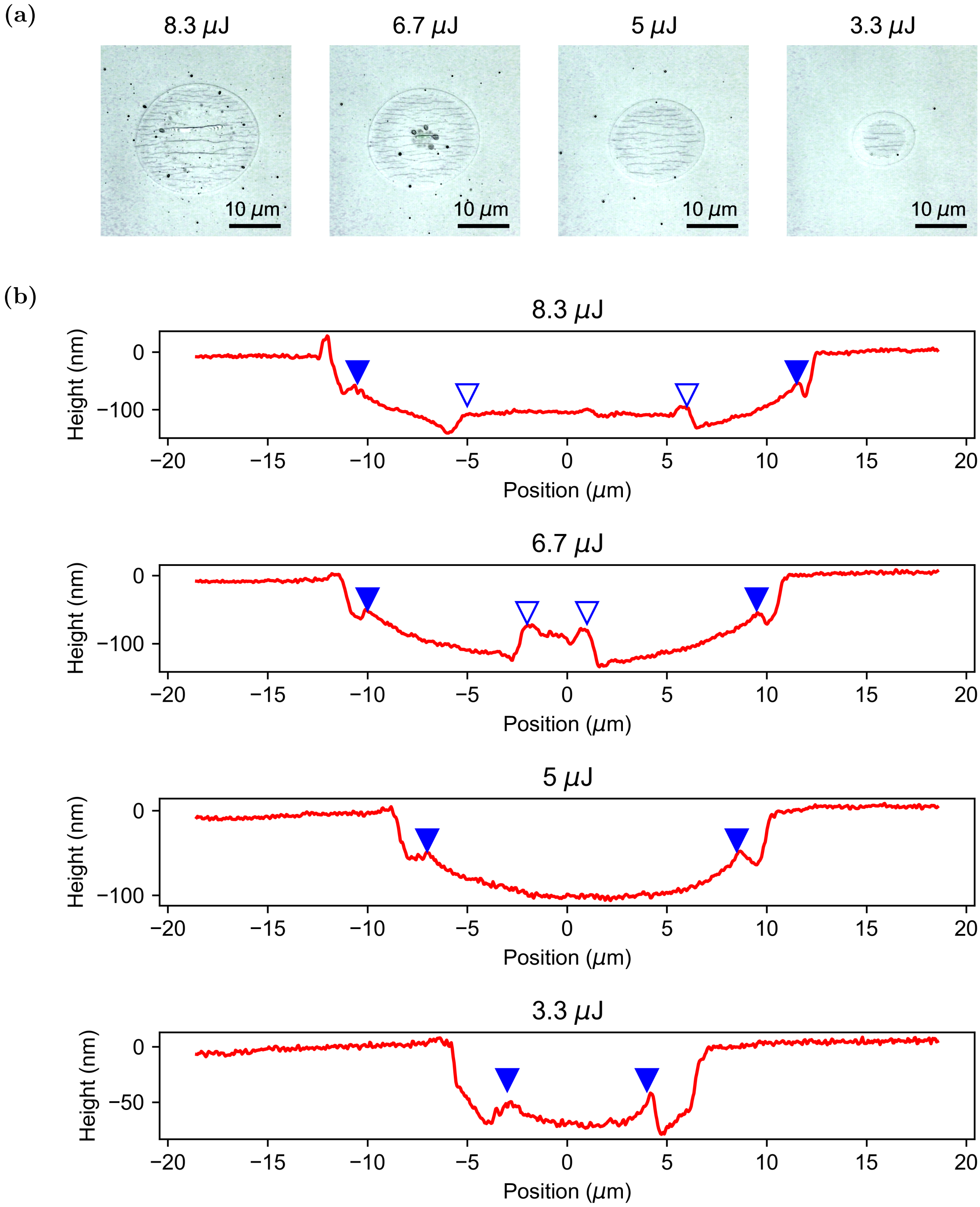

Figure 4.4.1.: (a) Microscope images of the ablated craters at 760 nm at different pulse energies. (b) Corresponding crater profiles horizontally through the center of the image.

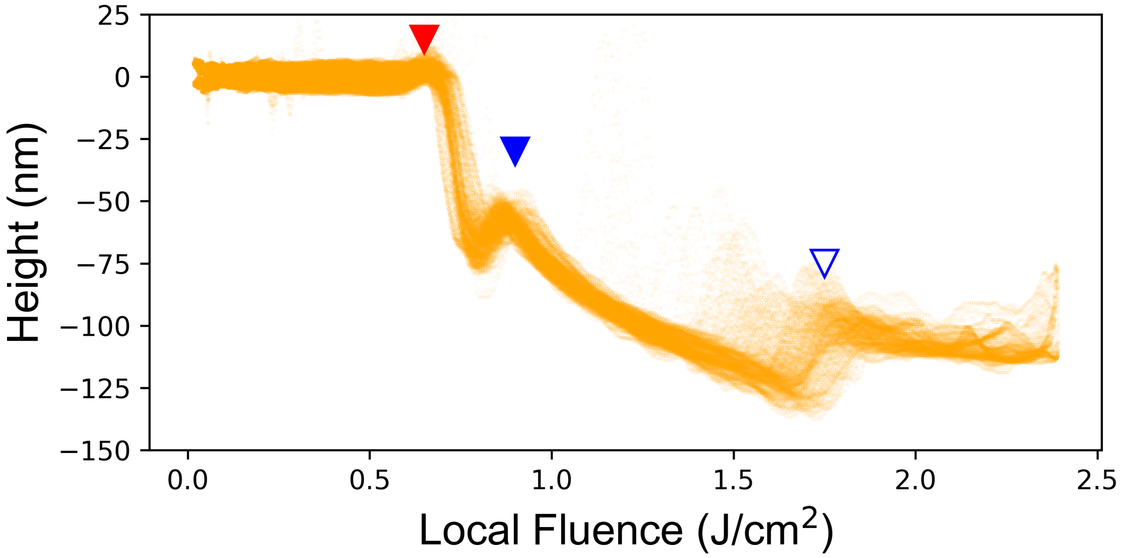

Figure 4.4.2.: Fluence map of ablation by a 8.3 μJ pulse at 760 nm wavelength.

μJ crater is shown in Figure 4.4.2. Morphologies corresponding to the plateau features can be observed in the map. The boundaries to each corresponding region are highlighted with the same blue markers in the figure. The threshold fluence corresponds to where the crater structure begins. We highlight the approximate position with a red triangle in the figure.

A similar fluence map analysis was conducted for all craters, for a little under a hundred maps total. From the maps, we extract threshold values. In particular, we focus on the threshold fluence (solid red triangle) and the boundary to the first plateau region (solid blue triangle). We numerically extract these points from the fluence map by defining the thresholds as the local maxima of the height profiles.

4.5. Discussion: TiO$_2$

4.5.1. Crater morphology

Upon a cursory inspection of the fluence map, it was found that the curvatures of the different regions seem to be somewhat connected, and simply vertically offset. As introduced in Chapter 2, the theory of Puerto *et al.* predicts that, in the case of a multiphoton dominated crater depth, the crater depth should scale as $\propto (F^{-(m-1)} + F_{th}^{-(m-1)})$, where m is the multiphoton order [6]. A cursory fit with this function was found to be unsatisfactory. Here, to explain the phenomenological shape, we alter this function to accomodate new piecewise discrete jumps in height. We fit the fluence maps with the following function $h(F)$:

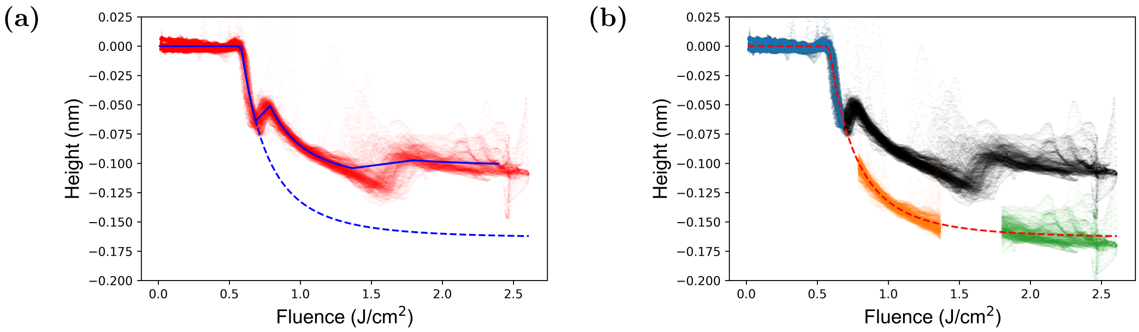

Figure 4.5.1.: (a) A fit of the fluence map profile of a crater ablated with a 680 nm pulse at 8.3 μJ, using equation (4.5.1). The fit parameters with $h_1 = h_2 = 0$ is shown as the dashed line. (b) The original fluence map (black) overlayed with the piecewise fit regions (blue, orange and green) adjusted by the offset heights from the fit. The corresponding non-offset fit profile is shown as a red dashed line as a guide for the eye.

$$h(F) = \begin{cases} 0 & (F \leq F_{th}) \\ -C(F^{-(m-1)} - F_{th}^{-(m-1)}) & (F_{th} < F \leq F_{th2}) \\ -C(F^{-(m-1)} - F_{th}^{-(m-1)}) - h_1 & (F_{th2} < F \leq F_{th3}) \\ -C(F^{-(m-1)} - F_{th}^{-(m-1)}) - h_2 & (F_{th3} < F). \end{cases} \tag{4.5.1}$$

Here, F_{th}, C, m , h_1, h_2 were taken as fitting parameters, corresponding to the crater threshold, a proportionality constant, the multiphoton order, and two offset heights, respectively. As the intermediate regions between the plateaus were noisy, these regions were removed from the fit region by hand, and corresponding boundary points were used as F_{th2} and F_{th3}.

A result of the fit for a fluence map from a 680 nm, 8.3 μJ pulse can be seen in Figure 4.5.1a. Considering the simple functional form, a satisfactory fit is achieved with the experiment. The offset heights from the fit yielded values of 48 nm for the first plateau, and 61 nm for the second. Using these fit values, we can offset the original fluence map vertically, as shown in Figure 4.5.1b. The “cut and pasted” crater exhibits a surprisingly continuous nature. The spatio-temporal scales involved in femtosecond ablation are known to occur at varied time scales, and this continuous morphology may be an indirect evidence of this. The scenario then would be as follows: first, a non-thermal process removes material from the surface, corresponding to approximately the dashed line of Figure 4.5.1a. At later times, excess energy in the electron system in the surrounding not-removed region heats the material, causing melting or boiling. The expansion and resolidification of this material causes bumps in the crater heights, the discrete nature corresponding to the discrete melting and boiling points of the material. The extensive melt-like features observed in the optical microscope measurements restricted to the plateau regions would further support this theory. However, it is difficult to draw a clear conclusion without more complete data regarding the composition of the material, or, better yet, time-resolved data.

The above stated picture would also suggest that the initial penetration depths (before vertical offset) may correspond to simpler physics, perhaps to the multiphoton mediated depths predicted by Puerto *et al.*. However, we were *not* able to make such a confirmation. The fit yields $m = 4.1$ at 680 nm, and 5.3 at 920 nm, notably different from the expected multiphoton order values of 2 and 3 for this 3 eV gapped material. The general trend of increasing m for longer wavelengths is confirmed, but the uncertainties in the crater shape make further exploration difficult. The actual curvature of the crater appears to be mediated by other unidentified physics.

The main takeaway of this analysis may be as follows: for morphological studies, the observed morphology is a result of the integration of all the different processes involved. Any analysis will need to take these effects into consideration, irregardless of the validity of the theory within its select timescale.

4.5.2. Wavelength dependent thresholds

4.5.2.1. Extracting the threshold with non-local effects

From the derived fluence maps, one can also validate the locality of the morphology. Quite unexpectedly, we found there to be a wavelength dependence to the locality: for longer wavelengths, a systematic deviation of the derived fluence maps were observed, while for shorter wavelengths, locality seemed to be assured within experimental precision (a few %). Two representative results are shown in Figure 4.5.2. It should be noted that while the pulse energies differ, due to the differing beam spatial profiles of the OPA output, the fluences (bottom axis) take similar values.

For the case of ablation with a 960 nm pulse (top), for example, by focusing on the ablation threshold (inset), a gradual shift from 0.7 J/cm^2 to 0.8 J/cm^2 can be observed. In contrast, no shift could be observed for the 760 nm case (bottom), suggesting that the mechanism causing the shift is wavelength dependent.

The extracted threshold fluence values are shown as a function of the peak fluence in Figure 4.5.3. In the case of a completely local ablation phenomenon, the points should all have the same threshold fluence value within experimental precision, as is the case for the 760 nm data. However, as seen in the fluence maps, it can be seen that the 960 nm data shows a large systematic deviation.

In order to arrive at a representative value for the threshold fluence, we usually treat (as do traditional methods) scattering as statistical error and take a simple average of the individual values. However, in the current case of non-local ablation, such a treatment will lead to systematic errors in the final fluence values which will reflect the range of the peak fluence values used to arrive at the average, i.e. data taken with more higher peak

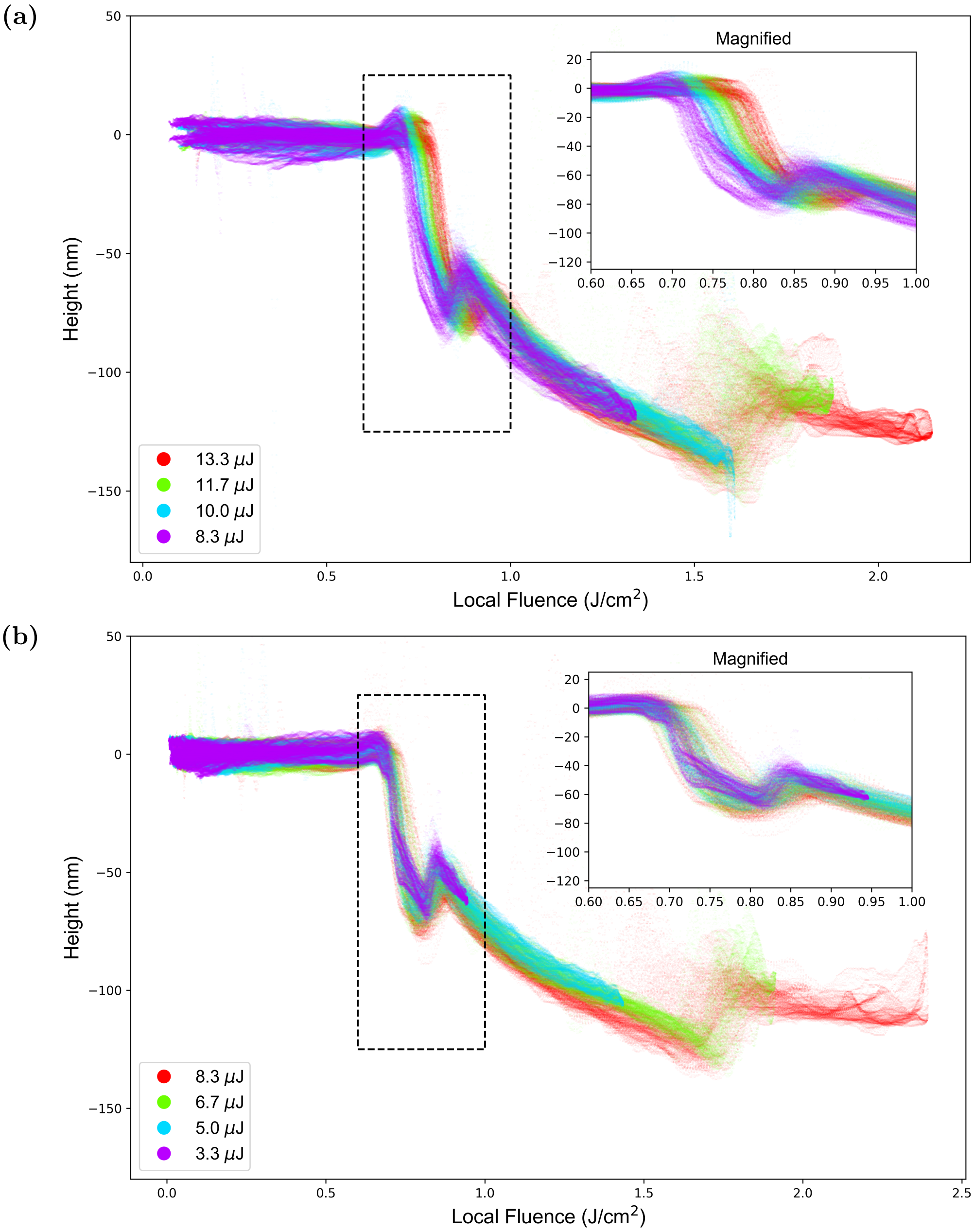

Figure 4.5.2.: (a) 4 fluence maps at 960 nm. A gradual shift of the fluence maps can be observed with changes in the pulse energy. (b) 4 fluence maps at 760 nm, where the ablated height seems to be determined by the local fluence irregardless of pulse energy.

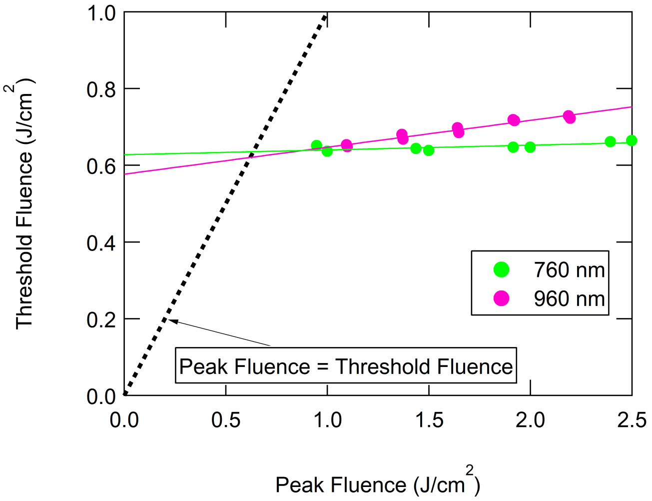

Figure 4.5.3.: Threshold fluence plotted as a function of the peak fluence.

fluence values will yield higher average threshold values. In order to resolve this problem, here we analyze the threshold fluence data by an extrapolation scheme. At its most basic definition, the threshold fluence should correspond to the position where the peak fluence of the pulse is equivalent to the threshold fluence. It was found that the experimental threshold values determined depended linearly with the peak fluence, as evidenced by the clean linear fits to the data shown in the figure. The physical reasons for is not yet known, but a linear fit was found to work consistently among all the wavelength data used. By extrapolating this linear fit and extracting the point where the peak fluence = threshold fluence, a pulse-energy independent fluence value could be deduced. Furthermore, the slope of the linear fit will correspond to the degree of drift in the fluence values, allowing us to gauge locality

The results of the analysis are gathered in Figure 4.5.4. The extracted threshold fluences are shown in Figure 4.5.4a, while the corresponding slopes to the linear fit are shown in Figure 4.5.4b. In both cases, the qualitative features were identical for the two thresholds extracted: the ablation threshold (red) and the threshold for the onset of the first plateau feature (blue).

In the thresholds, a step-like structure could be observed, with a decrease starting from 800 nm extending all the way up to 680 nm. The spectral width of this decreasing regime in threshold fluence is far greater than that of the case of Jupé *et al.*. The threshold wavelength dependence is also far weaker than that which was seen at 1000 pulses as well, with the largest contrasts being only 27% (between 800 nm and 680 nm), as opposed to the approximately 400 % difference seen before. We will discuss this again later.

As for the slopes, locality was seen to be well preserved where a two-photon absorption picture was assumed (left of the green dashed line in the figure). In contrast, a large drift could be observed for the values of the threshold right of this line, or in the three-photon

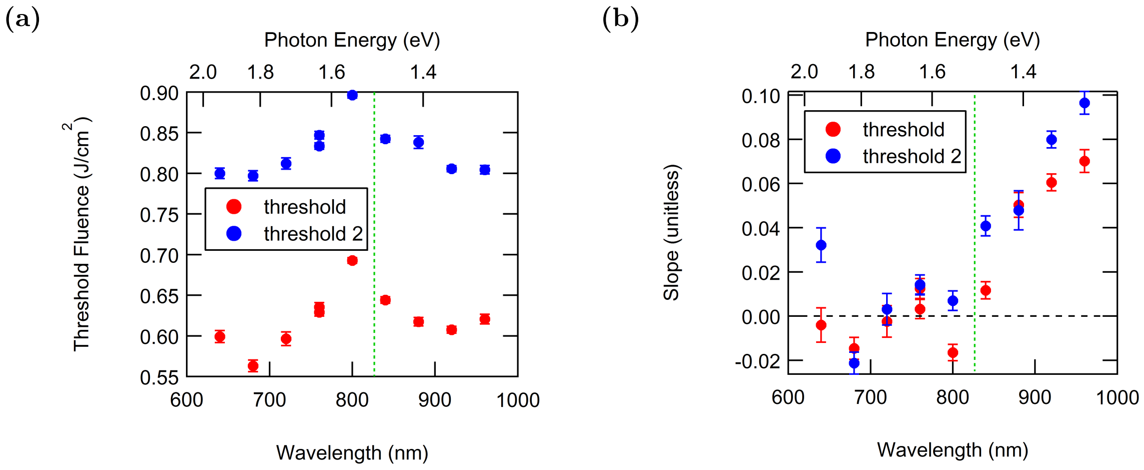

Figure 4.5.4.: (a) The ablation thresholds determined from the linear extrapolation of the local fluence values and (b) the slopes of the linear fits. The zero slope location, corresponding to a pulse-energy independent result, is shown as a dashed black line. In both figures, threshold (red) points correspond to the onset of the main crater, while threshold 2 (blue) points corresponds to the position of the onset of the first plateau. The green dashed line in both figures corresponds to a photon energy of 1.5 eV, where naively a change from two-photon to three-photon absorption would be expected. Error bars correspond to one standard deviation. The two data points at 760 nm for each measurement correspond to values measured on different days on different samples, provided as a measure of the general repeatability of the measurement.

absoprtion dominated regime. As typical threshold fluences were around 0.6 J/cm^2, a slope of 0.08 (threshold fluence/peak fluence) corresponds to an approximately 10% change in the ablation threshold over the currently studied range. As such a macroscopic shift was not observed for sapphire at similar wavelengths and with similar procedures, it is believed to *not* be an experimental artifact.

Simple non-locality (or locality) of the ablation phenomenon itself has not been directly observed in the literature before. Correspondingly, the wavelength dependence of this behavior is also an undocumented result. In order for locality to be violated, some movement of energy (either through the direct transport of electrons, or else through thermal paths later on) must occur. The spatial gradients of energy distribution should become larger for higher-order processes, as spatial differences in local power are amplified by the n-th power. This may be a reason for the deviation becoming more prominent for lower photon energies. However, this explanation alone is far from sufficient, as then we would expect ablation with sapphire to be all highly non-local as the multiphoton orders are of far-higher orders; however, we saw in the previous chapter that ablation appeared to be local within experimental precision. A wider range of material and laser parameter need to be explored to come to a more definitive conclusion. Nonetheless, the current results may prove as promising first-data regarding the avenues through which to explore the phenomenon of locality.

4.5.2.2. Multiphoton steps in TiO_2

In the following discussion, we focus on the values of the strong ablation threshold of TiO_2, or the red points in Figure 4.5.4a. As mentioned previously, the qualitative characteristics of the material differ greatly from previous works.

Before we analyze the data in more detail, one experimental aspect which we did not account for in the aforementioned analysis and a potential source of error is the change in the pulse duration for different wavelengths of the OPA. In femtosecond ablation, it has been shown that given a pulse duration of τ_p, the threshold fluence F_{th} could be expressed as [61]:

$$F_{th} = C\tau_p^{\kappa}, \tag{4.5.2}$$

where C and κ are constants. It was shown experimentally that, for 5 dielectric oxide films including TiO_2, $\kappa \approx 0.3$ independent of other material properties. While a completely empirical relationship based on experimental observations, the scaling law is often used to compare data sets between ablation at different pulse duration in the literature for arbitrary laser/material combinations [47, 98]. We were also able to verify this relationship for sapphire at 1030 nm from 200 fs to 1 ps in a separate set of experiments.

To gauge the significance of the pulse duration on the measured threshold, we employ the scaling of equation (4.5.2) to the current data. We use pulse duration values measured with an autocorrelator (*pulse*Check; A.P.E. GmbH), and rescale all threshold values to its equivalent value at 190 fs. The results are shown in Figure 4.5.5. As can be seen from the data, the qualitative features of the measurement did not change with this factor, leading us to believe the differences to be more intrinsic to the material properties.

In order to gain more information about the current results, we follow a similar rate equation approach as Jupé *et al.*. As the band gap is small, for simplicity, we model the electron excitation by a single rate equation:

$$\frac{dn_e}{dt} = W_{keldysh} + \frac{\sigma}{\epsilon_c n \varepsilon_0 c} I_{int} n_e - \frac{n_e}{\tau_{rec}}. \tag{4.5.3}$$

Here, $W_{Keldysh}$ is the Keldysh SFI rate (2.3.7), σ is the Drude conductivity (2.3.22), ϵ_c is the critical energy for impact ionization (2.3.35), ε_0 is the vacuum permittivity, c is the speed of light, I_{int} is the field intensity within the material, and τ_{rel} is a fast relaxation time into shallow traps. I_{int} was calculated by multiplying the incident intensity by the transmission coefficient calculated from the time-dependent dielectric constant of (2.4.2). The background dielectric function was calculated from the Sellmeier relationship of TiO_2, taken from [131]:

$$n^2 = 5.913 + \frac{0.2441}{\lambda^2 - 0.0803}. \tag{4.5.4}$$

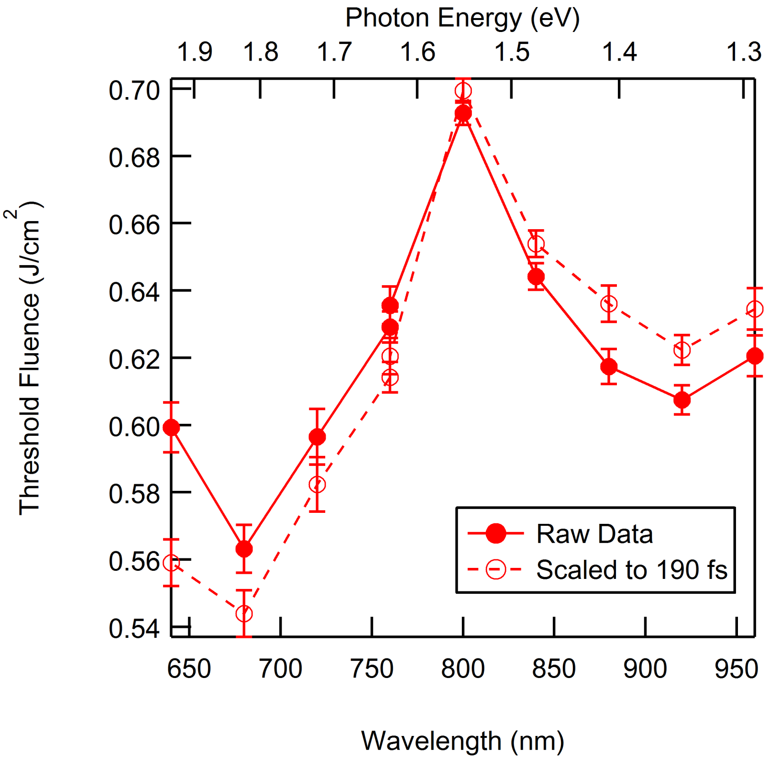

Figure 4.5.5.: The original and scaled threshold fluence values for TiO_2.

The relaxation time τ_{rel} was taken as 200 fs in accordance to Jupé *et al.*. For the incident pulse, a 190 fs FWHM pulse was used. The conduction band effective mass was taken as the electron mass, and the valence band electron mass was taken as 2.36 times the electron mass [132]. The band gap of TiO_2 and a static electric scattering time τ were left as fitting parameters.

The rate equation was numerically solved for an input fluence by converting the differential equation to a first-order finite-difference approximation, with a time-step of 1 fs. The ablation threshold was determined as the fluence where a set electron density was reached; this value was left as a fitting parameter. This fluence was found by using a bisection algorithm, where the fluence used to calculate the electron density was adjusted by $F_{ini}/2^k$, where k is the iteration number according to whether the maximum electron density was above or below the critical electron density. 15 iterations were done for each wavelength with an F_{ini} of 0.5 J/cm^2.

The results to the calculations are shown in Figure 4.5.6. Optimization of parameters yielded a scattering time of 1.1 fs, band gap of 3.17 eV, and electron density at ablation of 6.2×10^{21} cm^{-3}, all values within reasonable agreement with typical values in the literature. It can be seen that while the threshold agrees by factors, the step size is over-estimated in the calculation. Change in calculation parameters, namely adjusting the relationship between the SFI rate and the avalanche ionization rate, as well as the choice of breakdown electron density will all lead to changes in the threshold fluence by

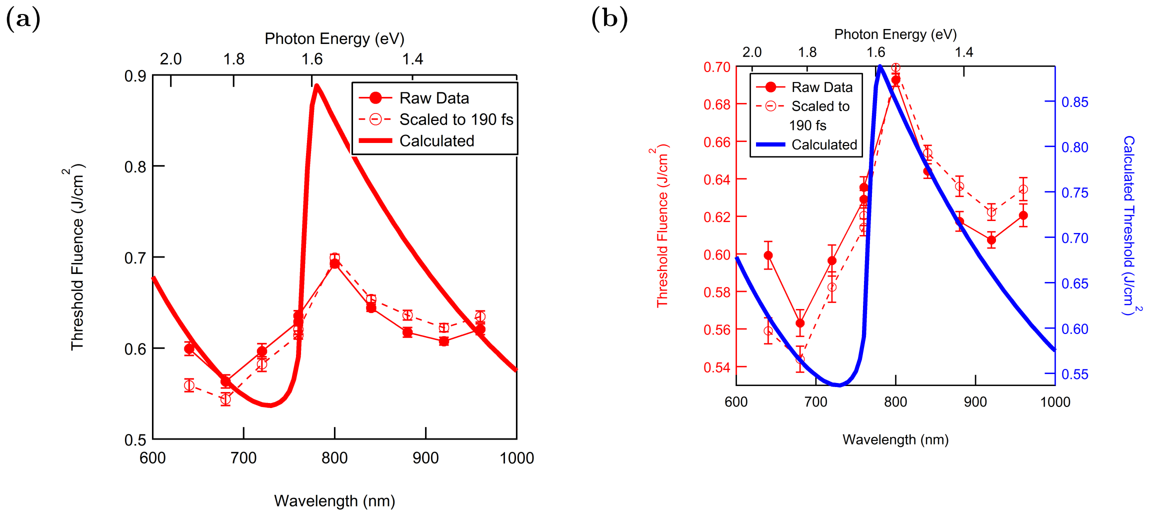

Figure 4.5.6.: (a) Single-rate equation calculation of the threshold plotted with the experimental results. (b) The same plot with axes adjusted

factors. By optimizing these parameters through other parameters, it may be possible to come to a more globally optimized result. In general, a larger threshold difference across a multiphoton step corresponds to a larger contribution from the SFI rate: thus a stronger avalanche and weaker SFI rate may be required. However, without more information to corroborate experimental parameters beyond simply the threshold, it is hard to verify the validity of any derived parameter from just this data.

A second major difference between the calculated results and the experiment is the width of the transition regime. As was the case in the experimental and theoretical work of Jupé *et al.*, the calculated region of threshold decrease with increase in photon energy (the “width” of the step) is of the order of 20 nm. However, the experimental results showed a far more gradual decrease. To accentuate this observed difference, the vertical scales are adjusted in Figure 4.5.6b.

By adjusting calculation parameters within the rate equation (and the multiple rate equation as well), we can change the relationship between the SFI rate and the avalanche ionization rate as aforementioned. While this may lead to a lessening of the step width, or shifts in regards to its location, this does not, in general, lead to macroscopic changes in the step width. This is especially true for lower multiphoton orders (with large Keldysh parameters) where the multiphoton order “smearing” effects of tunnel ionization do not take effect. From this, it is believed that the broadening of the two-photon to three-photon transition is caused by an effect *not* considered in the traditional rate equation.

As the step-like behavior within the calculated threshold originates from the SFI term, the problem is believed to reside in the use of the Keldysh equation, some of which were listed in chapter 2. For the current use of the Keldysh equation mainly within the multiphoton regime, the main factors that may cause broadening of the multiphoton-order transition are:

- the non-monochromatic nature of the laser source,
- many-body effects due to the high-density excitation, and
- contributions of the band shape and/or other bands.

Regarding the non-monochromatic effect of the laser pulse, the current spectral width of the femtosecond light source is of the order of a few nanometers at most, and is believed to not play a large role. In addition, if this were the case, the work of Jupé *et al.* utilize an even shorter pulse (130 fs), and their step should be even more broadened accordingly.

Many-body effects would also be expected to play an effect. The Keldysh equation is formulated under the single-active electron approximation with ionized electrons assumed to act independently. However, at the high excitation levels present in ablation, many-body effects such as band-gap renormalization (which would decrease the gap) or carrier blocking (which would increase the gap) are expected to come into effect [69]. As the electron population would vary with time, the band gap would also take transient values, thus smearing the step structure. Many-body effects are mainly undocumented in the context of laser ablation, and their quantitative effects largely unknown. To gauge the magnitude of this effect, it should be helpful to consider the shift of the band gap at electron densities seen by the laser field near the peak of the pulse, when multiphoton ionization is strongest. In ablation with pulse durations of a couple hundred femtoseconds, the electron density increases by orders of magnitudes due to the avalanche process at the latter half of the pulse to reach the critical density; thus, typically, the electron densities near the peak of the pulse are believed to be moderate, around the order of 10^{18-19} cm^{-3} [4, 54]. In the context of heavy carrier doping ($\approx 10^{19}$ cm^{-3}), TiO_2 has been shown to have band-gap renormalization (which generally decreases the gap) and/or Moss-Burstein shifts (which would increase the gap) as large as 200 meV [133, 134]. The current transition regime is broadened to a width of around 250 meV, or an equivalent one-photon broadening of 500 meV; while larger, these values vary only by factors and are not completely without possibility. However, a shift in the fundamental absorption edge would not explain the differences seen in the results of our experiment and Jupé *et al.*, as both would require similar high-density excitation to destroy the material which should induce similar shifts (albeit their experiment should also involve multiple-pulse irradiation effects, another complex problem). In light of these difficulties, we follow the convention in the literature and ignore many-body contributions.

This leaves us with the third option. The Keldysh SFI rate is often used without much consideration as to the actual band structure of the material. The rate is calculated by plugging in the fundamental band gap value, an effective mass value for the electron, and the frequency of the laser. However, the actual strong field ionization process is believed to be far-more complex, reflecting far more facets of the material electronic structure.

The band structure of rutile TiO_2 near the Γ point is shown in Figure 4.5.7a, taken from [132]. They calculated the direct fundamental band gap to be 2.97 eV. The

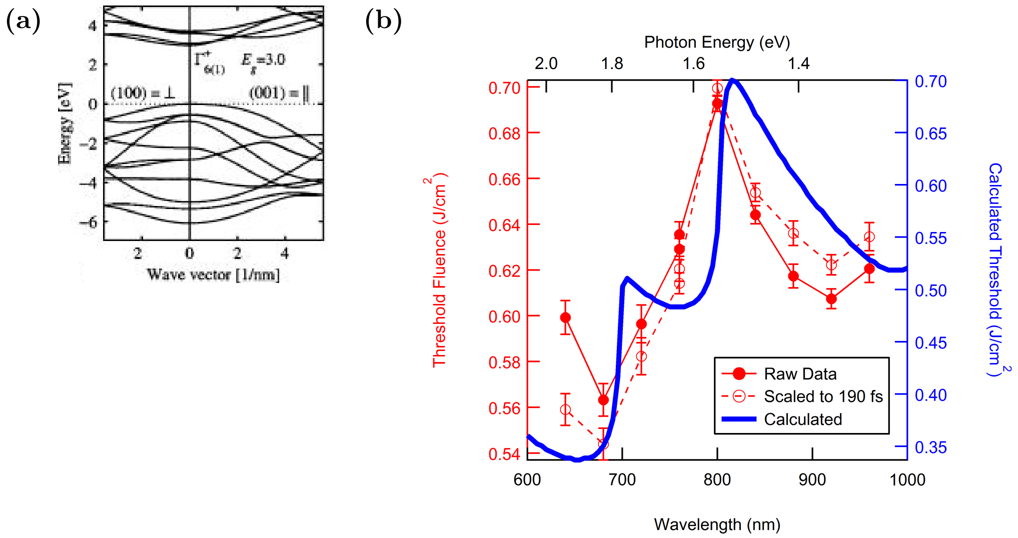

Figure 4.5.7.: (a) The band structure of TiO_2 around the Γ point, calculated by DFT using the local density approximation in combination with a on-site self-interaction correction potential, taken from [132]. (b) Calculated multiphoton band structure with contributions from the second conduction and second valence bands.

conduction band consists of two bands 0.11 eV apart, and higher lying conduction bands are 0.62-0.73 eV above the CB minimum. The top of the valence band consists of a rather flat band, while the second and third valence bands lie 0.54-0.57 eV below the valence band minimum. Other DFT calculations also yield similarly offset higher-order valence and conduction sub-bands [135].

While a rigorous treatment of the strong-field ionization rate for this band-structure is out of the scope of this thesis (see for example, [136]), we would like to gauge the qualitative effects of roughly taking into account the higher-order bands to the rate equation approach. To do this, we focus on the excitation from the energetically close second and third valence band to the two lowest conduction bands, which we approximate to be separated around 3.5 eV. We do this by adding a second Keldysh term to the rate equation:

$$\frac{dn_e}{dt} = 2W_{keldysh}(E_g) + 4W_{keldysh}(E_g + 0.5\text{eV}) + \frac{\sigma}{\epsilon_c n \varepsilon_0 c} I_{int} n_e - \frac{n_e}{\tau_{rec}}. \tag{4.5.5}$$

We add prefactors of 2 and 4 to reflect the possible transition combinations. The effective masses for the second valence band was taken as 0.74 m_e [132], E_g was taken as 3 eV, and the scattering time was altered to 3 fs to adjust the general calculated threshold values to the correct order; all other parameters were taken equivalent to the original rate equation calculation. While a rough estimate, we hope to gain some phenomenological insight from this simple treatment.

The results are shown in Figure 4.5.7b. The absolute values are predictably different, but the qualitative features are more similar than for the original rate equation. In the calculation, two clear “sub”-steps (at 700 and 800 nm) can be observed; we believe this to be an artifact of the current treatment, where the 6 transitions considered from the different bands were treated in just two categories (3 eV gapped and 3.5 eV gapped transitions). In reality, each band would have different effective masses and transition probabilities. This would be expected to shift the transition energies relative to each other, thus smearing out the total ionization rate into one macroscopic step (making individual steps indiscernible), as was seen in the experimental results. The total width of the transition regime would then correspond to the combined width of all relevant bands: the step would start at the lowest-gapped bands, and stop at the highest gapped band with non-negligible excitation probabilities. Furthermore, the slight increase in the threshold at longer wavelengths (>900 nm) is also qualitatively reproduced; a slight increase in the threshold is observed in the multi-band calculation, while this was not visible in the previous single-band calculation.

With this interpretation, differences seen between the work of Jupé *et al.* may correspond to changes in the peak power (about five times lower for our short-wavelength results). The pulse energies used in their experiments are smaller, and thus, higher-order transitions are expected to be further suppressed. Instead, in their experiment, the differences in the lowest-order excitation are amplified by the continued irradiation with 1000 pulses. To reach a more definitive conclusion, however, experiments with other materials and other numbers of irradiation pulses would be required, as other parameters (material and pulse duration) are different between the experiments.

The conclusions of our measurements of the threshold for TiO_2 are as follows. The wavelength dependence of the threshold in the single-pulse regime is far weaker than predicted in the theory, suggesting a weaker contribution from the direct ionization term than what is predicted from typical parameter values. Furthermore, the width of the transition was found to differ between experiment and theory. We believe this to be caused by higher-order band effects; the relatively energetically close valence and conduction sub-bands may play a non-negligible role in the initial ionization process.

4.6. Results: Al_2O_3

We next cover in this section the results for the wavelength dependent thresholds of Al_2O_3. The main difference between TiO_2 is the wide band-gap of the material: the main question being if whether multiphoton resonances are still visible in this high-order material.

The qualitative features of the crater and fluence maps were identical to that introduced in the previous chapter. We were unable to discern a significant qualitative changes induced by a change in wavelength despite the large wavelength range utilized, from 400 nm to 900 nm.

As with the case of TiO_2, we extract the main (strong) ablation threshold of the material by finding the location of the maximum near the crater lip in the fluence map. Threshold values were found to not show systematic non-locality like in the case of TiO_2 at longer wavelengths. Thus, differences in threshold values for different pulse energies was treated as a statistical error, and a simple average was taken to determine the threshold values. The standard deviation of the summation was used to gauge the error. While two on-axis locations were ablated, the results did not differ significantly between the two, and thus only one set was analyzed for the following discussions. This corresponds to a total of around 130 craters.

The results to the measurement are shown in Figure 4.6.1a. Systematic changes in the pulse duration of the OPA output are believed to be causing the large distortions and discontinuities in the data. However, even here, some features suggestive of multiphoton steps can be seen. In particular, there are two clear steps in the signal data at around 700 and 800 nm. If this is a true signal, to the author's knowledge, this is the first direct observation of multiphoton steps in a wide band-gap dielectric. The step structures in our data are observed to be fairly small (approximately 10 % of the threshold value); this small fluctuation makes practical extraction of the threshold challenging with conventional threshold measurements. Errors are generally greatest at the emission edges of the OPA, where the laser spatio-temporal quality degrades, and the idler light, where the beam spatial profile was observed to have notably non-Gaussian artifacts. Some representative profiles are provided in Figure 4.6.1b.

4.7. Discussion: Al_2O_3

As was the case for TiO_2, we use the 0.3-th power scaling law to normalize all thresholds to their predicted values at 190 fs. The results are shown in Figure 4.7.1.

The results are still fairly difficult to interpret, especially near 600 nm, where the data between the signal and the second-harmonic of the idler do not connect continuously, suggesting some form of systematic error. However, the periodic undulations, with peaks at 880 nm, 800 nm, 700 nm, and 520-540 nm, are believed to be due to multiphoton transitions. With increasing photon energy, the steps become increasingly larger; this is consistent with a weakening avalanche and stronger direct ionization rate as predicted from theory and in our calculations, introduced below.

A naive picture of the multiphoton steps would expect the peaks to come at integer orders of the band gap. However, this is not the case, where possible combinations of integer multiples yielded band gap values differing in eV order. The peak positions, especially at longer wavelengths, are particularly sensitive to parameters other than the wavelength. To illustrate this point, we show the calculated threshold for Al_2O_3, adjusting only the electron collision time from 1 fs to 3 fs in Figure 4.7.2. We use the same rate equation as the form of equation (4.5.5), with a couple of changes reflecting material properties. The conduction and valence band electron mass was taken as $0.38m_e$

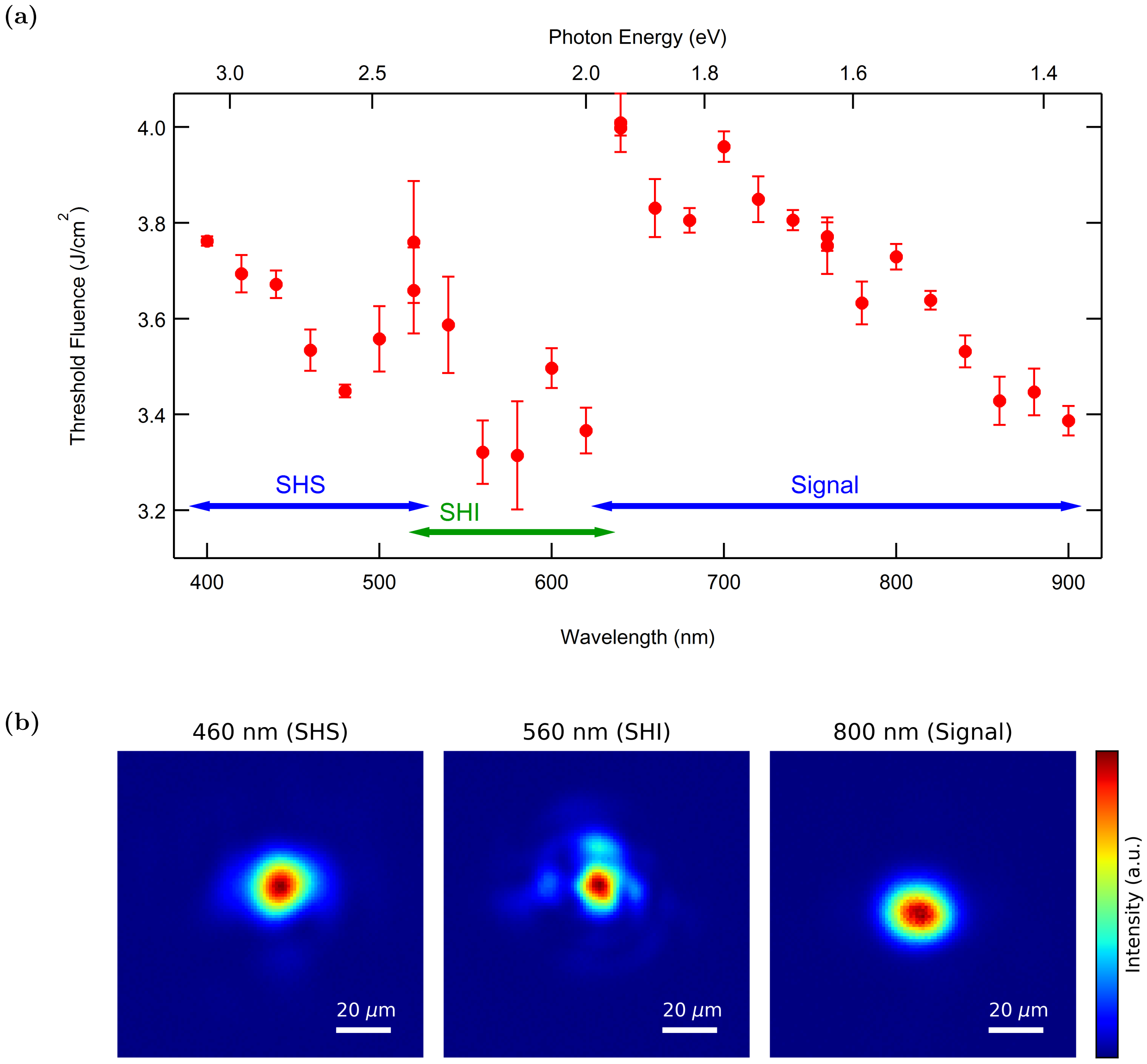

Figure 4.6.1.: (a) Measured ablation threshold of sapphire from 400 to 900 nm. The wavelength range of the output of the OPA are labeled near the bottom axis, where SHS and SHI are the second harmonic of the signal and idler, respectively. Wavelengths with multiple points correspond to points taken on different samples on different days to give a general estimate on experimental reproducibility. (b) Representative beam profiles for the SHS, SHI, and Signal beams.

and $3.99m_e$, respectively [137]. The band gap was taken as 9 eV, and the recombination term was removed, due to the slow recombination rates measured in the literature [90, 82]. The refractive index was modeled by the following Sellmeier function [24]:

$$n^2 = 1 + \frac{1.4313493\lambda^2}{\lambda^2 - (0.0726631)^2} + \frac{0.65054713\lambda^2}{\lambda^2 - (0.1193242)^2} + \frac{0.53414021\lambda^2}{\lambda^2 - (18.0228251)^2} \tag{4.7.1}$$

From the calculation, it can be seen that due to this shift, it becomes difficult to unambiguously identify the band gap of the material from the position of longer-wavelength step positions. The positions are generally unstable owing to the small Keldysh parameters (around 1) for the longer wavelengths, making the multiphoton orders dependent on the intensity, which varies by time. It makes sense then to use UV wavelengths where the Keldysh parameter is smaller to determine the band-gap unambiguously. However, due to bandwidth limitations of the half-waveplate in the optical setup, we were not able to measure thresholds below 400 nm, and unable to measure the final step developing near 400 nm. As such, while we attempted to find good rate equation forms (including multiple-rate equation and ionization delay models) by hand and also parameter optimization by least-square fitting routines, we were unable to get a satisfactory fit across the whole regime. Whether this is a problem with the rate equation or with the numerical procedures will require further study.

As for the macroscopic trends, we did not observe a global decrease in the ablation threshold for shorter wavelengths, as was measured by Jia *et al.* and Gallais *et al.* [46, 47] (about a 50 % decrease from 900 to 400 nm). Neither did we measure an increase, as

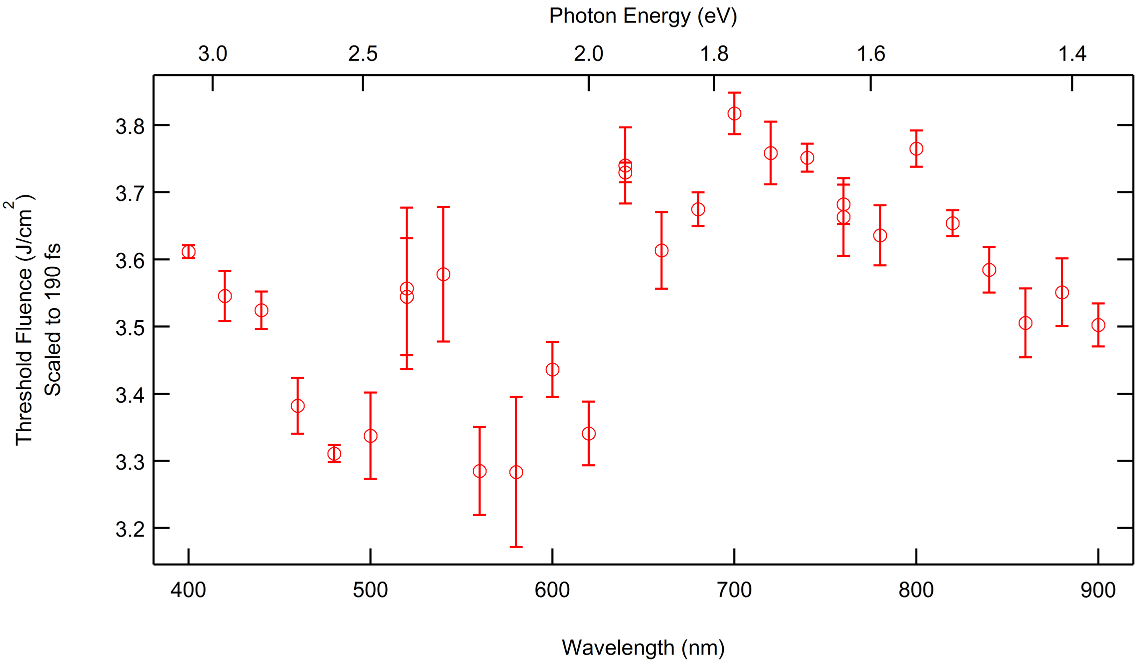

Figure 4.7.1.: The thresholds of Figure 4.6.1 scaled to 190 fs according to equation (4.5.2)

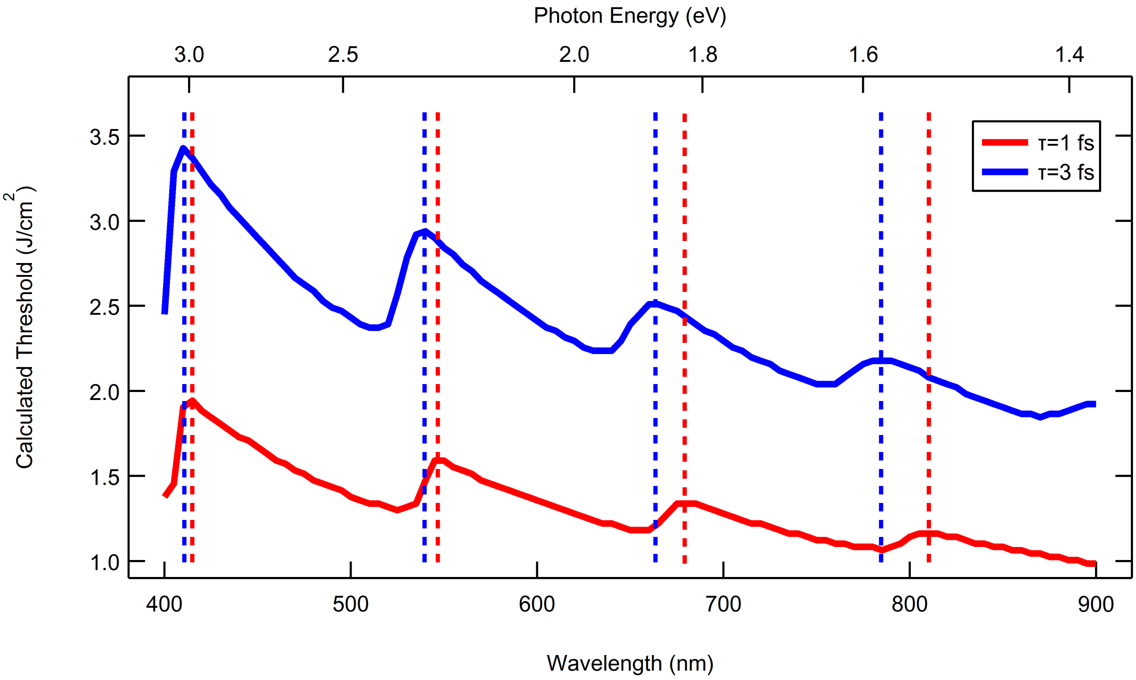

Figure 4.7.2.: Thresholds for Al_2O_3 calculated for two different values of the electron collision time. Peak positions of the multiphoton peaks are shown in dashed lines; the shifts become larger for longer wavelengths.

was the case for water with Linz *et al.* [98] (a 50 % increase from 900 to 400 nm). Instead, the derived values were flat across the whole spectrum, with fluctuations of only about 20 %. It should be emphasized that the laser systems and materials used in this experiment were different from that of the works in the literature. More experimentation with different materials and pulse durations are necessary to come to a more general conclusion.

4.8. Summary and Prospects

In the previous chapter, we introduced the fluence mapping technique as a method particularly robust to non-Gaussian laser intensity profiles. A light source where differing beam profiles have been particularly hard to compensate for has been the OPA. While the wavelength selectivity of OPAs are attractive, the systematic errors induced by their changing spatiotemporal characteristics has made extracting systematic wavelength dependence data from this light source particularly difficult.

In this chapter, we utilized the strengths of the fluence mapping technique to explore the wavelength dependence of the ablation thresholds of materials by a single femtosecond laser. While the spectral response of a phenomenon is usually one of the first characteristic studied in traditional light-matter interaction studies, the systematic errors induced by high-power OPA light sources has made it particularly difficult to extract accurate data, and the wavelength dependence of the ablation threshold has remained one of, if not the last independent parameter not extensively studied in single-pulse ablation. As representative materials, in this chapter we explored two materials: TiO_2 and Al_2O_3. The former was used a comparison to literature, while the latter was selected as a typical wide band gap material.

For TiO_2 we measure the ablation threshold for wavelengths around the 2 to 3 photon absorption transition of the material, at approximately 3 eV (820 nm). While we saw general qualitative agreement with the rate equation approach in our results, we also observed large differences in the spectral width of the multiphoton step. This broadened width may be due to multi-band effects in the excitation process.

For Al_2O_3, we explore a wider range of wavelengths, from 400 nm to 900 nm, to observe both the global and microscopic characteristic of the ablation threshold in this wide band gap material. For the first time in the literature for a wide band gap material, we observe what we believe to be multiphoton transition induced quantized behavior of the threshold in the data. While the complex nature of the threshold and residual systematic errors made a microscopic analysis difficult, we were able to confirm some general features of the steps, such as the gradually increasing step heights with the photon energy. The general trends also showed that Al_2O_3 has very weak wavelength dependence over this regime, with an almost flat threshold response, whereas the rate equation approach often predicts a large fluctuation.

As stated in the introduction to this chapter, the multiphoton nature of the ablation process has long been postulated in multiple-rate equation based ablation models. Although qualitative, we believe that the current result is a direct demonstration of how the microscopic electronic excitation properties of multiphoton ionization translates to the overall macroscopic phenomenon of optical breakdown. The fact that these structures appear is non-trivial in and of itself, and further analysis of their structure may yield more fundamental information regarding avalanche and strong-field ionization rates. While the state of current theories make quantitative explanations of the experimental results difficult, it should be stressed that we believe this highlights not the experimental limitation of our work, but more the theoretical limitation of our understanding. The superior robustness of our current methodology to systematic errors allowed us to resolve these structures with unprecedented accuracy.

The current results provide for promising future prospects. For one, this may be the first demonstration of *ablation threshold spectroscopy* as a viable method of probing the fundamental energy absorption characteristics in the non-perturbative, high-field setting of ablation. One may think of this as a high-field analogue to traditional absorption spectroscopy, which yields some of the most important fundamental information regarding light-matter interactions in studies on optical processes in solids. By comparing the results predicted by traditional theories, one may be able to extract effective material parameters, such as the band gap or electron scattering rates, at non-equilibrium, high-field settings. Sweeping the wavelength as opposed to the currently popular method of changing the pulse duration is advantageous in fundamental studies for two reasons: the timescale of the interaction remains nearly constant, and the peak intensities remain comparable. As these two facets are often critical to justifying approximations used in modeling ablation, the fact that these are held constant increases the simplicity of the interpretation. While in this work we focused on two representative materials, by studying the ablation threshold spectroscopic “fingerprints” of many materials, a more collective understanding of relationships between the basic material structure and absorption characteristics may be constructed, much akin to the spectroscopic fingerprinting of molecules and how we understand the absorption properties of various molecular substructures today. In short, we believe this method to be a significant step forward in transforming the current case-by-case understanding of optical breakdown to a more encompassing and consistent theory.

From an application point of view, understanding which wavelengths to use to effectively couple the energy from the electromagnetic field to the material is critical to increasing ablation efficiency. Identification of effective wavelengths to ablate materials at allows one to properly calculate the total photon cost and benefit of wavelength conversion. Furthermore, by understanding the dominant fundamental contribution, the possibility of enhancing ablation through tailor-made multichromatic ablation schemes can be more scientifically explored.

Chapter 5.

Empirical Characterization of Damage Incubation for Displaced Pulses

While the previous chapters covered the determination of the threshold and ablation for single pulses, a great majority of applications in laser processing utilizes multiple pulses. In order to bridge fundamental studies to real-world applications, differences in these two modes need to be carefully characterized. A key factor which differentiates multiple-pulse ablation from that of the single pulse is changes in the material parameters. In this chapter, we develop a method to incorporate these effects into the simple case of laser grooving.

5.1. Introduction

5.1.1. Damage incubation and the multiple-pulse ablation threshold

For ablation with pulses with comparatively long pulse durations, the question of the effect of sample quality has always been of concern. This concern can be seen in even one of the earliest reviews of laser ablation by Bloembergen in 1974 [1], where a significant portion of the paper is devoted to documenting the effect of imperfections. These imperfections include both morphological, such as grooves and incisions on the material surface, and more structural, such as defect and impurity states within the material. With lower available peak intensities, extraction of intrinsic material properties from the background of these extrinsic effects was, and still is, a difficult task.

With ultrashort laser ablation, the high peak powers allows for a significant strong-field ionization rate which was believed to overcome the effects of the native electron population within shallow trap and defect states. For the shortest pulses, a lack of sufficient time for an avalanche process to develop was also believed to suppress fluctuations caused by the initial population. The high determinism observed led many to believe that most situations in ultrashort laser ablation were governed by intrinsic material properties, and insensitive to damage. This lack of concern often manifested in the methodology as well.

Experimental damage thresholds of materials were often determined with multiple laser pulses to "enhance" damage features, such as approximately 600 pulses for the work of Stuart *et al.* [58], or 50 pulses for Lenzner *et al.* [89], while the corresponding theoretical work often postulated pristine material properties.

However, it was soon understood that ablation *was* in fact sensitive to material quality. This sensitivity is most readily observed as a dependence of the damage threshold on the number of laser pulses irradiated on the sample. Varel *et al.* found as early as 1996 that damage thresholds were consistently *lower* in the case of 5-pulse irradiation when compared to the case of a single pulse [100]. Such differences were believed to be due to incubation effects, where laser-induced electronic defect states, such as color centers, are formed with electronic excitation [12, 138, 66]. Such defects provide sub-band-gap levels which serve as easily excitable sources for subsequent electronic excitation. These slight changes in optical property are magnified in the highly nonlinear excitation process of ablation, leading to macroscopic changes in not only the ablation threshold, but also the morphology of observed processed regions [19]. It was later found by Lenzner *et al.* that even for pulses as short as 5 fs, the effects of incubation could be observed [139], where the threshold for 50 pulses was found to be around 1 J/cm^2, significantly lower than that for a single pulse, at approximately 4.9 J/cm^2. Thus, it is believed to be a near universal effect independent of pulse duration, although the magnitude of its significance may differ.

Several empirical and semi-empirical models were proposed to model the changes in threshold fluence due to damage incubation. One of the most widely used is a model proposed by Rosenfeld *et al.* in 1999 [99]. There, they found satisfactory agreement with experimental data for a wide class of materials when the damage threshold fluence of a material at N pulses was modeled as

$$F_{th}(N) = F_{th}(\infty) + (F_{th}(1) - F_{th}(\infty)) \exp[-k(N-1)], \tag{5.1.1}$$

where $F_{th}(N)$ is the threshold at N pulses, and k is a parameter describing the strength of the incubation effect on the absorption cross section for subsequent pulses. While extremely simple, the above equation captures the essence of experimental trends observed in incubation. The threshold is highest for the single pulse, and gradually decreases over a characteristic number of pulses $1/k$, and eventually saturates at a value of $F_{th}(\infty)$, below which no amount of laser irradiation will damage the material. While several models have extended this simple model by considering timescales [67], or the possibility of multiple processes [123], the above model remains popular as a general starting point.

As is the case for the single-pulse laser threshold, the multiple-pulse damage threshold and incubation characteristics are highly dependent on laser and material parameters. Even for the same material, incubation characteristics have been shown to depend on pulse duration [140], pulse repetition rate [60, 140, 141, 123], laser polarization [123], and the surrounding atmosphere (both composition and pressure) [142], to list a few. For more, see for example [13, 123]. In each case, a unique coefficient is determined through fits to the experimental data.

In general, incubation studies have focused on determining the ablation threshold dependence on the number of incident pulses. Thus there is still a rather limited amount of knowledge regarding how incubation works above the N-pulse damage threshold, as well as how to model incubation for cases where the N-pulses have varying pulse energies.

5.1.2. Laser grooving

One of the most common form of laser processing is the laser direct write process, where the laser pulse is focused onto a spot and moved, hence "writing" a pattern upon the material surface. The laser grooving/scribing process, where the laser is scanned in a linear manner, may be considered the simplest form of laser direct writing. Single lines serve as scribe marks for scribe-and-break processes, or microchannels for microfluidics, while repeated scanning would allow for free-form cutting of materials.

In laser grooving, two parameters are usually tuned to achieve the desired morphology: the pulse energy and the scanning velocity. While the first parameter is straightforward, standardization of the second parameter is less so. For example, even for the same scan speed, a use of a larger beam spot size would result in more "overlapped" laser pulses. Thus, it makes sense to normalize distance somehow in terms of the beam diameter. In order to gauge the degree of overlap, a commonly used parameter η is defined as (in units of percents):

$$\eta = \begin{cases} 100\left(1 - \frac{d}{2w_0}\right) & (0 \leq d \leq 2w_0) \\ 0 & (d > 2w_0), \end{cases} \tag{5.1.2}$$

where d is the distance between adjacent pulse centers, and w_0 is the $1/e^2$ beam radius. η takes a value of 100% when the beam is stationary, i.e. $d = 0$, and 0% when the two pulse centers are spaced further apart than the beam diameter. The intermediate cases are linearly interpolated. It should be noted that the parameter, while used for arbitrary pulse shapes, makes strict physical sense only for the case of a spatially flat-top pulse, as η does not properly account for spatial energy distributions.

While most grooving processes are tuned through trial-and-error, there have been efforts to replace this process with numerical simulations. Traditional calculations of grooving depths have mostly been done for metals with high-power CW or longer pulsed lasers (such as CO_2 lasers or Nd:YAG), owing to the industrial significance of this combination. In such cases, the relevant physics usually centers on the thermodynamic properties of the problem [143]. However, the average powers (hundreds of watts in the case of [143]) are far displaced from what is usually available for ultrafast pulsed lasers.

For lower average powers, for example Canteli *et al.* have modeled the case of laser scribing of the transparent conductive oxides (TCOs) indium doped tin oxide (ITO) and aluminum doped zinc oxide (AZO) films with a 12 ns pulsed-laser source at 355 ns. Because the photon energy is higher than the band gap of these two materials, single-photon absorption dominates and the ablated depth follows a logarithm of the incident fluence [106]. In their work, a linear combination of the ablated depth for each pulse, scaled by their respective fluence, yielded good agreement with experiment for moderate overlaps below 90%. Correspondingly, they found that incubation was insubstantial up to 11 pulses, which is the maximum approximate number of pulses incident upon a spot on the sample for the overlap value.

In dielectric materials not excitable by a single photon, the modeling of crater profiles for a *single* pulse is still considered a difficult task, mostly owing to the highly non-linear nature of the initial electron excitation. Hence, work on multiple-pulse morphology modeling has been comparatively limited. A pioneering early work by Vázquez de Aldana *et al.* have worked to model the laser grooving situation for fused silica [92, 144]. In their model, they calculate the local electric fields incident upon the material through the Maxwell equations, and model the corresponding electron excitation through a single rate equation model. They succeed in recreating many qualitative features of the grooving process, such as the evolution of the groove from a U-shaped profile to a V-shaped profile, and the eventual saturation of groove depths due to diffraction effects. However, quantitative agreement was not achieved, and the evolution rates did not match with the experiment [92].

A more recent work by Sun *et al.* have conducted similar research regarding the grooving of alkaline earth boro-aluminosilicate glass (Corning Eagle XG®) [145, 73, 146], a major change from the work of Vázquez de Aldana *et al.* being a reduction in numerical cost allowing for simulation of picosecond pulses. Sun *et al.* achieved much closer quantitative agreement with experiment, not only for the groove morphology, but also for the distribution of surrounding damaged regions. It should be noted that the range of pulse numbers simulated was limited to 10 (or 90% overlap) and less than the range studied by Vázquez de Aldana *et al.* (up to 55) in their study.

5.1.3. Open questions

In previous studies on the laser grooving of materials, changes of the optical properties of the sample itself is not considered. While this does not play a large effect in cases of materials where incubation effects are weak, or where pulse numbers are relatively small (or conversely very large), this is not always the case. A notable example is the laser processing of sapphire. In sapphire, damage incubation is known to cause material removal rates to vary by orders of magnitude [19]. These phases are especially pronounced for picosecond laser pulses [118].

There remain several non-trivial questions regarding the incorporation of incubation effects into the laser grooving situation. In laser grooving, the local incident fluence of a spot varies pulse-to-pulse. How do we translate the "number of pulses" required for traditional incubation arguments to this system? As aforementioned, incubation studies mainly take into account situations where the pulse energy is below the threshold. How do we deal with a real processing situation, where each pulse is well above the threshold? How can incubation effects be gauged in this system?

As a first step towards understanding how incubation effects laser grooving, we seek to derive empirical scaling relationship between the incident pulse energy and overlaps with the ablated depth. We gauge such effects through simplified arguments, and derive analytic relationships regarding the two input parameters and depth. Lastly, we create grooves with a picosecond laser on sapphire, and compare the results with that predicted by our model.

5.2. Model

5.2.1. Empirical incubation model for laser grooving

We model the essence of the laser grooving setup with incubation effects as follows. We think of an infinite train of pulses traveling along a one-dimensional path with spacing d, as seen in Fig. 5.2.1. We focus on a certain point, coinciding to the center the 0-th pulse, as indicated by the orange arrow in Fig. 5.2.1, and calculate behaviors of the ablated depths depending on the inter-pulse spacing and pulse energies of at this point. We do this by first calculating the absorbed total energy at this point, and then assume that this energy and ablated depth have a one-to-one correspondence. By rescaling experimental data in terms of this absorbed energy, we should be able to derive a single universal curve describing the depth as a function of the scaled irradiated energy.

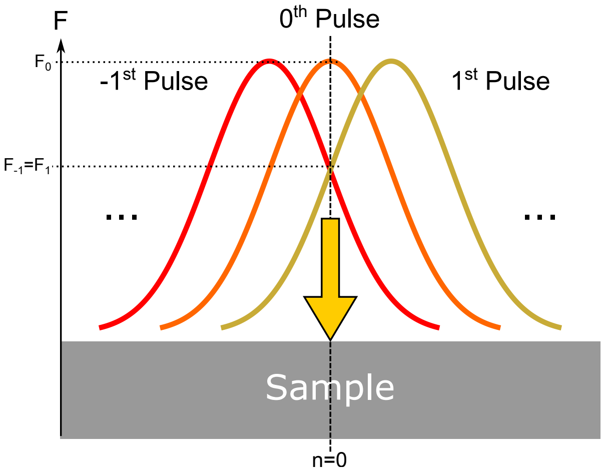

Figure 5.2.1.: Overview of the model calculation situation, where a train pulses labeled from $n = -\infty$ to $+\infty$ spaced d apart are sequentially incident upon the sample. The center of the 0-th pulse is taken as the origin. A local fluence of F_n is incident on the sample surface from the n-th pulse.

It should be noted that relationships between absorbed energy and ablated depth is a non-trivial problem. In the case of sapphire, it has been shown that ablated depth to pulse energy relationships based on Lambert-beer type (logarithmic) penetration depths of the local incident fluence fail to explain experimental results [6]. In addition, most models deal with *single pulse* ablation depths, and no models exist to our knowledge which deal with damage incubative situations, where the correspondence between incident pulse energies and ablated depths can vary by an order of magnitude even for the same pulse energy [19]. As the essence of incubation effects is believed to reside in the non-linearity of the absorption, and not in the penetration depths of absorbed energies, we simplify the connection between ablated depth and absorbed energy density to a relationship between their total values. We assume that key nonlinearities reside in *how much* energy is absorbed.

In our model, we restrict discussions to pulses with energies moderately above the damage threshold, a regime in which, while initial processes are highly nonlinear, the majority of the energy absorption is done nearly metallically by the excited free-electron plasma via inverse bremsstrahlung [12]. Thus, we postulate an effective absorption coefficient a_n for the n-th incident pulse with incident local fluence F_n, and assume that the material absorbs energy $F_n \cdot a_n$ of the pulse. We include incubation effects into a_n through the following equation:

$$a_{n+1} = a_n + \beta(a_s - a_n)F_n/F_0 \tag{5.2.1}$$

Here, a_s is some saturation absorption coefficient, F_n is the local incident fluence of the n-th pulse, F_0 is the peak fluence (i.e. the peak fluence of the 0-th Gaussian pulse), and β is an incubation strength factor. In the case of constant fluence, (5.2.1) yields an asymptotic increase of the absorption to a_s; β determines how fast the absorption coefficient approaches this asymptotic value. As we are only concerned with scaling relationships and not on absolute values, these parameters are taken with arbitrary units. It is also experimentally known that the incubation behavior which causes a gentle-to-strong ablation transition in sapphire has a weak pulse energy dependence for picosecond lasers, depending more on the number of incident pulses [147]. Thus, the second term is normalized by F_0 to reflect this weak pulse energy dependence.

A more general form of equation (5.2.1) would consider several terms with several β and a_s, each corresponding to incubation processes with their characteristic physics (for example, that of electron relaxation or heat diffusion). As the creation of stable color centers is the dominant incubation process within the timescale of typical laser repetition rates, we take these other β to be negligible, arriving at the single β form of above.

With this model, the total amount of energy absorbed at the monitored point can be expressed as:

$$E_{tot} = \sum_{n=-\infty}^{\infty} F_n \cdot a_n \tag{5.2.2}$$

We expect the depth to to have a one-to-one correspondence with this total value. We take the summation from $n = -\infty$ to $n = \infty$ to make the problem analytically easier to solve, although the pulse number is finite in reality. This treatment is valid because pulses with large n contribute little to the total sum derived by a more rigorous summation of finite pulses with local fluences above a threshold value. We use spatial Gaussian pulses $F_n = F_0 \exp[-2(nd/w)^2]$, where w is the $1/e^2$ beam intensity radius. For simplicity, we rescale distance in terms of w, i.e. we set $w = 1$ and make d unitless.

5.2.2. Solutions

The simplicity of equation (5.2.2) allows us to calculate E_{tot} analytically for two limiting cases. The first one is the *quasi-static absorption limit*, where changes in a_n are minimal near $n = 0$. This occurs when incubation is either very strong ($a_0 \approx a_s$) or very weak ($a_s \approx a_{+\infty}$). In such cases we can set $a_n = Const.$, and the total absorbed energy simply becomes a discrete summation along a Gaussian profile. Consequently,

$$E_{tot} \propto \sum_{n=-\infty}^{\infty} F_n = F_0 \cdot \vartheta_3(0, e^{-2d^2}), \tag{5.2.3}$$

where

$$\vartheta_3(z, q) \equiv \sum_{n=-\infty}^{\infty} q^{n^2} e^{2niz}, \tag{5.2.4}$$

is the Jacobi theta function of the third kind [148]. While the above is a rigorous equality, one can transform the theta function (a summation of Gaussians) in Eq. (5.2.3) as:

$$\begin{aligned} \sum_{n=-\infty}^{\infty} & \exp[-(\sqrt{2}d)^2 n^2] \\ & = \frac{1}{d}\sqrt{\frac{\pi}{2}} \sum_{m=-\infty}^{\infty} \exp\left(-\frac{\pi^2 m^2}{2d^2}\right), \end{aligned} \tag{5.2.5}$$

where we have utilized Poisson's summation formula [149]. When $d \ll \pi/(2\sqrt{2}) \approx 1.1$ (or $e^{-\pi^2/(4d^2)} \ll 1$) as is typical in grooving, the summation of the exponential on the right hand side of the equation quickly decays to zero for nonzero m, and we see the value become proportional to $1/d$. The total absorbed energy in Eq. (5.2.3) can then be seen to scale as F_0/d.

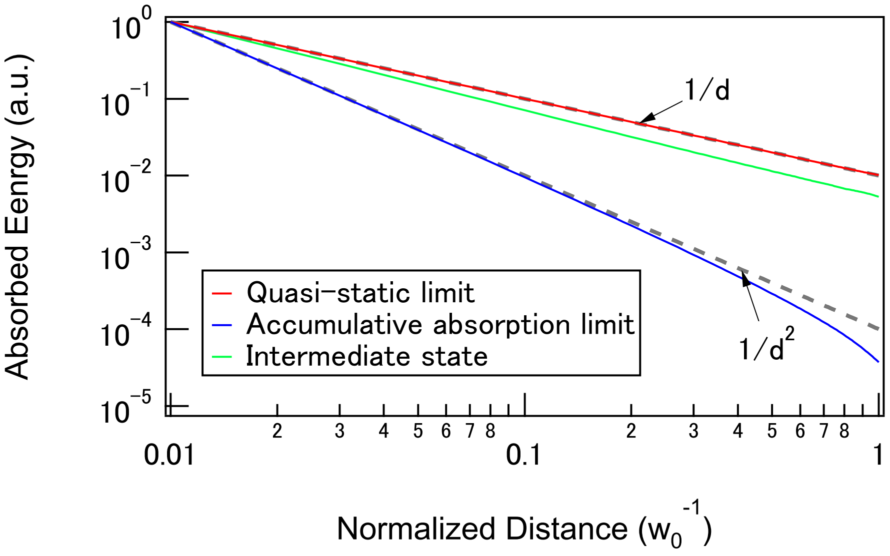

Figure 5.2.2.: Calculated total accumulated energy for (red) the quasi-static limit, (blue) the accumulative absorption limit, and (green) an intermediate set of parameters ($a_0 = 0.01, a_s = 1, \beta = 0.016$). Values are normalized to 1 at $d = 0.01$. The $1/d$ scaling behavior for the quasi-static limit and the $1/d^2$ scaling behavior (labeled dashed lines) for the accumulative absorption limit can be clearly observed.

The second limiting case is the *accumulative absorption limit*, when the strong absorption change near $n = 0$ takes place (in cases where $a_s \gg a_0$ in Eq. (5.2.1)):

$$\begin{aligned} E_{tot} &\propto \sum_{n=-\infty}^{\infty} \left(F_n \sum_{m=-\infty}^{n-1} F_m / F_0 \right) \\ &= \frac{1}{2F_0} \left[\left(\sum_{n=-\infty}^{\infty} F_n \right)^2 - \sum_{m=-\infty}^{\infty} F_n^2 \right]. \end{aligned} \tag{5.2.6}$$

By employing the Jacobi theta function and approximation for $d \ll \pi/(2\sqrt{2})$ as before:

$$\begin{aligned} E_{tot} &\propto \frac{F_0}{2} \left([\vartheta_3(0, e^{-2d^2})]^2 - \vartheta_3(0, e^{-4d^2}) \right) \\ &\approx \frac{F_0}{2} \left(\frac{\pi}{2d^2} - \frac{\sqrt{\pi}}{2d} \right). \end{aligned} \tag{5.2.7}$$

As the first term dominates for small d, total absorbed energy which scales as approximately F_0/d^2.

In Fig 5.2.2, calculations for the two analytical results (red and blue), and a numerical calculation for a case in between (green; parameters $a_0 = 0.01$, $a_s = 1$, $\beta = 0.016$) are shown, where the total absorbed energy at $d = 0.01$ is normalized to 1. We can clearly see the $1/d$ and $1/d^2$ dependencies (dashed lines) for the quasi-static absorption limit and

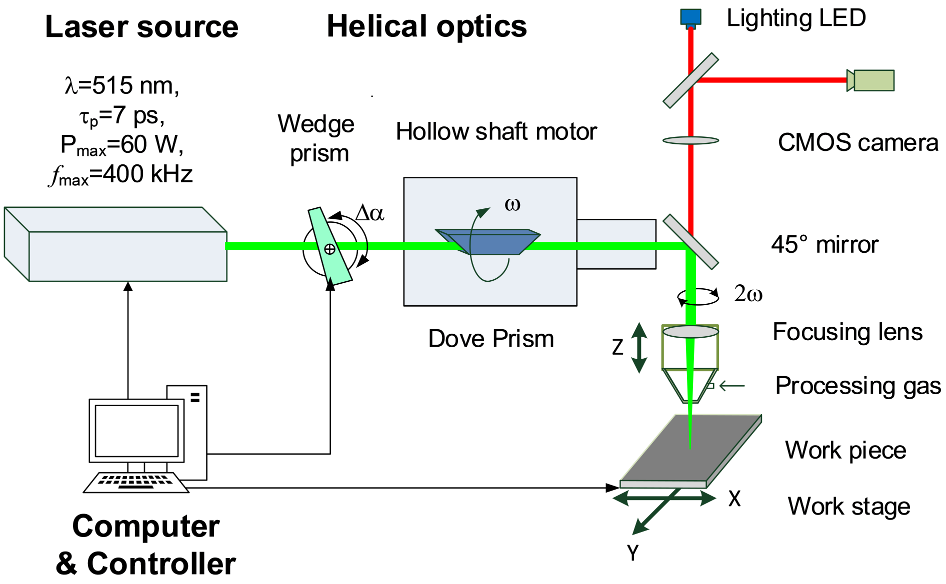

Figure 5.3.1.: Experimental Setup.

the accumulative absorption limit, respectively. Discrepancies at higher d originate from the small d approximation employed during the derivation of the scaling relationship. For parameters not at the two limits, the absorption scaling characteristic behaves in the middle of the two, bounded by the two limiting cases.

5.3. Experiment

We next introduce the experiment to verify our predicted scaling behaviors. It is often difficult to explore a certain facet regarding ablation effects systematically, as many competing processes occur with different governing physics. To overcome these difficulties, it is essential to tailor a purpose-made experiment in order to isolate the physics under study: that is, in our case, incubation effects. Here, we first introduce our experimental setup and our reasoning for such design, and later discuss the potential effects of other competing processes.

Differences in ablation processes originating from incubation effects should be most pronounced with differing pulse overlaps. In order to systematically and stably create single scan grooves at different pulse spatial overlap, a helical drilling setup is utilized, as shown in Fig. 5.3.1 [150, 151, 152, 153]. In this setup, a rotating Dove prism rotates the laser path into a circular spatial trajectory, the angular speed equal to twice the mechanical rotation speed of the Dove prism. By focusing this laser onto the sample surface, it is possible to drill circular paths onto the sample surface. In our experiment, we utilize this setup to systematically alter the overlap of subsequent pulses in an easy to characterize, compact circular track on the sample surface. A wedge plate is also present before the Dove prism system, and by adjusting its angle, the rotational radius of the laser beam (or helical radius: r_h) at the focus can be tuned. By changing the rotation speed of the Dove prism or the position of the wedge plate, it is possible to achieve various angular speed and trajectory radii. From the circumference $2\pi r_h$, laser frequency f, and the time it takes for the laser to make one rotation T_{rot}, it is possible to calculate the average number of pulses per unit length $p_{pl} = f \cdot T_{rot}/2\pi r_h$ along the ablated grooves. The degree of overlap η can be calculated from p_{pl} as:

$$\eta = 1 - \frac{1}{2w \cdot p_{pl}}, \tag{5.3.1}$$

where w is the beam radius.

Another factor in varying incubation effect behavior is believed to be the laser pulse energy. This can be controlled by an integrated power attenuator in the laser system. The laser system used in the experiment is a 515 nm central wavelength picosecond laser system (TRUMPF, TruMicro 5270) with a pulse duration of 7 ps. The maximum pulse energy is 150 μJ, and the laser is used at 50 kHz for the experiments. On-off switching of the laser is controlled by an external computer.

The rest of the ablation setup is standard. The rotating laser beam from the helical drilling setup is focused onto the sample surface by a 60 mm focal length processing lens equipped with a custom nozzle to allow for on-axis application of processing gasses. In the experiment, compressed air at 2 bars pressure is used to prevent contamination of the optical system from processing debris. The focus position is adjusted by moving the processing lens, mounted on a linear stage. Real-time monitoring of the sample is possible from a focus-calibrated, coaxial camera illuminated by a red LED. The laser spot size at the focus is determined in-situ before each experiment by an ablated area extrapolation scheme often used to determine laser damage thresholds [108]. Such measurements yield a slightly elliptical laser spot, with major and minor axis radii of 9.9 and 9.3 μm. When a radius value is required in the analysis, the average of the two values is used.

Using this setup, we ablate a sapphire plate, with the c-plane oriented on the surface ($\geq$99.99% purity, 2-inch diameter; Siegert Wafer). The thickness of the wafer is approximately 430 μm, with both front- and back-side polishing. The wafer is attached to a motorized xy-stage by a custom vacuum suction holder to ensure high mechanical stability during processing.

The actual processing conditions are as follows. The rotation speed of the Dove prism is varied from 120 revolutions per second (rps) to 10 rps in increments of 10 rps. To increase the range of overlaps available, processing is done at two helical radii of 31 μm and 65 μm. These values are measured after the experiment from the damage tracks on the sample surface. At each rps, in order to restrict the ablation to a single revolution, the laser is programmed to turn on for 1/(2·rps) seconds, which is the amount of time it takes for the laser to make one optical revolution. Due to latency in the laser switching, the laser is not at full power for the duration of the programmed time, but slightly lower directly after starting and before stopping. These portions are omitted from analysis. Each ablated groove in the experiment is done at new locations on the sample surface.

Grooves are translated at least 50 μm away edge-to-edge to reduce cross-contamination effects, such as debris and thermal-induced stress accumulation.

After the experiment, samples undergo ultrasonic cleaning in an ethanol bath for 30 minutes to remove residual debris. After samples are cleaned, their morphologies are observed under a laser scanning microscope (LSM; Keyence, VK9700). With this, the height profile can be measured with sub-micron vertical resolution. Due to decreasing brightness in high aspect ratio holes, the range of the depth observable by the LSM are limited to around 20 μm. Only holes where the whole hole is within resolution are analyzed, which consequently restricts analysis to situations where all grooves are an order of magnitude shallower than the Rayleigh length of the processing beam. Hence, defocusing effects are ignored in the analysis.

In quantitative analysis, we focus on the maximum depth of the ablated grooves. The reasoning for this, as opposed to analyzing the volume or whole cross section, is mainly to avoid effects of changing groove shapes. The grooves are roughly U-shaped in our experiments; the light in the groove center sees a relatively flat surface. This allows us to ignore differences caused by an angled projection of the incident fluence, and diffraction effects, which are more pronounced at curved (at scales relative to the wavelength) surfaces. Furthermore, we would like to avoid the chipping and/or recast that is predominantly seen at the crater edges, which is mostly irrelevant to the physics under discussion.

Lastly, we would like to comment on heat accumulation and plasma shielding as possible competing factors affecting morphology. Wide-spread heat accumulation effects, as in dependence of ablation on the locality of the groove trajectory, is seen to have little significance in our geometries, as the two tested helical radii conditions yielded similar results, as will be shown in the following section. While it is difficult to completely rule-out more local heat accumulation, we gauged its significance by conducting multiple-rotation experiments, where two to five beam rotations were done on the same trajectory. We found that as long as the total incident pulse numbers were similar (for example, a single rotation compared to two rotations at twice the speed), the morphologies were as well. If local, subsequent-pulse heat accumulation were significant, a more dramatic change should be observable, as two order of magnitudes of time are different for the pulse-to-pulse interval seen by the material (during which heat dissipation can occur) in the two cases. Plasma shielding is mitigated in our experiment due to the moving laser (i.e. the laser spatially avoids developed clouds), as well as by our choice of wavelength, which is more robust to scattering compared to longer infrared wavelengths. The aforementioned multiple-rotation experiments also help rule out plasma shielding as a significant player, as shielding should also be dependent on the spacial order in which grooves are ablated. As a final remark, it should also be noted that fixing the repetition rate of the laser is also conscientious, as both these competing processes are heavily dependent on inter-pulse delays. This underlies our choice to vary the helical drilling conditions as opposed to the laser repetition rate to achieve varying pulse overlaps.

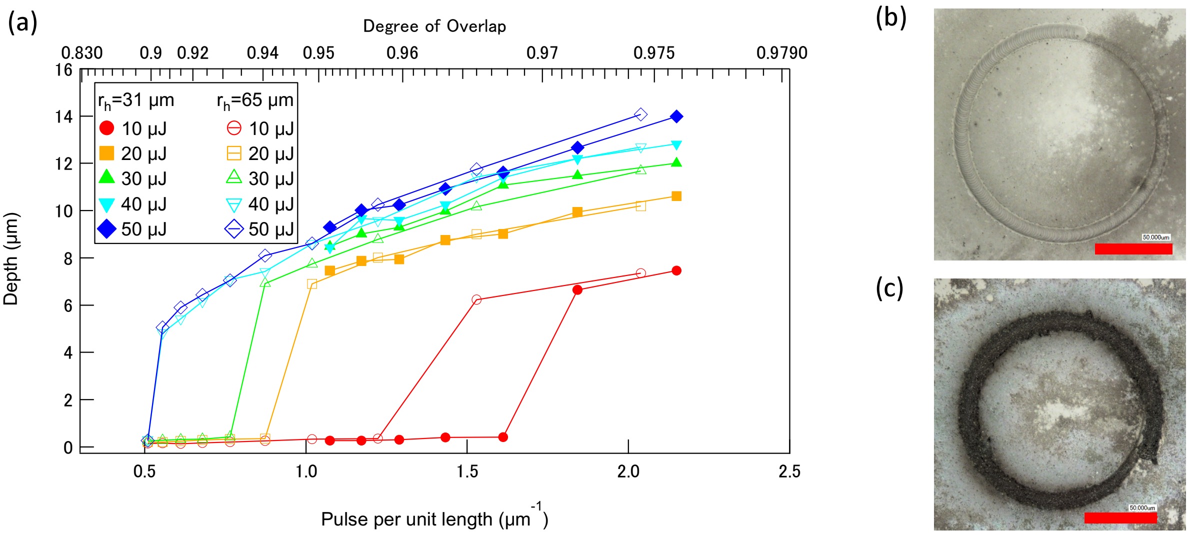

Figure 5.4.1.: (a) Plot of measured deepest depth as a function of pulse per unit length. Standard deviation of the depth points are of the order of the marker size. Microscope images of: (b) a typical ablation track in the gentle ablation phase at 20 μJ, 0.68 p_{pl} ($\eta = 92.3\%$), and $r_h = 65$ μm; (c) a typical ablation track in the gentle ablation phase at 20 μJ, 1.22 p_{pl} ($\eta = 95.7\%$), and $r_h = 65$ μm. Red scale bars in images correspond to 50 μm.

5.4. Results

The deepest depth of the grooves as a function of p_{pl} is shown in Fig. 5.4.1(a). Corresponding values of η are shown on the upper scale of the figure. It can be seen that the helical radius has little influence on the total achieved depth, apart from some discrepancy for the 10 μJ data near 1.5 p_{pl}, the reason explained later.

It is clear from the graph that there are two distinct regimes of ablation in sapphire. These are a shallow ablation regime characterized by a smooth morphology (Fig. 5.4.1(b)), and a deep ablation regime characterized by a fractured morphology (Fig. 5.4.1(c)). These two regimes are what is referred to as “gentle” and “strong” ablation in the literature [118, 19]. Gentle ablation, often associated with melting and vaporization, or in the case of ultrashort pulses, coulomb explosion [19], is favored in our experiment when pulse energies are low and overlap between pulses is small. On the other hand, strong ablation, associated with strongly thermal processes such as material phase explosion [154], takes place at high pulse energies and when there is considerable overlap (exceeding 90%) between pulses. A crucial factor in the transition from gentle to strong ablation is believed to be damage incubation [118]. An increase in energy absorption through incubation allows for a later pulse to gain the critical energy needed to initiate strong ablation processes. The probabilistic nature of the defect accumulation is most pronounced in the transition regime (the sudden jump in the depths in Fig. 5.4.1(a)), which we believe to be the origin of the discrepancy for the 10 μJ data in Fig. 5.4.1(a). In this regime, grooves with mixed strong and gentle ablation regimes could also be observed.

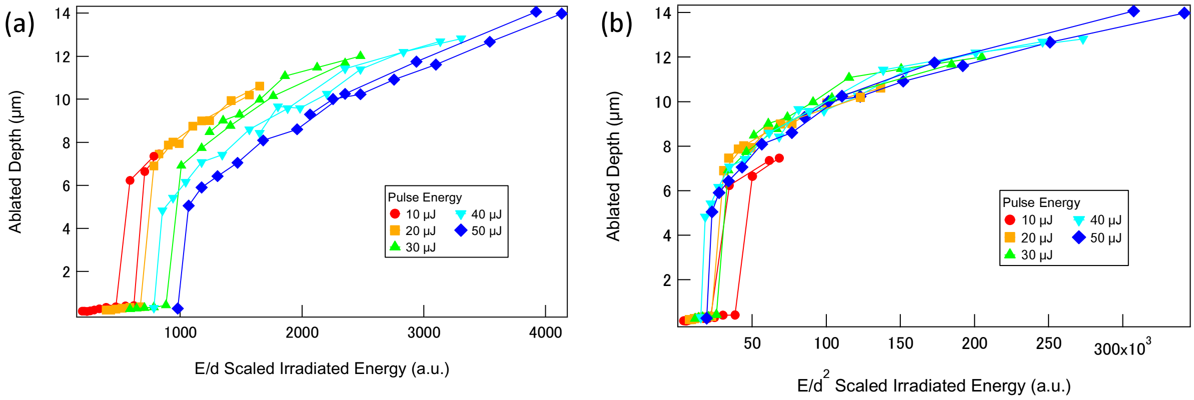

Figure 5.5.1.: (a) Quasi-static absorption scaling (E_p/d) and (b) accumulative absorption scaling (E_p/d^2) for the experimental data. The latter shows better agreement along a broad range of pulse energies, signifying the strong role that incubation plays.

5.5. Discussion

To analyze our experimental data in the context of our newly formed model, we first scale our ablated depth results according to the quasi-static scaling behavior, which is physically equivalent to plotting ablated depth against the incident energy linear density, effectively ignoring incubation effects. The result of this rescaling is shown in Fig 5.5.1(a). It can be seen that the results are unsatisfactory in achieving agreement among different pulse energies, with a highly pulse energy dependent discrepancy between data with the same E_p/d ratio.

Next, we scale the data according to the accumulative absorption scaling prediction of E_p/d^2. Results of such rescaling is shown in Fig. 5.5.1(b). Especially when compared with quasi-static scaling, great agreement is observed with the experimental results in the range of 20 to 50 μJ. The result is consistent with the strong incubation effects seen in laser processing of sapphire. Because the absorption characteristics of the material change dynamically in the accumulative absorption situation, it is better suited to model the evolving ablation behavior in sapphire. A noticeable deviation is seen for the 10 μJ data from the other data, possibly attributed to a couple of factors, such as the relatively low pulse energy in disagreement with our initial assumption of high pulse energy, or to the fact that the high pulse numbers saturates incubation, i.e. a more proper fitting with a non-limiting case (of currently an unknown analytical form) may then yield even better agreement. The accuracy of the depth scaling despite the highly simplified arguments regarding energy absorption mechanisms and the subsequent material ablation phenomenon displays just how dominant incubation effects are in comparison to other factors in this shallow grooving regime.

From a microscopic standpoint of the physics involved, the relevant defects associated in sapphire are believed to be neutral and charged F-centers: oxygen vacancies in the sapphire lattice with one (F^+-center) or two (F-center) trapped electrons. Creation of such defects may be facilitated by vacancy-interstitial pair formation, or else by emission of certain atom types from the material surface [59, 155]. The formation of color centers in sapphire has traditionally been studied under pulsed-electron and neutron irradiation [156], but has recently been directly observed in ultrashort pulse-laser processed sapphire by photoluminescence excitation [157]. Electrons captured in F-centers have relative energies 6-7 eV below the conduction band minimum [158], and are easier to excite than electrons in the valence band (requiring around 9 eV), considering the multiphoton nature of the initial excitation in ultrashort pulsed-laser excitation. This slight difference in optical absorption is believed to be amplified by avalanche ionization mechanisms, which is highly sensitive to seed electron density, and allows the damaged material to absorb more of the incident energy. The $1/d^2$ dependence of the accumulative absorption case can be thought of as two increasing mechanisms working in tandem: a $1/d$ contribution from increasing the energy density, and another $1/d$ contribution from increasing defect concentrations.

A last remark on timescales should be made. Through interferometry [16] and double-pulse measurements [159], the free-carrier like response of excited electrons in sapphire has been shown to have lifetimes in the sub-nanosecond to single-nanosecond range. Additionally, from photoluminescence excitation measurements in ref. [160], luminescence lifetimes of F-centers were determined to be 35 ms, while lifetimes of F^+-centers were shorter than 7 ns. The 50 kHz laser used in the current experiment has a 20 μs inter-pulse spacing, and thus, residual electron excitation is only affected by residual F-center excited electrons. As this lifetime is long, and provided the ignored heat accumulation effects can still be ignored, similar scaling would be expected for similar kHz to MHz lasers used in typical ultrashort pulsed-laser processing. Outside this range, different transient inter-pulse absorption characteristics will come into play and the current results will not trivially hold. For example at GHz repetition rates, it should be possible to re-excite “free” electrons before significant relaxation, which will make subsequent energy absorption notably different.

5.6. Summary

In this work, we have focused on qualifying the effects of damage incubation on the ablated morphology of a material, in this case, sapphire. We create a phenomenological model considering damage incubation and subsequent energy absorption changes. We derive analytical expressions which, for certain common conditions, reduces to simple scaling relationships explaining ablated depths in terms of the incident pulse energy and overlap. To verify our predictions, we perform a purpose-made experiment to best isolate incubation effects in a laser grooving. We see clear morphological evidence of incubation-induced changes in the morphology, and depth dependence which is nonlinear to the incident total energy density. We succeed in explaining this observed ablated depth behavior for varying pulse energies and overlaps in the context of our model.

The arguments used to derive the new scaling relationship are highly general, and thus should also hold validity for other materials. While beyond the scope of the current thesis, it may be possible to create a simple “incubation parameter” to properly describe the functional form of the non-limiting behaviors, thus allowing similarly general arguments for a broader class of materials not just behaving in either of the two limiting regimes. It may also be interesting to link the relationship between the traditional incubation parameter for damage incubation below the single pulse threshold with that of the current damage incubation above threshold. Related to the above, exploration of the physical mechanisms of the microscopic processes governing incubation and how they manifest to the observed macroscopic consequences may lead to enhanced understanding of ultrafast ablation dynamics, leading to greater process control.

This work not only helps in furthering our understanding of energy absorption mechanisms in the multiple-pulse regimes for future modeling, but also provides a highly simple tool to analyze and organize experimental results.

Chapter 6.

Characterization and Utilization of Morphology Evolution

In the previous chapter, we introduced damage incubation and its effects on the morphology of materials during multiple-pulse ablation. With repeated irradiation, however, these effects become less prominent, and what then becomes a controlling factor is the morphology itself. In this chapter, we introduce the relative processes limiting achievable ablation depths, and introduce an application of this process to fabricate functional sub-wavelength structures on material surfaces.

6.1. Introduction

In industrial settings, there is a high demand for high aspect-ratio and low taper angle holes and grooves. High aspect-ratio holes allow for miniaturized structures such as through-hole vias, which will be essential for stacked semiconductor structures essential to future processor integration [161]. High-aspect ratio grooves (or cuts) minimizes material loss in cutting procedures, cutting costs. Thus, it has always been an important research goal to further the machining capabilities of laser processing in these regards.

Limits on achievable depths have been well-studied for holes. For example, an early work by Varel *et al.* studied in detail the multiple pulse micromachining (percussion drilling) characteristics of quartz when irradiated with 120 fs pulses centered at 790 nm with a repetition rate of 1 kHz [162]. Holes were found to generally change from a tapered cone-like profile to a linear channel-like formation. The former shape is dominated by the fluence profile of the incident Gaussian pulse, while the latter is believed to be due to propagation effects of the pulse affected by the tapered entrance [163]. Hole depths saturate after a certain depth (typically around 1 mm), the main cause of which they attribute to material ejection limitations. Similar cone-like profiles have been observed for laser grooving [144]. Various works have focused on improving the possible depths and removing taper angles with methods beyond changing pulse energies, for example, by changing the ambient atmosphere [162], using liquid assisted material ejection [164], scanning pulses vertically [165], combining with etching [165, 166], changing repetition rate (including so-called “burst mode” implementations) [165], or tailoring the profile of the pulse itself, usually into Bessel beams or similar profiles with large focal lengths [167, 168, 169].

On the other hand, the taper angles and morphologies realized in the early stages of drilling are highly reproducible [163]. Whereas other limiting factors are often environment dependent, the tapering angle is mostly a geometrical effect, only dictated by the local fluence. As will be elaborated later, it serves as a robust and natural limit for a laser/material combination. Recent works by Schütz *et al.* have suggested implementing these natural formations as ways to create tapered protrusions on surfaces [170]. Through such methods, structures can be created in a deterministic manner, particularly important in large-area structuring applications, where it becomes hard to control laser parameters and scanning for long durations.

In this chapter, we explore the possibility of structuring high resistivity silicon, a material commonly used in microwave and terahertz wave optical components. We experimentally explore the trends predicted by Schütz *et al.*, and utilize these results to manufacture anti-reflection patterns for the THz wavelength scale on a silicon plate.

6.2. Principles

As a natural limiting factor of ablation Schütz *et al.* propose the concept of projected fluence. During ablation processes, holes are created with slopes. In the case of beams illuminating a slanted surface, the fluence at the material surface becomes smaller due to the larger surface area. The situation is depicted in Figure 6.2.1. Here, we assume that the Rayleigh lengths are long enough to ignore the effects of defocusing.

The flank angle is defined as the angle that the material surface makes with regards to the beam, where 0 degrees corresponds to normal incidence, as shown in Figure 6.2.1a. A flank angle of α is depicted in Figure 6.2.1b. Given an initial incident fluence of F_{in},

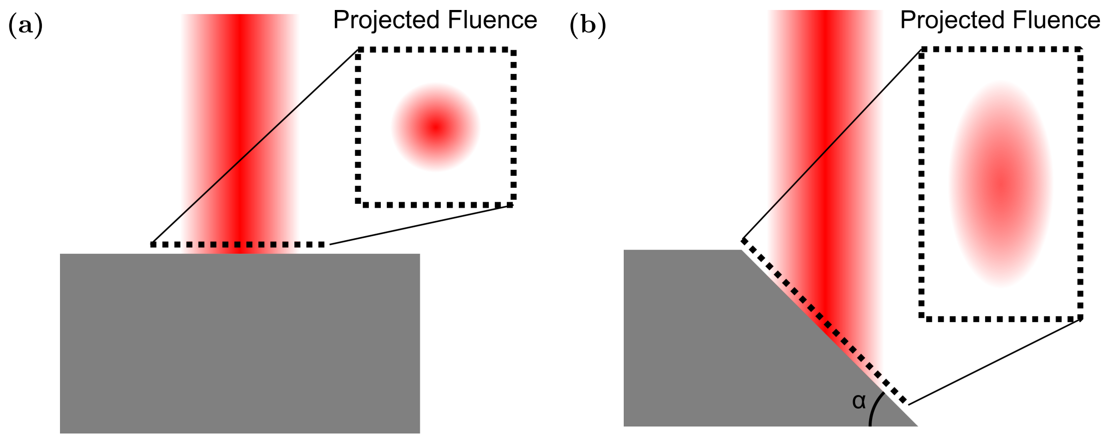

Figure 6.2.1.: Projected fluence at flank angles of (a) 0 degrees and (b) α degrees.

the projected fluence for a flank angle of α becomes

$$F_{pr} = F_{in}\cos(\alpha). \tag{6.2.1}$$

During ablation, the material first sees a pristine material surface as depicted in Figure 6.2.1a. As ablation continues, slopes form naturally between non-ablated regions and ablated regions. When these slopes cross a flank angle α_{crit} where $F_{pr} < F_{th}$, F_{th} being the multiple-pulse damage threshold of the material, ablation stops at that region. Assuming that slopes increase gradually during processing, repeated scanning of a laser across a region should allow for the creation of deterministic angled structures without tuning of scanning patterns or parameters. For example, for the creation of 60-degree angled structures, machining with a laser fluence of twice the damage threshold should be sufficient.

6.3. Experimental setup

We take a moment now to introduce the experimental setup utilized to experimentally explore the projection-limited properties of ablation. The optical setup is shown in Figure 6.3.1, similar to the one used for the previous experiments. The output from a Yb:KGW based regenerative amplifier (Light Conversion, PHAROS-SP) is input to a pair of polarizers to adjust its power. The light is then focused by a single plano-convex lens with focal distance of 50 mm. The pulse duration of the laser is 190 fs, the central frequency is 1028 nm, and the repetition rate is set at 6 kHz. Laser on-off is controlled by a mechanical shutter.

The focal position and the beam characteristics at the focus was determined by knife-edge method, as we are not too concerned with the absolute fluence. A knife was mounted onto the sample mount surface, and the transmitted signal was measured by a photodetector behind the stage setup, as shown in the dotted boxed region in Figure 6.3.1. The beam radius at the focus was found to be approximately 8 μm. We use this value

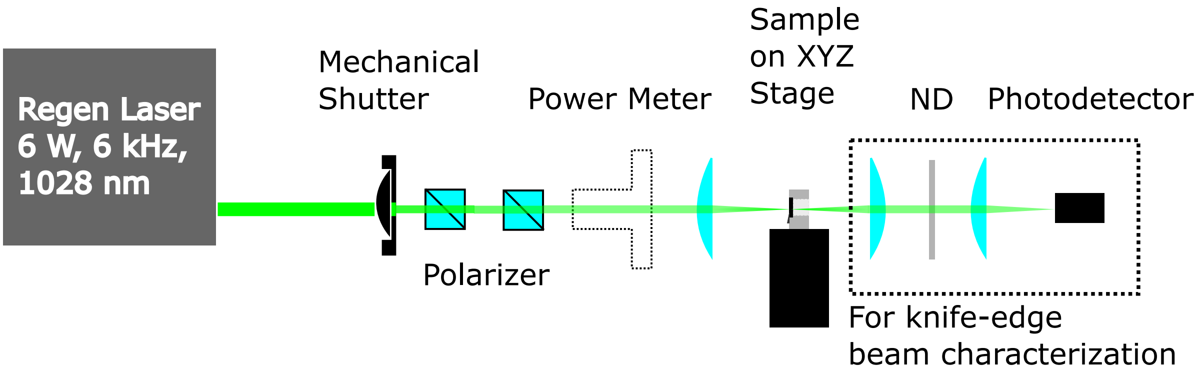

Figure 6.3.1.: The optical setup utilized for processing.

for all subsequent conversions between average power or pulse energy to fluence. All processing was done with the sample surface at the laser focal position.

By controlling the mechanical XYZ stage, arbitrary patterns could be inscribed onto a silicon surface. For grooving experiments, silicon with resistivity of $> 0.01\ \Omega$ were used, while THz samples were made with high-resistivity silicon (> 10 kΩ). No significant differences in the ablation characteristics could be observed between the two materials in the multiple-pulse ablation schemes of the current experiment. This is in agreement with literature, where negligible differences in the infinite-pulse ablation threshold of silicon were found for samples with different N- and P-type dopant concentrations [171]. Thicknesses of the processed silicon ranged from 300 or 500 μm for single-side processing, to 700 μm for double sided processing. In either case, samples were significantly thicker than the processed depths. Again, sample thickness was found to lead to no real differences in the ablation outcome.

After laser processing, all samples were cleaned in a bath of ultrasonic water for 3 minutes to remove processing debris. Profiles were measured by a laser scanning microscope (Keyence, VK-X260).

6.4. Characterization of silicon ablation

6.4.1. Processing algorithm

In order to verify the flank-angle limited properties of ablation, we make grooves on the surface of silicon. To minimize recast and propagation effects, as well as the specifics imposed by the Gaussian spatial profile of the beam, we create an enlarged single groove with several offset laser lines on the sample surface. The situation is shown schematically in Figure 6.4.1. By moving the sample relative to the stationary laser via mechanical stage, the laser is "scanned" across the surface of the sample. Scanning speed is constant

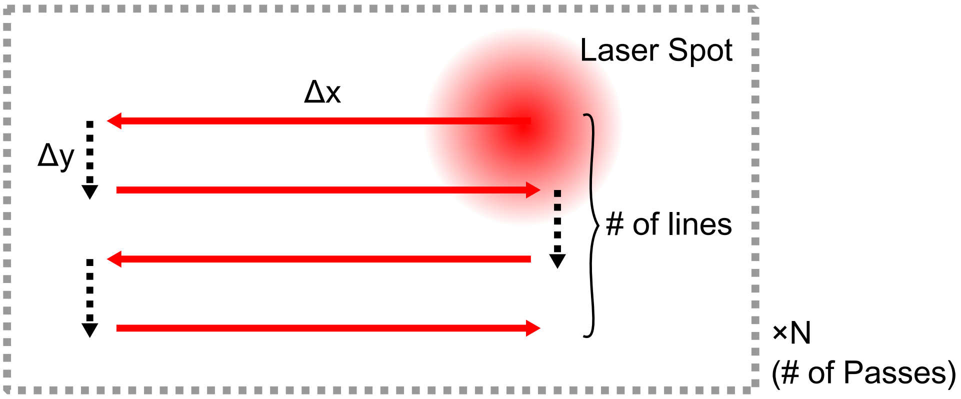

Figure 6.4.1.: The grooving scan schematic. Note that in the actual process, the sample is scanned relative to the laser.

at 1 mm/s. Red lines show the trajectory of the laser when on (mechanical shutter is open), whereas the black dotted lines show sections where the laser is off (mechanical shutter is closed) and the sample is translated to move to the next sequential “line”. One macroscopic groove consists of a finite *number of lines*, chosen to be an even number between 4 and 10. The length of the individual lines (Δx) is typically a couple mm, while the offset of the lines (Δy) is taken as a value smaller than the beam radius so as only one macroscopic groove is created. While the depth and widths of the grooves *are* sensitive to the choice of Δy, the asymptotic trends regarding the flank angle were found to be the same (as long as the values were smaller than approximately the beam radius). Furthermore, within these limits, relatively lower values of $\Delta y \lesssim 6$ μm were found to result in more stable results. Thus, we introduce only the results for $\Delta y = 4$ μm, for simplicity. To achieve greater depths , the above grooving process is repeated. We define the *number of passes* as this repetition number.

Multiple different groovees were created on the same silicon sample. Each groove was spaced at least 100 μm apart center-to-center to avoid cross-contamination.

6.4.2. Results

In Figure 6.4.2, laser microscope images for grooves made by processing at an average laser power of 30 mW (pulse energy 5 μJ or fluence 5.0 J/cm^2) with 4 lines is shown (analogous to the situation shown in Figure 6.4.1). Figure 6.4.2a shows the optical image. The white regions correspond to the smooth silicon surface, while the black parts correspond to the grooves. The processed region appear black due to the increased roughness, and hence decreased specular reflection compared to the pristine surface. Each line from top to bottom correspond to different pass numbers ranging from 1 to 7 in the picture. Figure 6.4.2b shows the height profile of the corresponding region, where height 0 is taken as the unprocessed material surface. With each successive pass, an increase in achieved groove depth is clearly visible. Figure 6.4.2c shows the cross section of the grooves, taken at the position indicated by the blue, dashed line in Figure 6.4.2a from top (corresponding to the left side) to bottom (right side). The straight angled behavior can be clearly observed. There is slight asymmetry between the left and right side of the grooves. This is due to the order of the line scan, where the right side is scanned last. Recast of this process develops predominantly on the opposite groove wall, causing the asymmetry. Even for this relatively minimal number of passes, the saturating behavior for the depths and correspondingly, the flank angles, can be observed. For example, the 3-pass groove has a depth of approximately 30 μm, whereas the 7-pass groove has a depth of only 50 μm, less than the value predicted from the ratio of pass numbers (slightly over two times).

In order to mitigate the results of the recast (the asymmetry), in lieu of directly measuring the crater angles, we calculate the average flank angle α from the ablated

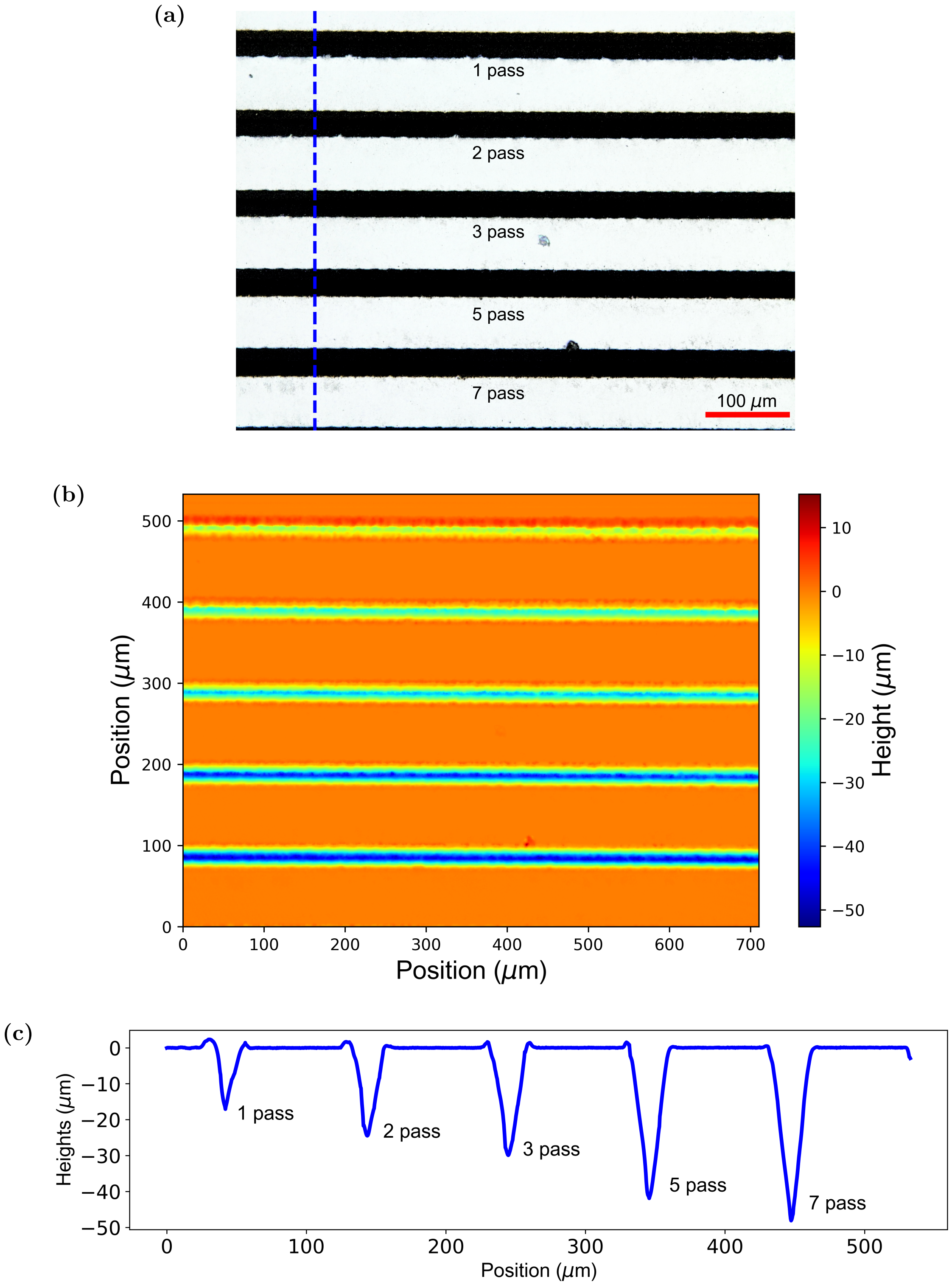

Figure 6.4.2.: (a) Optical microscope picture of the ablated grooves. (b) Height profiles of the above grooves. (c) Cross-section of the grooves corresponding to the blue, dashed line in (a).

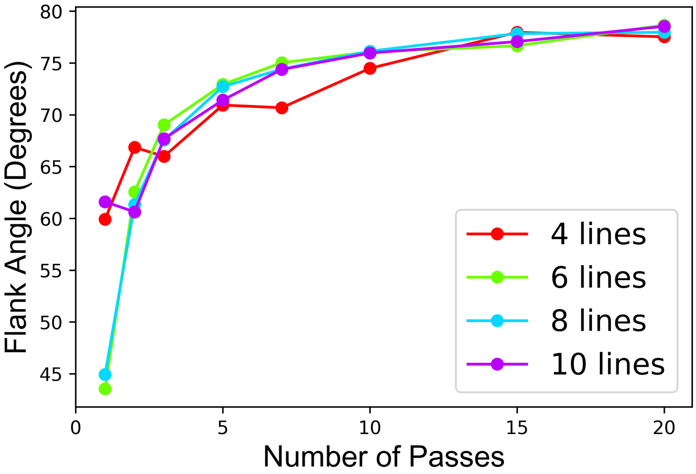

Figure 6.4.3.: Flank angles determined for various grooves made at 30 mW average power.

width w and depth d of the grooves as

$$\alpha = \arctan(2d/w). \tag{6.4.1}$$

This definition is also more closely related to limits on the aspect ratio, which is important when considering application.

The measured flank angles for the various grooves made at a laser intensity of 30 mW are gathered in Figuare 6.4.3. It can be seen that although values differ in the case of low pass numbers, where the morphologies are most affected by random cracking and recast, the values for the different scans all converge at a limiting flank angle around of 75 degrees for the larger scan numbers. Values from grooves made with more lines are more accurate in general, due to their larger dimension sizes.

In order to analyze the universal trends, we simplify the data by averaging the flank angles for the different line numbers. In order to mimic the asymptotic approach to a limiting flank angle seen in the data, we model the angle as an exponential function of the number of passes N, where

$$\alpha(N) = \alpha_0 - \exp(-(N-1)/\tau). \tag{6.4.2}$$

Here, α_0 is the limiting flank angle, and τ is a characteristic saturation pulse number. We use equation (6.4.2) to fit the averaged data (weighed by their standard deviation) mentioned above. The result for the 30 mW data is shown in Figure 6.4.4. While the model is wholly empirical, in general, good agreement is seen with the data.

In a similar manner, grooves were made and analyzed at a total of 5 average powers: 10 mW, 30 mW, 50 mW, 70 mW, and 90 mW. The data (filled circles) and their respective fits (dashed lines) are gathered in Figure 6.4.5. The model function appears to satisfactory represent the data over all the average powers tried.

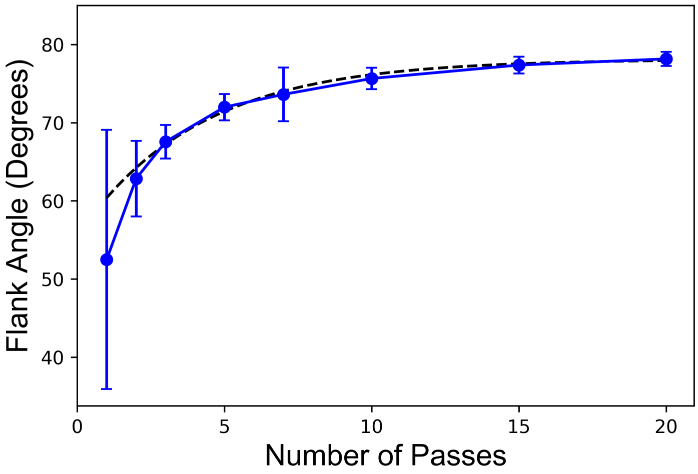

Figure 6.4.4.: Averaged flank angles at 30 mW (blue, solid) fit with the exponential model (black, dashed). Error bars denote one standard deviation.

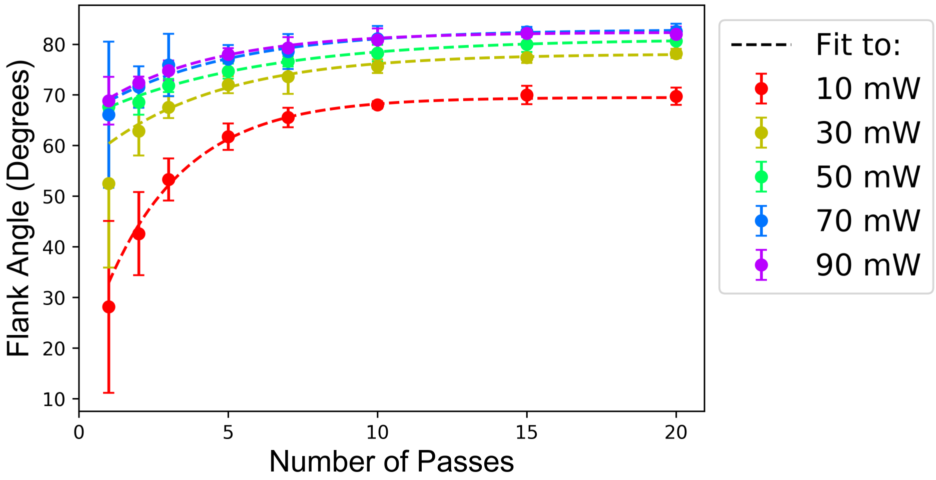

Figure 6.4.5.: Averaged flank angles fit for various average powers. Error bars denote one standard deviation.

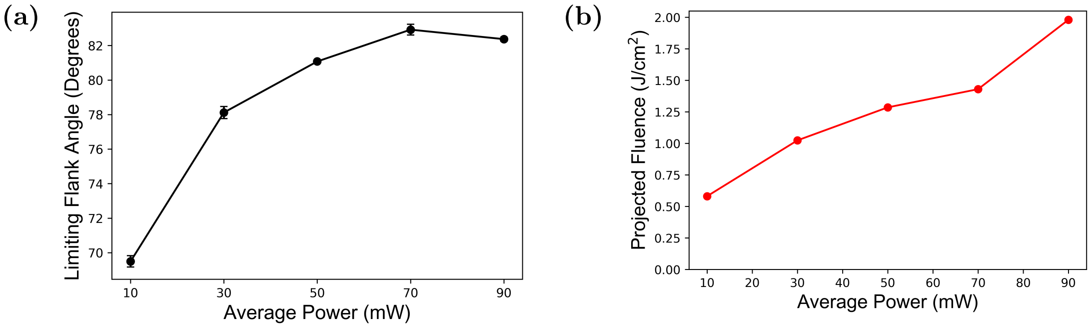

Figure 6.4.6.: (a) Limiting flank angles determined from the fits to experiment. (b) Limiting threshold fluences as predicted from the framework of Schuütz *et al.*. Propagated errors are of the order of the marker size.

From the fits, we gain the limiting flank angle, as shown in Figure 6.4.6a. With the exception of the 90 mW data, the angles all increase monotonically, as is expected. This saturation may be due to other competing depth saturation processes becoming significant at these high angles.

Next, we can then convert these flank angle values into a limiting projected fluence value believed to correspond to the threshold fluence. Given a pulse energy of E_p, the peak fluence of the pulse is calculated as

$$F = \frac{2E_p}{\pi w^2}. \tag{6.4.3}$$

The fluence is projected onto the slanted surface of the processed sample, to arrive at an effective value calculated from equation (6.2.1). The derived values from this process are shown in 6.4.6b.

The values of the projected fluences are notably high, with values close to the ablation thresholds of transparent dielectrics. It can also be seen that the calculated limiting fluence values vary between the different pulse energies. While there are sources of systematic error in our current methodology, such as defocusing, recast effects, and other errors related to positioning, these errors should lead to errors generally independent of power. They should not lead to the large systematic difference observed between the 10 mW threshold and the 90 mW threshold values predicted here. This suggests a different cause for the discrepancy.

An important aspect of ablation ignored in the above discussion is the fact that ablation is determined by values of the fluence which is able to couple *into* the material, not the incident fluence. Although for normal incidence, these values have a one-to-one correspondence and hence the threshold fluence values in the literature are often cited as the incident fluence values, this is not the case for oblique incidence. As was shown by Liu *et al.*, in the case of oblique illumination, both geometric effects and optical effects, namely the differing transmission coefficients of the material at different incidence angles, must be taken into consideration [172]. In their experiments, Liu *et al.* found good

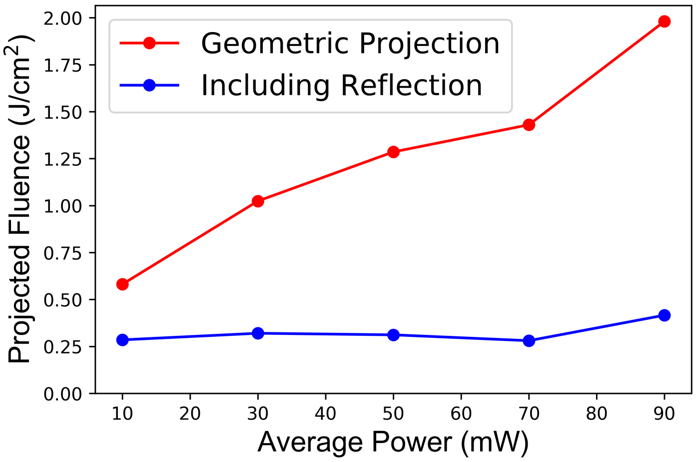

Figure 6.4.7.: Projected fluences at the limiting flank angles with only geometric considerations (red) and with added reflection loss compensation (blue).

agreement between fluences of oblique illumination when incident fluence was adjusted for by the Fresnel coefficients of the unexcited sample.

In the current experiment, the polarization of the laser was parallel to the scanning direction (the x direction in Figure 6.4.1). Thus, in regards to the sloped surface, the incident light is s-polarized. The Fresnel coefficient for s-polarization at an angle θ can be calculated as

$$R_s = \left| \frac{n_1 \cos\theta - n_2\sqrt{1 - \left(\frac{n_1}{n_2}\sin\theta\right)^2}}{n_1 \cos\theta + n_2\sqrt{1 - \left(\frac{n_1}{n_2}\sin\theta\right)^2}} \right|^2 \tag{6.4.4}$$

where n_1 and n_2 are the refractive indices of air and silicon respectively. We take n_1 as 1, and $n_2 = 3.57 + 0.0003i$ for the refractive index of the respective materials at 1028 nm (room temperature) [173]. Using these values, the transmitted fluence values within the sample can be calculated. We then renormalize these values to the corresponding incident fluence values required to achieve the same transmitted fluence at normal incidence, to facilitate comparison with values in the literature. In equation form, the final projected fluence F'_{pr} becomes

$$F'_{pr} = F_{pr}\frac{1 - R_s(\alpha_0)}{1 - R_s(0)}. \tag{6.4.5}$$

The adjusted values are shown in Figure 6.4.7. The agreement between the different pulse energy values are far better, in support of the current procedure.

In regards to the absolute value, the threshold fluence is notably *higher* than the values which appear in the literuatere: the infinite-pulse damage threshold for silicon is generally regarded to be between 0.05 and 0.1 J/cm^2 [171, 174]. This difference may be due to two reasons, both pulse-energy independent. The first is the fact that the projected fluence was calculated with *peak fluence* values of the pulse, analogous to how threshold fluences are calculated for Gaussian pulses. However, this value is a maximum value that can be seen during processing. The majority of processing occurs at local fluences not corresponding to the peak location; the fluence is thus systematically overestimated in the current case. Another factor that was ignored is recast effects. For processing to continue, material must be ejected from the groove. However, for the high aspect ratio grooves created in the current experiment, a vast majority of the material is expected to redeposit onto the groove walls owing to the small solid angle leading out of the sample in these cases. The practical flank angle would be expected to be a quasi-static equilibrium between the removal and re-deposition process, which should be a higher value. Lastly, for the deepest grooves, the effects of defocusing may come into play. For the current focusing conditions, the Rayleigh lengths are approximately 200 μm. These values are approached for the deepest grooves made; the laser power/positioning should be adjusted correspondingly to maintain a constant fluence value. Altogether, the values derived remain reasonable for the current experimental accuracy.

To conclude this section: we were able to recreate the asymptotic behavior of structure flank angles with the progression of laser processing, as predicted and demonstrated by Schütz *et al.* in their work. However, by exploring pulse-energy dependence as well, we found that the geometric effects alone could not explain the inconsistencies found in the limiting projected fluence values. We were able to explain our results by newly incorporating changes in optical reflection due to changes in incidence angle, demonstrating the importance of considering the *transmitted* fluence (as opposed to the incident fluence) when comparing threshold values across varying conditions.

6.5. Application

As an application for the angled structured behavior, Schütz *et al.* have proposed structuring of large-area moth-eye anti-reflection (AR) structures. Moth-eye structures are a type of graded refractive index structure which operates by eliminating large discontinuities in the refractive indices between two mediums at an interface from which strong reflection arises. The moth-eye structure in particular consists of sub-wavelength period, tapered protrusions on the material surface [1]. As the structures are smaller than the wavelength, the effective refractive index at a spatial point can be approximated as a function of the amount of material present. Tapered structures result in a smoothly varying material spatial filling fraction, and correspondingly, changes in the refractive index also become smoothed resulting in AR functionality. For a moth-eye structure to function, two conditions must be met [175]:

---

[1] As can be seen on the eyes of a moth, for which the structures were named.

1. The period of the structures must be smaller than the wavelength to suppress diffraction, and
2. The height of the structures must be taller than approximately half the wavelength for the gradient to be sufficiently "smooth".

At all wavelengths, AR structures are in high demand to reduce unnecessary loss factors. In particular, the moth-eye AR approach is particularly attractive for the microwave to THz regime, where optical materials are limited for traditional coating implementations, and the application bandwidths are often very broad. However, it remains challenging to fabricate such AR structures. This is due to the unique scales required, where structures with scales in the tens to hundreds of μm order are too small for traditional machining techniques, yet too large for traditional nanostructuring techniques. However, it just so happens that these scales are compatible with the scales of laser processing.

In their processing algorithm, Schütz *et al.* use lasers to create intersecting vertical and horizontal grooves. The positions where the laser neither ablates in the vertical and horizontal direction remain as unablated "islands" on the sample surface, which remain as protrusions. These protrusions retain the tapered features of the original grooves. Their group has employed this processing to create AR structures for the microwave regime for both sapphire [170, 176] and silicon [177] using high-power picosecond lasers. In our current work, we seek to employ a similar algorithm for the THz regime. This requires the creation of structures which are approximately 10 times smaller than that of Schütz *et al.*.

While there are many implementations of THz-AR structures in the literature including moth-eye based structures, these previous works usually require complex fabrication processes, and their bandwiths have traditionally been limited [178]. In particular, full AR coverage of typical THz time-domain spectroscopy (TDS) bandwidths, from 0.1 to 3 THz, has been a goal for many studies. Recently, laser ablation has come into focus as a convenient way to create graded refractive index structures, for example, by laser drilling arrays of holes onto the substrate surface [179]. In regards to moth-eye like structures, one previous study by Brahm *et al.* created structures by picosecond laser ablation in a rectangular grid in a similar approach as Schütz *et al.* [180]. In this study, they were able to fabricate structures with approximately 120 μm height and 30 μm pitch, and observe an increase in transmission from 0.1 to 1.5 THz. However, they do not characterize the structure performance above 1.5 THz, important to many THz-TDS measurements. Furthermore, thermal damage to the silicon material resulting from picosecond laser processing is of concern.

In this application, we focus on creating anti-reflection structures on high-resistivity silicon optimized for THz bandwidths of 0.5 to 2.5 THz, covering a majority of the common THz-TDS range. This amounts to moth-eye structures with pitch smaller than 35 μm, and height greater than 100 μm. We create these structures by femtosecond laser ablation, in order to mitigate any potential thermal damage to the sample. We verify the performance of the created structures by THz-TDS, and later present an application of

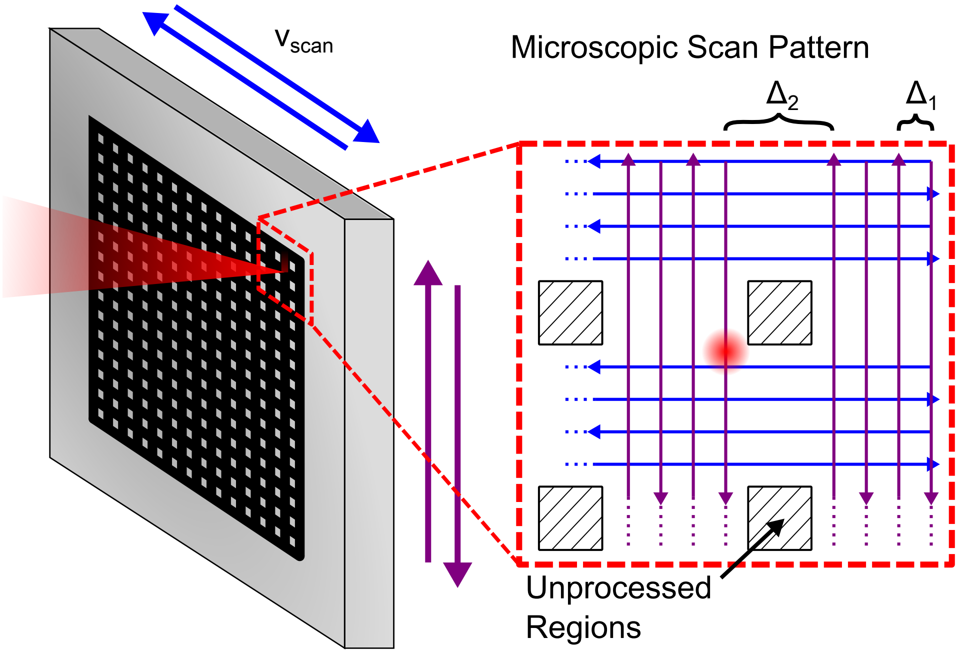

Figure 6.5.1.: Processing algorithm for moth-eye structure fabrication, where successive offset grooves are processed onto the surface of the sample by translating the sample in plane at a speed of $v_{scan} = 1$ mm/s. One macroscopic groove takes the form of four lines, each spaced $\Delta_1 = 3$ μm apart. Macroscopic spacing between these grooves are taken as $\Delta_2 = 23$ μm. The unprocessed regions between the grooves remain as the moth-eye protrusions.

such anti-reflection structures for the efficient emission of THz radiation from magnesium doped lithium niobate (Mg:LN) crystals.

6.5.1. Fabrication

In order to fabricate AR silicon, we employ the same setup introduced in Figure 6.3.1. We change the scan pattern from the groove pattern of Figure 6.4.1, to an intersecting groove pattern, as shown in Figure 6.5.1. The areas where the laser is not irradiated (grey square areas in the figure) remain to form the moth-eye protrusions. Each line in the grid (black) consists of multiple parallel-offset linear passes (similar to the experiment in the previous section), as shown in the microscopic grid inset in the figure. In the current experiment, one macroscopic groove is made with 4 parallel linear scans, each spaced $\Delta_1 = 3$ μm apart. A gap of $\Delta_2 = 23$ μm is placed between these four line scans, to create macroscopic grooves with $3\Delta_1 + \Delta_2 = 32$ μm period, which should also corresponds to the final moth-eye period.

The stage is scanned at a speed of $v_{scan} = 1$ mm/s across a total process area of 6.4 μm^2, corresponding to a total of 200 macroscopic grid lines in each direction. To achieve greater protrusion aspect-ratios, similar to the grooving experiments, the aforementioned grid scan is iterated. The processing was done with the laser average power set at 70 mW.

As was seen in the grooving experiments, increases in aspect ratio gradually saturates beyond approximately 5 passes, thus we stop processing after 5 iterations. It should be noted that while higher iterations and greater pulse energies should lead to greater aspect ratios, these values were limited by the mechanical strength of the created moth-eye structures. We found that further processing resulted in higher probabilities of fractured moth-eye structures. Thus, while flank angles discussed above are the fundamental limits of the aspect ratios possible with this method, the current limiting factor appeared to be based on different physics.

The final fabricated sample is shown in Figure 6.5.2a. The corresponding topology data of the processed region is also shown in Figure 6.5.2b, along with the profiles along various directions. Along the horizontal (Figure 6.5.2c) and vertical (Figure 6.5.2d) directions, the moth-eye height is between 60-80 μm. The asymmetry between the two direction is believed mostly to be due to asymmetry in the processing algorithm, where the horizontal direction was machined second, and hence suffered less recast effects, as well as astigmatism in the focused beam, where the depth ratio could be controlled to an extent by adjusting the out-of-plane positioning of the focus point. Polarization, which was along the horizontal direction (or parallel to the red line in the figure), should also play a role, but we cannot come to a conclusion from the current experiment. As depths have not saturated, the corresponding transmitted fluence values calculated from the realized flank angles were found to be inconsistent for the two directions.

In the diagonal direction, heights were found to approach 150 μm, as seen in Figure 6.5.2e. The peaks observed within the grooves is believed to mostly be a measurement error on the part of the laser scanning microscope. The reflected signals from these portions were weak, and the microscope returns inconsistent values at these locations. The approximate value being nearly the addition of the vertical and horizontal groove depth values is an intuitive result, as the intersection point is ablated with beams scanned in both directions.

6.5.2. Characterization

To verify the THz transmission properties of the fabricated samples, we conduct standard THz-TDS measurements [181]. We utilize surface THz emission from an indium arsenide crystal for the broadband THz source [182], and use a 1 mm thick gallium phosphide crystal as the electro-optical (EO) detection crystal in a conventional EO-sampling setup [183, 184]. We focus the THz light into a double-side processed sample, and measure the transmitted THz waveform. THz polarization was oriented along the horizontal (red line) direction of Figure 6.5.2.

The results to the THz-TDS measurement is shown in Figure 6.5.3a. The black trace is the time-domain signal of the THz wave passing through a bare silicon plate, while the red represents the corresponding signal through the moth-eye structured plate. A slight time delay between the two results due to material removal by laser ablation, which alters the effective optical path length between the two samples, can be seen. In the case

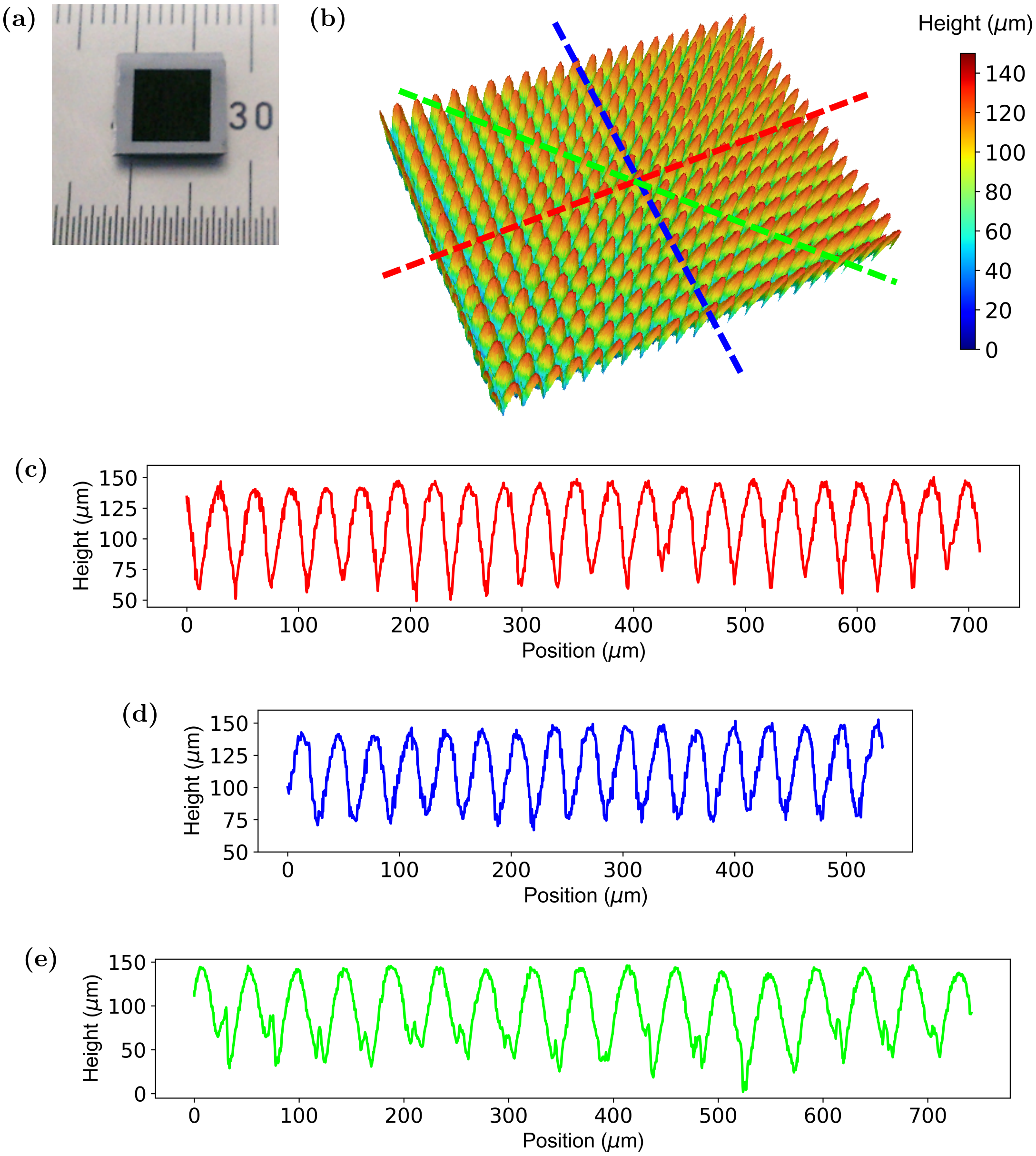

Figure 6.5.2.: (a) Picture of the fabricated moth-eye sample. The black square is the processed region. (b) 3D profile of the fabricated moth-eye structure measured by laser-scanning microscope. The profiles along the dashed lines in (b) are shown, where (c) for the horizontal (red), (d) for the vertical (blue), and (a) for the diagonal (green) line.

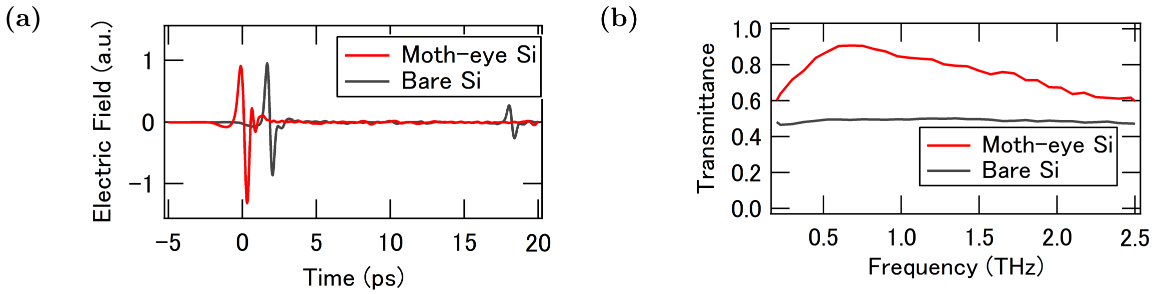

Figure 6.5.3.: (a) THz-TDS measurement of the transmitted transmitted pulse through the moth-eye structured plate, with the signal from the original substrate shown as reference. (b) The transmissivity power spectrum of the THz-TDS measurement, normalized by the signal measured without a sample in place.

of the bare silicon, a clear duplicate of the main pulse can be observed approximately 15 ps behind the main pulse. This satellite pulse is believed to be due to multiple-reflections within the silicon plate. The time delay corresponds well to what would be predicted from the optical path length of the silicon plate (15.9 ps). For the AR structured silicon, this reflection pulse is clearly absent. Signal strength is also higher due to the reduction of the Fresnel loss. Both are strong indications of the anti-reflection properties of the moth-eye processed sample.

To understand the spectral properties of the moth-eye sample, we take a Fourier transform of the THz-TDS waveform. The result is shown in Figure 6.5.3b. For clarity, Fabry-Perot fringes are removed by selecting a time window of 20 ps around the peak of the sample (6.7 ps before and 13.3 ps after the main positive peak), corresponding to a time range where reflection pulses are not included. Compared to the bare silicon plate, a clear increase in transmission can be observed for the moth-eye processed plate from 0.5 to 2.5 THz. Transmission peaks at around 90% transmission at 0.6 THz. The decrease in THz transmission at lower frequencies is caused by the heights of the moth-eye structures becoming comparable to the THz wave-length. The high-frequency decrease in THz transmissivity is unexpected as a property of an ideal moth-eye structure. We return to this point later.

To better understand the results, we calculate transmissivity from the measured morphology by rigorous coupled-wave analysis (RCWA) method [185]. The material was divided into three sub-components: two moth-eye sub-components (from microscope measurements) of 120 μm height, and a sandwiched bulk component, for a total thickness of 650 μm, as shown in Figure 6.5.4a. This unit cell was aligned periodically at 32 μm pitch. Transmission was calculated at normal incidence. Calculations were done with RSoft DiffractMOD software [2].

Calculated results compared with the Fourier transform spectrum of the full time-range of Figure 6.5.3a (with Fabry-Perot fringes) are shown in Figure 6.5.4b. Results calculated for the moth-eye structure made with lossless silicon is shown in dashed blue.

---

[2] https://www.synopsys.com/optical-solutions/rsoft/passive-device-diffractMOD.html

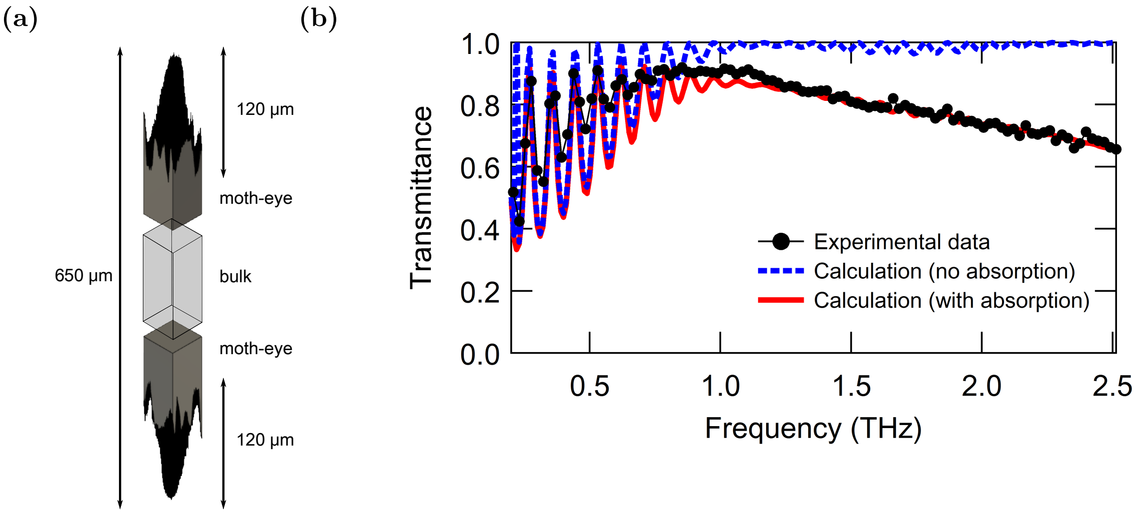

Figure 6.5.4.: (a) Unit cell of the model used for the numerical simulations. (b) Calculated transmissivity, with (blue dashed) and without (red solid) absorption.

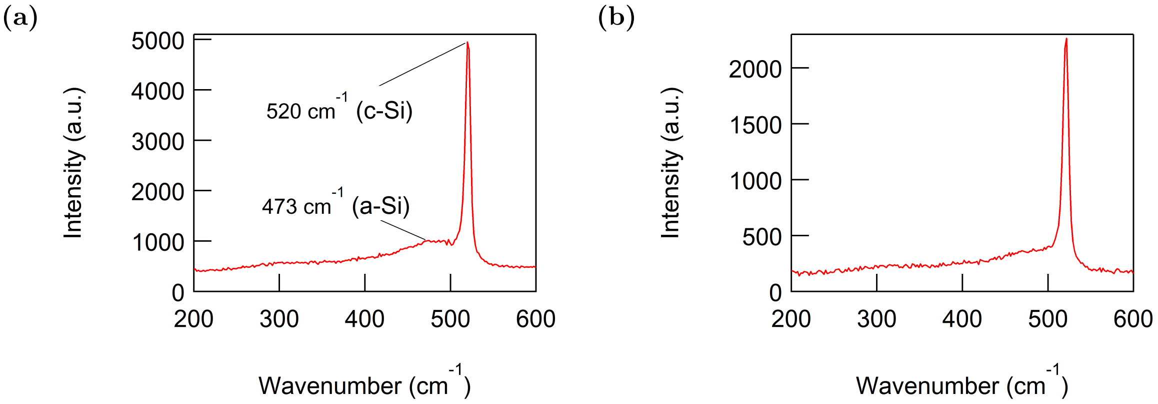

Figure 6.5.5.: Raman spectra of (a) processed and (b) unprocessed silicon.

Fabry-Perot fringes visible in the lower frequencies are due to partial AR functionality, as was mentioned previously. Differences in fringe depths between the calculations and measurements suggest an underestimation of the moth-eye height, which is believed to be in part due to the limits in the spatial and depth resolution of the laser scanning microscope. At higher frequencies, both calculation and data show no fringes, suggesting complete AR functionality; however, the transmission for the experimental data is notably smaller. It was found that the inclusion of an imaginary part into the refractive index of the silicon material in the moth-eye portion of the calculated region ($n_i = 0.032$) well-reproduced the high-frequency decrease in transmission, as shown in the red, solid line in Figure 6.5.4b. This suggests some form of laser-induced changes to the optical property of the material.

It is known that ultrafast laser-irradiation results in amorphization silicon [186]. To observe if this also occurs on our sample, we take the Raman spectra of samples under

532 nm CW laser irradiation by confocal Raman microscope (inVia Reflex St; Renishaw). We take spectra of silicon processed with a single pass of 70 mW irradiation, as well as the pristine sample surface as reference. The results are shown in Figure 6.5.5. A characteristic peak at approximately 520 cm^{-1} corresponding to first-order LO- and TO-phonon scattering mode in crystalline silicon (c-Si) can be observed in both samples. In the case of the processed sample, a small peak can be seen to develop near 473 cm^{-1} which is characteristic for amorphous silicon (a-Si). Both peaks are labeled in Figure 6.5.5a. While weak, the amorphous peak was consistently visible in various processed regions at various intensities.

Other changes are known to occur in silicon, such as the formation of a polycrystalline region. While the THz optical properties of such materials are not known, these may be affecting the performance of the fabricated moth-eye samples. For high-frequency use, reducing sample damage will be key to further increasing THz transmission.

6.5.3. Applications of anti-reflective properties

Fabricated AR plates may be used as effective filters of shorter-wavelength pulses in THz setups or else as efficient THz beam-splitters in the case of single-sided processing. Here, as a more exotic application of the fabricated moth-eye plate, we propose and demonstrate a THz output coupler for Mg:LN crystals, currently one of the most commonly used nonlinear crystal for the generation of intense THz light from an ultrafast NIR pump source [187]. Mg:LN is valued for its high nonlinear coefficients, but is also known to have a high refractive index of 5.2 in the THz regime [188]. Due to this high refractive index, close to half of THz power generated within the crystal is reflected back within the crystal due to the refractive index mismatch between the crystal and ambient air. This portion of the THz wave is subsequently absorbed by the crystal, and is effectively wasted. However, by impedance matching the interfaces, it should be possible to couple out a greater portion of this power to free-space, where it can be utilized.

As directly processing and creating moth-eye structures on the crystal is both costly and may yield unwanted artifacts in the THz generation process, we propose the use of fabricated moth-eye structured plates as an output coupler for the Mg:LN crystals. The high refractive index of silicon combined with an ideal AR performance surface should be enough to couple a theoretical maximum of 96% of the generated THz out of the crystal, thus nearly doubling the output power. The proposed schematic is shown conceptually in Figure 6.5.6a.

To implement this structure, a device to hold the Mg:LN crystal and moth-eye structured silicon plate together is constructed. A 3D printed cover is used to mechanically stabilize the silicon to the crystal. The holder is shown in Figure 6.5.6b and 6.5.6c. While such mechanical attachment of the two components will lead to micrometer level gaps between the silicon plate and the crystal, this is in fact beneficial to the current setup. This gap allows generated THz, with wavelengths on the order of a couple hundreds of micrometers, to pass evanescently into the silicon, while the pump NIR pulse is totally

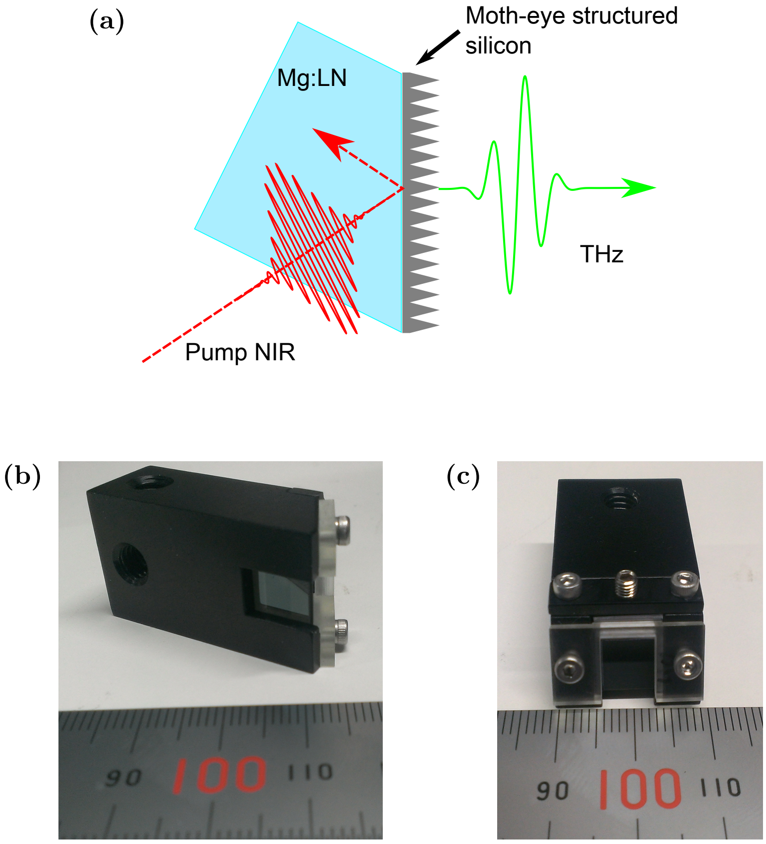

Figure 6.5.6.: (a)The schematic for the use of the moth-eye for THz output coupling from Mg:LN. The (b) side view with the Mg:LN crystal exposed, and (b) front view of the implemented device, where the moth-eye processed silicon can be seen.

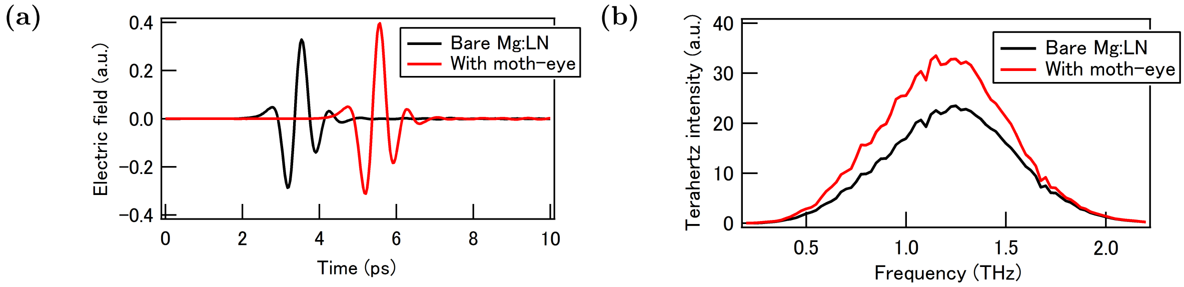

Figure 6.5.7.: (a) THz-TDS spectrum of the THz generated from the crystal with and without the moth-eye processed plate attached. (b) Power spectrum of the THz-TDS data.

internally reflected from the interface. Were the NIR pulse to be able to enter the silicon plate, it would excite free carriers in the silicon, resulting in free-carrier absorption, and hence loss, of THz power.

THz-TDS measurments of the THz emission optimized for the case with (red) and without (black) the silicon plate attached are shown in Figure 6.5.7a. We see clear increase in the THz generation, as evidenced by the greater peak values in the electric field. Figure 6.5.7b shows the Fourier transformed power spectra. We see broadband increase in the THz intensity yield across the whole emission spectrum of Mg:LN. Altogether, a 40% increase in the total THz intensity yield was observed in the current experiment. By improving the moth-eye fabrication process, this value may be improved further.

As THz yield from Mg:LN crystals are currently limited by the damage threshold of the crystal itself, this factor increase is significant for application. While the conventional solution would be to increase crystal area, the current implementation only requires the attachment of the moth-eye plate, the process of which requires no specialized equipment. Comparatively, we believe this process to be more practical and cost-efficient.

6.6. Summary

In this chapter, we explored the macroscopic morphological aspect of laser processing. Processing results in slanted angles, which has been known as a limiting factor as this reduces the effective fluence incident upon the sample surface. We first verify the fundamental aspects of this property, where we were able to observe clear saturating behaviors in the processing. By changing the processing average power, we were able to show that this saturation angle depends not only on the geometric projection, but also must take into the effect of changes in the optical reflectivity.

In the second half of the chapter, we explore a use of this structure as a way to fabricate moth-eye AR structures. We create AR structures for the THz regime, and characterize its properties in detail. Lastly, we demonstrate a novel use for these structures in THz generation.

From the results, it can be seen that two major difficulties remain in facilitating widespread utilization of ultrafast laser microfabricated THz structures. The first is the problem posed by the mechanical strength of the material. Current structure aspect ratios were found to be limited not by a diminishing effective fluence value (as was seen in the first section), but due to mechanical cracking and fracturing of the fabricated moth-eye structures. Elucidating the nature of the mechanical stress generated during ultrafast laser processing may lead to new strategies to reduce this mechanical damage, and would be an important step in overcoming this limit. A second aspect is surrounding damage to the material. The optical characteristic of the material were changed due to laser processing. Through simulations, we find extraneous absorption of THz power, which we attribute to changing material optical properties. New fabrication strategies or post-processing treatment may be necessary to effectively utilize laser processed structures in THz applications. In the context of the moth-eye AR structure, the first factor limits mainly the low-frequency performance, while the latter affects mainly the high-frequency performance.

Despite these setbacks, the combination of THz technologies and laser processing is a promising new venue for the realization of new, exotic devices. The spatial scales of laser processing and the spatial scales of THz metamaterials are well matched, and promise for fast and convenient solutions to traditionally difficult machining morphologies. Conversely, THz radiation may also prove to be an effective way to probe the quality of laser-processed materials. Future work will focus on improving the aformentioned points, on top of other practical concerns, such as processing time, which is currently limited by the translation abilities of the mechanical stage.

Chapter 7.

Concluding Remarks

7.1. Summary

In this dissertation, we set out to uncover properties of the ultrafast breakdown of dielectrics through morphological studies. Here, we summarize the main results.

Development of the fluence mapping technique

As a new method to link the ablated morphology to the spatial intensity profile of the incident pulse, we create the fluence mapping technique. By imaging the raw beam profile and correlating this to the ablated crater profile, we were able to plot the ablated depths as a function of the incident local fluence. Through this, we were able to utilize the full morphology information contained in a crater.

This technique shows several distinct advantages to conventional morphology studies. As the beam profile is taken as an arbitrary profile, the technique does not suffer from systematic errors suffered from traditional Gaussian regression analysis. This makes this method particularly useful in measuring the ablation thresholds of materials. Additionally, this technique allows for the evaluation of the *locality* of the ablation phenomenon, i.e. if the ablation phenomenon depends only on the incident local fluence. In this section, we demonstrate that for sapphire at NIR wavelengths, this is the case.

Exploration of wavelength dependence in ablation

As a use of the fluence mapping technique, we set out to measure the wavelength dependence in the ablation of wide band gap materials. This measurement has traditionally been limited by the large systematic errors induced by the high power OPA light sources required for the experiment.

In the thesis, we deal with two materials: TiO_2 (rutile) and Al_2O_3. For TiO_2, we were able to observe the quantization of the ablation threshold due to transitions from two photon to three photon absorption around a photon energy of 3 eV, a similar feature as to what was reported in the literature for thin-film TiO_2 [94]. However, as a fundamentally different feature, we also observe a spectral broadening of the transition step. As discussed in the discussions section, we believe this step to be associated to the effects of absorption from higher-order bands.

For Al_2O_3, we observe what we believe to be the first direct observation of the multiphoton step structures in the ablation threshold for a wide band gap material. We confirm qualitative features predicted from theory, such as the gradually widening step heights for larger photon energies. Global fluctuations in the threshold were found to be smaller than that predicted by most theories in the literature. The local fluctuations were also small as well, with only a 10 % fluctuation between different orders. While we were unable here to corroborate results with the microscopic rate equation model, the data is an important benchmark for future fundamental studies.

The empirical treatment of damage incubation in displaced pulses

A major hurdle in connecting the knowledge gained from fundamental studies to actual laser processing techniques is characterizing multiple-pulse effects. While previous studies on multiple-pulse effects mainly dealt with determining the multiple-pulse ablation threshold of materials, here, we deal with a more realistic scenario: the case of incubation effects for pulses 1) well above the material damage threshold and 2) where the pulse is spatially displaced, as in a traditional laser scanning scheme. We construct a simple empirical model regarding the energy absorption mechanism, and analytically solve this model to arrive at two limiting scaling behaviors of the processing in regards to pulse energy and spatial density. We experimentally verify this behavior in the processing of sapphire.

Characterizing the effects of changing morphology

Another multiple-pulse effect seen in ablation is the gradual saturation of the ablation rate. In processing, it is known that hole depths eventually saturate. In the simplest case, this is due to the changing geometry. We experimentally observe this behavior for silicon, where the changing incident angle of the laser results in a smaller effective fluence, as well as increasing Fresnel reflection from the surface.

While the saturation effect is usually regarded as a hurdle to processing, used properly, it can be used to create uniform slanted structures on the surface of materials. We demonstrate a use for such structures in the form of moth-eye anti-reflection structures on the surface of high-resistivity silicon. By using these structures we were able to achieve over 90% peak transmission of terahertz waves, compared ot the near 50% for a bare silicon sample. We also demonstrate a use of these structures as an efficient enhancer for terahertz generation from lithium niobate crystals.

7.2. Future prospects

With the development of the fluence mapping technique, a new fundamental question has come to attention: what determines the locality of ablation. We know that the locality is not only material dependent, but also wavelength dependent for the same material. In order to elucidate the physics behind this, it is necessary to catalog the ablation behaviors for a wider class of materials.

Further analysis of the fluence map may yield more information on the depth dependent energy deposition within the material during ablation. However, as shown in the analysis for the morphology of TiO_2, care must be taken in the interpretation of the depths, as processes at different time scales are all ingrained within the final profile. In these cases, combinations with time-resolved measurements may prove critical.

Another possibility opened up with this technique is the use of the ablated area as a clear physical parameter. In the case of very fine dependence in a parameter, such as the crystal orientation of the material [116], it is often difficult to extract differences in the threshold values from changes in the diameter. However, if one were to measure changes in the ablated area, these small changes will be multiplied by the circumference of the crater, and potentially measurable. Provided that the locality of the ablation is confirmed, it will then be possible to correlate this area value to a physically meaningful fluence value as well. While the absolute (systematic) errors may persist, one can extract a meaningful differential signal in this way.

In regards to connecting to applications, a treatment of damage beyond the simple empirical model discussed in the dissertation is necessary for a full first-principles modeling of the processing phenomenon. Damage incubation leads to not only changes in the ablation rate (as seen in chapter 5), but also in the optical properties of the material (as seen in chapter 6 with the induced absorption in silicon). More microscopic analysis, through for example, raman spectroscopy, will be necessary to fully elucidate the relevant physics behind damage. Inversely, finding ways to efficiently increase absorption in a material may lead to high-efficiency ablation methods.

Lastly, the combination with cutting-edge spectroscopic techniques should shed new light onto the ablation phenomenon. In ablation, the material properties changes dramatically; these changes should lead to large changes in any spectroscopic measurement. In these regards, the combination of ablation with single-shot spectroscopy techniques [189], where the S/N ratio is often limited, should be a very interesting venue to explore.

References

[1] N. Bloembergen, Quantum Electron. IEEE J. **QE-10**, 375 (1974).

[2] W. Steen, K. Watkins, and J. Mazumder, *Laser Material Processing* (Springer London, 2010).

[3] G. Gladush and I. Smurov, *Physics of Laser Materials Processing: Theory and Experiment*, Springer Series in Materials Science (Springer Berlin Heidelberg, 2011).

[4] B. C. Stuart, M. D. Feit, A. M. Rubenchik, B. W. Shore, and M. D. Perry, Phys. Rev. Lett. **74**, 2248 (1995).

[5] N. Ashcroft and N. Mermin, *Solid State Physics* (Brooks/Cole, 1976).

[6] D. Puerto, J. Siegel, W. Gawelda, M. Galvan-Sosa, L. Ehrentraut, J. Bonse, and J. Solis, Journal of the Optical Society of America B **27**, 1065 (2010).

[7] E. Arola, IEEE Journal of Quantum Electronics **50**, 709 (2014).

[8] S. K. Sundaram and E. Mazur, Nat. Mater. **1**, 217 (2002).

[9] B. Rethfeld, K. Sokolowski-Tinten, D. von der Linde, and S. I. Anisimov, Appl. Phys. A **79**, 767 (2004).

[10] N. M. Bulgakova, R. Stoian, and A. Rosenfeld, Quantum Electron. **40**, 966 (2010).

[11] E. G. Gamaly, Phys. Rep. **508**, 91 (2011).

[12] P. Balling and J. Schou, Reports Prog. Phys. **76**, 036502 (2013).

[13] D. Ristau, ed., *Laser-Induced Damage in Optical Materials*, 1st ed. (CRC Press, 2014) p. 551.

[14] D. Arnold, E. Cartier, and D. J. DiMaria, Phys. Rev. B **45**, 1477 (1992).

[15] A. Kaiser, B. Rethfeld, M. Vicanek, and G. Simon, Phys. Rev. B **61**, 11437 (2000).

[16] S. Guizard, P. Martin, P. Daguzan, G. Petite, P. Audebert, J. P. Geindre, A. D. Santos, and A. Antonnetti, Europhys. Lett. **29**, 401 (1995).

[17] R. W. Boyd, *Nonlinear Optics*, 3rd ed. (Academic Press, Inc., Burlington, MA, USA, 2008).

[18] M. J. Weber, *Handbook of Optical Materials*, Laser & Optical Science & Technology (Taylor & Francis, 2002).

[19] R. Stoian, D. Ashkenasi, A. Rosenfeld, and E. E. B. Campbell, Phys. Rev. B **62**, 13167 (2000).

[20] P. Stampfli and K. H. Bennemann, Appl. Phys. A Mater. Sci. Process. **60**, 191 (1995).

[21] H. Zhang, C. Li, E. Bevillon, G. Cheng, J. P. Colombier, and R. Stoian, Phys. Rev. B **94**, 224103 (2016).

[22] Y. Tanaka and S. Tsuneyuki, Appl. Phys. Express **11**, 046701 (2018).

[23] H. J. Pain, *The Physics of Vibrations and Waves, Sixth Edition*, 6th ed. (Wiley-Blackwell, 2005).

[24] E. R. Dobrovinskaya, L. A. Lytvynov, and V. Pishchik, *Sapphire: material, manufacturing, applications* (Springer Science & Business Media, 2009).

[25] P. Lorazo, L. J. Lewis, and M. Meunier, Phys. Rev. Lett. **91**, 225502 (2003).

[26] L. Keldysh, Sov. Phys. JETP **20**, 1307 (1965).

[27] M. Wegener, *Extreme Nonlinear Optics* (Springer, 2005).

[28] C. J. Joachain, N. J. Kylstra, and R. M. Potvliege, *Atoms in Intense Laser Fields* (Cambridge University Press, 2012).

[29] Z. J. Long and W.-K. Liu, Can. J. Phys. **88**, 227 (2010).

[30] M. Y. Ivanov, M. Spanner, and O. Smirnova, J. Mod. Opt. **52**, 165 (2005).

[31] A. Becker and F. H. M. Faisal, J. Phys. B At. Mol. Opt. Phys. **38**, R1 (2005).

[32] A.-C. Tien, S. Backus, H. Kapteyn, M. Murnane, and G. Mourou, Phys. Rev. Lett. **82**, 3883 (1999).

[33] V. E. Gruzdev, J. Opt. Technol. **71**, 504 (2004).

[34] V. E. Gruzdev, Phys. Rev. B **75**, 205106 (2007).

[35] V. E. Gruzdev and J. K. Chen, Appl. Phys. A **90**, 255 (2007).

[36] J. R. Gulley, Opt. Eng. **51**, 121805 (2012).

[37] J. R. Gulley and T. E. Lanier, Phys. Rev. B **90**, 155119 (2014).

[38] G. L. Yudin, L. N. Gaier, M. Lein, P. L. Knight, P. B. Corkum, and M. Y. Ivanov, Laser Physics **14**, 51 (2004).

[39] L. N. Gaier, M. Lein, M. I. Stockman, P. L. Knight, P. B. Corkum, M. Y. Ivanov, and G. L. Yudin, J. Phys. B At. Mol. Opt. Phys. **37**, L57 (2004).

[40] L. N. Gaier, M. Lein, M. I. Stockman, G. L. Yudin, P. B. Corkum, M. Y. Ivanov, and P. L. Knight, J. Mod. Opt. **52**, 1019 (2005).

[41] D. Du, X. Liu, and G. Mourou, Appl. Phys. B **621**, 617 (1996).

[42] K. K. Thornber, J. Appl. Phys. **52**, 279 (1981).

[43] D. Du, X. Liu, G. Korn, J. Squier, and G. Mourou, Appl. Phys. Lett. **64**, 3071 (1994).

[44] J. D. Jackson, *Classical Electrodynamics*, 3rd ed. (John Wiley & Sons, 1999).

[45] M. Sparks, D. L. Mills, R. Warren, T. Holstein, A. A. Maradudin, L. J. Sham, E. Loh, and D. F. King, Phys. Rev. B **24**, 3519 (1981).

[46] T. Q. Jia, H. X. Chen, M. Huang, F. L. Zhao, X. X. Li, S. Z. Xu, H. Y. Sun, D. H. Feng, C. B. Li, X. F. Wang, R. X. Li, Z. Z. Xu, X. K. He, and H. Kuroda, Phys. Rev. B **73**, 054105 (2006).

[47] L. Gallais, D.-B. Douti, M. Commandré, G. Batavičiūtė, E. Pupka, M. Ščiuka, L. Smalakys, V. Sirutkaitis, and A. Melninkaitis, J. Appl. Phys. **117**, 223103 (2015).

[48] P. K. Kennedy, IEEE J. Quantum Electron. **31**, 2241 (1995).

[49] J. Noack and A. Vogel, IEEE J. Quantum Electron. **35**, 1156 (1999).

[50] B. Rethfeld, Phys. Rev. Lett. **92**, 187401 (2004).

[51] B. Rethfeld, Phys. Rev. B **73**, 035101 (2006).

[52] B. Rethfeld, O. Brenk, N. Medvedev, H. Krutsch, and D. H. H. Hoffmann, Appl. Phys. A **101**, 19 (2010).

[53] B. H. Christensen and P. Balling, Phys. Rev. B **79**, 155424 (2009).

[54] M. Sun, J. Zhu, and Z. Lin, Opt. Eng. **56**, 011026 (2016).

[55] B. K. Ridley, *Quantum Processes in Semiconductors*, 5th ed. (Oxford University Press, 2013).

[56] S. C. Jones, P. Braunlich, R. T. Casper, X.-A. Shen, and P. Kelly, Opt. Eng. **28**, 1039 (1989).

[57] L. V. Keldysh, Sov. Phys. JETP **21**, 1135 (1965).

[58] B. C. Stuart, M. D. Feit, S. Herman, A. M. Rubenchik, B. W. Shore, and M. D. Perry, Phys. Rev. B **53**, 1749 (1996).

[59] S. S. Mao, F. Quéré, S. Guizard, X. Mao, R. E. Russo, G. Petite, and P. Martin, Appl. Phys. A **79**, 1695 (2004).

[60] M. Li, S. Menon, J. P. Nibarger, and G. N. Gibson, Phys. Rev. Lett. **82**, 2394 (1999).

[61] M. Mero, J. Liu, W. Rudolph, D. Ristau, and K. Starke, Phys. Rev. B **71**, 115109 (2005).

[62] I. H. Chowdhury, A. Q. Wu, X. Xu, and A. M. Weiner, Appl. Phys. A **81**, 1627 (2005).

[63] B. Chimier, O. Utéza, N. Sanner, M. Sentis, T. Itina, P. Lassonde, F. Légaré, F. Vidal, and J. C. Kieffer, Phys. Rev. B **84**, 094104 (2011).

[64] P. Audebert, P. Daguzan, A. Dos Santos, J. C. Gauthier, J. P. Geindre, S. Guizard, G. Hamoniaux, K. Krastev, P. Martin, G. Petite, and A. Antonetti, Phys. Rev. Lett. **73**, 1990 (1994).

[65] P. Martin, S. Guizard, P. Daguzan, G. Petite, P. D'Oliveira, P. Meynadier, and M. Perdrix, Phys. Rev. B **55**, 5799 (1997).

[66] M. Mero, Opt. Eng. **44**, 051107 (2005).

[67] L. A. Emmert, M. Mero, and W. Rudolph, J. Appl. Phys. **108**, 043523 (2010).

[68] L. Jiang and H. L. Tsai, J. Appl. Phys. **100**, 023116 (2006).

[69] T. Winkler, L. Haahr-Lillevang, C. Sarpe, B. Zielinski, N. Götte, A. Senftleben, P. Balling, and T. Baumert, Nat. Phys. **14**, 74 (2017).

[70] R. Stoian, A. Rosenfeld, D. Ashkenasi, I. V. Hertel, N. M. Bulgakova, and E. E. B. Campbell, Phys. Rev. Lett. **88**, 097603 (2002).

[71] N. M. Bulgakova, R. Stoian, A. Rosenfeld, I. V. Hertel, and E. E. B. Campbell, Phys. Rev. B **69**, 054102 (2004).

[72] A. Weiner, *Ultrafast Optics* (Wiley Publishing, 2009).

[73] M. Sun, U. Eppelt, S. Russ, C. Hartmann, C. Siebert, J. Zhu, and W. Schulz, Opt. Express **21**, 7858 (2013).

[74] L. Jiang and H. L. Tsai, J. Phys. D. Appl. Phys. **37**, 1492 (2004).

[75] P. Yu and M. Cardona, *Fundamentals of Semiconductors: Physics and Materials Properties*, 4th ed., Graduate Texts in Physics (Springer-Verlag Berlin Heidelberg, 2010).

[76] R. Biswas and V. Ambegaokar, Phys. Rev. B **26**, 1980 (1982).

[77] K. Sokolowski-Tinten and D. von der Linde, Phys. Rev. B **61**, 2643 (2000).

[78] K.-M. Lee, C. Min Kim, S. A. Sato, T. Otobe, Y. Shinohara, K. Yabana, and T. Moon Jeong, J. Appl. Phys. **115**, 053519 (2014).

[79] E. G. Gamaly and A. V. Rode, J. Opt. Soc. Am. B **31**, C36 (2014).

[80] S. Guizard, A. Semerok, J. Gaudin, M. Hashida, P. Martin, and F. Quéré, Appl. Surf. Sci. **186**, 364 (2002).

[81] K. Wædegaard, D. B. Sandkamm, L. Haahr-Lillevang, K. G. Bay, and P. Balling, Appl. Phys. A **117**, 7 (2014).

[82] M. Garcia-Lechuga, L. Haahr-Lillevang, J. Siegel, P. Balling, S. Guizard, and J. Solis, Phys. Rev. B **95**, 214114 (2017).

[83] J. R. Peñano, P. Sprangle, B. Hafizi, W. Manheimer, and A. Zigler, Phys. Rev. E **72**, 036412 (2005).

[84] G. M. Petrov and J. Davis, J. Phys. B At. Mol. Opt. Phys. **41**, 025601 (2008).

[85] K. J. Wædegaard, D. B. Sandkamm, A. Mouskeftaras, S. Guizard, and P. Balling, EPL (Europhysics Lett. **105**, 47001 (2014).

[86] D. von der Linde and H. Schüler, J. Opt. Soc. Am. B **13**, 216 (1996).

[87] J. Siegel, D. Puerto, W. Gawelda, G. Bachelier, J. Solis, L. Ehrentraut, and J. Bonse, Appl. Phys. Lett. **91**, 082902 (2007).

[88] A. Mouskeftaras, S. Guizard, N. Fedorov, and S. Klimentov, Appl. Phys. A **110**, 709 (2013).

[89] M. Lenzner, J. Krüger, S. Sartania, Z. Cheng, C. Spielmann, G. Mourou, W. Kautek, and F. Krausz, Phys. Rev. Lett. **80**, 4076 (1998).

[90] F. Quéré, S. Guizard, and P. Martin, Europhys. Lett. **56**, 138 (2001).

[91] K. Starke, D. Ristau, H. Welling, T. V. Amotchkina, M. Trubetskov, A. A. Tikhonravov, and A. S. Chirkin, in *Proc. SPIE*, Vol. 5273, edited by G. J. Exarhos, A. H. Guenther, N. Kaiser, K. L. Lewis, M. J. Soileau, and C. J. Stolz (2004) p. 501.

[92] J. R. V. D. Aldana, C. Méndez, L. Roso, and P. Moreno, J. Phys. D. Appl. Phys. **38**, 2764 (2005).

[93] L. Jiang and H.-L. Tsai, J. Appl. Phys. **104**, 093101 (2008).

[94] M. Jupé, L. Jensen, A. Melninkaitis, V. Sirutkaitis, and D. Ristau, Opt. Express **17**, 12269 (2009).

[95] H. Takayama and T. Maruyama, Appl. Surf. Sci. **261**, 705 (2012).

[96] X. Jing, Y. Tian, J. Zhang, S. Chen, Y. Jin, J. Shao, and Z. Fan, Appl. Surf. Sci. **258**, 4741 (2012).

[97] G. Geoffroy, G. Duchateau, N. Fedorov, P. Martin, and S. Guizard, Laser Phys. **24**, 086101 (2014).

[98] N. Linz, S. Freidank, X.-X. Liang, and A. Vogel, Phys. Rev. B **94**, 024113 (2016).

[99] A. Rosenfeld, M. Lorenz, R. Stoian, and D. Ashkenasi, Appl. Phys. A Mater. Sci. Process. **69**, S373 (1999).

[100] H. Varel, D. Ashkenasi, A. Rosenfeld, R. Herrmann, F. Noack, and E. E. B. Campbell, Appl. Phys. A Mater. Sci. Process. **62**, 293 (1996).

[101] X. Li, T. Jia, D. Feng, and Z. Xu, Appl. Surf. Sci. **225**, 339 (2004).

[102] N. Sanner, O. Utéza, B. Bussiere, G. Coustillier, A. Leray, T. Itina, and M. Sentis, Appl. Phys. A **94**, 889 (2009).

[103] C. Pasquier, P. Blandin, R. Clady, N. Sanner, M. Sentis, O. Utéza, Y. Li, and S. Y. Long, Opt. Commun. **355**, 230 (2015).

[104] I. Mirza, N. M. Bulgakova, J. Tomáštík, V. Michálek, O. Haderka, L. Fekete, and T. Mocek, Sci. Rep. **6**, 39133 (2016).

[105] A. Sikora, D. Grojo, and M. Sentis, J. Appl. Phys. **122**, 045702 (2017).

[106] S. Nolte, C. Momma, H. Jacobs, A. Tünnermann, B. N. Chichkov, B. Wellegehausen, and H. Welling, J. Opt. Soc. Am. B **14**, 2716 (1997).

[107] M. Grehn, T. Seuthe, M. Höfner, N. Griga, C. Theiss, A. Mermillod-Blondin, M. Eberstein, H. Eichler, and J. Bonse, Opt. Mater. Express **4**, 689 (2014).

[108] J. M. Liu, Opt. Lett. **7**, 196 (1982).

[109] J. Chalupský, L. Juha, J. Kuba, J. Cihelka, V. Hájková, S. Koptyaev, J. Krása, A. Velyhan, M. Bergh, C. Caleman, J. Hajdu, R. M. Bionta, H. Chapman, S. P. Hau-Riege, R. a. London, M. Jurek, J. Krzywinski, R. Nietubyc, J. B. Pelka, R. Sobierajski, J. Meyer-ter Vehn, A. Tronnier, K. Sokolowski-Tinten, N. Stojanovic, K. Tiedtke, S. Toleikis, T. Tschentscher, H. Wabnitz, and U. Zastrau, Opt. Express **15**, 6036 (2007).

[110] D. Puerto, W. Gawelda, J. Siegel, J. Solis, and J. Bonse, Appl. Phys. Lett. **92**, 219901 (2008).

[111] M. N. Christensen, J. Byskov-Nielsen, B. H. Christensen, and P. Balling, Appl. Phys. A **101**, 279 (2010).

[112] O. Uteza, B. Bussière, F. Canova, J.-P. Chambaret, P. Delaporte, T. Itina, and M. Sentis, Appl. Surf. Sci. **254**, 799 (2007).

[113] M. Henyk, R. Mitzner, D. Wolfframm, and J. Reif, Appl. Surf. Sci. **154-155**, 249 (2000).

[114] M. E. Shaheen, J. E. Gagnon, and B. J. Fryer, Laser Phys. Lett. **12**, 066103 (2015).

[115] X. Wang, G. Lim, H. Zheng, F. Ng, W. Liu, and S. Chua, Appl. Surf. Sci. **228**, 221 (2004).

[116] L. Qi, K. Nishii, M. Yasui, H. Aoki, and Y. Namba, Opt. Lasers Eng. **48**, 1000 (2010).

[117] S. H. Kim, I. B. Sohn, and S. Jeong, Appl. Surf. Sci. **255**, 9717 (2009).

[118] D. Ashkenasi, R. Stoian, and A. Rosenfeld, Appl. Surf. Sci. **154-155**, 40 (2000).

[119] J. Canny, IEEE Trans. Pattern Anal. Mach. Intell. **PAMI-8**, 679 (1986).

[120] P. Dierckx, *Curve and surface fitting with splines* (Oxford University Press, 1995).

[121] A. E. Martirosyan, C. Altucci, A. Bruno, C. de Lisio, A. Porzio, and S. Solimeno, J. Appl. Phys. **96**, 5450 (2004).

[122] N. Sanner, O. Utéza, B. Chimier, M. Sentis, P. Lassonde, F. Légaré, and J. C. Kieffer, Appl. Phys. Lett. **96**, 071111 (2010).

[123] Z. Sun, M. Lenzner, and W. Rudolph, J. Appl. Phys. **117**, 073102 (2015).

[124] C. W. Carr, H. B. Radousky, and S. G. Demos, Phys. Rev. Lett. **91**, 127402 (2003).

[125] M. Cao, J. Cao, M. Liu, Y. Sun, M. Wu, S. Guo, and S. Gao, J. Appl. Phys. **123**, 135105 (2018).

[126] N. Linz, S. Freidank, X.-X. Liang, H. Vogelmann, T. Trickl, and A. Vogel, Phys. Rev. B **91**, 134114 (2015).

[127] U. Diebold, Surf. Sci. Rep. **48**, 53 (2003).

[128] J. Pascual, J. Camassel, and H. Mathieu, Phys. Rev. B **18**, 5606 (1978).

[129] R. C. Santos, E. Longhinotti, V. N. Freire, R. B. Reimberg, and E. W. Caetano, Chem. Phys. Lett. **637**, 172 (2015).

[130] M. J. Weber, *Handbook of Optical Materials*, Vol. 19 (CRC press, 2002).

[131] J. R. DeVore, J. Opt. Soc. Am. **41**, 416 (1951).

[132] C. Persson and A. Ferreira da Silva, Appl. Phys. Lett. **86**, 231912 (2005).

[133] E. Baldini, L. Chiodo, A. Dominguez, M. Palummo, S. Moser, M. Yazdi-Rizi, G. Auböck, B. Mallett, H. Berger, A. Magrez, C. Bernhard, M. Grioni, A. Rubio, and M. Chergui, Nat. Commun. **8**, 13 (2017), arXiv:1601.01244 .

[134] B. Bharti, S. Kumar, H.-N. Lee, and R. Kumar, Sci. Rep. **6**, 32355 (2016).

[135] M. Landmann, E. Rauls, and W. G. Schmidt, J. Phys. Condens. Matter **24**, 195503 (2012).

[136] K. Yabana, T. Sugiyama, Y. Shinohara, T. Otobe, and G. F. Bertsch, Phys. Rev. B **85**, 045134 (2012).

[137] J. E. Medvedeva, E. N. Teasley, and M. D. Hoffman, Phys. Rev. B **76**, 1 (2007), arXiv:0706.1986 .

[138] A. Hertwig, S. Martin, J. Krüger, and W. Kautek, Appl. Phys. A **79**, 1075 (2004).

[139] M. Lenzner, J. Krüger, W. Kautek, and F. Krausz, Appl. Phys. A Mater. Sci. Process. **69**, 465 (1999).

[140] D. N. Nguyen, L. Emmert, M. Mero, W. G. Rudolph, D. Patel, E. Krous, and C. S. Menoni, in *Proc. SPIE*, edited by G. J. Exarhos, D. Ristau, M. J. Soileau, and C. J. Stolz (2008) p. 71320N.

[141] D. N. Nguyen, L. A. Emmert, D. Patel, C. S. Menoni, and W. Rudolph, Appl. Phys. Lett. **97**, 191909 (2010).

[142] D. N. Nguyen, L. A. Emmert, P. Schwoebel, D. Patel, C. S. Menoni, M. Shinn, and W. Rudolph, Opt. Express **19**, 5690 (2011).

[143] A. Stournaras, K. Salonitis, P. Stavropoulos, and G. Chryssolouris, Int. J. Adv. Manuf. Technol. **44**, 114 (2009).

[144] J. R. Vázquez de Aldana, C. Méndez, and L. Roso, Opt. Express **14**, 1329 (2006).

[145] M. Sun, U. Eppelt, S. Russ, C. Hartmann, C. Siebert, J. Zhu, and W. Schulz, in *Proc. SPIE*, Vol. 8530, edited by G. J. Exarhos, V. E. Gruzdev, J. A. Menapace, D. Ristau, and M. J. Soileau (2012) p. 853007.

[146] M. Sun, U. Eppelt, C. Hartmann, W. Schulz, J. Zhu, and Z. Lin, Opt. Laser Technol. **80**, 227 (2016).

[147] R. Stoian, H. Varel, A. Rosenfeld, D. Ashkenasi, R. Kelly, and E. Campbell, Appl. Surf. Sci. **165**, 44 (2000).

[148] E. Whittaker and G. Watson, *A Course of Modern Analysis 4th Edition*, 4th ed. (Cambridge Mathematical Library, 1962) p. 620.

[149] I. Imai, *Applied Hyperfunction Theory* (Springer Science+Business Media Dordrecht, 1992) p. 438.

[150] C. Fornaroli, J. Holtkamp, and A. Gillner, Phys. Procedia **41**, 661 (2013).

[151] C. He, F. Zibner, C. Fornaroli, J. Ryll, J. Holtkamp, and A. Gillner, Phys. Procedia **56**, 1066 (2014).

[152] C. He, C. Hartmann, C. Fornaroli, F. Zibner, and A. Gillner, Lasers Manuf. Conf. 2015 , 1 (2015).

[153] F. Zibner, C. Fornaroli, J. Holtkamp, J. Ryll, and A. Gillner, in *Proc. SPIE*, Vol. 9582, edited by J. Sasián and R. N. Youngworth (2015) p. 95820C.

[154] A. Miotello and R. Kelly, Appl. Phys. A Mater. Sci. Process. **69**, S67 (1999).

[155] N. Itoh and A. M. Stoneham, *Materials Modification by Electronic Excitation* (Cambridge University Press, New York, 2001).

[156] J. Valbis and N. Itoh, Radiat. Eff. Defects Solids **116**, 171 (1991).

[157] T. Kudrius, G. Šlekys, and S. Juodkazis, J. Phys. D. Appl. Phys. **43**, 145501 (2010).

[158] B. D. Evans, G. J. Pogatshnik, and Y. Chen, Nucl. Inst. Methods Phys. Res. B **91**, 258 (1994).

[159] A. V. Hamza, R. S. Hughes, Jr., L. L. Chase, and H. W. Lee, in *Proc. SPIE*, Vol. 1624, edited by H. E. Bennett, L. L. Chase, A. H. Guenther, B. E. Newnam, and M. J. Soileau (International Society for Optics and Photonics, 1992) pp. 429–435.

[160] M. Itou, A. Fujiwara, and T. Uchino, J. Phys. Chem. C **113**, 20949 (2009).

[161] J. H. Lau, Microelectron. Int. **28**, 8 (2011).

[162] H. Varel, D. Ashkenasi, A. Rosenfeld, M. Wähmer, and E. Campbell, Appl. Phys. A Mater. Sci. Process. **65**, 367 (1997).

[163] S. Döring, S. Richter, A. Tünnermann, and S. Nolte, Appl. Phys. A **105**, 69 (2011).

[164] D. Hwang, T. Choi, and C. Grigoropoulos, Appl. Phys. A Mater. Sci. Process. **79**, 605 (2004).

[165] S. Karimelahi, L. Abolghasemi, and P. R. Herman, Appl. Phys. A **114**, 91 (2014).

[166] S. Juodkazis, K. Nishimura, H. Misawa, T. Ebisui, R. Waki, S. Matsuo, and T. Okada, Adv. Mater. **18**, 1361 (2006).

[167] M. K. Bhuyan, F. Courvoisier, P.-A. Lacourt, M. Jacquot, L. Furfaro, M. J. Withford, and J. M. Dudley, Opt. Express **18**, 566 (2010).

[168] M. K. Bhuyan, F. Courvoisier, P. A. Lacourt, M. Jacquot, R. Salut, L. Furfaro, and J. M. Dudley, Appl. Phys. Lett. **97**, 081102 (2010).

[169] F. He, J. Yu, Y. Tan, W. Chu, C. Zhou, Y. Cheng, and K. Sugioka, Sci. Rep. **7**, 40785 (2017).

[170] V. Schütz, K. Young, T. Matsumura, S. Hanany, J. Koch, O. Suttmann, L. Overmeyer, and Q. Wen, J. Laser Micro/Nanoengineering **11**, 204 (2016).

[171] R. N. Oosterbeek, C. Corazza, S. Ashforth, and M. C. Simpson, Appl. Phys. A **122**, 449 (2016).

[172] X.-L. Liu, W. Cheng, M. Petrarca, and P. Polynkin, Appl. Phys. Lett. **109**, 161604 (2016), arXiv:1608.05884 .

[173] M. A. Green, Sol. Energy Mater. Sol. Cells **92**, 1305 (2008).

[174] J. Fang, L. Jiang, Q. Cao, K. Zhang, Y. Yuan, and Y. Lu, Appl. Opt. **53**, 3897 (2014).

[175] S. Wilson and M. Hutley, Opt. Acta Int. J. Opt. **29**, 993 (1982).

[176] T. Matsumura, K. Young, Q. Wen, S. Hanany, H. Ishino, Y. Inoue, M. Hazumi, J. Koch, O. Suttman, and V. Schütz, Appl. Opt. **55**, 3502 (2016).

[177] K. Young, Q. Wen, S. Hanany, H. Imada, J. Koch, T. Matsumura, O. Suttmann, and V. Schütz, J. Appl. Phys. **121**, 213103 (2017), arXiv:1702.01768 .

[178] Y. W. Chen and X.-C. Zhang, Front. Optoelectron. **7**, 243 (2014).

[179] Y. Zhang, M. Yuan, L. Chen, B. Cai, R. Yang, and Y. Zhu, Opt. Commun. **361**, 148 (2016).

[180] A. Brahm, S. Döring, A. Wilms, G. Notni, S. Nolte, and A. Tünnermann, Appl. Opt. **53**, 2886 (2014).

[181] D. Grischkowsky, S. Keiding, M. van Exter, and C. Fattinger, J. Opt. Soc. Am. B **7**, 2006 (1990).

[182] P. Gu, M. Tani, S. Kono, K. Sakai, and X.-C. Zhang, J. Appl. Phys. **91**, 5533 (2002).

[183] Q. Wu and X. Zhang, Appl. Phys. Lett. **67**, 3523 (1995).

[184] A. Nahata, A. S. Weling, and T. F. Heinz, Appl. Phys. Lett. **69**, 2321 (1996).

[185] M. G. Moharam, T. K. Gaylord, E. B. Grann, and D. A. Pommet, J. Opt. Soc. Am. A **12**, 1068 (1995).

[186] J. Bonse, K.-W. Brzezinka, and A. Meixner, Appl. Surf. Sci. **221**, 215 (2004).

[187] J. Hebling, K.-L. Yeh, M. C. Hoffmann, B. Bartal, and K. A. Nelson, J. Opt. Soc. Am. B **25**, B6 (2008).

[188] M. Theuer, G. Torosyan, C. Rau, R. Beigang, K. Maki, C. Otani, and K. Kawase, Appl. Phys. Lett. **88**, 071122 (2006).

[189] J. Liang and L. V. Wang, Optica **5**, 1113 (2018).

[190] J. Keaveney, Rev. Sci. Instrum. **89**, 035114 (2018), arXiv:1801.06508 .

[191] M. A. Hossain, J. Canning, K. Cook, and A. Jamalipour, Opt. Lett. **40**, 5156 (2015).

[192] G. Langer, A. Hochreiner, P. Burgholzer, and T. Berer, Opt. Lasers Eng. **51**, 571 (2013).

[193] T. Wilkes, A. McGonigle, T. Pering, A. Taggart, B. White, R. Bryant, and J. Willmott, Sensors **16**, 1649 (2016).

Appendix A.

Common Units

In studies involving strong-field physics, of which ablation is a part of, three units are often used to represent pulsed-laser field strengths: the fluence, intensity, and electric field. Here, we define these values.

The *fluence* of a laser pulse is defined as the pulse energy delivered per unit area. The units for fluence are usually expressed in J/cm^2. For laser pulses with non-uniform power distributions, such as a Gaussian beam profile, there is some ambiguity involved in defining the area of a beam. For a Gaussian pulse, the following terminology is commonly used.

The *average fluence* ($F_{average}$) of a Gaussian pulse is defined as the pulse energy E divided by the effective beam area, defined from its spot radius w as πw^2. Thus,

$$F_{average} = \frac{E}{\pi w^2}. \tag{A.0.1}$$

The *local fluence* (F_{local}) is defined as the fluence at a local spatial point in the beam. The *peak fluence* (F_{peak}) is the highest local fluence value. The peak fluence for a Gaussian pulse can be calculated analytically as follows. Representing the radial distance from the center of the pulse as r,

$$F_{peak} = \frac{2E}{\pi w^2} \lim_{r \to 0} \frac{\int_0^r \exp\left(\frac{-2r'^2}{w_0^2}\right) 2\pi r' dr'}{\pi r^2} = E \lim_{r \to 0} \frac{1 - \exp\left(\frac{-2r^2}{w_0^2}\right)}{\pi r^2}, \tag{A.0.2}$$

where the first prefactor term normalizes the pulse energy. The limit can be evaluated through use of l'Hôpital's rule, hence

$$E \lim_{r \to 0} \frac{1 - \exp\left(\frac{-2r^2}{w_0^2}\right)}{\pi r^2} = E \lim_{r \to 0} \frac{\left(\frac{4r}{w_0^2}\right) \exp\left(\frac{-2r^2}{w_0^2}\right)}{2\pi r} = \frac{2E}{\pi w_0^2}. \tag{A.0.3}$$

and

$$F_{peak} = \frac{2E}{\pi w_0^2}. \tag{A.0.4}$$

From this equation, it can be seen that the peak fluence is equal to two times the average fluence.

The local fluence of a Gaussian pulse thus follows as

$$F_{local} = F_{peak} \exp\left(\frac{-2r^2}{w_0^2}\right). \tag{A.0.5}$$

In this thesis, where non-Gaussian energy distribution is accepted, the local fluence is often calculated numerically as

$$F_{local} = \frac{\Delta E}{\Delta A}, \tag{A.0.6}$$

Where ΔE is the portion of the beam power incident on a small area ΔA. Correspondingly, the peak fluence becomes

$$F_{peak} = \max(\{F_{local}\}), \tag{A.0.7}$$

where $\{F_{local}\}$ is the set of all calculated numerical local fluences.

The *intensity* of a laser beam is defined as the optical power per unit area, and typically has units of W/cm^2. Lasers are typically assumed to have a Gaussian temporal profile. While the spatial dimensions are often expressed in terms of the $1/e^2$ radius value, the temporal pulse duration Δt is typically given as a full with at half maximum (FWHM) value. The relationship between the $1/e^2$ pulse duration t_p (more convenient for calculations) and the FWHM pulse duration is given as

$$\Delta t = \sqrt{2 \ln 2}\, t_p = 1.177 t_p. \tag{A.0.8}$$

As the pulse energy incident at a point is equal to the integrated optical power, it follows that

$$F_{local} = \int I dt, \tag{A.0.9}$$

where the integral is over the pulse duration. From this, we can derive the relationship between the *peak intensity* I_0 of a laser pulse with the local fluence:

$$F_{local} = \int I_0 \exp\left(\frac{-2t^2}{t_p^2}\right) = I_0 t_p \sqrt{\pi/2} \tag{A.0.10}$$

Lastly, the absolute values of the *electric field* $|\mathbf{E}|$ are converted from the intensity values as

$$I = \frac{1}{2} n \varepsilon_0 c |\mathbf{E}|^2. \tag{A.0.11}$$

Here, n is the refractive index value of the medium, and ε_0 the dielectric permittivity of the vacuum. Electric field values are expressed in units of V/m, or more conveniently in V/nm or V/Å.

In the case of a local fluence of 1 J/cm^2, the peak intensity of a 190 fs will be approximately 3.5 TW/cm^2 and electric field values of approximately 5.1 V/nm (assuming a refractive index of 1).

Appendix B.

Development of the PiCamera Beam Profiler

Here, we expand on the details in the development of the beam profiler used in the single-pulse ablation experiments.

B.1. Exposing the CMOS sensor

In order to use the camera as a beam profiler, the bare CMOS sensor must be exposed. This requires removal of the camera lens. The decomposition process is shown in Figure B.1.1.

The removal of the lens is a simple process, and has practically no risk of damaging the sensor. The lens has cog-like protrusions, and with a provided plastic piece (or simply with your fingers), the lens can be twisted off by applying some torque to these protrusions. The situation with the lens removed is shown in the middle picture. If a spatial resolution of 2.24 microns is sufficient, use with this slight modification is the safest option.

However, to do any modification to the sensor itself, further exposure of the CMOS sensor is necessary: i.e. the plastic encasing and the glass protector (or IR filter in some models) attached to the encasing should be removed. The plastic encasing to which the lens is screwed onto is glued onto the substrate that the CMOS sensor is attached to, and the glass protector is attached to this encasing as well. Thus, exposing the sensor can be achieved by removing the encasing. While somewhat risky, the easiest way is to simply cut the encasing away from the edges of the board. In this case, one should be wary not to damage the capacitors surrounding the CMOS sensor, which are relatively close to the edges. In addition, any damage to the gold wiring surrounding the sensor will most likely render the sensor unusable. One should cut away at the portions farthest from the capacitors, after which the encasing can be "peeled" off, with relatively little risk. If available, the use of a proper organic solvent[1] will allow for a safer, chemical solution to

---

[1] We believe the glue to be epoxy based.

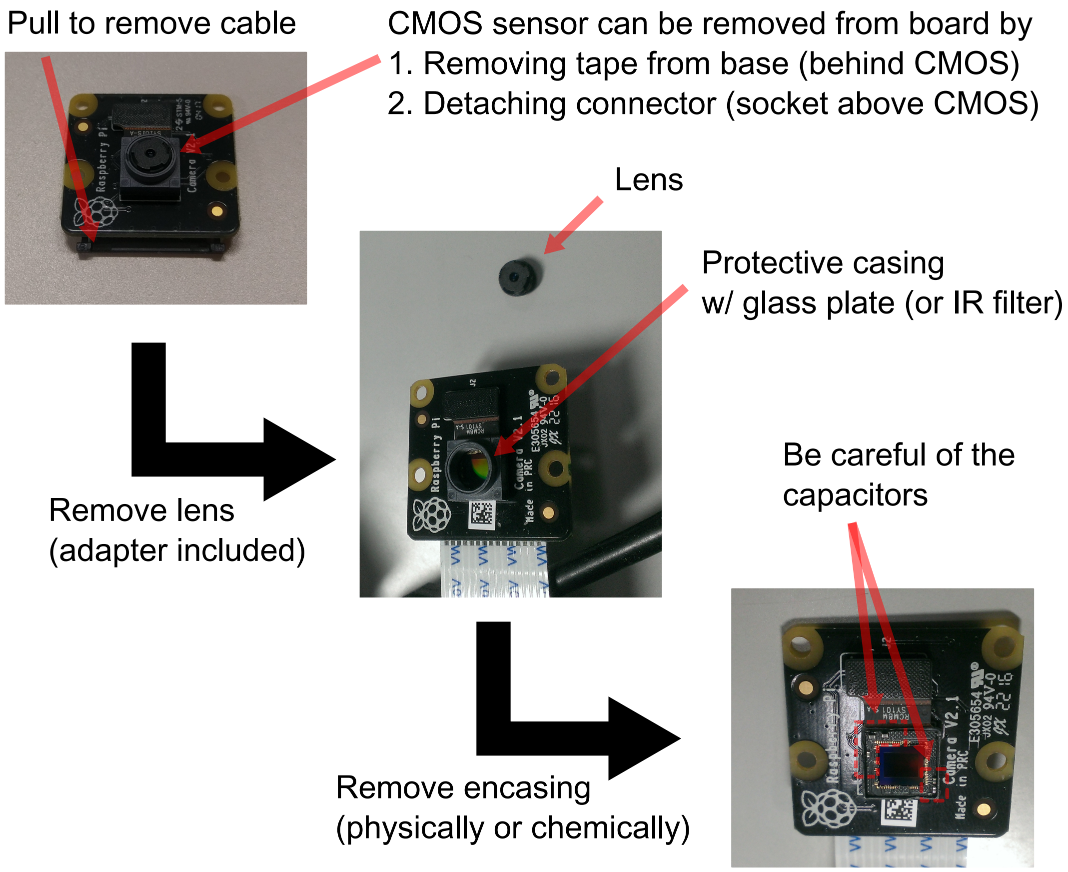

Figure B.1.1.: Pictures of the camera module gradually decomposed to the bare CMOS sensor.

removing the encasing. Immersion in standard photoresist remover[2] was found to dissolve the glue attaching the encasing in a few minutes. The module was found to work after full immersion[3], but those seeking to mitigate the risk may isolate the sensor portion of the module from the other electronics by first removing the tape holding the sensor in place, and then detaching the connector from its socket (above the CMOS sensor).

B.2. Bayer filter removal

A laser scanning microscope image of a portion of the CMOS sensor surface at 150× resolution is shown in Figure B.2.1. Each dot in the picture corresponds to a camera pixel. The dots are correspondingly spaced 1.12 μm apart. the curved features correspond to the microlens on top of each pixel, which work to gather light onto the active region of each pixel and improve efficiency.

---

[2] For example, a solution of 60% dimethyl sulfoxide and 40% N-methyl-2-pyrrolidone available in the clean rooms at the University of Tokyo was found to work, among others.

[3] In this case, however, one should *not* apply any ultrasonic, as this may damage the on-board clock on the camera module board.

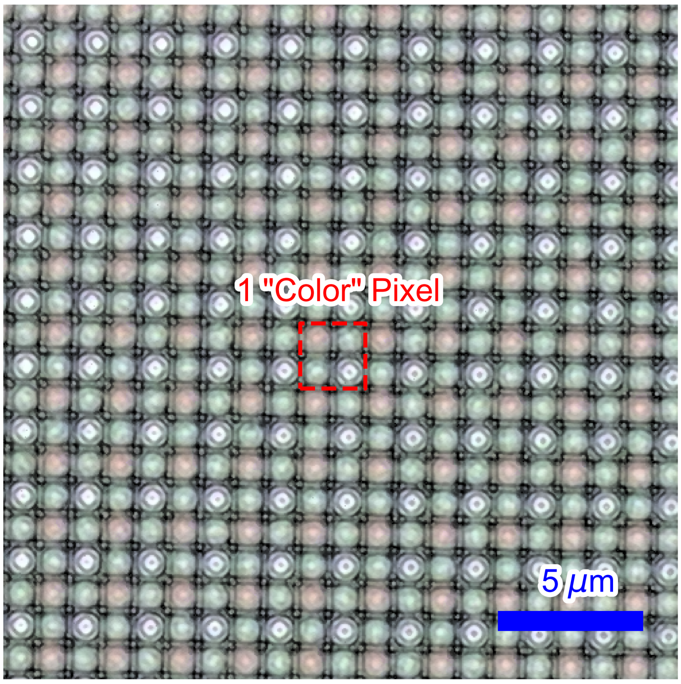

Figure B.2.1.: Laser scanning microscope image of the CMOS sensor surface.

It can be seen that the pixels in the array have systematically varied tints. This tint corresponds to the light that is reflected back to the laser microscope, and hence, the color corresponding to the transparency of the Bayer color filter. As labeled in the figure, one pixel of a color picture taken by this camera corresponds to the compound information gained from a 2×2 pixel array, consisting of one red (top left), two green (top right and bottom left), and one blue (bottom right) pixel. By properly balancing the information from each color channel (white balancing), proper color information may be retrieved. However, in the case of beam profiling, we do not need the color information, and would ideally like to have an equivalent spectral sensitivity across all pixels.

Several other works have focused on transforming normal color cameras into cheap and convenient beam profilers in the recent years. As modern CMOS sensors have the Bayer filter incorporated and hence difficult to remove, many groups have focused on utilizing the camera as-is, with some precautions. Implementations include using only a single red, green, or blue channel (depending on the laser wavelength) [190], calibrating each color channel's spectral response with a monochromator [191], or numerically calibrating the obtained image to reduce the spatial Fourier component of the grid pattern which forms due to the filter pattern [192]. However, in all implementations, keeping the Bayer filter intact compromises either the spatial resolution, or else the dynamic range of the camera. It is also inconvenient to calibrate all results for multiple wavelengths, as is the case for experiments involving OPAs or otherwise wavelength-tunable sources. Thus, it still remains attractive to find a simple method to remove the Bayer filter, as most commercially available (at the time of writing) CMOS sensors with small pixel sizes are made for compact, high-resolution color imaging in portable devices.

A previous work by Wilkes *et al.* have found an elegant solution for the removal of the Bayer color filter [193]. They found that a commercial photoresist remover could remove the Bayer filter of the Raspberry Pi v1 camera module. This chemical method provides for a uniform finish, and proves to be a near-ideal method. However, we were unable to reproduce such results with the Raspberry Pi v2 module. This may be due to the difference in suppliers (v1 was supplied by Omnivision whereas the v2 by Sony), and correspondingly, the different processes and materials used in the production of the sensors.

While obtaining the v1 camera (currently out of production) and using it is one solution, the v2 module is more readily available, and the pixel size is smaller for the latter (1.12 μm vs 1.4 μm for the v1), advantageous for our current application. As we were unable to find a chemical solution for the de-Bayering of the v2 camera, we resort to a more primitive solution: manual scraping. The back-illuminated sensor architecture allows for the scraping of the sensor surface without damaging sensitive circuitry, which is below the silicon surface of the material.

For the scraper, we use a fragment of a razor blade. This fragment was created by manually breaking off portions from a larger, commercial razor blade. Ideal fragment sizes were around 500 μm in width. The blade fragments were held with pliers; the whole contraption was used to gently scrape the camera surface. Done with enough force, the blade removes the outer layers, with minimal damage to the underlying silicon surface. Finer remains were scraped with a toothpick. Debris were washed off with ethanol, and ultrasonically cleaned as well after the process was over. As the surrounding of the sensor has many sensitive wires protruding from it[4], only the middle portion of the sensor was scraped.

The edge portion of the scraped region is shown in Figure B.2.2, with appropriate regions annotated. The green surrounding region is the pristine CMOS surface, as is shown magnified in Figure B.2.1. It appears predominantly green due to the predominantly green pixels in the Bayer array. The microlens array on top of the Bayer can be scraped off, which reveals several layers of material underneath. While the specific composition of each layer is as of yet unknown, it was found that when the material was scraped to the gray layer in the picture, all color-response of observed images was lost. We believe this layer to be some sort of buffer layer. There is another layer below the gray region (gold in the picture), which is believed to be the bare silicon itself. While scraping to this layer results in improved sensitivity, the probability of damage to the sensor itself was found to increase substantially. In our current use, we want to view focused laser light, where sensitivity is not an issue. Thus, we mainly stopped scraping at the gray layer to create our monochromatic sensors with less chance of damage.

---

[4] By the wiring, we refer not only to the gold wiring around the sensor, but wiring surrounding the active area of the sensor itself. Any scratches to this region resulted in a high-probability of sensor malfunction, so care must be taken not to touch these sections.

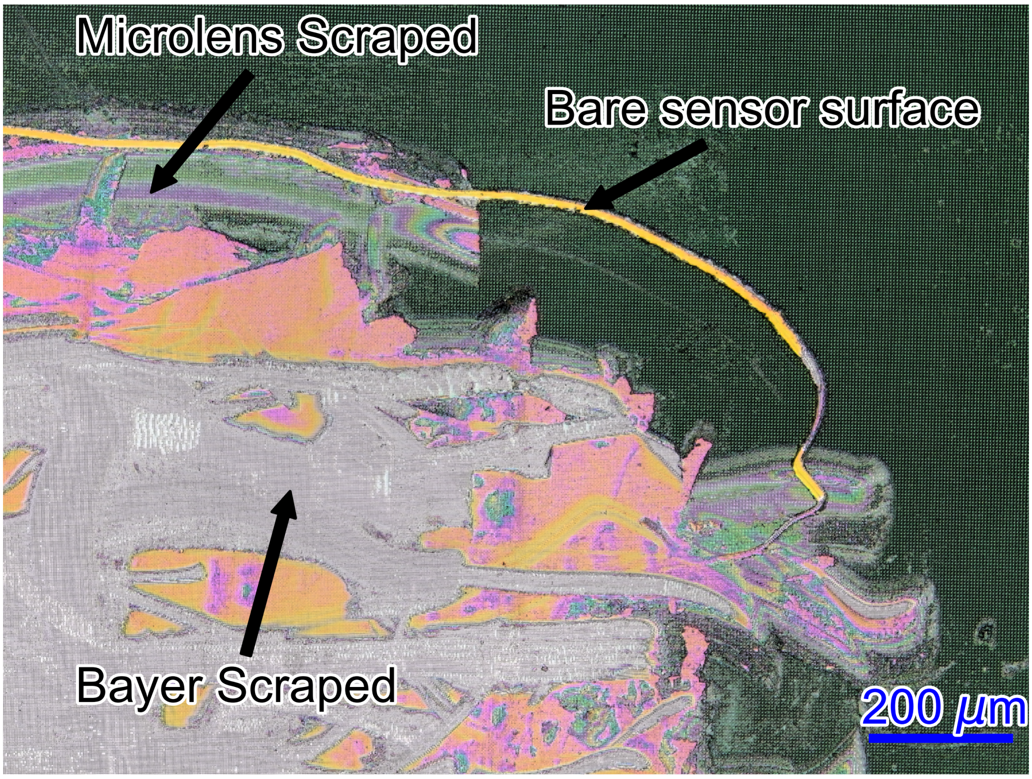

Figure B.2.2.: Laser scanning microscope image of the bayer-scraped CMOS sensor surface.

Figure B.2.3.: Picture taken with a scraped camera of scattered light from a red laser pointer (640 nm wavelength).

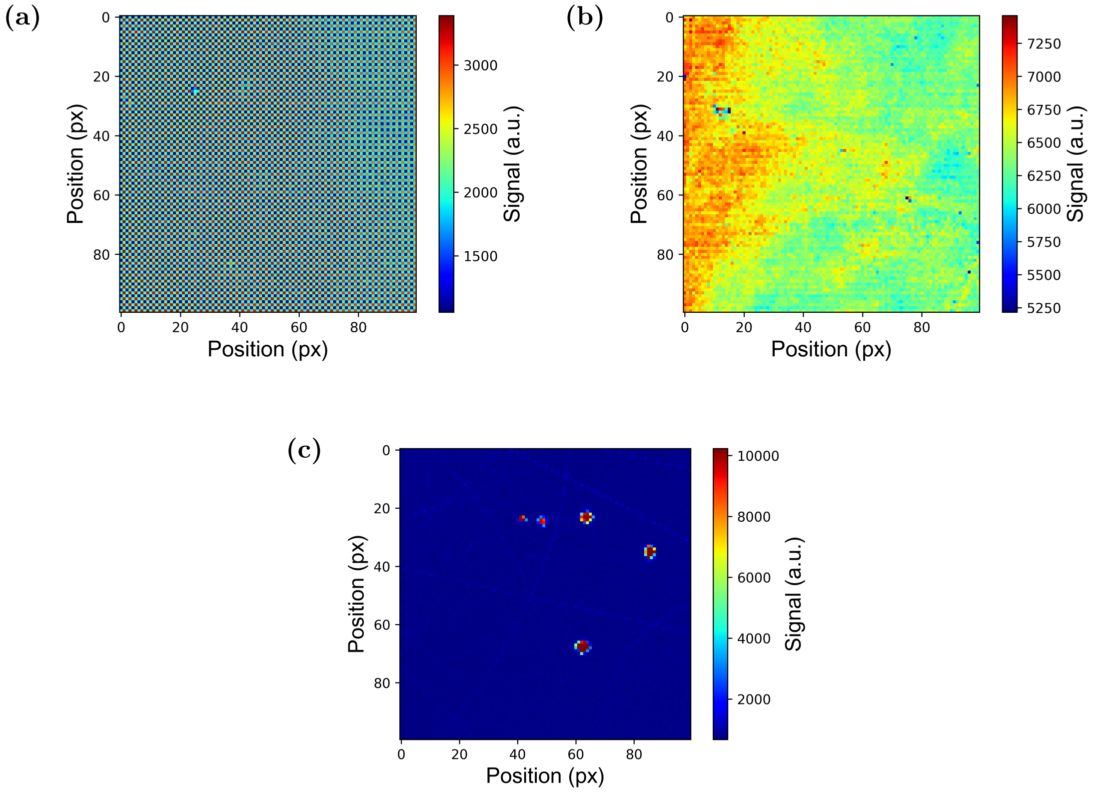

Figure B.2.4.: (a) Scattered 750 nm light from an OPA imaged with an unprocessed camera. (b) The same light imaged with the scraped sensor. (c)) The same light imaged with a sensor scraped to the silicon, with damage spots.

A color picture image taken from the scraped sensor is shown in Figure B.2.3. The sensor here was exposed to scattered light from a red laser pointer. The surrounding regions where the sensor still functions registers the light as red. However, as the light in the scraped regions activates all color pixels, the camera registers light from these regions as white. The large scratch in the bottom right portion of the scraped region corresponds to a section where the sensor was scraped to the underlying silicon; the spectral response is similar, but the sensitivity is much higher.

To illustrate further the effect of removing the bayer filter, we take images of scattered 750 nm light from an OPA The images from a pristine, scraped, and damaged camera are shown in Figure B.2.4. Ten 10-bit frames were averaged to make each image (Thus, the intensity scales from 0 to 10230). In the picture for the Bayer signal, the differing spectral response from each pixel can be observed clearly, where the highest signals come from the red pixels, intermediate signals from the green, and lowest signals from the blue pixels. The color scale coincidentally corresponds to the type of pixels in this case. For the scraped sensor, a locally uniform response independent of the pixel position can be observed. The gradual change in signal level is due to the non-uniform illumination of the sensor. While slight spots with higher or lower response can be observed, provided the surface is cleaned further and a better location is selected, these artifacts can be

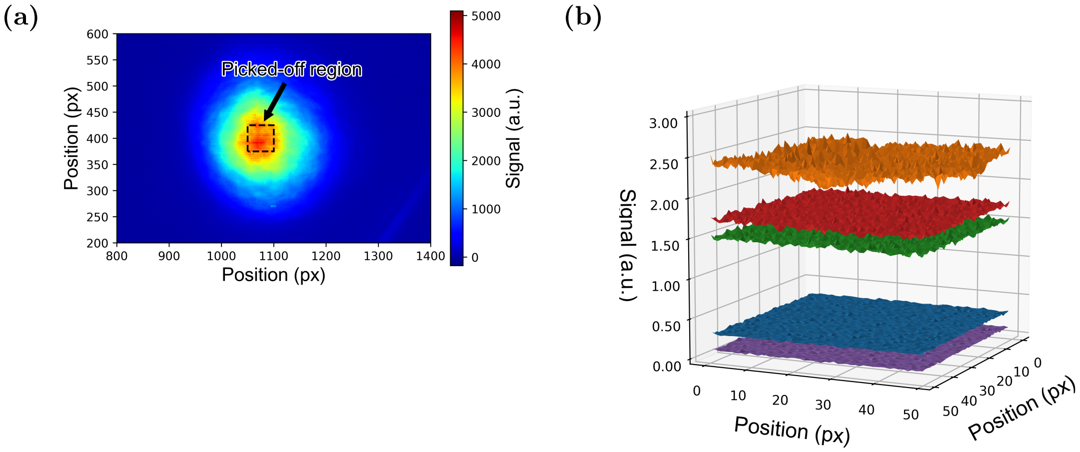

Figure B.2.5.: (a) One of the frames taken of an unfocused beam of 750 nm light. (b) The signal strength of the picked-off region (labeled in (a)) relative to a reference frame.

reduced. Slight lateral striations in the signal can also be observed, which we believe to be mostly due to some form of readout noise. The fluctuations were found to be of an order of a few percent. Finally, the case for a sensor scraped to the bare silicon substrate is also shown in Figure B.2.4c. Point-like damage to this surface will often result in hot-spots, which manifest as saturated spots irregardless of the incident light. Five hot spots can be seen in the figure. For this reason, it was found to be generally safer not to scrape to the bare sensor.

In order for the scraped camera to work effectively as a profiler, two conditions should be met. The first is power linearity. While we do not directly confirm the linearity here, previous works have found the global linearity of the camera module to be good [193, 190]. The removal of the Bayer filter should not affect this property, but the presence of partially removed filters may affect the local linearity. To roughly gauge the uniformity of the sensor linearity, we shine the attenuated output of an OPA at 750 nm onto the sensor surface without focusing, as shown in Figure B.2.5a. Again, each image taken is the sum of ten 10-bit frames. We take several of these profiles at differing OPA powers, subtracting the values from a background picture. We then normalize the intensity distribution of all frames by dividing by a single reference frame with moderate intensity, to compensate for the intrinsic laser spatial distribution.

The result of the normalized power-dependence is shown in Figure B.2.5b. An ideal sensor would show a flat response, indicating that each pixel linearity is equivalent. The fluctuations observed correspond to a standard deviation of around 2% at moderate intensities. Thus, we believe that while the large-area uniformity is expected to be inferior due to the rough nature of the scraping process, small sections suficient for focused beam profiling still exhibits uniformity comparable to that of chemical methods [193].

The second condition is the uniformity of the signal itself. While we did not have a uniform light source at hand, the pixel-to-pixel differences for an unfocused beam should be small. Thus, the local gradient should allow us to gauge the values of the local

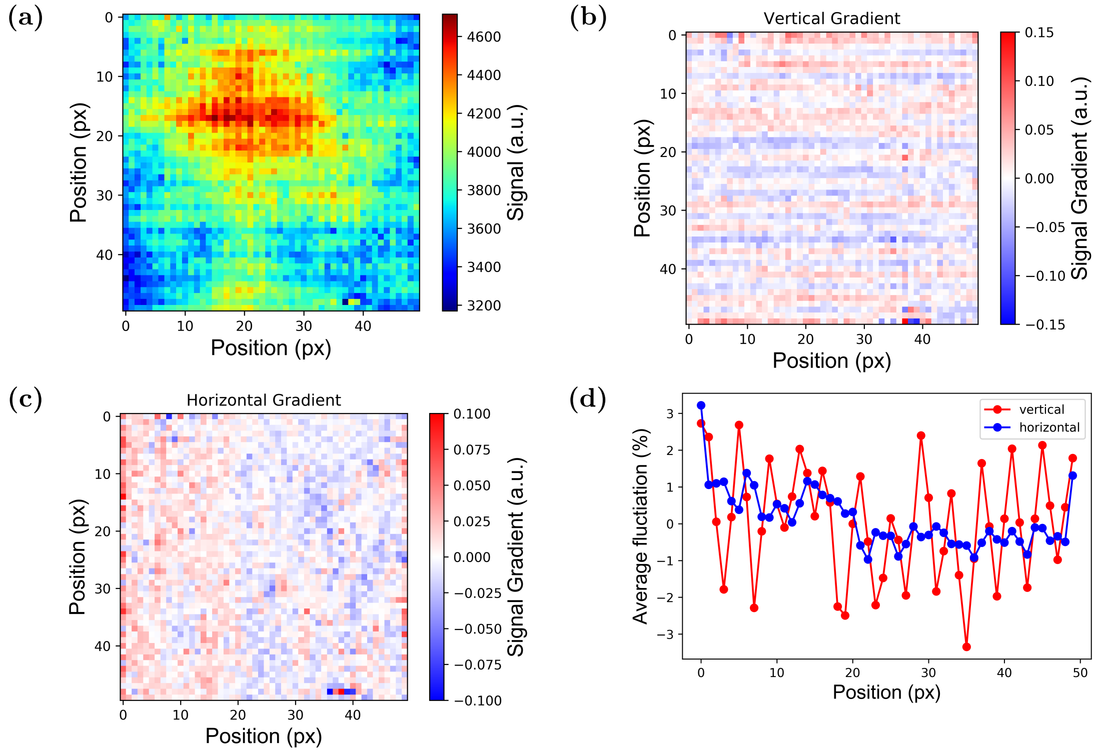

Figure B.2.6.: (a) The central region of the reference frame shown in Figure B.2.5a. The normalized differential signal in the (b) vertical and (c) horizontal directions. (c) The averaged signal fluctuations in the vertical and horizontal directions.

fluctuations. We take the pixel-to-pixel differential of the central region in Figure B.2.5a, as shown in Figure B.2.6a. We then take the vertical and horizontal differential value, and normalize this value by the pixel intensity. The results are shown in Figure B.2.6a and B.2.6a, respectively. Clear striations are visible in the vertical gradient. To better extract trends, the striations are averaged in their respective directions, as shown in Figure B.2.6d. A clear period of 4 pixels for the striations can be observed in the vertical direction, while no clear trend can be seen in the horizontal. The average amplitude for the vertical oscillation is around 4% of the signal peak-to-peak. As the scraping process is not expected to create such uniform striations, we believe this to be mainly due to intrinsic readout noise in the camera. While this may be a problem for the profiling capabilities for beams with sizes comparable to this striation period, as we deal with moderately focused beams (with beam diameters of around 30 μm) in this thesis, the striations are believed to effectively average out.

While the specifics of the camera beam profiler, such as the uniformity, are still inferior to commercial beam profilers, the large pixel sizes allows the camera to resolve structures more clearly. Typical commercial beam profilers have pixel sizes of 4 to 6 μm. The developed profiler correspondingly has an order of magnitude more pixels per area than a conventional profiler. This results in a difference of 25 or so active pixels for a 20 μm diameter beam, to 400 pixels, which was key to resolving focused beams in this work.

B.3. Beam profiler application

While beam profiling from the command line is possible, to facilitate easy use, a graphical user interface (GUI) application was created to enable basic functions of a standard beam profiler: mainly finding the beam, measuring the beam, and saving the data. All code was made in the Python programming language. The GUI was made with the PyQT5 library[5]. Control of the camera was done with the picamera library[6], which provides functions and classes to manipulate and retrieve data from the camera. Visualization of this data was done with the matplotlib python 2D plotting library[7], while underlying operations (cropping and saving) were done with the numpy library[8], a standard array manipulation library. Simple fitting and beam profile generation was done with the laserbeamsize module[9]. The program consists of a main python file, and several .ui (in XML format) template files, which provide information regarding the GUI layout used to render the application.

B.3.1. Basic operation

Upon execution of the main python file, the main screen of the program is shown. A screenshot of the application is shown in Figure B.3.1. The menu has four screens:

- *Beam Image*: The current beam profile (full or cropped)
- *X-Profile*: The signal profile taken along the vertical slider (left to Y-Profile)
- *Y-Profile*: The signal profile taken along the horizontal slider (above X-Profile)
- *Background*: The image used as background, if a background is taken

The *x pos* and *y pos* boxes display the coordinates of the profile sliders, with (0,0) corresponding to the bottom left (as in a normal coordinate plane).

The buttons are used to manipulate the image. Their effects are rather self-explanatory:

- *Take Background*: Takes a background frame. If a background image is present (shown in the bottom right window), subsequent images will show the signal automatically subtracted by the background.
- *Take Profile* (Shortcut: Ctrl+D): Takes an image with the camera, with settings according to the current camera settings (explained later).
- *Fit!* (Shortcut: Ctrl+F): Conducts a D4σ analysis of the image. It should be noted that this will only yield accurate results in pictures with 1. relatively little

---

[5] http://pyqt.sourceforge.net/Docs/PyQt5/

[6] https://picamera.readthedocs.io/en/latest/

[7] https://matplotlib.org/

[8] http://www.numpy.org/

[9] https://github.com/scottprahl/laserbeamsize

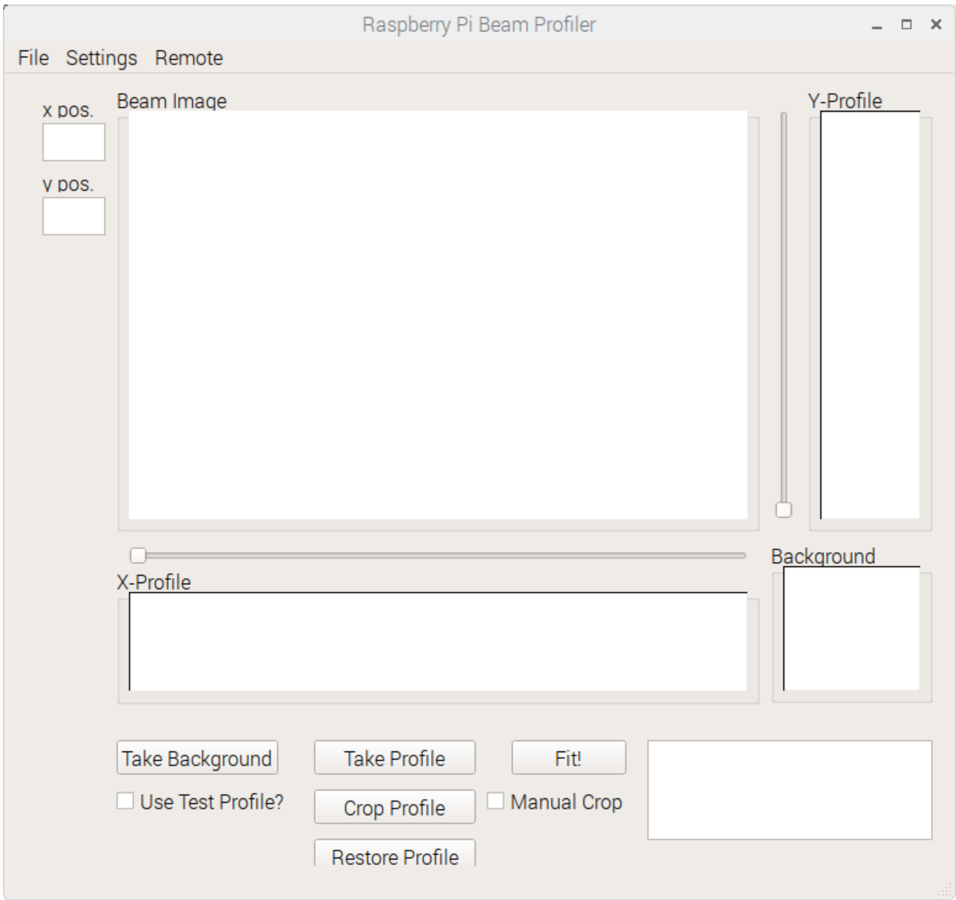

Figure B.3.1.: Screenshot of the starting screen

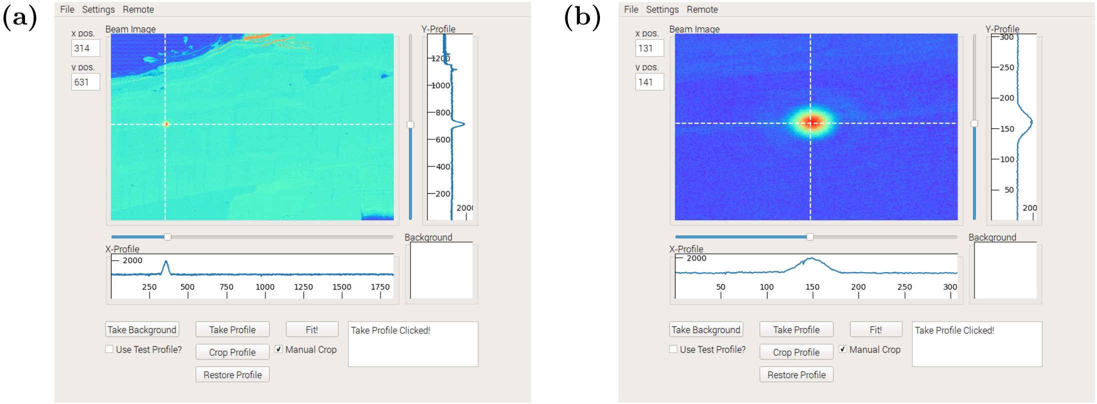

(a)

x pos. 314

y pos. 631

☐ Use Test Profile?

☑ Manual Crop

Take Profile Clicked!

(b)

x pos. 131

y pos. 141

☐ Use Test Profile?

☑ Manual Crop

Take Profile Clicked!

Figure B.3.2.: (a) A full image of a beam profile. The X- and Y-Profile cut positions are overlayed as white dashed lines. (b) The cropped beam profile. No background image is taken for the current image.

noise and 2. with proper background subtraction already conducted. Results are displayed in the text box next to this button.

- *Crop Profile* (Shortcut: Ctrl+G): Crops (zooms into a rectangular sub-region) the current beam image according to the settings set in the crop settings menu (explained later). A manual based on user-inputted settings, or an automatic crop based on fit values may be chosen with the check mark to the button's right.
- *Restore Profile* (Shortcut: Ctrl+R): Restore the profile to the pre-cropped full image.

An image crop can also be conducted graphically by clicking and dragging the mouse over the corresponding beam region. A red box will highlight the extracted range. Hovering over the beam image also reveals a hover-text which shows the (x,y) coordinates of the point, as well as the signal value at that point. When a crop is enacted, the (x,y) coordinates are reset to the (0,0) position. Coordinates are always relative to the current image. Thus, a raw image of size 1001 will have coordinates 0 to 1001; this image cropped to a 201 pixel range between 400 and 600 will yield an image with coordinates varying from 0 to 200. Restated, crops do not preserve the original coordinate location[10]. After each crop, the color scale of the image is reset so that the highest pixel value is red, while the lowest is purple.

Taking a background image allows for the removal of the background noise. It should be noted that the camera is still limited to a 10-bit (0 to 1023) signal. The background frame is only used in post-processing, and does not increase the dynamic range of the camera. Profiling should all be done in the dark. Typical background counts for a 100 ms exposure time is around 60 counts. A background compensated image is shown in Figure B.3.3. A miniaturized image of the background is visible in the lower-right frame.

---

[10] Thus, one should *not* enact multiple crops, as the coordinates will not make sense for the cropped image. In some cases, the coordinates will be outside the range of the image and result in an error.

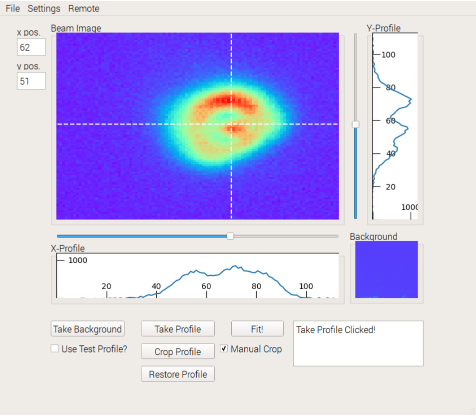

x pos. 62
y pos. 51
☐ Use Test Profile?
☑ Manual Crop
Take Profile Clicked!

Figure B.3.3.: A beam image with the background substracted. The donut shape of the beam is due to spherical abberation in the focusing setup.

Along the top of the window is the menu bar, with three main items. The composition of the menu bar is shown below:

```
Menu Bar
 |__File
 |   |__Save Cropped Profile   Ctrl+S
 |   |__Save Full Profile   Ctrl+A
 |__Settings
 |   |__Camera Settings
 |   |__Crop Settings
 |__Remote
     |__Remote Setup
     |__Start Remote
```

The commands are:

- *Save Cropped Profile* (Shortcut: Ctrl+S): Saves the current beam profile image into a text file. Upon execution a file menu will allow for selection of a filename and directory.
- *Save Full Profile* (Shortcut: Ctrl+A): Saves the original full-size image taken from the camera (1640×1232 pixels) in the middle of the sensor.
- *Camera Settings*: Loads the Camera Settings menu.
- *Crop Settings*: Loads the Crop Settings menu.
- *Remote Setup*: Loads the Remote Setup menu.
- *Start Remote*: Starts remote mode of the program, where the device can be remotely controlled by tcp communication commands sent via Ethernet cable.

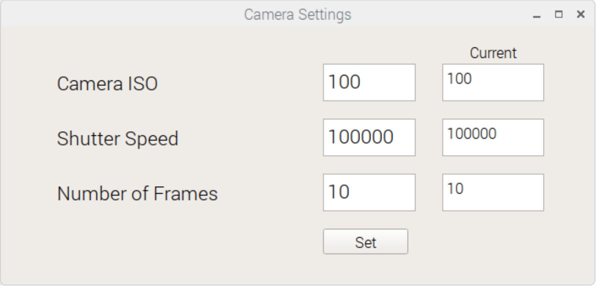

		Current
Camera ISO	100	100
Shutter Speed	100000	100000
Number of Frames	10	10

Figure B.3.4.: Screenshot of the Camera Settings menu.

The Camera Settings menu is shown in Figure B.3.4. The setting allows the user to change three parameters: the camera ISO, the shutter speed, and the number of frames. The "camera ISO" determines the digital and analog gain of the camera sensor, with 100 being low gain and higher values corresponding to higher gains. For beam profiling of a focused beam, the signal of the beam is usually very strong, and the lowest setting of 100 is sufficient. The "shutter speed" determines the electronic shutter speed of the camera in units of μs. It should be noted that the raspberry pi operates with a rolling shutter. Shutter speeds comparable to fluctuations in the capturing image will result in rolling shutter noise. In the case of profiling pulsed lasers, this results in ripple-like artifacts in the image. The "number of frames" is the number of images to integrate into the final beam profile. Typically, the experiments in the thesis were done with an ISO of 100, shutter speed of 100 ms, and 10-frame profiles.

The Crop Settings menu is shown in Figure B.3.5. The menu is divided vertically into two parts: the automatic crop settings and the manual crop settings. In the automatic crop settings, the cropped range in an automatic crop can be adjusted in units of the calculated beam radius from a D4σ analysis. A rectangular range centered around the beam center and with widths of the crop setting on either side will be made. Similarly, a manual crop allows the specification of a rectangular region based on a center pixel

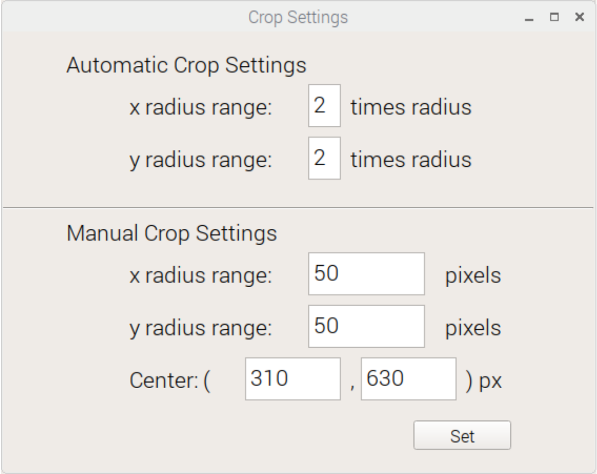

Automatic Crop Settings

x radius range: 2 times radius

y radius range: 2 times radius

Manual Crop Settings

x radius range: 50 pixels

y radius range: 50 pixels

Center: (310 , 630) px

Figure B.3.5.: Screenshot of the Crop Settings menu.

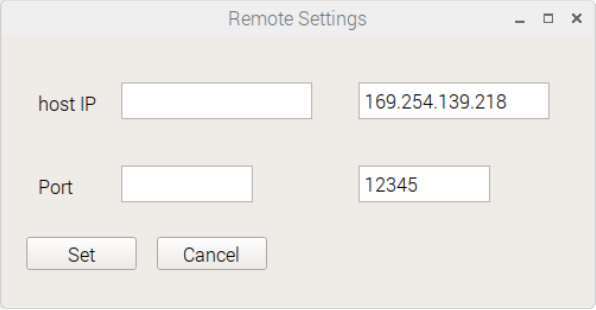

host IP 169.254.139.218

Port 12345

Figure B.3.6.: Screenshot of the Remote Settings menu.

coordinate instead of the fit center, and two x- and y-pixel range values instead of the beam radius.

The Remote Settings menu allows the configuration of the TCP communication used in the remote mode. A screenshot of the menu is shown in Figure B.3.6. The host IP is the IP address of the Ethernet port of the current Raspberry Pi module, and the Port should be an arbitrary value not already attributed to other TCP communication protocols (in general, an arbitrary high integer value should work).

B.3.2. Video mode

In order to assist in aligning the beam, two video modes were implemented.

The *full video mode* shows the video feedback from the camera in real-time as an overlay over the Raspberry Pi display. The mode can be accessed by pressing “F1” and exited by pressing “F2”. In the video screen, the whole sensor is shown. The relevant region used in beam profiling are highlighted in green, and labeled on the screen correspondingly. This mode is useful for initial alignment.

A second *zoomed video mode* shows a zoomed-in video feedback from the camera. It is displayed likewise as a real-time overlay on the Raspberry Pi display. The zoomed region is approximately the region specified by the manual crop region set in the Crop Settings menu. This menu can be accessed by pressing “F3” and exited by pressing “F2” (the exit button is common between the two modes). This mode is good for finding an optimal position to an already moderately focused beam, where the full video mode resolution is insufficient to make out the finer details.

B.3.3. Remote mode

By clicking the Start Remote option in the menu, the remote mode may be accessed. The raspberry pi acts as a host server, and waits for a client to connect. For example, the client could be a PC running LabView, connected to the Raspberry Pi by Ethernet cable.

Once connected, the Raspberry Pi can accept byte messages from the client. Four basic commands were implemented:

- *take*: Functions as if the take profile button was clicked.
- *crop*: Functions as if the crop profile button was clicked in manual mode.
- *save*: Functions as if the save cropped profile button was clicked. When prompted, the Raspberry Pi will send a byte message of "filename?\r\n" to the client, where \r and \n are the carriage return (CR) and line feed (LF) ASCII codes, respectively. The client should send the desired filename in bytes in return. The file will be saved to the same directory as the beam profiler program.
- *quit*: Quits the remote mode, returning the device to normal operation.

By using the remote mode, the beam profiler can be flexibly incorporated into experimental systems controlled by another master computer as a slave device.